The Dissertation Committee for Thomas Earl Dyson Certifies that this is the approved version of the following dissertation:

Experimental and Computational Investigation of Film Cooling on a Large Scale C3X Turbine Vane Including Conjugate Effects

Committee:

David Bogard, Supervisor

Sean Bradshaw

Jayathi Murthy

Venkat Raman

Li Shi

Experimental and Computational Investigation of Film Cooling on a Large Scale C3X Turbine Vane Including Conjugate Effects

by

Thomas Earl Dyson, B.S., M.S.E.

Dissertation

Presented to the Faculty of the Graduate School of

The University of Texas at Austin

in Partial Fulfillment

of the Requirements

for the Degree of

Doctor of Philosophy

The University of Texas at Austin

December, 2012

Acknowledgements

First, I would like to thank Dr. David Bogard for his guidance and support throughout the last several years. His efforts have been instrumental to the production of this work and my development as an engineer. I would also like to gratefully acknowledge the financial support of Pratt & Whitney and UTC. I would particularly like to thank Dr. Sean Bradshaw for his technical guidance on the project and for teaching me how to use ANSYS FLUENT. I also would like to thank Mrs. Geraldine Campbell Naschke for her financial support through the Thrust 2000 Endowed Fellowship in Engineering.

I would also like to thank Cengiz Vural for keeping the UT HPC center running smoothly and working with me to get the most out of the department's computational resources. The production of the test vanes used for this study was only possible through the efforts of Aaron Frost and Scott Allen of the UT ME shop. Their input on the construction and building of the vane and hatches was invaluable.

Lastly, but certainly not least, I would like to thank the other members of the TTCRL group for their help in collection of data and processing the results. John McClintic, Emily Boyd, Todd Davidson, Jason Albert, Randy Williams, David Kistenmacher, and Jason Dees all contributed in one way or another to the production of this work. Without their help it never would have been completed.

Experimental and Computational Investigation of Film Cooling on a Large Scale C3X Turbine Vane Including Conjugate Effects

Thomas Earl Dyson, PhD

The University of Texas at Austin, 2012

Supervisor: David Bogard

This study focused on the improvement of film cooling for gas turbine vanes using both computational and experimental techniques. The experimental component used a matched Biot number model to measure scaled surface temperature (overall effectiveness) distributions representative of engine conditions for two new configurations. One configuration consisted of a single row of holes on the pressure surface while the other used numerous film cooling holes over the entire vane including a showerhead. Both configurations used internal impingement cooling representative of a 1st vane. Adiabatic effectiveness was also measured. No previous studies had shown the effect of injection on the mean and fluctuating velocity profiles for the suction surface, so measurements were made at two locations immediately upstream of film cooling holes from the fully cooled cooling configuration. Different blowing conditions were evaluated. Computational tools are increasingly important in the design of advanced gas turbine engines and validation of these tools is required prior to integration into the design process. Two film cooling configurations were simulated and

compared to past experimental work. Data from matched Biot number experiments was used to validate the overall effectiveness from conjugate simulations in addition to adiabatic effectiveness. A simulation of a single row of cooling holes on the suction side also gave additional insight into the interaction of film cooling jets with the thermal boundary layer. A showerhead configuration was also simulated. The final portion of this study sought to evaluate the performance of six RANS models (standard, realizable, and renormalization group k-ε; standard k-ω; k-ω SST; and Transition SST) with respect to the prediction of thermal boundary layers. The turbulent Prandtl number was varied to test a simple method for improvement of the thermal boundary layer predictions.

Table of Contents

List of Tables

List of Figures

Nomenclature

Bi	Biot number ($h_f t/k$)
c	vane chord (531 mm)
d	hole diameter (usually 6.35 mm)
D	diameter (generic)
h	heat transfer coefficient
H	vane height (547 mm)
I	momentum flux ratio
k	turbulent kinetic energy or thermal conductivity
M	mass flux (or blowing) ratio
NHFR	net heat flux reduction
Nu	Nusselt number
P	pressure
Pr	Prandtl number
PS	pressure side
q	heat flux
RANS	Reynolds-averaged Navier-Stokes
Re	Reynolds number
RKE	realizable *k*-*ε* (turbulence model)
RNG	renormalization group (*k*-*ε* turbulence model)
SH	showerhead
SS	suction side
t	wall thickness

T	temperature
u	stream-wise velocity
v	wall-normal velocity
w	span-wise velocity
y	wall-normal coordinate

Greek Letters

α	film cooling stream-wise injection angle
β	relative thermal boundary layer strength parameter
γ	specific heat ratio
δ	boundary layer thickness (99% if not otherwise specified)
ε	turbulent dissipation
η	efficiency, adiabatic effectiveness, or a similarity variable
θ	momentum thickness or non-dimensional temperature
κ	von Karman constant
Λ	turbulence integral length scale
ν	kinematic viscosity
τ	shear
ϕ	overall effectiveness
χ	coolant warming factor
ω	specific turbulent dissipation

Subscripts, Accents

atm	atmospheric

aw	adiabatic wall
c	coolant
e	condition at the edge of the viscous boundary layer
f	with film cooling
i	blade or vane internal property
j	impingement jet
o	orifice plate
p	predicted inviscid velocity
rms	root-mean-square (of fluctuating velocity)
sp	superposition
t	turbulent
w	wall
θ	momentum thickness
0	without film cooling
95	95% boundary layer thickness
99	99% boundary layer thickness
∞	mainstream
‘	fluctuating component of Reynolds decomposition
“	per unit area
+	inner velocity scale ($\propto u_\tau$)
*	turbulent near-wall scaling ($\propto k^{½}$) or momentum flux ratio using approach velocity

Chapter 1 – Introduction

Since the 1950s, the gas turbine has been an important means of producing propulsive power for aircraft. Their capability to produce large quantities of thrust in a relatively small, light package makes them an ideal choice for aircraft application. While the vast majority of gas turbines are still used in aviation, they have also become an increasingly important part of the electrical power grid. Because gas turbines can ramp up from a dead stop to full power in a matter of minutes, they have long been used for load following and "peaking" operations when traditional generation sources would have difficulty meeting demand. However, gas turbines can also be used in combined cycle plants that may exceed 60% thermal efficiency [1] and produce hundreds of MW. Combined with increased concern over the pollution produced by coal fired plants and the low cost of natural gas, there has been increased use of gas turbines for base-load generation.

Even with the high efficiency available from modern engines, the cost of fueling gas turbines remains high. The US air fleet alone consumes approximately 500 million barrels of fuel, which even at the low prices of fuel in 2009 represented over $36 billion in fuel costs [2]. The cost of natural gas for power generation in the US was approximately $39 billion in 2010 [2], and that value will only increase as new plants are built to increase capacity and replace old coal fired generators (nearly 12 GW of new gas turbine capacity was added to the grid in 2011 [3]). With costs this high, even an incremental improvement of

less than 1% would stand to save aircraft operators and power companies hundreds of millions every year.

1.1. The march toward higher temperatures

Gas turbine engines operate using the Brayton cycle, which was first described in 1872 [4]. The details of the cycle place certain thermodynamic limits on the efficiency that can be obtained from any engine that uses it. A representation of the cycle using isentropic expansion and compression, neglecting other losses, and a few other simplifying assumptions (*e.g.*, ideal gas) arrives at two expressions that can be used to represent the efficiency, η [5]:

$$\eta = 1 - \frac{T_4 - T_1}{T_3 - T_2} \tag{1.1.1}$$

$$\eta = 1 - \frac{1}{\left(P_2/P_1\right)^{(\gamma-1)/\gamma}} \tag{1.1.2}$$

where P is the pressure, T is the temperature, γ is the specific heat ratio, and the numbers correspond to the states shown in Fig. 1.1.1.

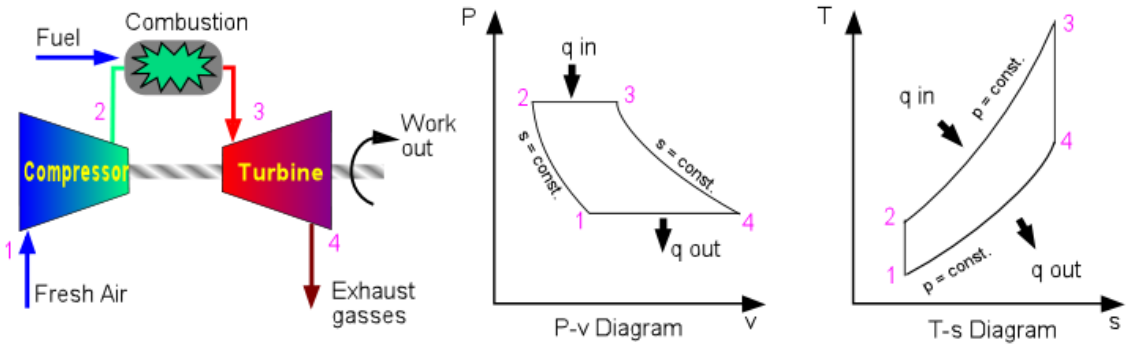

Figure 1.1.1: An ideal Brayton cycle [6]

For an ideal system, these expressions show that there are only a few methods that may be used to improve the efficiency of the cycle:

- Increase P_2/P_1, the compressor pressure ratio
- Reduce T_2, the combustion inlet temperature
- Reduce T_1, the compressor inlet temperature
- Reduce T_4, the turbine exhaust temperature
- Increase T_3, the turbine inlet temperature

Increasing the compressor pressure ratio also increases T_2 (this is not shown in Eqn. 1.1.2 because of the isentropic compression assumption), so it cannot be increased without bound. The ideal value varies with other factors, but lies on the order of 30:1, which is easily achievable in modern engines. Reduction of T_2 is useful for land based gas turbines, but because it generally requires bulky, heavy intercoolers, it is impractical for aircraft applications. Some measure of control of the inlet temperature is available for aircraft, which can climb to higher altitudes. Additionally, water mist can be sprayed into the airstream to cool it through evaporation. However, the required weight of water is prohibitive for aircraft, so this is typically only used during takeoff where the

additional thrust is needed. Reduction of T_4 is also limited in aircraft due to packaging considerations (*e.g.*, the weight of additional turbine stages) and thrust availability. Thus, increasing the turbine inlet temperature has been a key focus for improving the power and efficiency of aircraft engines.

Increasing turbine inlet temperature is quite challenging, as it is easy to exceed the permissible operating temperature of various components. Nevertheless, turbine inlet temperatures have steadily risen over the last 60 years (shown in Fig. 1.1.2) as increasingly advanced materials and cooling technologies were developed. Modern engines have reached a point where the inlet temperatures may be near 2,250 K [7], which is nearly hot enough to boil silver and approximately 550 K hotter than the melting point of the nickel based alloys that engine components are constructed from [8]. Further, in order for these parts to have an acceptable service life (20,000 hours has become common) the surface temperatures of the turbine components should not exceed approximately 1,300 K [9]. The capabilities of modern engines are astounding, but there is continued pressure to continue to improve designs for even higher temperatures. Of particular interest to this study are the cooling technologies used for turbine blades and vanes.

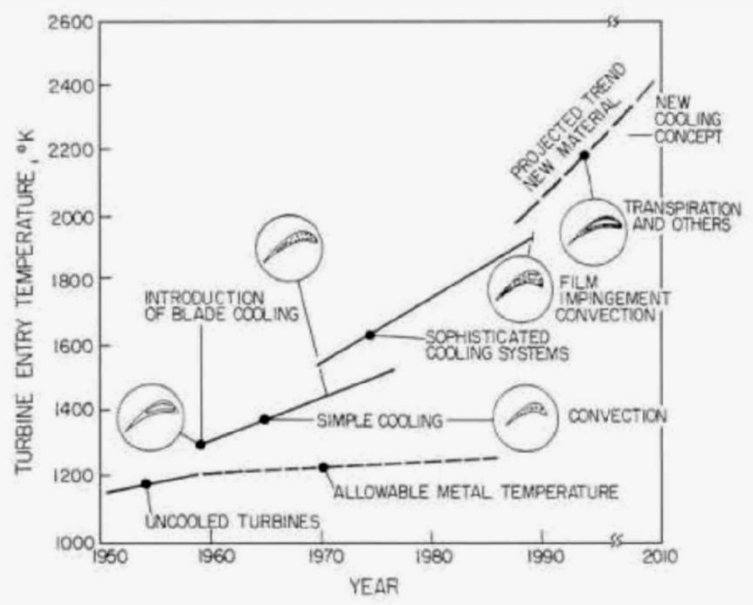

Figure 1.1.2: Progression of T_3 over the past 60 years, from Han *et al.* [10]

1.2. Turbine cooling basics

There are three basic means available to turbine designers to keep surface temperatures within an acceptable range. The first, and conceptually simplest, method is to coat the parts with a material that can withstand higher temperatures than the metal, such as a ceramic, to insulate the part. However, this thermal barrier coating can only function in the presence of some form of active cooling, which can take many forms. A turbine blade containing many forms of active cooling is shown in Fig. 1.2.1. All these techniques rely on the use of relatively cool air drawn from the compressor stage of the turbine. However, it is important that this coolant be used efficiently; any air extracted for use as coolant is lost to the cycle and therefore represents a loss.

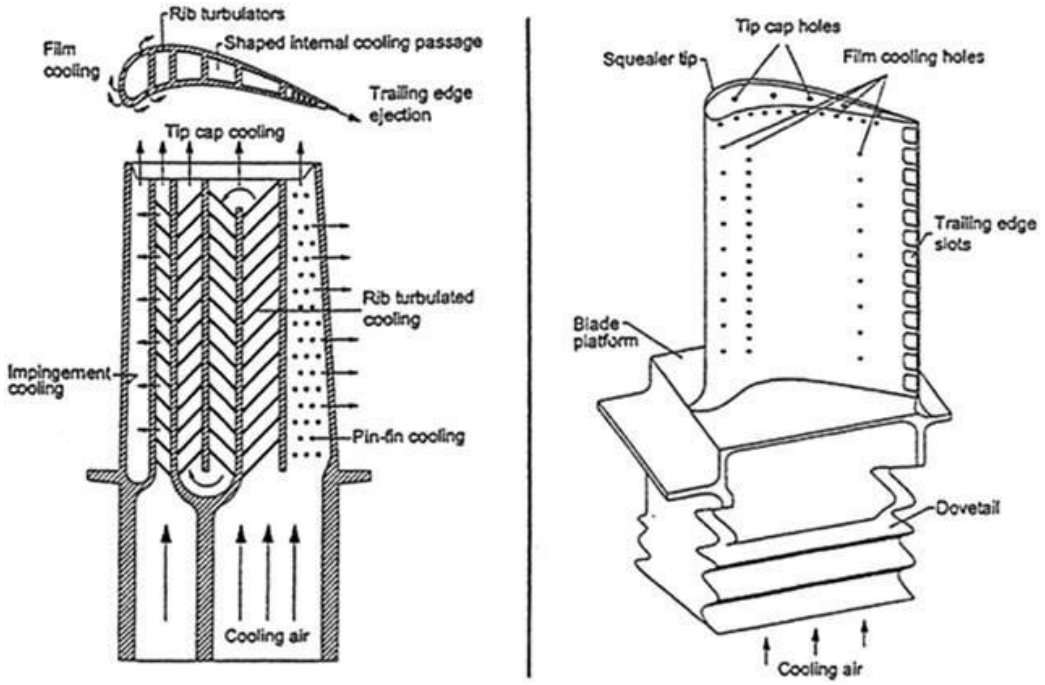

Figure 1.2.1: Schematic of a turbine blade employing many internal (left) and external (right) cooling techniques, from Han *et al.* [10]

Coolant enters the turbine blades through the root, where it passes through internal channels that may have features such as ribs, pin fins, or impingement holes designed to increase heat transfer. The optimal use of internal coolant passages without the creation of unacceptably high pressure losses is an area of active research. The coolant can either be returned through the root of the blade, or it can be exhausted out of holes in the surface of the part. These holes, known as film cooling holes, are specially designed to provide additional cooling and protection from the hot mainstream.

1.2.1. Film cooling

The basic idea of film cooling is illustrated by Fig. 1.2.1.1, which shows coolant passing through holes in the surface and forming a protective layer on the exterior of the part. This protective layer can continue to cool the part while blocking mainstream gas from penetrating to the wall.

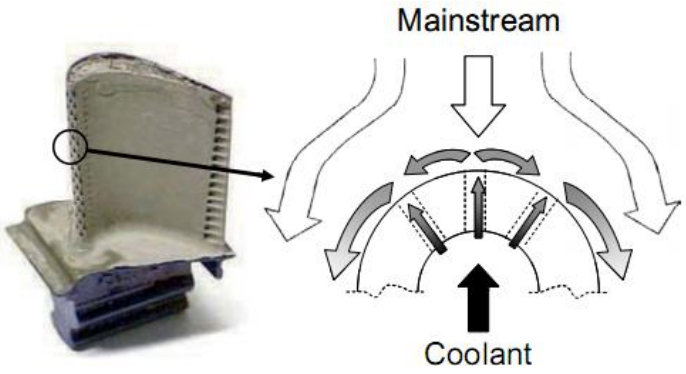

Figure 1.2.1.1: Diagram showing the basic idea behind film cooling, from Terrell [11]

Because testing new designs at engine conditions is difficult and expensive, many techniques have been developed to allow the development of advanced cooling designs under laboratory conditions. Conventionally, the heat transfer coefficient is defined:

$$h = \frac{q''}{(T_\infty - T_W)} \qquad (1.2.1.1)$$

where T_w is the wall temperature, T_∞ is the mainstream temperature, and q'' is the heat flux per unit area. However, this will produce values of h that change with the coolant temperature. Goldstein [12] proposed that the adiabatic wall

temperature, T_{aw}, may be used an alternative temperature in the definition of heat transfer coefficient:

$$h_f = \frac{q''}{(T_{aw} - T_W)} \tag{1.2.1.2}$$

This expression gives a means of predicting heat transfer independent of the coolant temperature. Therefore, one of the earliest – and still common – methods used is the construction of scale models from a low conductivity material, such as wood, plastic, or foam.

The adiabatic wall temperature may be normalized by the coolant temperature at the exit of the film cooling holes, $T_{c,exit}$:

$$\eta = \frac{T_\infty - T_{aw}}{T_\infty - T_{c,exit}} \tag{1.2.1.3}$$

which is known as the adiabatic effectiveness. This parameter is one of the most used metrics in film cooling design. It provides a means of comparing the relative performance of different hole configurations. However, η alone does not tell the full story. The introduction of coolant disrupts or destroys the boundary layer, dramatically altering the near-wall flow field and creating additional turbulence. Figure 1.2.1.2 shows the complex flow structure that accompanies the injection of a normal jet in cross-flow. Of particular importance to film cooling is the counter-rotating vortex pair because it is the dominate structure for inclined jets. The increased heat transfer produced by coolant injection may offset the benefit of the film. The method used to characterize the effect on heat transfer is to take the ratio of heat transfer coefficients with and without film cooling:

$$\frac{h_f}{h_0} = \frac{(q''/(T_{aw} - T_w))_{with\ film\ cooling}}{(q''/(T_{aw} - T_w))_{without\ film\ cooling}} \qquad (1.2.1.4)$$

to find what is usually called the heat transfer coefficient augmentation factor, h_f/h_0.

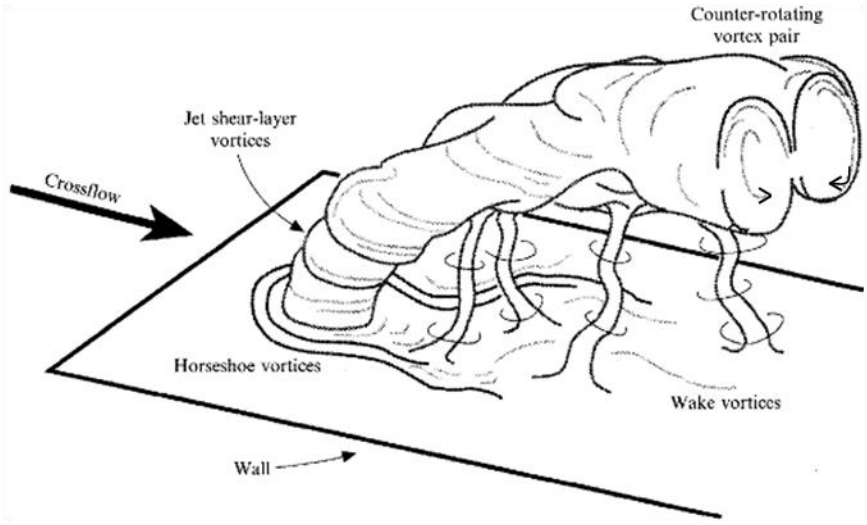

Figure 1.2.1.2: Diagram of the flow structures surrounding a normal jet in cross-flow from Fric and Roshko [13]

A convenient method for combining the effects of heat transfer augmentation with adiabatic effectiveness was proposed by Mick and Mayle [14] and independently by Sen *et al.* [15]. The technique starts with the assumption that the heat flux into the part changes with the addition of film cooling by:

$$\Delta q_r = 1 - \frac{q_f''}{q_0''} = 1 - \frac{h_f(T_{aw} - T_w)}{h_0(T_\infty - T_w)} \qquad (1.2.1.5)$$

where Δq_r is the net heat flux reduction (NHFR). This expression may be further reduced through application of Eqn. 1.2.1.3:

$$\Delta q_r = 1 - \frac{h_f}{h_0}\left(1 - \frac{\eta}{\phi}\right) \tag{1.2.1.6}$$

An additional parameter, ϕ, was introduced to normalize T_w. This parameter, often called the overall effectiveness, and is defined:

$$\phi = \frac{T_\infty - T_w}{T_\infty - T_{c,i}} \tag{1.2.1.7}$$

To use ϕ in Eq. 1.2.1.6 it must be assumed that the coolant temperatures $T_{c,i}$ and $T_{c,exit}$ are the same (generally not true) and that the wall temperature remains the same with and without film cooling (a major weakness of this analysis). Additionally, ϕ is typically unknown. Therefore, most NHFR analyses rely on the assumption that ϕ = 0.6 proposed by Mick and Mayle without justification. Despite its weaknesses, this parameter has become an important metric in film cooling design because it gives a single performance number which may be used to compare multiple configurations.

One of the key parameters affecting film cooling performance is the coolant flow rate. There are several ways of normalizing the coolant flow, but one of the most common is the blowing, or mass flux, ratio:

$$M = \frac{\rho_c U_c}{\rho_\infty U_\infty} \tag{1.2.1.8}$$

where ρ_c and ρ_∞ are the coolant and mainstream density, respectively, and U_c and U_∞ are the bulk coolant velocity exiting a film cooling hole and the over-lying mainstream velocity. Though this performance parameter is often used, Sinha *et al.* [16] showed that the momentum of the coolant jet was important for determining when a coolant jet would separate from the surface, reducing effectiveness. An alternative normalization, the momentum flux ratio, was better for scaling the performance when jet separation could occur:

$$I = \frac{\rho_c U_c^2}{\rho_\infty U_\infty^2} \tag{1.2.1.9}$$

One means of combining adiabatic effectiveness results from disparate tests is the method of superposition. The basic principle of superposition in film cooling, first proposed by Sellers [17], is that if the laterally averaged (*i.e.*, the average of η over a portion of the span, denoted by $\bar{\eta}$) adiabatic effectiveness distribution is known for a series of individual holes at different stream-wise position, then they may be added together using:

$$\bar{\eta}_{12} = \bar{\eta}_1 + \bar{\eta}_2(1 - \bar{\eta}_1) \tag{1.2.1.10}$$

which may be repeated for additional rows. The theory is that additional coolant injected downstream of another row of holes adds its coolant to the film, bringing the effectiveness closer to the maximum value of 1.0. It has long been known that this method has limitations. Goldstein [12] noted that it works reasonably well only for coolant flow rates that are not excessively large when jets from adjacent rows do not interact greatly, or are very far downstream from previous

injection. Metzger *et al.* [18] confirmed this with the additional restriction that a row of holes could not influence performance downstream of more than two downstream rows of holes. Ames [19] found that staggered rows (*i.e.*, adjacent rows of holes are positioned such that they cover different *z/H* positions) produced higher effectiveness than superposition would indicate because of reduced interaction, but this additional performance was reduced at high mainstream turbulence.

Typical practice uses adiabatic effectiveness from measurements or superposition and heat transfer augmentation as boundary conditions for an FEA solver. However vast, proprietary databases of empirical correlations are needed to augment and correct these predictions. In part this is necessary because adiabatic effectiveness does not include conjugate effects created by the interaction of the thermal fields with a conducting wall.

An alternative approach to predicting the surface temperature is to build a model that scales the external wall temperature to that of an engine part. Albert *et al*. [20] first demonstrated the practicality of measurements of this type. Using a 1D analysis, they demonstrated the scaling parameters required to build such a model.

1.2.2. Overall Cooling Effectiveness

While the analysis of Albert *et al*. was informative, it did not necessarily show all the correct scaling parameters. A more complete analysis for three dimensions starts with a section of wall some distance, *x*, downstream of a film

cooling hole, which is visualized by Fig. 1.2.2.1. Imagine that this segment of wall repeats periodically in the span-wise direction, *z*.

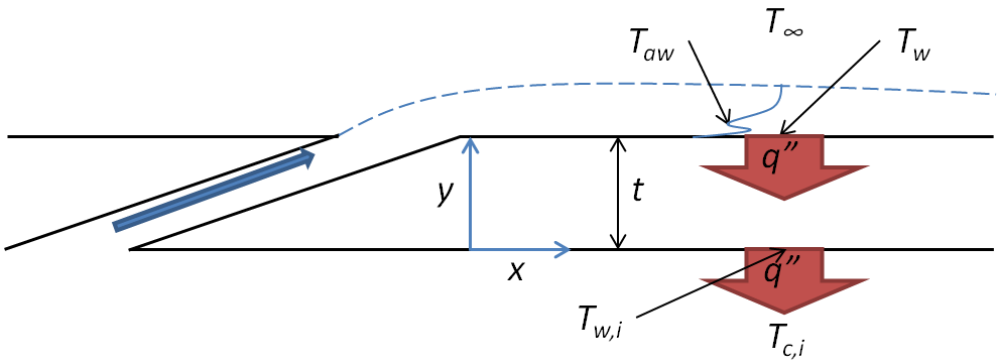

Figure 1.2.2.1: A simplified representation of the heat transfer through a film cooled part

The steady state heat diffusion equation for constant properties (in an engine part the temperature across the wall may in fact create substantial variation in *k*; however, this complication does not change the results of the current analysis) governs the solution for temperature through the wall of the part:

$$\frac{\partial^2 T}{\partial x^2} + \frac{\partial^2 T}{\partial y^2} + \frac{\partial^2 T}{\partial z^2} = 0 \qquad (1.2.2.1)$$

The boundary conditions for the solution at the inner and outer faces are:

$$-k \left.\frac{\partial T}{\partial y}\right|_{y=0} = h_i \left(T|_{y=0} - T_{c,i}\right) \qquad (1.2.2.2)$$

$$-k \left.\frac{\partial T}{\partial y}\right|_{y=t} = h_f \left(T_{aw} - T|_{y=t}\right) \qquad (1.2.2.3)$$

for the inner and outer surfaces $y = 0$ and $y = t$. Here, k is the thermal conductivity of the wall material and h_i is the heat transfer coefficient on the inner

surface. In general, h_f, h_i, and T_{aw}, may be functions of x and z. At this point a solution can be obtained by selection of a third appropriate boundary condition. However, this analysis is focused on discovery of non-dimensional parameters that can be matched between experimental and engine conditions, so a solution is unnecessary. The presence of T_{aw} suggests that Eqn. 1.2.1.3 may be applied to introduce adiabatic effectiveness. Thermal conductivity can be non-dimensionalized using the Biot number:

$$Bi = \frac{h_f t}{k} \tag{1.2.2.4}$$

and a non-dimensional temperature can be defined:

$$\theta = \frac{T_\infty - T}{T_\infty - T_{c,i}} \tag{1.2.2.5}$$

One final parameter is needed to account for the different coolant temperature definitions used in the definition of θ and η:

$$\chi = \frac{T_\infty - T_{c,exit}}{T_\infty - T_{c,i}} \tag{1.2.2.6}$$

which was first suggested by Williams *et al*. [21] as the coolant warming factor. This accounts for the fact that the coolant will warm up as it passes through internal cooling features and the hole itself (*i.e.*, $T_{c,i} \neq T_{c,exit}$, unlike the assumption used in the NHFR analysis). Application of these parameters and $\mathcal{y} = y/t$ to Eqns. 1.2.2.2 and 1.2.2.3 yields:

$$\left.\frac{\partial\theta}{\partial\mathcal{y}}\right|_{\mathcal{y}=0} = Bi\frac{h_i}{h_f}\left(1-\theta|_{\mathcal{y}=0}\right) \quad (1.2.2.7)$$

$$\left.\frac{\partial\theta}{\partial\mathcal{y}}\right|_{\mathcal{y}=1} = Bi\left(\theta|_{\mathcal{y}=1}-\eta\chi\right) \quad (1.2.2.8)$$

Any solution to this set of equations would necessarily include all the non-dimensional parameters already defined. The final insight from this exercise is that at $\mathcal{y}$ = 1, the solution will produce a representation of the wall temperature, or:

$$\theta|_{\mathcal{y}=1} = \frac{T_\infty - T_w}{T_\infty - T_{c,i}} = \phi \quad (1.2.2.9)$$

This final parameter, ϕ, is the overall effectiveness. If all parameters are matched, it will represent the metal temperature for engine components. This temperature is often life-limiting and is very useful for the designer. If the 1D assumption is applied (*i.e.*, h_f, h_i, and T_{aw} are functions of x only and stream-wise conduction is neglected), a single equation for the external wall temperature containing all the relevant parameters is acquired:

$$\phi = \frac{1-\chi\eta}{1+Bi+{}^{h_f}\!/_{h_i}} + \chi\eta \quad (1.2.2.10)$$

Equation 1.2.2.10 is similar in form to the original analysis of Albert *et al.* [20], though their analysis implicitly assumed that χ = 1. This expression shows that an experimental model that has been built to match the Biot number, the internal to external heat transfer coefficient ratio, the coolant warming factor, and the adiabatic effectiveness will produce results that are representative of engine

temperatures. Note that this analysis has used the conventional assumption that T_{aw} is the correct driving temperature for heat transfer on the external wall. This assumption results in the use of η in the final forms of the equations, but is not strictly required. Alternate driving temperatures would result in a different parameter in place of η that would still represent the influence of coolant on the external wall.

1.3. The role of computational simulations

Engineers have long sought means of predicting the performance of a design before it is built. Models and correlations based on scaled experiments and fundamental principles are used to aid in the design of everything from bridges to office chairs. Computers have been an increasingly powerful tool for solving many engineering problems. Problems that were previously intractable due to the lack of an exact analytical solution can often easily – even trivially – be solved through discretization of the fundamental equations to generate a numerical solution.

However, solutions in fluid mechanics have remained stubbornly insoluble even in the age of supercomputers capable of quadrillions (10^{15}) of operations per second. Though the Navier-Stokes equations in their full, time-resolved formulation exactly solve any fluid flow problem, the restrictions on the solution imposed by turbulence have made the demands of solving real flows almost impossible. The problem lies in the fact that turbulence contains a range of length and time scales from the very small (the Kolmogorov scale) to the full size of the

problem domain. The result is that the computational effort required to solve the exact equations for any given geometry scales with Re^3. By one estimate, even with available computational power continuing to increase geometrically it may not be possible to directly solve many common problems in fluid mechanics until 2080 or later [22].

This does not mean that computational solutions are useless for the design of turbine film cooling. Simplified models of turbulence are available that can yield solutions in hours or days on moderate computing clusters.

1.3.1. Reynolds-averaged Navier-Stokes models

Osborne Reynolds developed the idea that an unsteady term in any equation may be decomposed into mean and fluctuating components [23]. This idea may be applied to the equations of motion for fluid flow; further time averaging of this form of the equations produces what are commonly referred to as the Reynolds-averaged Navier-Stokes (RANS) equations. The time averaging process eliminates the majority of the unsteady terms, but the gradient of the Reynolds stress tensor:

$$-\frac{\partial\left(\rho\overline{u_i'u_j'}\right)}{\partial x_j} \tag{1.3.1.1}$$

remains. A common method for closing the RANS equations is to assume that this term may be approximated as being equivalent to viscosity, that is:

$$-\rho\overline{u_i'u_j'} = \mu_t\left(\frac{\partial u_i}{\partial x_j}+\frac{\partial u_j}{\partial x_i}\right)-\frac{2}{3}\left(\rho k+\mu_t\frac{\partial u_k}{\partial x_k}\right)\delta_{ij} \tag{1.3.1.2}$$

where μ_t is the turbulent viscosity. The solution to the RANS equations can then be found if a suitable expression for μ_t can be found. There are numerous methods by which μ_t can be estimated. Most of these involve the definition of additional transport equations (*e.g.*, equations for k and ε) that must be solved.

RANS models of this type offer significantly reduced computational cost (~ 10^{13} times less [22]) compared to direct numerical solutions. However, the inherent simplifications used to close the RANS equations, such as the assumption of isotropic turbulence employed by most turbulent viscosity models, means that the solutions are fundamentally limited. The use of RANS simulations to solve real flows must therefore be validated against experimental results so that the inaccuracies introduced by the underlying approximations can be well understood prior to application of any predictions to designs.

1.4. Research Objectives

Broadly, the aim of this work was to aid in the design of gas turbine engines through better understanding of film cooling physics. This overall goal was approached from multiple angles: new overall and adiabatic effectiveness measurements for a realistic vane, velocity and turbulence field measurements on the suction side of the vane, computational simulations attempting to duplicate both adiabatic and overall effectiveness for two cooling configurations, and comparison of several turbulence models to evaluate their performance in the prediction of temperature profiles off-the-wall. Each of these goals represents novel work that is justified in more detail in the following sub-sections.

1.4.1. Summary of goals for this study

The primary goals of this work are to:

- Measure the adiabatic and overall effectiveness for a single row of holes on the pressure side. These measurements will compliment similar data from the suction side and provide a means of performing a superposition analysis.
- Measure the adiabatic and overall effectiveness for a vane with a cooling configuration representative of a 1^{st} stage vane. These data will help to better understand the impact of row-to-row interaction on wall temperature for a realistic configuration.
- Measure the impact of film injection on the flow field near the wall on the suction side of the vane.
- Perform a RANS simulation for a single row of holes on the suction side to validate the code and gain insight into the behavior of the flow field governing the film cooling performance.
- Perform a RANS simulation of the showerhead region of a vane. No other work has attempted to duplicate experimental results in this region including conjugate effects.
- Evaluate the performance of RANS models for the prediction of the thermal boundary layer development over the vane. Additionally, an attempt will be made to improve the models through variation of the turbulent Prandtl number.

1.4.2. Overall effectiveness measurements

While there has been more than 40 years of research into the adiabatic performance of film cooling designs, very few studies have investigated the overall effectiveness. For many years, virtually the only available data that made use of a conducting vane were the studies of Hylton *et al.* [24] [25]. However, these works made no attempt to match the Biot number or the internal to external heat transfer coefficient ratio and the results consisted of a single line of thermocouples along the mid-span, so their data were of limited use.

While there are a few other studies that made use of conducting material (*e.g.,* [26]), they did not attempt to match scaled parameters to engine conditions. The previously mentioned study of Albert *et al.* [20] was the first to experimentally apply the matched Biot number technique. Their model consisted of a cylindrical leading edge section with a bluff body trailing region with three rows of shaped holes designed to mimic a simple showerhead configuration. There has long been an expectation that conduction effects eliminate the temperature gradients seen in plots of adiabatic effectiveness. A major finding from Albert *et al.* was that while these gradients are reduced, they were not eliminated. This leaves open the possibility of life-limiting “hot spots” on the part that may not be predicted using a conventional analysis.

Further development of the overall effectiveness technique was performed by Mouzon *et al.* [27], who compared the predictions made from a NHFR analysis to the actual temperatures measured with a matched Biot number model. They found that NHFR was reasonable for predicting trends in laterally

averaged values, but was substantially off when it came to finding the location of potential hot spots. Dyson *et al.* [28] measured overall effectiveness with varying hole pitch for a leading edge model. They characterized performance in terms of the “lateral minimum” overall effectiveness, ϕ_{min}, a measure of the hottest point on the leading edge at each *x/d* position. They found that the increase in pitch had surprisingly little effect on the laterally averaged ϕ, while the change in ϕ_{min} was more significant. This once again showed the importance of using the matched *Bi* model to identify hot spots.

These blade leading edge experiments proved the usefulness of the matched Biot number technique, paving the way for more complete experiments. The first study to evaluate a complete vane using the matched *Bi* technique was the work of Dees *et al.* [29]. Their vane was cooled through a simple circuit design alone, in part to simplify the model for computational study. Continuing work using the same vane in [30] showed that the external temperature was substantially affected by the addition of ribbed walls, which enhanced the internal cooling. This result was not unexpected, but served as an important verification of the ability of the matched Biot number technique to show the effects of different internal cooling configurations on the external surface of the part. Dees *et al*. [31] added a row of holes on the suction side of the vane. This work showed that the overall effectiveness was less sensitive to jet separation than adiabatic effectiveness due to the presence of internal cooling and through-hole convection.

All of the works of Dees *et al.* used the same simple internal circuit design that was more representative of a later stage blade or vane. Williams *et al*. [21] used the same vane profile but employed an internal impingement scheme more representative of a 1st stage vane, which is exposed to the highest heat loads. Additionally, unlike previous studies, the internal cooling rate was tied directly to the coolant flow through the holes (*i.e.,* all the coolant that entered the vane was exhausted through the film cooling holes). This feature meant that ϕ_0, the overall effectiveness without film cooling (a measure of internal cooling performance), and ϕ would vary together because the internal cooling improved with increasing coolant flow rate as the impingement jet Reynolds number increased. The result of this was that the overall effectiveness actually peaked at a higher blowing ratio than the adiabatic effectiveness.

These studies have so far left out two important areas on the vane: the showerhead and the pressure side. Albert and Bogard [32] performed a study on a vane with a simple three row showerhead and a single row of cooling holes on the pressure side. The internal cooling was identical to that used by Dees *et al.* They tested two cooling configurations: one with standard, cylindrical holes and another with a “trench” feature designed to spread the coolant in the span-wise direction as it exits the holes. They showed that between the showerhead and the downstream row of cooling holes, both adiabatic and overall effectiveness increased continuously with coolant flow rate. However, the downstream row of holes showed the opposite trend due to separation of the jets from the surface for

the region immediately downstream of the holes. Farther downstream the coolant jets reattached to the surface and showed increasing performance.

The work of Albert and Bogard was limited in that the internal cooling was maintained as constant, which is not a realistic condition for varying blowing ratio. Additionally, they did not separate the effects of the showerhead and the pressure side cooling. To address both of these shortcomings, one goal of this project was to measure the adiabatic and overall effectiveness for the pressure side without the influence of the showerhead, and with a more realistic internal cooling scheme. These data can be compared with the work of Nathan *et al.* [33], who measured the showerhead alone for the same vane, to gain additional insight into the overall effectiveness on the pressure side.

Another feature missing from the available literature is a study that provides measurements of a vane with cooling truly representative of a 1st stage vane. A major goal of this study was to measure the adiabatic and overall effectiveness for a vane with many rows of cooling holes, similar to what might be found on a real vane exposed to the harsh conditions immediately downstream of the combustor section. Comparison to all the previous configurations with simpler film cooling configurations will provide new insight into the contributions of internal cooling and the impact of upstream blowing on the overall and adiabatic effectiveness.

1.4.3. Impact of film injection on velocity and turbulence fields on the suction side

An important aspect of film cooling design is the impact of the film jets on the flow around the airfoil. It has already been mentioned that film cooling jets

impact the local turbulence levels, leading to augmentation of the heat transfer coefficient. Numerous studies of the impact of film cooling on the heat transfer coefficient (*e.g.*, [34], [35], and [36]) have been performed. In general, film cooling from cylindrical holes will only moderately impact the heat transfer coefficient when the local boundary layer is already turbulent (< ~ 10%). In regions where the local flow would be laminar, jets trip the flow and cause more substantial augmentation (> ~ 30%).

Of interest to this study is the impact of upstream blowing – and particularly the showerhead – on the performance of downstream holes. Comparatively few studies have investigated this. Sinha *et al*. [16] showed using a flat plate that the primary impact of upstream blowing was to generate a thicker approach boundary layer. They concluded that the thicker boundary layer allowed the downstream jets to penetrate further into the mainstream, decreasing their performance for a given flow rate due to increased separation. Cutbirth and Bogard [37] studied the impact of showerhead blowing on the pressure side of a model vane. They showed that the showerhead injection produced turbulence levels much higher than would be expected for a turbulent boundary layer as far downstream as 30 hole diameters from the injection. This high turbulence level was shown to dramatically affect the coolant dispersion from downstream holes.

No similar study could be found that investigated the impact of showerhead blowing on the suction side. There was an expectation that blowing would increase turbulence levels and boundary layer thickness, but the strong acceleration present on the suction side immediately downstream of the

showerhead suppresses turbulence [38], so the exact magnitude is difficult to estimate. An additional goal of this study was therefore to measure the impact of showerhead film injection on the turbulence levels and boundary layer velocity profiles at two positions on the suction side. Additionally, the impact of an additional row of holes on the farthest downstream location was investigated. Because the performance of downstream holes is often treated as independent of upstream blowing, better understanding of the affect of upstream blowing on the approach flow may lead to better performance estimates.

1.4.4. RANS simulation of two conjugate film cooling configurations

The application of RANS models to simulations of film cooling is not a new idea. The focus of these works has typically been the prediction of the laterally averaged adiabatic effectiveness. Many studies (*e.g.*, [39], [40], and [41]) have successfully predicted the laterally averaged adiabatic effectiveness for some regions, while many have not (*e.g.*, [42], [43]). Use of the realizable k-ε (RKE) turbulence model was common to the successful predictions of laterally averaged η (though very near the stagnation line on a leading edge model predictions were inaccurate), while the less successful predictions made use of different models. However, even where the laterally averaged values were well predicted, York and Leylek [40], Dobrowolski *et al.* [44], and Mathew *et al.* [41] all showed that the local values for η were substantially off. This was attributed to over-prediction along the center-line of the jet due to inadequate jet diffusion in the computational predictions; however, Mathew *et al.* also showed that the level of jet separation was not well predicted, leading to a jet that was too close to the

wall. They went on to show that the *k-ω* SST model was closer to matching the experimental level of jet separation, but jet diffusion was even more poorly predicted, so the overall performance was worse.

Recently, there has been an increasing interest in the use of RANS CFD for prediction of conjugate performance. This presents an extra challenge because the simulation must not only correctly predict η, but h_f and h_i. Garg and Ameri [45] compared the results of several turbulence models to experimental data and found that typically, the models were able to predict h_f/h_0 on the pressure side of the vane, but had a tendency to over-predict heat transfer on the suction side. Harrison and Bogard [46] demonstrated using a simple flat plat simulation that the best RANS model for predicting laterally averaged η (the standard *k-ω* model in their case) was not the best for predicting heat transfer coefficients (they found that a Reynolds stress model performed the best). They also found that the RKE model did the worst for predicting $\bar{\eta}$, which points out that no single model can be relied upon to consistently perform the best for any given configuration. Added to the knowledge that a given model may predict η well but fail to predict h_f, there cannot be said to be a correct choice for turbulence model in a conjugate simulation.

There have been numerous recent computational studies that included conjugate effects (*e.g.,* [47], [48], [49]) which have served to point out the importance of modeling conjugate effects. However, very few studies have included experimental validation of their predictions. Several studies have compared to the works of Hylton *et al.* [24] [25]. The former study lacked any film

cooling, while the later included film cooling from a showerhead and downstream holes. Both of the Hylton *et al.* configurations included only sparse measurements of the mid-span temperatures, but many studies have compared to these data as validation because of the scarcity of alternative data. The work of Facchini *et al.* [50] used several different k-ε turbulence models to simulate the internally cooled C3X of Hylton *et al*. and found that all of them under-predicted the cooling performance. This was attributed to an under-prediction of h_i (which was not measured by Hylton *et al.*), but Facchini *et al.* also showed that each model they tested over-predicted the heat transfer coefficient over the entire surface of the vane. Ledezma *et al.* [51] used different turbulence models and near-wall treatments for the internally cooled Hylton *et al.* vane. They had better success at predicting the heat transfer coefficient, especially on the pressure side, but the simulations still failed to properly predict the heat transfer coefficient on the suction side prior to transition. This resulted in reasonable predictions of surface temperature where the external heat transfer was well predicted. Ledezma *et al.* also investigated the performance of RANS models in predicting the film cooled results of Hylton *et al.* They found that all the models tested (standard k-ω, k-ω SST, and standard k-ε) were able to fall within the experimental uncertainty for predicted wall temperature. Mangani *et al.* [52] performed a similar study including the v^2f model that showed that although the v^2f model under-predicted the heat transfer coefficient on the pressure side and over-predicted on the suction side, it was still able to achieve reasonable (*i.e.*, within experimental uncertainty) predictions of surface temperature.

More recent data collected using matched Biot number models have allowed exploration of different geometries and surface temperature other than the mid-span only data provided by the Hylton *et al.* studies. Dobrowolski *et al.* [44] compared to the overall effectiveness data of Maikell *et al.* [53] for a model blade leading edge with three rows of film cooling holes that simulated a simple showerhead. They found that the overall effectiveness was over-predicted near the leading edge and under-predicted farther downstream. This was attributed to the previously mentioned over-prediction of the adiabatic effectiveness along the center-line of the jet. Ravelli *et al.* [54] compared to a model of identical geometry, but included the internal impingement in their predictions. Their results showed similar over-predictions along the leading edge, but matched the experimental results for the lower of the two flow rates farther downstream. Most recently, Ledezma *et al.* [55] attempted to reproduce the leading edge data of Albert *et al.* [20] using a *k-ω* model with a limit imposed on the rate of turbulence production away from the wall (the standard *k-ω* does not deal well with low free-stream turbulence). Their $\bar{\phi}$ predictions were within the experimental uncertainty of the measurements, but only at the higher two of three tested coolant flow rates and away from the leading edge.

There are also a series of studies that compare to the overall effectiveness for a full vane. The Dees *et al.* [30] study with internal cooling only also attempted to predict the overall effectiveness using the standard *k-ω* model. Their simulations under-predicted ϕ_0 over the entire surface of the vane with low free-stream turbulence, but did well when mainstream turbulence was increased.

This was likely due to the fact that the standard *k-ω* cannot accurately predict heat transfer rates with low free-stream turbulence, but was shown to perform well with high free-stream turbulence. In addition to their leading edge work, Ledezma *et al.* [55] also provided a companion study to Dees *et al.* [31] that attempted to predict the overall effectiveness for a single row of holes on the suction side in a region of high curvature. For all three flow rates investigated, the CFD substantially under-predicted the performance within approximately 15 *d* of the film cooling holes, probably due to an over-prediction of the level of jet separation. Farther downstream, the predictions were only near the experimental values for the highest (*i.e.*, fully separated) coolant flow rate.

The added difficulty of predicting jet separation for the high curvature (and therefore high acceleration) region of the suction side significantly impacted the Ledezma *et al.* study. Additionally, all the works of Dees *et al.* used the simple internal cooling scheme, and only provided three film cooling flow rates. One of the goals of this study was to simulate the work of Williams *et al.* [21], who used a vane with an internal impingement scheme. Their geometry also included a single row of holes on the suction side, but the holes were located in a region more closely resembling a flat plate. Simulation of this geometry should provide better limits on the performance of RANS CFD in predicting overall effectiveness and allow further insight into the film cooling behavior.

Though the Hylton *et al.* [25] data included an active showerhead, that part of the vane was physically separate from the rest of the model and there were no temperature measurements in the leading edge region. No available

study compared experimental results for a conducting showerhead in a configuration including a whole vane. Therefore, a goal of this study was the simulation of the work of Nathan *et al*. [33], the only study to have experimentally measured overall effectiveness in a realistic showerhead.

1.4.5. Thermal performance assessment for RANS turbulence models

The solution to the energy equation in tandem with the Navier-Stokes equations for momentum is an important part of any computational simulation. Because energy is transported by the same turbulent eddies that affect momentum transport, the solution to the energy equation for a turbulent flow is subject to the same difficulties in solving the Navier-Stokes equations. Rather than solve the full Reynolds-averaged energy equation, the typical approach has been to focus on the development of the thermal boundary layer. Common practice is to apply the idea of the law-of-the-wall to the thermal boundary layer using:

$$U^* = \frac{1}{\kappa}\ln(Ey^*) \tag{1.4.4.1}$$

$$\theta^* = Pr_t(U^* + P) \tag{1.4.4.2}$$

where θ^*, U^*, and y^* are the temperature, mean velocity, and wall normal coordinate normalized using turbulent kinetic energy:

$$\theta^* = \frac{\rho C_p(T_w - T)\sqrt{k}}{q''_w} \tag{1.4.4.3}$$

$$U^* = \frac{U\sqrt{k}}{\tau_w/\rho} \tag{1.4.4.4}$$

$$y^* = \frac{y\sqrt{k_e}}{\nu} \tag{1.4.4.5}$$

E and *κ* are empirically determined constants, k_e is the turbulent kinetic energy at the edge of the hydrodynamic boundary layer, and *P* arises from the correlation of Jayatilleke [56] for pipe flow data:

$$P = 9.24\left(\left(\frac{Pr}{Pr_t}\right)^{3/4} - 1\right)\left(1 + 0.28e^{-0.007\frac{Pr}{Pr_t}}\right) \tag{1.4.4.6}$$

The last two parameters, *Pr* and Pr_t, are the molecular and turbulent Prandtl numbers. The turbulent Prandtl number is usually defined as the ratio of turbulent viscosity to turbulent diffusivity:

$$Pr_t = \frac{\overline{u'v'}\dfrac{\partial T}{\partial y}}{\overline{T'v'}\dfrac{\partial U}{\partial y}} \tag{1.4.4.7}$$

The use of * normalization is preferred because it allows the thermal law-of-the-wall to be applied where shear stress is rapidly varying (*e.g.*, near a reattachment point) and other conditions that would make a thermal prediction using the y^+ form of the law-of-the-wall invalid (see Launder [57] for a more complete discussion).

It is recognized that within the viscous sub-layer, Eqn. 1.4.4.1 is no longer valid. Instead, very near the wall:

$$U^* = y^* \tag{1.4.4.8}$$

$$\theta^* = PrU^* \tag{1.4.4.9}$$

and a blending function is applied. There are many available blending functions, but a common one (employed by ANSYS® FLUENT™ [58]) was proposed by Kader [59]. Further modifications have been made to include the effects of pressure gradients and compressibility (*e.g.,* using White and Christoph [60] and/or Huang *et al.* [61]), but the basic approach remains the same.

In order to solve the temperature profile using Eqn. 1.4.4.2, the turbulent kinetic energy and turbulent Prandtl number must be specified. Values of k will be obtained as part of any solution to the RANS equations, which leaves only the specification of Pr_t. The experimental determination of Pr_t was the subject of intensive investigation for many years after the experimental techniques required to effectively measure it became available. Kays [62] provides an excellent review of this work, and, though his report is nearly a decade old, very little new data have been gathered since. The conclusions of primary interest for air are:

- Over a wide range of flow conditions ($1{,}500 < Re_\theta < 15{,}000$) $Pr_t = 0.85$ through the log-layer
- Pressure gradients have at most a very weak effect on Pr_t
- Surface roughness has no impact on Pr_t
- Very near the wall ($y^+ < 20$) Pr_t rapidly increases, approaching 2 at the limits of measurement ($y^+ \sim 7$)

Because the calculation of the thermal boundary layer relies on the thermal law-of-the-wall and Pr_t is constant through the log-layer, a constant $Pr_t = 0.85$ or 0.9 has typically been used in RANS models. One exception is the renormalization group k-ε (RNG) model of Yakhot *et al.* [63]. By construction, the

RNG k-ε model ties Pr_t to the effective turbulent viscosity. The rapid increase in Pr_t approaching the wall has typically been neglected (*e.g.,* the default value for near-wall Pr_t in FLUENT is 0.85).

Though there is strong theoretical backing for the use of the thermal law-of-the-wall approach, there is surprisingly little work that evaluates its performance when coupled with RANS turbulence models. The approximations used in a RANS model to produce k may mean that the specification of $Pr_t = 0.85$ will produce inaccurate results. One consequence of poor prediction of off-the-wall temperature profiles would be a failure to properly predict h. It has already been shown in section 1.4.3 that the available turbulence models have some difficulty in predicting the heat transfer coefficient. Prior to the current study, the only available study that compares computational simulations of off-the-wall thermal fields to experimental data was the work of Dees *et al.* [64]. They used a C3X vane model with constant external heat flux to produce a thermal boundary layer, which they then compared to computational predictions using the standard k-ω model with a production limiter in the free-stream. For low free-stream turbulence, their predictions of the thermal profiles were considerably off everywhere on the vane. The performance for high free-stream turbulence was improved on the pressure side, where only the farthest downstream position was not matched within the experimental uncertainty. The performance on the suction side was not notably improved.

One of the main goals of this study was to provide a more comprehensive comparison of the thermal performance for several turbulence models.

Additionally, an easy adjustment for the models would be to alter the turbulent Prandtl number. Liu *et al.* performed two studies ([65], [66]) that explored the effects of varying Pr_t on adiabatic effectiveness for two different hole configurations. They found that η simulations could be improved by reducing Pr_t, but the best value varied with coolant flow rate. Better performance was obtained when using a model that applied different Pr_t values at different span-wise positions. Lakehal [67] used a DNS based correlation to predict experimentally measured effectiveness distributions almost exactly. However, Lakehal also employed a k-ε model modified to incorporate anisotropic turbulence behavior in the boundary layer [68], which was shown to have nearly the same performance without the addition of the Pr_t model. No study could be found that looked at how the thermal boundary layer was affected by Pr_t alteration. Therefore, another goal of this work was to see if the alteration of Pr_t could improve the thermal performance of a RANS turbulence model.

EXPERIMENTAL MEASUREMENTS

A major portion of this study concerned new experimental measurements. The adiabatic and overall effectiveness were measured for two different film cooling configurations. Additionally, the impact of film injection on the suction side velocity and turbulence profiles was investigated using hot wire measurements. The methods used to collect these data, the key results, and the significance of the findings are discussed in the following chapters.

Chapter 2 – Experimental Apparatus and Procedures

The many experimental techniques that were employed to gather the data for this study are outlined in this chapter. Additionally, the various procedures that were employed to reduce uncertainty and improve repeatability are outlined here. The uncertainties of the measurements are also examined in detail.

2.1. Wind tunnel facility

All the experiments performed in the course of this study made use of the Turbulence and Turbine Cooling Research Laboratory's "large" recirculating wind tunnel, which is diagramed in Fig. 2.1.1. The flow was driven using a 50 hp, variable speed, three-phase motor.

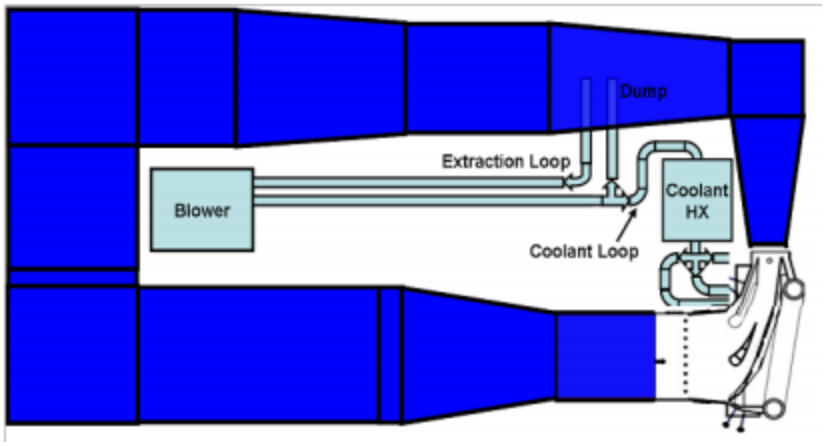

Figure 2.1.1: Diagram of the TTCRL wind tunnel used for this study

The test section consisted of a “three” vane cascade with a 560 by 1020 mm inlet. Only one of the vanes had a complete profile, as shown in Fig. 2.1.2. The other “vanes” consisted of partial profiles with bypass bleeds and adjustable walls. To match the pressure distribution for an infinite cascade, the walls were adjusted until the pressure distribution on the test vane matched the results of a computational simulation for an infinite cascade. This was first done for the work of Dees *et al.* [29], who used simulations provided by a third party. Since that time, new simulations conducted in-house as a part of this study were used to verify that the pressure distribution retained a profile within tolerance. Figure 2.1.3 shows the ideal distribution compared to the data of Dees *et al.* and more recent measurements collected after the experiments used for this study. The data show that even though many modifications have been made to the tunnel, the pressure distribution remained stable. Because of the showerhead design used for the film cooling studies, great care was taken to set the stagnation line position by adjusting the bypass suction.

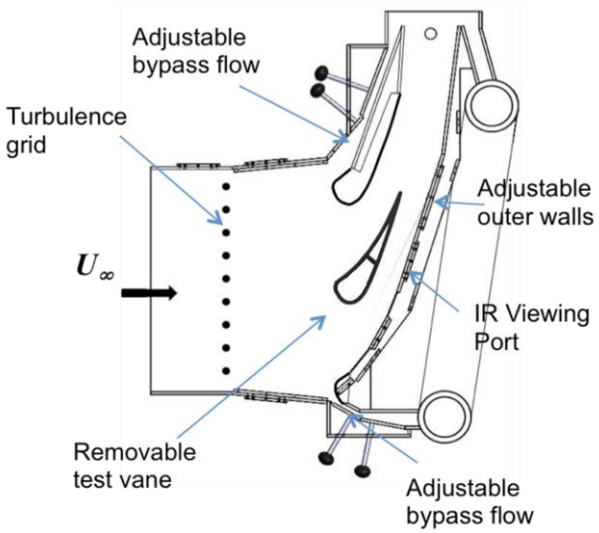

Figure 2.1.2: Detail view of the test section

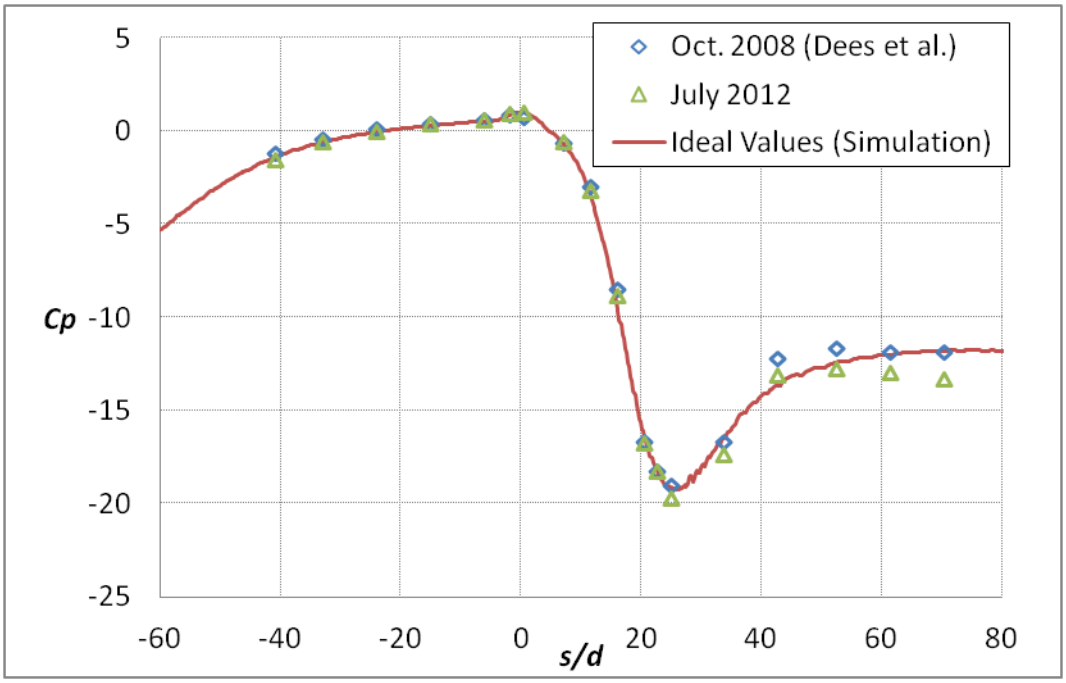

Figure 2.1.3: Comparison of the distribution used by Dees *et al*. [29], more recent measurements, and the ideal values determined by CFD simulation

The vane exit angle was 72°, with a vane pitch of 18” (457 mm). The true chord of the vane was 531 mm, which was extracted from the solid model used for construction of the vanes. The geometry used was the NASA C3X geometry described by Hylton *et al.* [24]. This model was 3.88 times larger than the Hylton *et al*. model, which was in turn a 3 times scale model of the original helicopter engine part. This resulted in a vane that was approximately 8 times larger than that of a commercial aircraft part [69] (a value somewhat dependent on what parameter is chosen).

To match engine representative flow conditions, the approach flow was set to U_∞ = 5.8 ± 0.05 m/s, resulting in a Reynolds number based on chord and exit velocity of Re = 700,000. Two turbulence conditions were used for these experiments. The first was a low turbulence condition with Tu = 0.5% and Λ_∞ = 30 cm and the second was a high turbulence condition representative of the exit flow from a combustor at Tu = 20% and Λ_∞ = 3.7 cm. These measurements were taken by Pichon [70] at x/c = -0.27 upstream of the vane and showed agreement with the past measurements of Cutbirth [71]. Pichon also measured the pitch-wise uniformity of the test section, and found that though U varied due to the presence of the vane, u_{rms} and Λ_∞ were uniform. Previous measurements by Polanka *et al.* [72] showed that U was uniform farther upstream. Turbulence was generated using an array of high solidity vertical rods that could be removed for the low turbulence case. Both Pichon and Cutbirth showed that the turbulence rods did not impact the velocity distribution at x/c = -0.27.

Coolant was fed through the vane by an auxiliary flow loop driven by a 7.5 hp constant speed centrifugal blower. Air was drawn from the wind tunnel and passed through a heat exchanger, as shown in Fig. 2.1.4. For the film cooling configurations, liquid nitrogen was used to cool the air to the desired temperature. The expended nitrogen was exhausted into the tunnel. Coolant entering the vane from a 2.5” pipe first passed through a 30.5 cm flow development section with the same internal profile as the airfoil, as shown in Fig. 2.1.5. This section was designed by Dees [73] to provide a uniform inlet flow. However, it was modified to use perforated plates instead of the wire mesh screens used by Dees. Though Dees noted that perforated plated provided less uniform flow, this modification was made to prevent frost formation from blocking the inlet at higher density ratios. The current design also had an additional contraction at the base of the vane to accommodate the impingement plate, which was expected to further reduce the coolant flow uniformity.

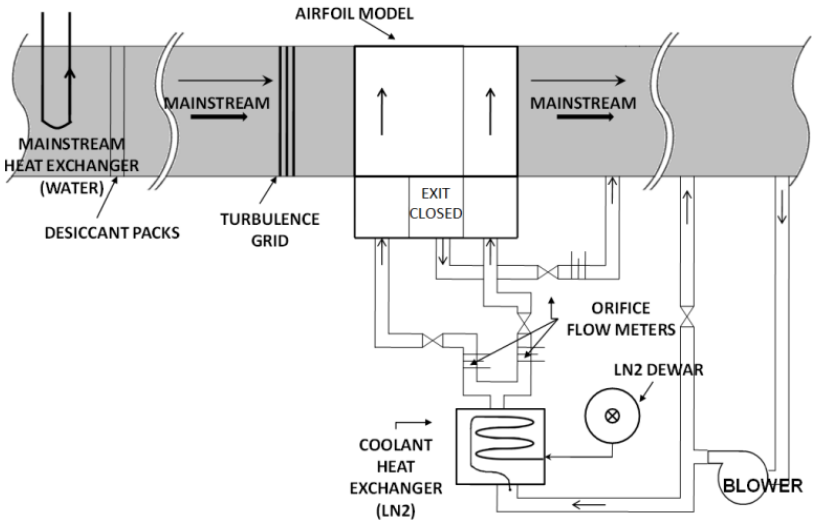

Figure 2.1.4: Flow diagram including the coolant flow loop

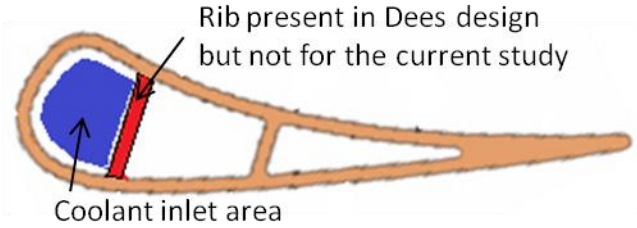

Figure 2.1.5: Coolant inlet

Flow was divided into two separate passages: fore, which fed coolant to approximately -0.4 < *s/c* < 0.7, and aft, which provided coolant for the remaining portion of the vane. The aft passage coolant inlet was unmodified from the design of Dees, who provided detailed flow inlet measurements. The two passages were controlled independently by restricting the flow with valves. Coolant flow rates were measured using orifice flow meters. The coolant piping did not allow the number of orifice diameters up- and downstream of the orifice

plates recommended for the use of standard correlations, so the flow meters were calibrated *in situ* using a laminar flow element inserted downstream of the control valves.

Because of the low temperatures encounters in the film cooling experiments, frost formation was a major concern. Not only could frost forming on the surface alter the emissivity – changing the apparent surface temperature – but ice formation within the coolant system could create blockages in the flow development section that altered the internal flow distribution. To reduce frost formation, the tunnel was purged of humidity prior to the experiment by running pure nitrogen into the tunnel until relative humidity levels were reduced to approximately 5%. Additionally, ceramic desiccant packs were inserted into the main flow to absorb residual moisture and keep levels low throughout the test. Typically relative humidity levels were 3-6% varying with the coolant flow rate (higher coolant flow rates required larger nitrogen flow rates).

Mainstream flow was maintained at a constant temperature during all experiments. The film cooling configurations typically were operated at 305 ± 0.5 K, which was maintained with a water-to-air heat exchanger placed in the main flow. A specific temperature was used because it was thought that the background temperature may affect the calibration of the IR cameras. For the hot wire experiments, no specific temperature was maintained, but the tolerance was reduced to ± 0.2 K to reduce the uncertainty.

2.2. Test vane design

Two vanes were used for this study. Both had identical geometry, but were constructed from different materials. One vane was made from General Plastics Manufacturing Co. Last-A-Foam® R-3315 rigid polyurethane foam. This closed cell foam had a thermal conductivity of k = 0.044 W/m·K [74], which made it suitable for measurement of adiabatic effectiveness. The second vane was machined from DuPont™ Corian®. This material was selected because it had thermal conductivity measured as k = 1.0 ± 0.1 W/m·K, which matched the manufacturer specification of 1.0 W/m·K [75], and was much easier to machine than the castable epoxy material used for the Dees *et al*. studies.

The selection of the appropriate conductivity came from an analysis of the scaling parameters in Eqn. 1.2.2.10. The adiabatic effectiveness was matched by matching *Re* and the film cooling geometry, which also required matching the wall thickness, t. Bunker [76] reported a surface average value of h_f = 5,850 W/m^2·K. Because the local value of h_f varies considerably with airfoil geometry, film cooling configuration, and operating conditions it is reasonable to assume that 1,000 < h_f < 10,000 represents a reasonable range of potential engine values. Bunker also gave a typical airfoil thickness of t = 2 mm, which combined k ~ 20 W/m·K [8] for the nickel based superalloys from which turbine parts are made gives 0.1 < *Bi* < 1.0 as an estimated range for typical engine Biot number. For the C3X geometry used in this study, the wall thickness (0.5” (13 mm)) and h_f distribution are fixed by the film cooling geometry. Selection of k = 1.0 W/m·K

gave $0.5 < Bi < 1.4$ over the surface of the model, which was considered a good match to engine conditions.

To match the ratio of external to internal heat transfer coefficient ratio for a 1st stage vane, h_f/h_i, an internal impingement scheme was used. It was specified using an estimate of the internal Nusselt number from a correlation for impingement on a concave surface [77]. Consultation with industry experts confirmed that the estimated range for the ratio of internal to external heat transfer coefficient was appropriate [78]. Additional details about this design are considered proprietary [79]. All the other parameters in Eqn. 1.2.2.10 were matched, so χ was also matched to engine conditions because the coolant warming occurs as a result of a combination of the internal and external heat transfer rates. The aft passage was cooled by convective cooling alone. Because the coolant flow rates were quite low for the aft passage, the internal h_f/h_i values may not have been representative of an engine 1st vane for the aft portion of the vane.

The vanes were designed with five removable hatches, which contained all the film cooling holes. The hatches were designed such that the seams would not impact the surface temperatures. For the adiabatic vane, this merely meant ensuring a good seal and a smooth finish obtained with a low density spackle. For the conducting vane, the seal had to also offer a minimal change in the local conduction. This was achieved by using Thermon® non-hardening heat transfer compound to seal the hatches. The conductivity of this material was given as 170 ± 57 W/m·K [80], which was considerably higher than the surrounding Corian.

However, the Thermon was contained only in a thin layer (~ 2 mm), so the local thermal resistance was only changed approximately 15%. The seam was then covered over with a vinyl spackle. In practice, the combination of spackle and Thermon was not visible in the IR images. For reference, the external hatch seams were located at *s/c* = -0.72, -0.42, -0.38, -0.16, -0.14, 0.12, 0.15, 0.32, 0.41, and 0.65.

A total of 149 film cooling holes were employed by this study. Figure 2.2.1 shows a cross-section of the vane with the locations of the rows of holes. Each row was named for its position relative to the stagnation line on the suction or pressure side of the vane. The showerhead design consisted of five rows of radially oriented holes and two adjacent, “gill” rows, which also had compound angles. The SS2 row of holes also had a compound angle, but all the other rows had stream-wise oriented holes. The PS used 3/16” (4.78 mm) holes while the showerhead and SS holes were ¼” (6.35 mm). All holes were cylindrical. A full specification of the film cooling design is given in Table 2.0.1. Note that hole pitch is given here relative to the local hole diameter, but all non-showerhead holes had the same dimensional pitch *p* = 1” (25 mm). Also note that the SS1 hole had to use a higher surface angle and a non-standard compound angle due to constraints imposed by the size of the leading edge hatch.

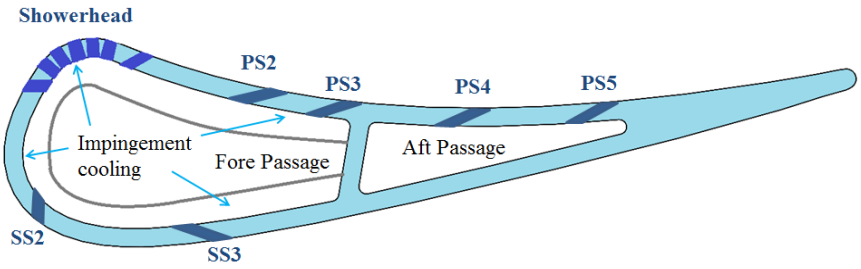

Figure 2.2.1: Cross-section of the fully cooled vane design

Table 2.2.1: Geometric specification for the film cooling holes

Row Name	Position (*s/d*)	Surface Angle (°)	Compound Angle (°)	*d* (mm)	Pitch (*p/d*)
PS5	-57.1	30	0	4.78	5.3
PS4	-43.3	30	0	4.78	5.3
PS3	-29.5	30	0	4.78	5.3
PS2	-21.1	30	0	4.78	5.3
PS1	-8.0	30	60	4.78	5.3
SH-PS2	-4.0	25	90	6.35	6
SH-PS1	-2.0	25	90	6.35	6
SH-Stag	0.0	25	90	6.35	6
SH-SS1	2.0	25	90	6.35	6
SH-SS2	4.0	25	90	6.35	6
SS1	7.0	35	68	6.35	4
SS2	22.9	30	60	6.35	4
SS3	42.9	30	0	6.35	4

For the configuration that used only a single row of holes on the pressure side, the PS part of the showerhead (including the stagnation row), PS1, PS3, and PS4 were blocked using clay. This was necessary because tape did not adhere well enough to the vane surface to prevent leakage during the test. The PS5 row of holes had to remain open to provide cooling for the aft passage during the conducting experiments.

Because coolant mass flow rate was only measured at the inlet of the vane, the local flow rates were calculated based on a flow split calculation that used the method of Gritsch *et al.* [81]:

$$\dot{m} = C_d A_{hole} P_{t,c} \left(\frac{P_{\infty,local}}{P_{t,c}}\right)^{\frac{\gamma+1}{2\gamma}} \sqrt{\frac{2\gamma}{(\gamma-1)RT_{t,c}}\left(\left(\frac{P_{t,c}}{P_{\infty,local}}\right)^{\frac{\gamma-1}{\gamma}} - 1\right)} \quad (2.2.1)$$

to calculate the mass flow through each hole based on estimates of the discharge coefficient, C_d. This was an iterative process in which a desired $\dot{m}$ for a given hole (or holes) was specified and the coolant pressure was adjusted to match. The C_d values for the holes were assumed to be the same as those measured by Albert [82], who found using a similar model that C_d = 0.62 and 0.69 for stream-wise and radially oriented holes, respectively. These values were nearly constant as long as the pressure ratio was greater than 1.003.

Albert's holes were the same size as those used on the PS of the current vane. Larger holes will have a slightly larger C_d. Additionally, local flow conditions (both internally and externally) may impact C_d. To verify that this was not an

issue, Albert's calculated value was compared to the value of C_d calculated from a simulation of a single row of holes on the SS (described in more detail in section 6.1.3). The calculated value was within the uncertainty of the measured value, so any changes due to hole size and local flow were assumed to be small. Albert did not measure discharge coefficients for compound angles other than 90°, so these had to be assumed. Gritsch *et al.* [81] tested the dependence of C_d on compound angle, and did not find a significant change for low Mach numbers. For this reason, the SS1 and PS1 rows were assumed to lie nearer the SH value of 0.69, and C_d = 0.68 was used. This process resulted in a "total" (*i.e.*, fore passage) flow rate that the operator could measure to obtain the desired coolant flow rates from any given row. The SS2 row, though it also had a compound angle, was mistakenly given the same discharge coefficient as the other downstream rows of holes. Had it been given the same discharge coefficient as the SS1 and PS1 rows, there would have been at most a 2% change in the total flow rate. Table 2.2.2 provides a description of the local blowing ratio for each row of holes for each of the overall showerhead momentum flux ratios tested. Note that because the local velocity for the stagnation row was zero, the conventional definition for *I* produced infinity. Instead, the coolant flow rate was non-dimensionalized using the approach flow as in:

$$I^* = \frac{\rho_c U_c^2}{\rho_\infty U_{approach}^2} \tag{2.2.2}$$

which was used for all the showerhead rows (as indicated by the *). Also note that the aft passage was controlled independently. Originally, the intent was to

match the mass flux from PS4 and PS5 to that of PS2 and PS3. However, this produced coolant flow rates that were too small to measure accurately, so the same flow rate was used for the lowest three fore passage momentum flux ratios. Because the focus of the study was on the performance for the impingement cooled region, this was considered acceptable.

Table 2.2.2: Momentum flux for each row of holes at the nominal showerhead coolant flow rates tested with the fully cooled geometry

Overall I^*_{SH}	SS3	SS2	SS1	SH-SS2*	SH-SS1*	SH-Stag*	SH-PS1*	SH-PS2*	PS1	PS2	PS3	PS4	PS5
0.83	0.40	0.39	0.85	1.06	0.78	0.69	0.76	0.88	1.75	0.94	0.77	0.62	0.87
1.88	0.45	0.43	1.44	2.10	1.82	1.73	1.80	1.92	3.71	1.80	1.37	0.62	0.87
3.33	0.53	0.49	2.26	3.56	3.27	3.19	3.26	3.37	6.47	3.00	2.22	0.62	0.87
5.21	0.63	0.56	3.33	5.43	5.15	5.06	5.13	5.25	10.01	4.55	3.31	0.88	1.39
7.50	0.75	0.65	4.63	7.73	7.44	7.36	7.43	7.54	14.34	6.45	4.64	1.20	2.04

For the PS2 only configuration, the suction side holes on the pressure side remained active so that the total coolant flow rate would remain high and keep the internal cooling closer to representative values. The coolant flow range measured was intended to capture the jet in several stages of attachment. Additionally, three momentum flux ratios equivalent to the values that the PS2 row experienced with all the holes active were measured. Table 2.2.3 shows the measured flow rates and the I^*_{SH} value that would produce that momentum flux ratio from the PS2 row of holes. Note that no coolant flow rate lower than I_{PS2} =

0.30 could be measured because the portion of the showerhead that remained open would have ingested mainstream air.

Table 2.2.3: Momentum flux ratios measured for the PS2 Only configuration and the I^*_{SH} values that would correspond to those flow rates had the showerhead been active

I_{PS2}	Equivalent I^*_{SH}
0.30	N/A
0.41	N/A
0.67	N/A
0.94	0.83
3.00	3.33
6.45	7.50

2.3. Infrared thermography measurements

Adiabatic and overall effectiveness values were collected by measuring the surface temperature of the vane using a pair of FLIR infrared cameras: one model P20 and one model P25. The tunnel walls were opaque to IR radiation, so the cameras observed the model vane surface through viewports. The P20 was always paired with a salt (NaCl) crystal window, while the P25 was typically paired with a zinc selenide (ZnSe) window. However, the lower transmissivity of the ZnSe window (~ 0.7 vs. ~ 0.9 for the NaCl) reduced the sensitivity of the camera, so some experiments used the NaCl window.

To account for the transmissivity of the windows and the surface emissivity, the cameras had to be calibrated. Prior to each experiment, a

separate calibration test was carried out. In these tests, the cameras were calibrated against E-type thermocouples attached to small copper plates. The copper plates helped to ensure that the thermocouple would be in a region of relatively uniform temperature. This was necessary because the spatial resolution of micro-bolometer type cameras can be impacted by sharp temperature gradients (*i.e.*, a transition that is in reality a sharp line will “bleed” across several pixels). Additionally, the use of copper plates allowed the thermocouples to be placed over the film cooling holes so that they could more easily achieve the low temperatures necessary to obtain a useful calibration (for adiabatic experiments, this was a necessity).

The raw IR images (an example for two camera views is shown in Fig. 2.3.1) were processed using FLIR Thermacam Research Pro 2.7 and a script written in Python. The images were saved to a Matlab file, which contained a record of the recorded temperature for each pixel. The location of each thermocouple was approximated based on markings drawn on the calibration plates using a low emissivity, high reflectivity silver paint. This estimated location was fed into a Python script that read the IR images for the test and used the given location as a starting point for a search. The program was written to identify the location in the image that provided the least scatter in the data for creating a calibration curve and output the temperatures there. More details about this script are available in Appendix A. The resulting calibration was used to convert the apparent IR temperature into an actual temperature.

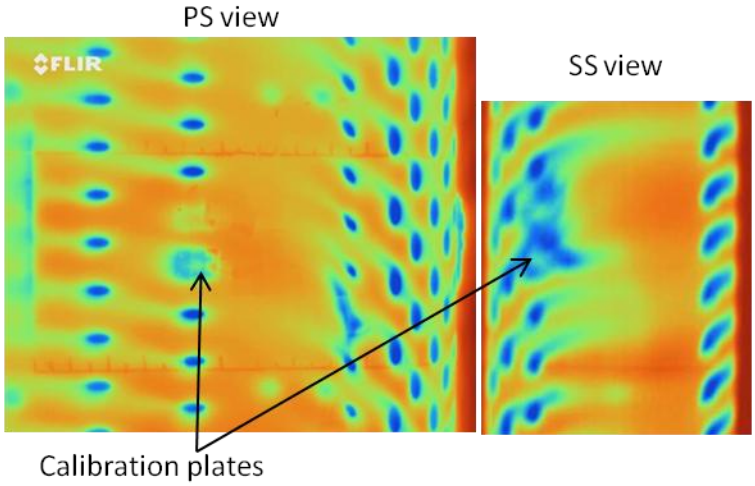

Figure 2.3.1: Example unprocessed IR image with visible calibration plates from an adiabatic test

The P20 camera exhibited excellent stability, with each calibration falling very close to all others and to the calibration of Albert [82], which was an average of over a year's worth of data. An example calibration obtained for the P20 is shown in Fig. 2.3.2. The standard calibration curve was used to process the P20 data for all experiments.

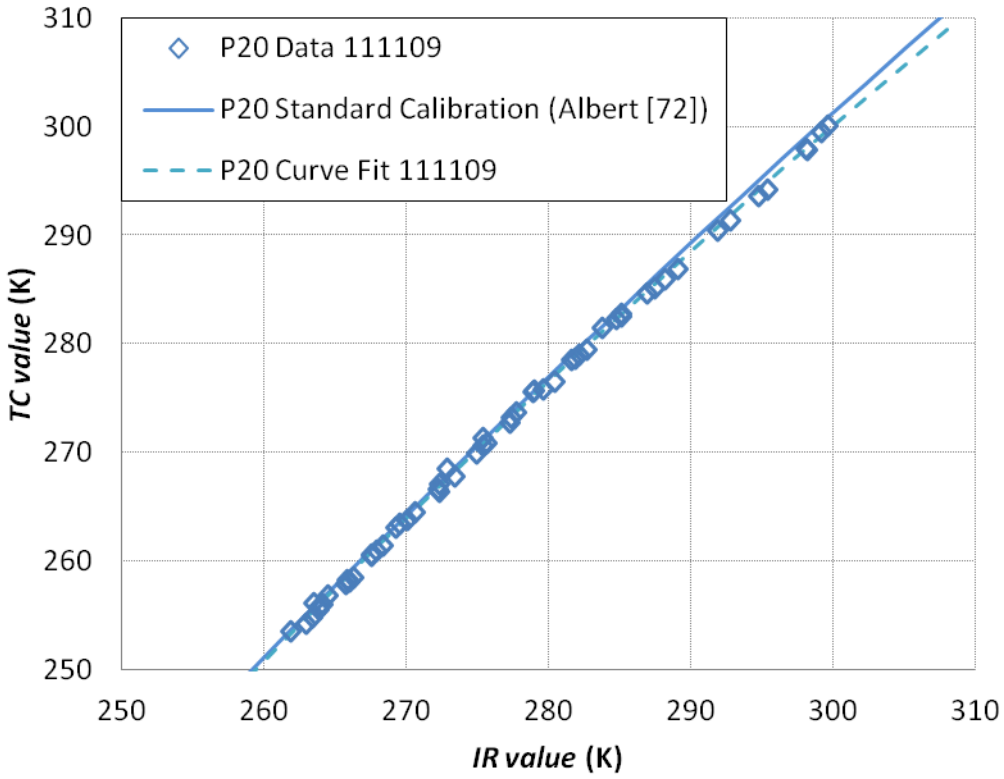

Figure 2.3.2: Example of a curve fit obtained using the calibration plates compared to the standard curve provided by Albert [82]

Unfortunately, the P25 camera did not show the same level of calibration stability. Figure 2.3.3 shows several calibrations collected during the testing of the fully cooled configuration compared the standard curves provided by Albert [82] and Davidson [83]. The huge range covered by these calibrations was alarming and prompted much investigation into the calibration process. Ultimately it was discovered that the calibration changes were due to damage to the camera that was preventing its internal self-calibration process from functioning properly. The camera was later repaired, but not until after the effectiveness measurements for the current study were completed. Because the P25 camera

calibration apparently changed on a day-to-day basis, no single calibration could be applied to the experiments. Instead, the calibration for each test was applied to only that experiment.

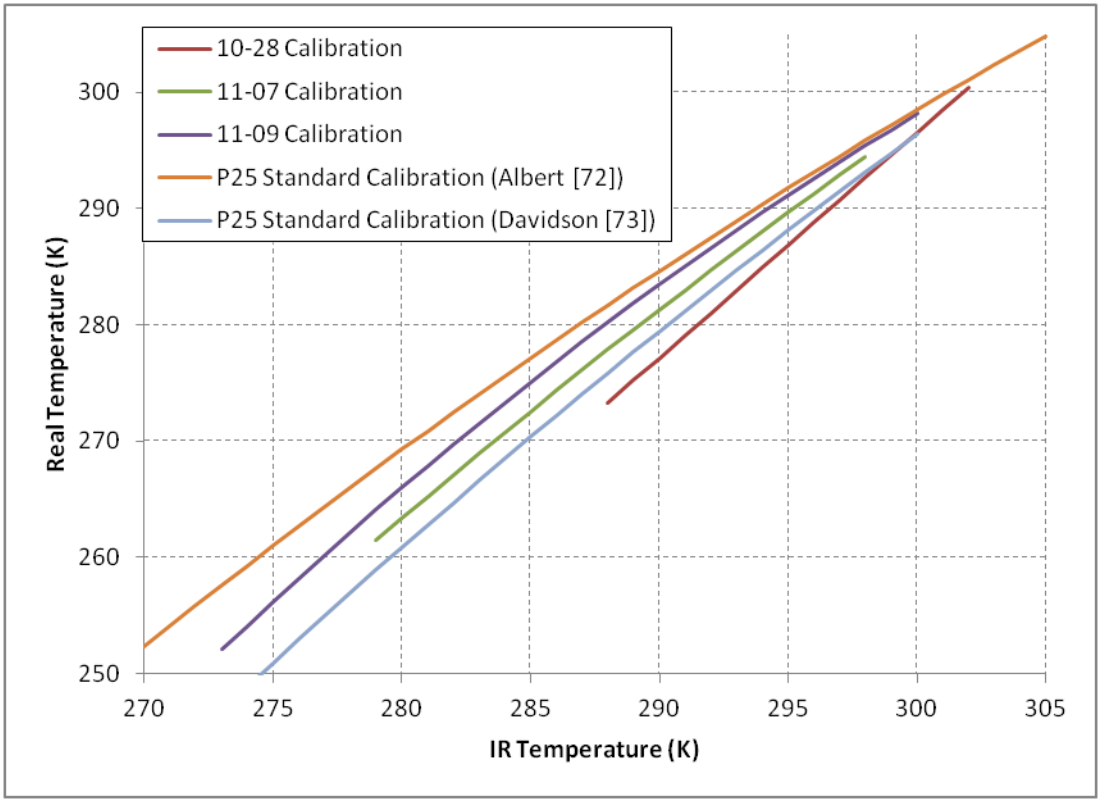

Figure 2.3.3: Some of the many calibration curves used for the P25 camera

No single view-port could image more than a small region of the vane, so multiple experiments were required to image the whole vane. Figure 2.3.4 shows the portions of the vane that could be observed from the available viewports. Note that the only way to image the aft portion of the vane was to look down

through the top of the wind tunnel. Only the mid-span region was imaged for this study. Figure 2.3.5 shows the portions of the vane visible through each viewport.

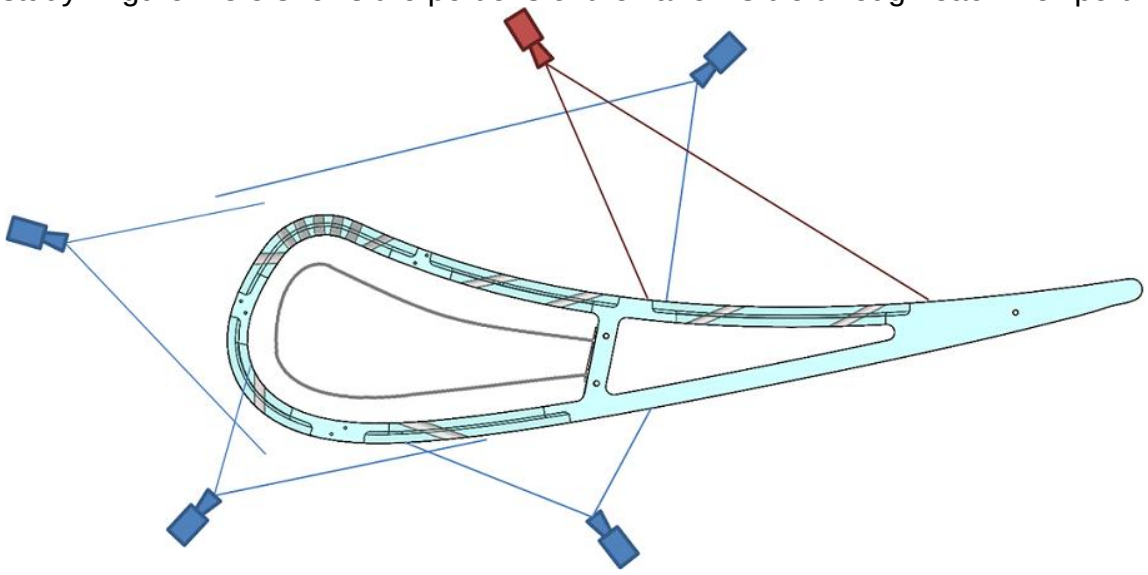

Figure 2.3.4: Top-down view showing the regions of the vane visible from the available viewports. The red camera indicates a view through the top of the tunnel.

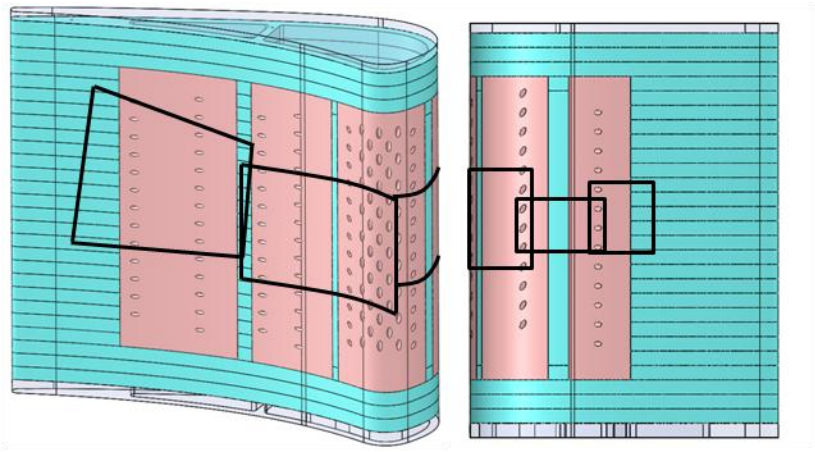

Figure 2.3.5: Front and back views of the regions imaged for this study

Care was taken to ensure some overlap between images to provide a measure of verification when using the P25 camera (*i.e.*, the calibrated temperatures from the P25 could be compared to the other camera or to temperatures from another test using a different calibration). However, there were no overlapping pixels for the showerhead region. Previous work by Nathan *et al*. [33] (who faced similar difficulty with the calibration of the P25) showed good agreement between the cameras in this region, so it was assumed that the lack of an overlap region would not pose a problem. However, later testing showed that the angle of the cameras relative to the surface could impact the apparent temperature. One of the cameras was pointed at a calibration plate at several known angles while the temperature was varied. The calibration for each angle was compared, which showed that for angles greater than approximately 55° the calibration produced temperatures more than 2 K different from the calibration performed at 0°. Measurement of the angle of various points on the vane to the camera found that the $-1 < s/d < 5$ region was potentially at an angle greater than 55° for both available views (the calibration plates were usually flat relative to the camera). Therefore, the data in this region were excluded from the results presented in this study.

When changing coolant flow rates from one point to another, each measurement was allowed to come to steady state before collection. For the conducting vane, 20-30 minutes were required. After the experiment, it was verified that steady state was achieved by comparison of multiple points taken separated by four or more minutes, as shown in Fig. 2.3.6. For the adiabatic

tests, much less time was required. Typically, several points were collected approximately one minute apart for five minutes. Points were considered steady if the variation between two points was equivalent to the noise from the camera (~ 0.005 ϕ).

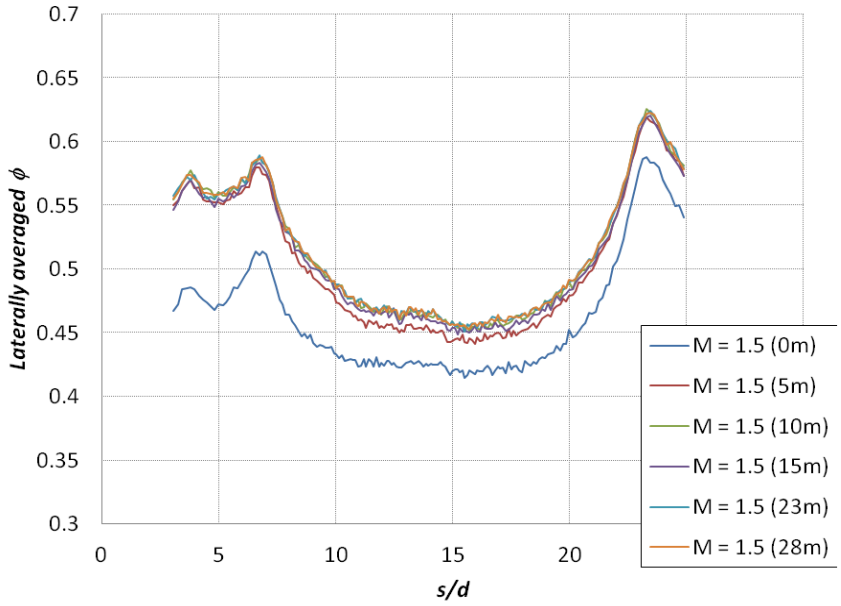

Figure 2.3.6: An example of the temperature stability desired for a steady state point

Adiabatic data for the PS2 only configuration were corrected for the fact that the foam used was not a perfect insulator. This was especially important for this study because of the strong internal cooling provided by the impingement plate. A conduction correction uses the following expression:

$$\eta = \frac{\eta_{measured} - \eta_0}{1 - \eta_0} \tag{2.3.1}$$

to correct the value measured by the camera, $\eta_{measured}$, during the film cooling experiment using the correction η_0 (This expression may be derived from first principles using a 1D assumption similar to what was used to derive the expression for matching ϕ). This correction was measured by blocking some holes in the model and measuring the surface temperature, as shown by Fig. 2.3.7. Due to the presence of the tape used to block the holes, the conduction correction immediately around the holes had to be estimated based on the conduction correction on either side of the taped region.

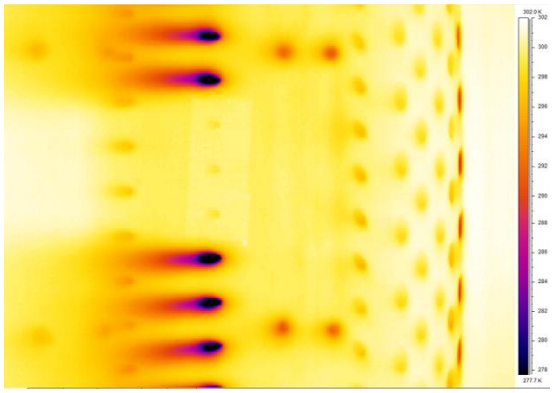

Figure 2.3.7: Example of a raw IR image from the conduction correction portion of the experiment.

2.4. Hot wire measurements

An A. A. Lab Systems Ltd. AN-1003 Hot Wire/Hot Film Anemometry System was used to make velocity measurements of the boundary layers at two locations on the suction side of the vane. These locations corresponded to locations just upstream of the SS2 and SS3 rows of holes, as shown in Fig.

2.4.1. For each position, the holes at the measurement location were blocked. The probe was a boundary layer type and consisted of a 5 μm diameter tungsten wire secured to hooked prongs separated by approximately 1.5 mm. Because these probes were very easily broken, they were made in-house by securing the wire to the prongs using conductive silver paint.

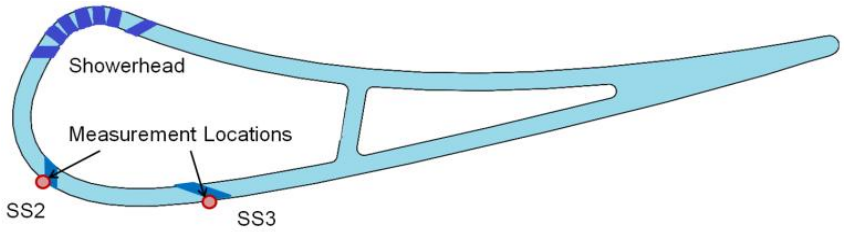

Figure 2.4.1: Diagram showing the relative position of the two hot wire measurement locations

Calibration of the hot wire was a complex process. First, reference velocity data were needed at a known location along a line normal to the wall. This was acquired by carefully positioning a pitot-static probe at a position far enough from the wall to be in the free-stream (measurements of the boundary layer from Dees *et al.* [64] were used to estimate the necessary clearance). The position used for the SS2 measurements is shown in Fig. 2.4.2. Note that the probe stem was notably bent, which complicated the locating process.

Figure 2.4.2: Photograph of the pitot-static probe ready to measure the reference velocity at the SS2 position. The probe was approximately ¼" from the wall.

Once positioned, the velocity at the reference position was recorded relative to the permanently installed pitot-static probe used to measure tunnel velocity. The ratio U_{SS2}/U_{∞} could then be used to calibrate a hot wire placed at the same location. This ratio was verified to be constant over a broad range of tunnel velocities. The position of the pitot-static probe was recorded by marking the walls of the tunnel in two positions on either side of the probe and subsequently using these marks to visually align the hot wire. Figure 2.4.3 shows how the marks were visually aligned with the end of the probe. This positioning system was estimated to be reproducible within a spherical volume of approximately 1 mm^3. Even at the SS2 position, where velocity was changing more rapidly in the freestream, this small deviation produced negligible uncertainty in the reference velocity.

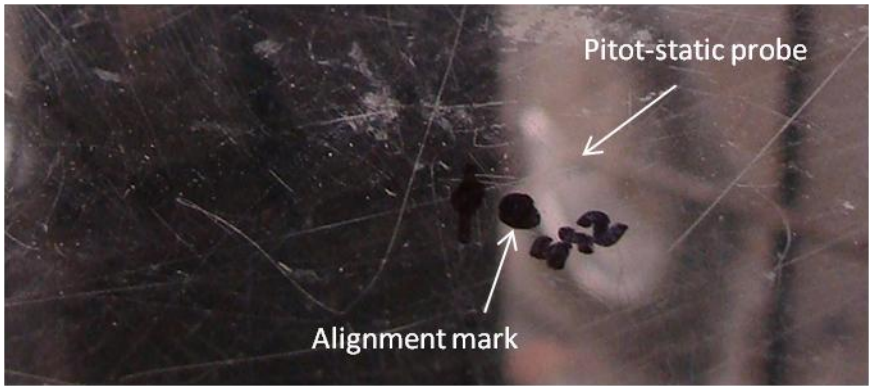

Figure 2.4.3: Photograph showing how the end of the pitot-static probe was used to create alignment marks on the tunnel wall

Once a hot wire probe was in position, it was calibrated by adjusting the tunnel velocity across the expected range of boundary layer velocities (*i.e.*, as low as the tunnel could go (~7 m/s) to ~24 m/s). This calibration had to be performed before and after each experiment because the hot wire system was notorious for changing calibration during a test (often for no apparent reason). If the two calibrations disagreed by more than approximately 1% the test was considered invalid and the process was repeated.

Data were collected using a linear traverse with a resolution of 0.0001" (2.5 μm) and a range of 1" (25.4 mm). The hot wire was positioned as closely as possible by using a telescope to observe the probe and its reflection from Kapton tape on the vane surface. At the SS2 position, the distance relative to the wall was estimated after-the-fact by fitting a parabola to the points very near the wall and adjusting y until $U = y = 0$ at the wall. A parabola was used because without blowing the boundary layer was laminar and with blowing some conditions produced profiles that were not clearly linear near the wall. Figure 2.4.4 shows

that when the profile was linear, the use of a parabola did not alter the results. This procedure was repeated with different combinations of near-wall points to estimate the uncertainty.

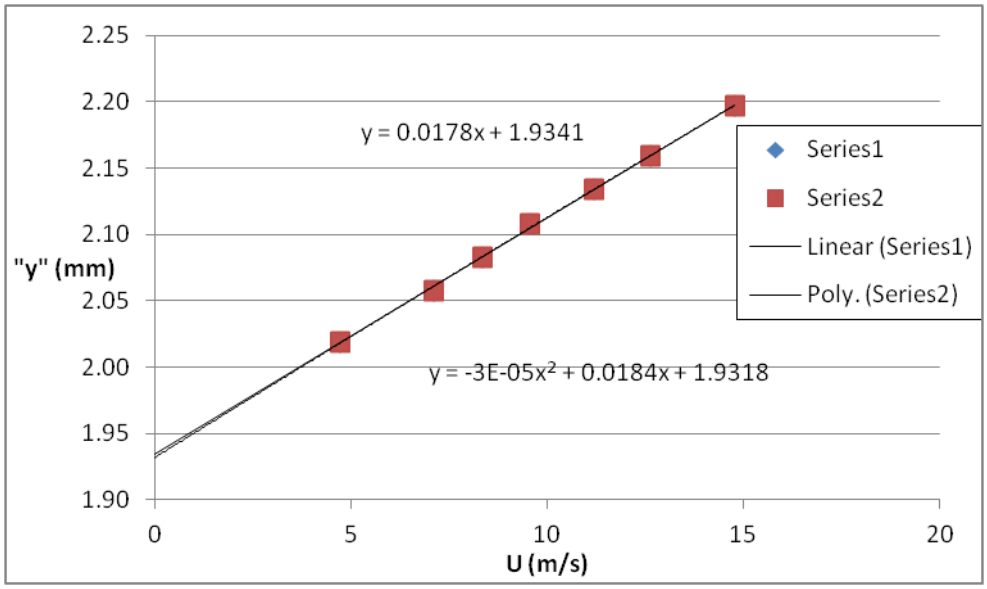

Figure 2.4.4: Example of the zeroing procedure for the SS2 position showing that regardless of fit type the adjustment was 1.93 mm

The average estimated distance from the wall for the first point was 0.07 mm (y^+ ~ 4-7), which was close to previous visual estimates based on the probe support size (0.1 mm). At the SS3 position, this procedure was not possible because the probe could not be positioned close enough to produce a good curve fit. Instead, the position was estimated visually based on the known size of the wire supports. Observing the probe at this position was difficult, so

positioning was done more conservatively, which resulted in an estimated distance from the wall of approximately 0.26 mm.

Multiple conditions were measured for each position. At the SS2 position, the flow field was measured for no blowing and showerhead blowing cases at high and low mainstream turbulence. Additionally, the showerhead used blowing ratios of M^*_{SH} = 2 and 3. Because the experiments were conducted at unit density ratio, these corresponded to I^*_{SH} = 4 and 9. Additionally, because the coolant from the showerhead was not uniformly distributed at the SS2 position, two different span-wise positions were tested corresponding to z/H = 0.49 and z/H = 0.58. For the upper position, $M^*_{SH} = I^*_{SH}$ = 1 was tested in addition to the other blowing ratios. At the SS3 position only the high mainstream turbulence condition was tested. This position was tested with no blowing, showerhead blowing, showerhead and SS2 blowing, and SS2 alone. For each case, the coolant flow rates were equivalent to M^*_{SH} = 2 and 3 (*i.e.*, the local flow rate for SS2 was matched to what it would be had the showerhead been active). The mean and fluctuating velocities were measured for each of these conditions. Additionally, length scale data were collected. Samples were taken at 10 kHz over 20 or more seconds. This sample rate and interval were selected based on the work of Waye [84], who found using the same anemometer system that integral length scales and RMS velocity were repeatable within 5% using these settings.

All experiments were conducted under an isothermal condition, as required by hot wire operation. In order to make sure that the tunnel temperature

did not vary more than ± 0.2 K during the experiment, the tunnel was activated approximately an hour before calibration and allowed to come to a steady temperature. The temperature was maintained for varying tunnel speeds by adjusting the temperature and flow rate of the water-to-air heat exchanger (see Fig. 2.1.4). For cases with blowing there was some concern that the heat added to the "coolant" by the blower would change the temperature around the hot wire and skew the results. However, measurements with a thermocouple probe showed that even when the "coolant" exiting the showerhead was more than 10 K above the tunnel temperature, there was less than 0.5 K change in the temperature near the hot wire (*i.e.*, less than the uncertainty in the TC probe).

2.4.1. Data reduction for the hot wire measurements

Collection of mean and RMS velocity information was handled by a Labview program which generated statistics after a data collection interval at each position. When length scale data were desired, the instantaneous velocity for the entire collection interval (20 s at 10 kHz) was saved for later autocorrelation. A Matlab script was written to correlate the time resolved data. The autocorrelation function:

$$\rho(s) = \frac{\langle u(t)u(t+s)\rangle}{\langle u(t)^2\rangle} \qquad (2.4.1.1)$$

for much of the data had very long tails, as can be seen in Fig. 2.4.1.1. This function was integrated to find the integral time scale, which was then converted to a length scale using the mean velocity. Because the function remained near –

but not below – zero for so long, the usual metric for selecting the time scale (first pass below zero) produced unreasonably long correlation times. For this reason, a 2% cutoff was imposed to produce more physically meaningful results. To verify that this cutoff was appropriate, the values of Λ far from the wall at the SS2 position were compared to Λ_∞, the length scale in the approach flow. At high mainstream turbulence, the results from the 2% cutoff were ~ 40 mm, which was approximately equal to the approach flow value of 37 mm.

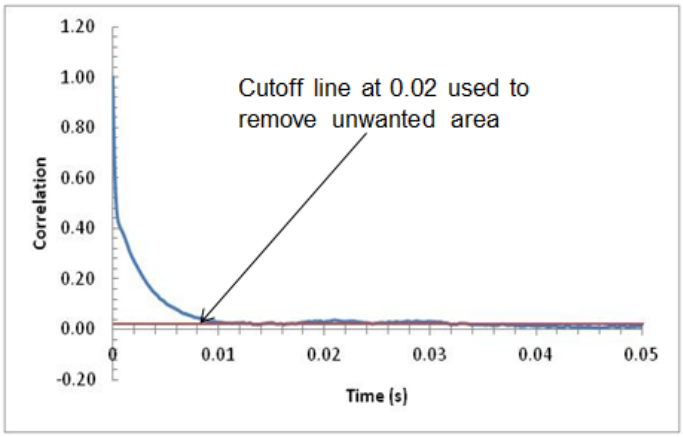

Figure 2.4.1.1: Example of the autocorrelation function for a length scale measurement with the 2% cutoff line

A key metric for comparison of the velocity profile data is the boundary layer thickness. For many studies, the calculation of the boundary layer thickness is a simple matter determining when the local velocity has reached 99% of the mainstream velocity. However, because of the strong acceleration around the vane, the SS2 position did not have a constant mainstream velocity. Figure 2.4.1.2 shows how the velocity was changing away from the wall. Instead of

using a constant velocity for the mainstream, a linear fit was put through the far-field points. This fit represents the velocity profile that would exist for an inviscid flow, so it provided the best means of representing the effect of viscosity. A computational simulation without viscosity confirmed that this line propagated all the way to the wall. This predicted inviscid velocity, U_p, was used to normalize much of the data at the SS2 position, and δ_{99} was calculated relative to this line. The off-the-wall velocity profile at SS3 did not have this problem because the local velocity profile resembles that of a flat plate.

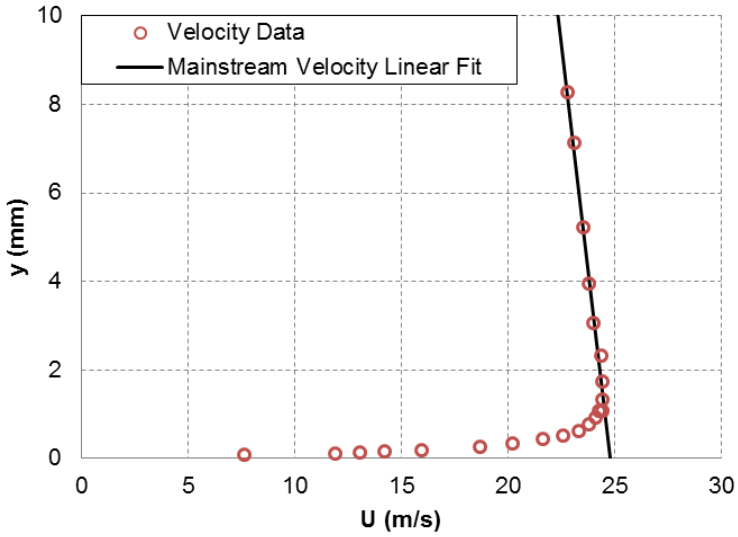

Figure 2.4.1.2: Example of a velocity profile at the SS2 position showing the linear fit for the "inviscid" velocity

2.5. Uncertainty analysis

The estimation of measurement uncertainty is a very important part of any experimental program. Periodic evaluation of possible sources of uncertainty was considered a part of normal testing procedure. In this section the estimation of the uncertainties for all important measured quantities is detailed, including the source uncertainties where available.

2.5.1. Momentum flux ratio

Because many other quantities (internal cooling rate, surface temperature, h_f/h_0, *etc*.) are dependent on the coolant flow rate, it is one of the most important parameters to understand the measurement accuracy. The first step in the calculation of *I** uncertainty was to reduce the expression used to find it into components uncertainties:

$$I^* = \frac{(P_{atm} + P_o) D_o^4 C_d^2 \Delta P_o T_c}{P_{atm}(N_{SH} d_{SH}^2 + N_{PS} d_{PS}^2)^2 (1 - \beta^4) \Delta P_\infty T_o} \qquad (2.5.1.1)$$

Several assumptions have been made to convert Eqn. 2.2.2 into this form. First, density was computed using the ideal gas law, and the composition of the coolant and the mainstream were assumed to be identical. This may not be strictly true; because the cooling process dumps pure nitrogen into the coolant stream it likely has a higher concentration of nitrogen than the mainstream, but even the maximum possible density change (pure nitrogen vs. air, an unrealistic situation) produces only a 3% change in density. From the calculation of flow rates (see section 2.2), the maximum pressure ratio P_o/P_∞ was found to be

approximately 1.007, so coolant and mainstream were assumed to be at the same pressure for density calculation purposes. The number of film cooling holes with each diameter (N_{SH} and N_{PS}) was constant, but β is the ratio of orifice diameter to the pipe diameter, which will have an uncertainty.

With Eqn. 2.5.1.1 it was then possible to apply the sequential perturbation procedure described by Moffat [85] using the source uncertainties listed in Table 2.5.1.1. Note that the C_d uncertainty calculation was an involved process that was performed by Davidson [83], who found an orifice Reynolds number dependence. The uncertainty that he found for 30,000 < Re_o < 60,000 was applied even though the current study had 50,000 < Re_o < 100,000 because the increased uncertainty was confined to the very low Reynolds number range.

Table 2.5.1.1: Source uncertainties for the calculation of *I**

Parameter	Uncertainty	Type	Source
P_{atm}	500 Pa	bias	Typical drift over the course of the experiment
P_o	0.03 in H_2O	combined	Typical max drift + precision
D_o	0.013 mm	bias	Caliper measurement limitation
C_d	0.0045	bias	Calculations by Davidson [83]
ΔP_o	0.007 in H_2O (typical fore)	combined	Typical max drift + precision
T_c	0.5 K	bias	Omega handbook
d_{SH}	0.013 mm	bias	Caliper measurement limitation

d_{PS}	0.013 mm	bias	Caliper measurement limitation
β	0.003	bias	Caliper measurement limitation
ΔP_{∞}	0.0005 in H_2O	combined	Typical max drift + precision
T_o	0.5 K	bias	Omega handbook

The result of this analysis was a total uncertainty for I^* of 2.4% for all flow rates. This represents the total uncertainty in the instantaneous measurement of I^*. There was some fluctuation in the actual I^* during the experiments – due variation in the output of the blower – that resulted in approximately a 1% variation in M^* (1.4% for I^*). Unfortunately, data to better quantify this fluctuation does not exist. Therefore, the best estimate for the total uncertainty in the reported value of I^* would be 2.5%. There was also additional uncertainty due to the flow split calculation. Uncertainty in C_d due to variation in the design from the when C_d was measured by Albert [82] was assumed to be 0.01, which produced an additional 1% uncertainty based on perturbation of Eqn. 2.2.1. The uncertainty for I^*_{SH} or any local I was estimated to be 3% independent of flow rate.

The same analysis for the aft passage showed that uncertainty was considerably greater. The problem was that the aft passage flow rate was very low; measured pressure drops approached the drift uncertainty. Therefore, I_{PS4} and I_{PS5} had an estimated uncertainty of $\delta I = \pm 0.2$, which was as high as 30% for the lowest flow rate.

2.5.2. Overall and adiabatic effectiveness

Precision uncertainty in the overall and adiabatic effectiveness can be determined in part based on in-test repeatability measurements. Test-to-test repeatability would be preferred, but for the current study only a single experiment was available for each configuration. Figures 2.5.2.1 and 2.5.2.2 show the in-test repeat points for the showerhead region of the fully cooled configuration and the PS2 only configuration, respectively. Note the refined scale of these images. Problems with the P25 camera meant that the uncertainty for portions of the vane that used that camera was higher, as shown by Fig. 2.5.2.1b, which shows the worst case of in-test variation for the three experiments that were part of the fully cooled overall effectiveness. Repeatability measurements may be used as a guide for the total precision uncertainty in the surface temperature. For the P20 camera, the uncertainty was < 0.01, while the P25 camera exhibited $\delta\phi$ = ± 0.02. These values were obtained by averaging the variance of the repeatability from disparate experiments together to find the 95% confidence from a combination of all the experiments. The same analysis for the adiabatic tests found better repeatability for the η measurements ($\delta\eta$ ± ~ 0.01) from the P25, suggesting that ± 0.02 was a high estimate for the overall effectiveness.

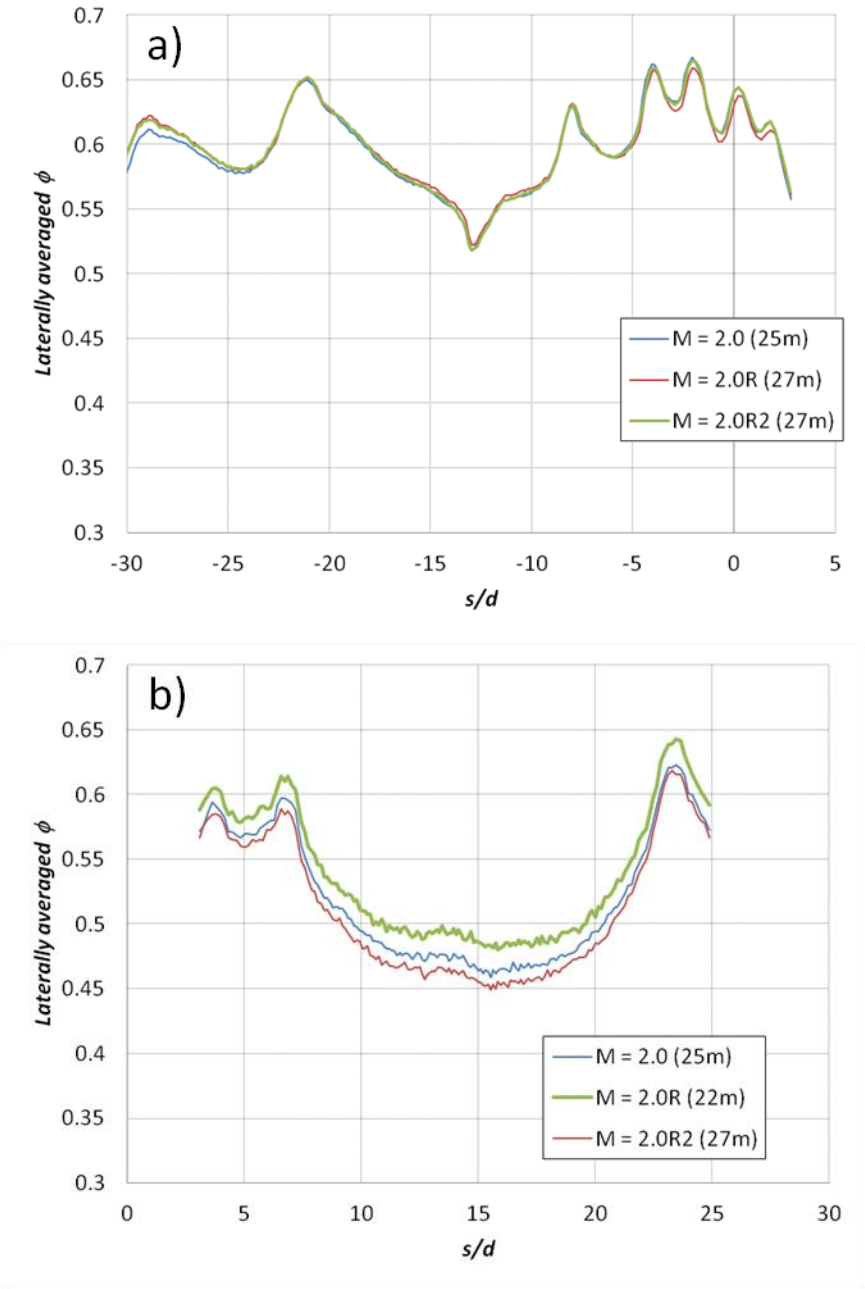

Figure 2.5.2.1: The in-test ϕ repeatability comparison for a) the pressure (P20) and b) suction (P25) sides of the showerhead for the fully cooled configuration

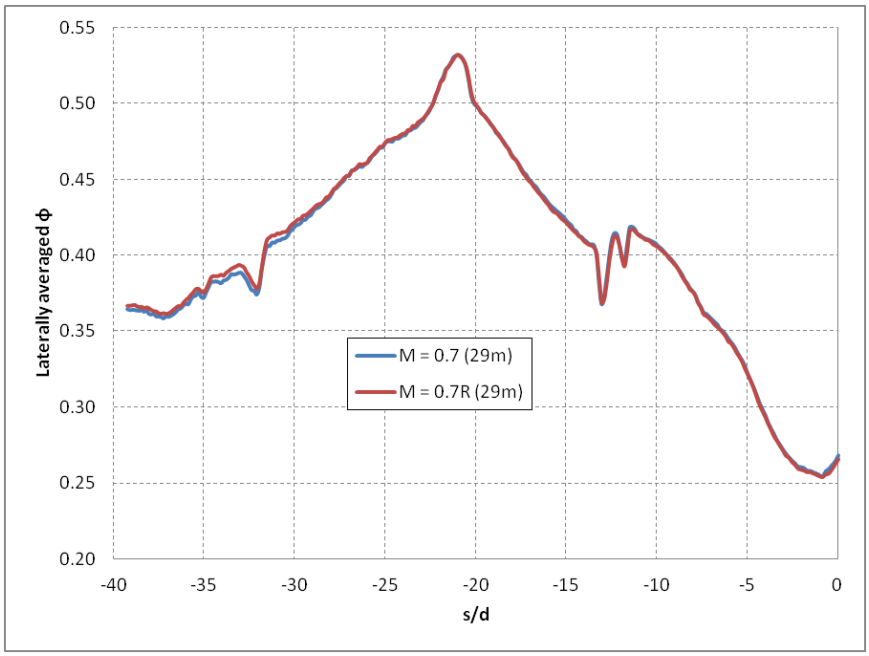

Figure 2.5.2.2: The in-test ϕ repeatability comparison for the PS2 only configuration using the P20 camera

Additional precision error comes from noise in the camera output. The variation can be seen in Fig. 2.5.2.1b especially. This noise was an unavoidable consequence of electronic and electromagnetic noise from the camera. Albert [82] reported that the standard deviation of individual calibration points from his curve (which was used as the standard for the P20) was ± 1.3 K. However, the refined calibration procedure used for the current study found considerably less deviation from the same curve (± 0.4 K). These values are used as an estimate for the uncertainty of a point temperature measurement from the camera due to noise. Calibrations from the P25 produced similar levels of scatter (± 0.5 K) even though the actual calibration changed from test to test. A perturbation analysis

applied to Eqn. 1.2.1.7 showed that the contribution of camera noise was negligible.

These estimates do not account for potential bias errors. Some possible sources of bias include the measurements of mainstream and coolant temperature, the coolant flow rate, and bias in the camera calibration. The total uncertainty in coolant flow rate was already shown to be at most 2.5%. Even for the portions of the showerhead most sensitive to I^*, a 3% difference in coolant flow rate would cause approximately a 0.003 change in $\bar{\phi}$, a negligible difference. The PS2 only configuration was even less sensitive. For η, a similar analysis finds that the showerhead may have a 0.005 change at some locations in the showerhead (but typically less than 0.001) and less than that for the PS2 only configuration. The aft passage had considerably greater uncertainty in flow rate and the range of I investigated did not show a clear trend for η that could be used to estimate $\partial\eta/\partial I$. However, because multiple points that were at nominally the same flow rate displayed up to $\Delta\eta$ = 0.04, this may be used to estimate the uncertainty for the aft passage only (*i.e.*, $\delta\eta$ = ± 0.04 from the statistics, a very high value).

All the thermocouples used for temperature measurement came from the same batch of wire, so their bias errors should be in the same direction (this was determined by another experimenter who calibrated many thermocouples against standard references), so in any perturbation analysis the bias for T_∞ and T_c should be applied together. For the E-type thermocouples used, 0.5 K is the reported limit of error from Omega, which experience has shown to be

reasonable. Uncertainty in the camera calibration in part relies on the thermocouples as well. It is easy to show that if the calibration temperature was off by 0.5 K, the resulting calibrated temperature would be offset by exactly 0.5 K as well. Therefore, because ϕ and η both include the same bias in all four temperatures, it cancels out completely. Realistically, the bias for each thermocouple was not identical, but because they were all similar this analysis shows that the bias error will be negligible.

An additional uncertainty for the adiabatic effectiveness measurements comes from the inclusion of the conduction correction. The uncertainty in the conduction correction was assumed to be similar to the uncertainty in $\eta_{measured}$ (< ± 0.01). Applying this uncertainty to Eqn. 2.0.1 using a perturbation analysis gives a total uncertainty for η of $\delta\eta$ < ± 0.014. Because $\eta_{measured}$ and η_0 were measured in the same experiment, this represents a precision uncertainty. The bias uncertainty would be the same.

2.5.3. Hot wire measurement uncertainties

There are many potential bias uncertainties in the operation of a hot wire system including: radiation losses to the environment, conduction losses to the prongs, tangential cooling from probe misalignment, and prong interference effects. Because the probe was calibrated *in situ*, these biases were automatically accounted for. The change in the radiation loss due to variation in the mainstream temperature (± 0.2 K) was negligible (<< 0.1%). Bias from the pressure transducer used for the measurements of mainstream velocity was 0.03 m/s [86], which was neglected. Thus the bias error for the velocity measurements

comes solely from the scatter in the calibration points, which was estimated using the standard deviation of individual calibration points from the curve (a method known to produce high estimates) as ± 0.20 m/s. Because this was only 3% of the minimum velocities measured, a better estimate was not computed.

Precision uncertainty in the U, u_{rms}, and Λ values were based on a statistical analysis of in-test repeat points. The uncertainty for U was found to be δU = ± 0.12 m/s (~ 2% at most) while δu_{rms} was somewhat less at ± 0.08 m/s (as high as 100% for regions with very low turbulence, but typically ~ 5% or less as predicted from the sample rate and duration [84]). The uncertainty in the integral length scale came from both the uncertainty in the integration time and the uncertainty in the local velocity. The integration time had approximately ± 0.04 ms uncertainty, due in part to the previously mentioned "cutoff" used. The combination of these factors leads to a typical 4% precision uncertainty in Λ, though at some locations with very small length scales the uncertainty was much higher (as high as 20%). The bias uncertainty in U had a negligible effect on Λ. Repeat points with different calculation intervals (10 s, 20 s, 30 s, 40 s) were done to confirm that the collection interval did not affect the Λ value.

Uncertainty in the velocity measurements also had a strong impact on the measurement of the boundary layer thickness. Not only did the precision uncertainty of U affect the location that would be selected as the edge of the boundary layer, there was additional uncertainty from the process of determining the "zero viscosity" line that was used to normalize the data. An extensive analysis of the points used to generate the lines was undertaken and the result

was an uncertainty in the boundary layer thickness of between ± 0.01 mm and ± 0.08 mm depending on flow condition, with ± 0.05 mm being typical (~ 5%). There was also considerable uncertainty in the boundary layer thickness due to the probe location uncertainty. The precision uncertainty in the probe location was considered negligible (the traverse was accurate to 0.0001”), but there was difficulty in the determination of zero. This procedure (outlined previously, see section 2.0) resulted in an uncertainty of ± 0.025 mm for the SS2 position and ± 0.05 mm for the SS3 position. Therefore a typical estimate for total uncertainty was $\delta\delta_{99}$ = ± 0.06 mm for SS2 (~ 6%) and $\delta\delta_{99}$ = ± 0.07 mm for SS3 (~ 1%).

2.5.4. Additional measurement uncertainties

There are a few miscellaneous measurement uncertainties not covered. The *x/d* and *s/d* uncertainties were estimated based on the difference in the position of known features from their calibrated position. While this bias was corrected so that *s/d* = 0 was positioned consistently, this resulted in slight differences in the *s/d* of downstream features. This additional bias tended to increase further from 0, but was typically less than $\delta s/d$ = ± 0.3. Because the same *s/d* was applied for any given experiment, this uncertainty only matters when comparing different testing conditions (*e.g.*, comparison of ϕ and η).

Chapter 3 – Pressure Side Only Configuration

This portion of the study investigated the film cooling performance of a single row of holes on the pressure side of the vane at *s/c* = -0.25, or *s/d* = -21.1. Both adiabatic and overall effectiveness were measured at this location for six momentum flux ratios: 0.3, 0.4, 0.7, 1.0, 3.2, and 6.8. Note that the last three values are slightly different than the showerhead matched values listed in Table 2.0.3 because of slight errors in the values of overall *M** used as targets for the experiments. Though these measurements were collected on the pressure side (negative *s/c*) they are presented in terms of *x/d*, which is defined such that *x/d* = 0 corresponds to the downstream edge of the film cooling hole and *x/d* increases with distance downstream.

3.1. Adiabatic effectiveness measurements

At this position, there is a favorable pressure gradient ($K = 1.05 \times 10^{-5}$), as shown in Fig. 3.1.1, so although the surface curvature here was low ($2r/d = -181$) the data may not compare well to flat plate experiments. However, the only work that roughly matched the mainstream turbulence used for this study was conducted using flat plate facilities. The work of Bons *et al.* [87], who had *Tu* = 17%, but only reported centerline measurements and had a higher injection angle of $\alpha = 35°$ vs. 25° for the current study. The work of Schmidt and Bogard [88] also reported *Tu* = 17% but had $\alpha = 30°$ and did not report centerline effectiveness for any matching momentum flux ratios. They also provided lateral averages at only a few select *x/d* positions, only one of which was near enough

to the holes for comparison to the current study. A comparison of the current study to the Bons *et al*. data (shown in Fig. 3.1.2.) showed comparable performance near the holes (x/d ≤ 10) only for the highest momentum flux ratio. Farther downstream the Bons data showed higher performance at high momentum flux ratios.

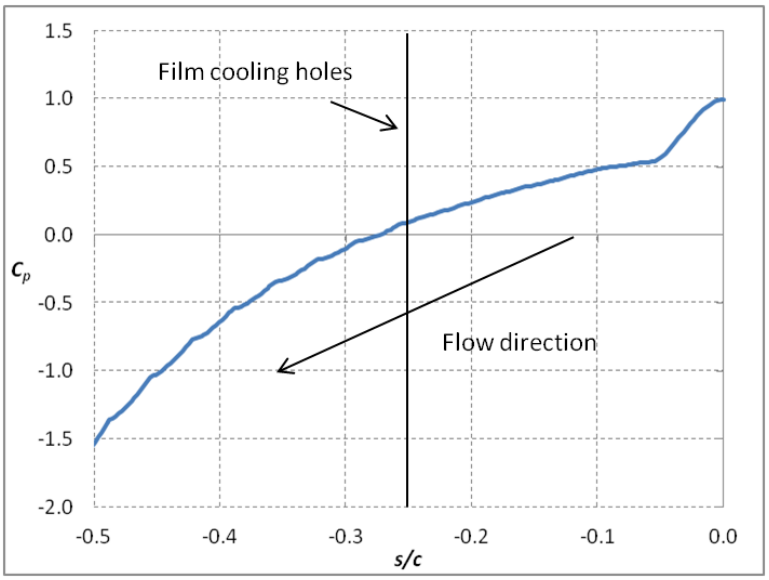

Figure 3.1.1: Pressure gradient over the extent of the effectiveness measurements for the PS2 only configuration

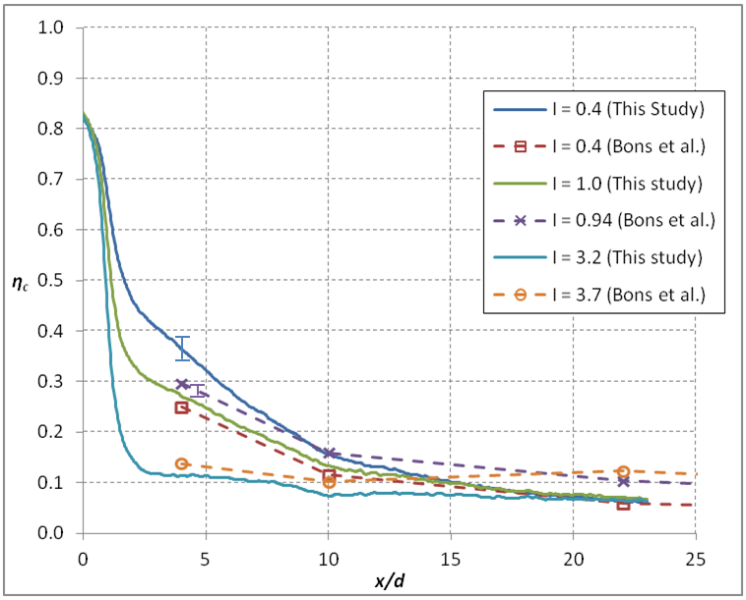

Figure 3.1.2: Comparison of centerline η values to the data of Bons *et al.* [87] with uncertainty shown (Bons *et al*. claimed $\delta\eta = \pm 0.01$)

The Schmidt and Bogard data also showed a peak performance near the holes for a much higher momentum flux ratio (I = 0.8 in their case) than the current data, which are shown in Fig. 3.1.3 as laterally averaged values. In fact, no peak was observed in the current study. This behavior was consistent with the work of Ito *et al.* [89], who studied the effects of curvature on film cooling. They showed that for concave curvature at α = 35° there was no peak effectiveness near the holes. They also showed that for $I \times \cos^2(\alpha) > 1$, the coolant would be driven back toward the wall on a concave surface through centrifugal action. For the current study, this was true for the I = 3.2 and I = 6.8 cases, where the jets could be seen to visibly reattach downstream of the holes. Figure 3.1.4 shows contours of η, which more clearly show the separation behavior. Even for the very strong curvature ($2r/d$ = -15) of Ito *et al.* the reattachment was shown o

primarily affect performance more than 20 *d* downstream of injection, so the current data do not extend far enough downstream to really show the reattachment. Note that the “cold spots” visible in Fig. 3.1.4 at *x/d* = ~ 10 were the PS3 row of holes, which blocked with clay but were still slightly visible. Also note that the conduction correction for these images was not valid for *x/d* < ~ 2.

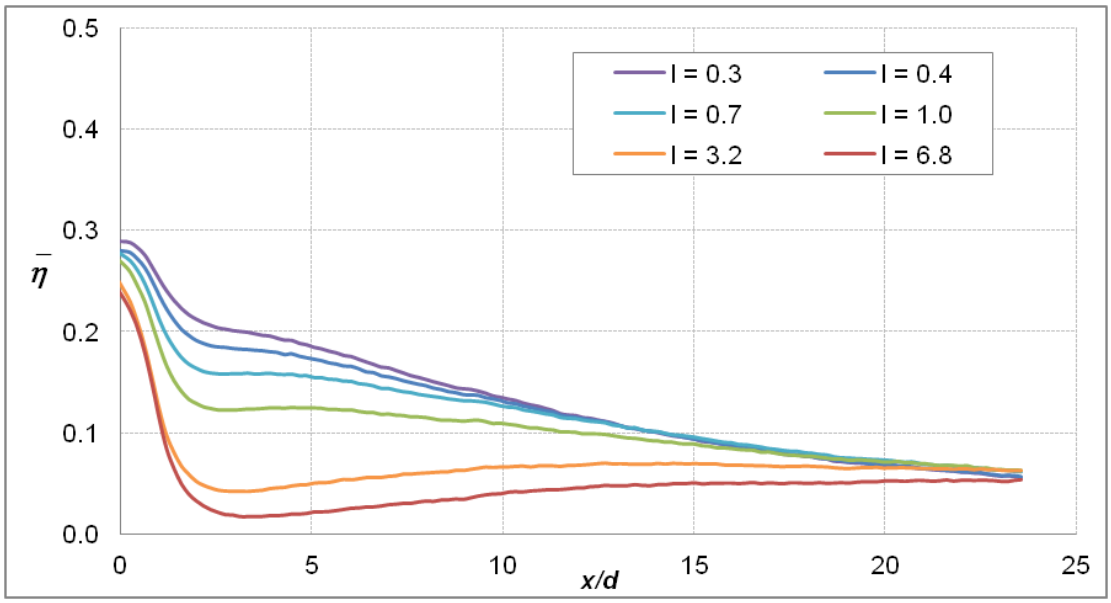

Figure 3.1.3: Laterally averaged adiabatic effectiveness for all measured values of I_{PS2}

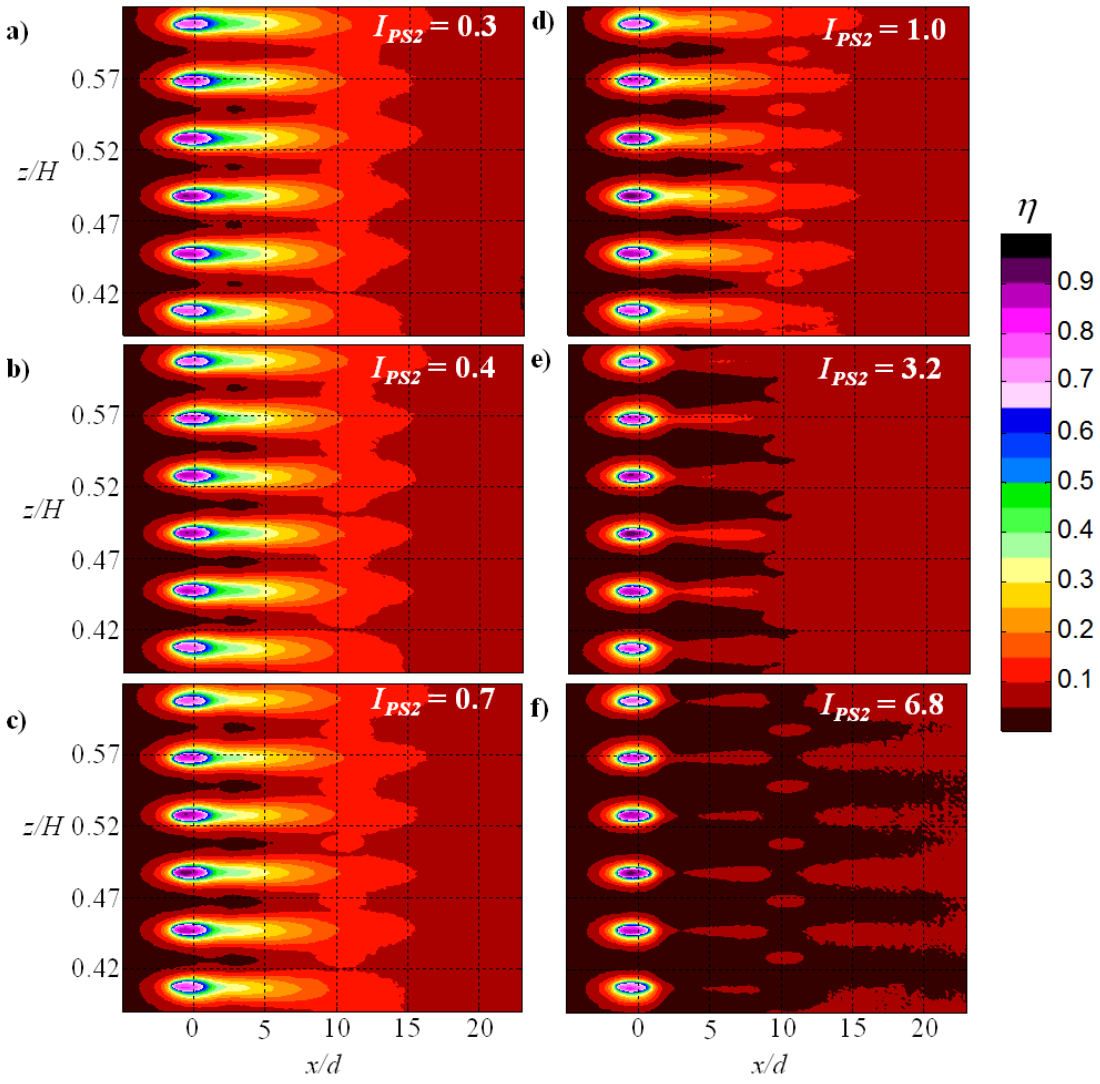

Figure 3.1.4: Contours of η for the PS2 only configuration

3.2. Overall effectiveness measurements

The overall effectiveness displayed much less sensitivity to coolant flow rate than η. This can be seen in Fig. 3.2.1, which shows the laterally averaged overall effectiveness. While $\bar{\eta}$ decreased from ~ 0.2 to ~ 0, $\bar{\phi}$ changed less than

0.1 over the full range of momentum flux ratios. It is also important to note that this change was in the opposite direction, that is, $\bar{\phi}$ improved with increasing coolant flow rates. Even though the precision uncertainty for these measurements was $\delta\bar{\phi} = \pm 0.01$, the difference for over an order of magnitude of change in I_{PS2} was within this band except very near the holes ($x/d < 3$), where conduction effects from through-hole convection were more significant. Note that downstream of the hatch seam located at $x/d = 14$, the internal cooling was provided by a separate radial channel, which was maintained at a constant flow rate with the exception of $I_{PS2} = 6.8$, so the collapse of overall effectiveness in this region was expected. For $x/d < 18$ at $I_{PS2} = 6.8$ there was a slight dip in performance because the aft passage could not be maintained at the same flow rate while the fore passage was at its maximum flow rate.

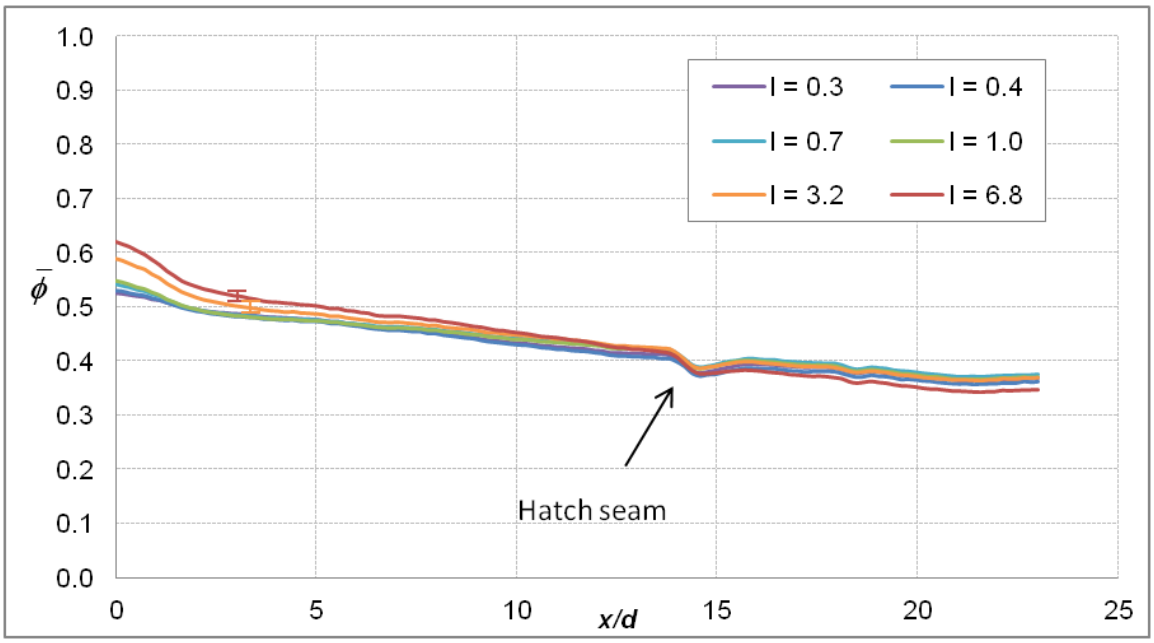

Figure 3.2.1: Laterally averaged overall effectiveness for all measured values of I_{PS2}

This lack of sensitivity was not entirely unexpected; because of the changing contribution of internal cooling vs. adiabatic effectiveness, the work of Williams *et al.* [21] had shown that when internal cooling was tied directly to the coolant flow rate, the performance increased with momentum flux ratio inside a narrow range. Because their work was performed on a similarly flat region on the suction side ($2r/d$ = 168) it may provide a reasonable comparison. Figure 3.2.2 compares similar momentum flux ratios for both studies. The Williams *et al.* data clearly show a much lower overall effectiveness, but because η values were similar for both tests, this was because of differences in the internal cooling (overall flow rates were much lower for their experiments, which produced much weaker internal impingement jets) and external h (suction side h_0 was 80% greater). However, it is still evident that for a similar range of I values, there was

minimal change in $\bar{\phi}$, and the small change near the holes had nearly the same magnitude.

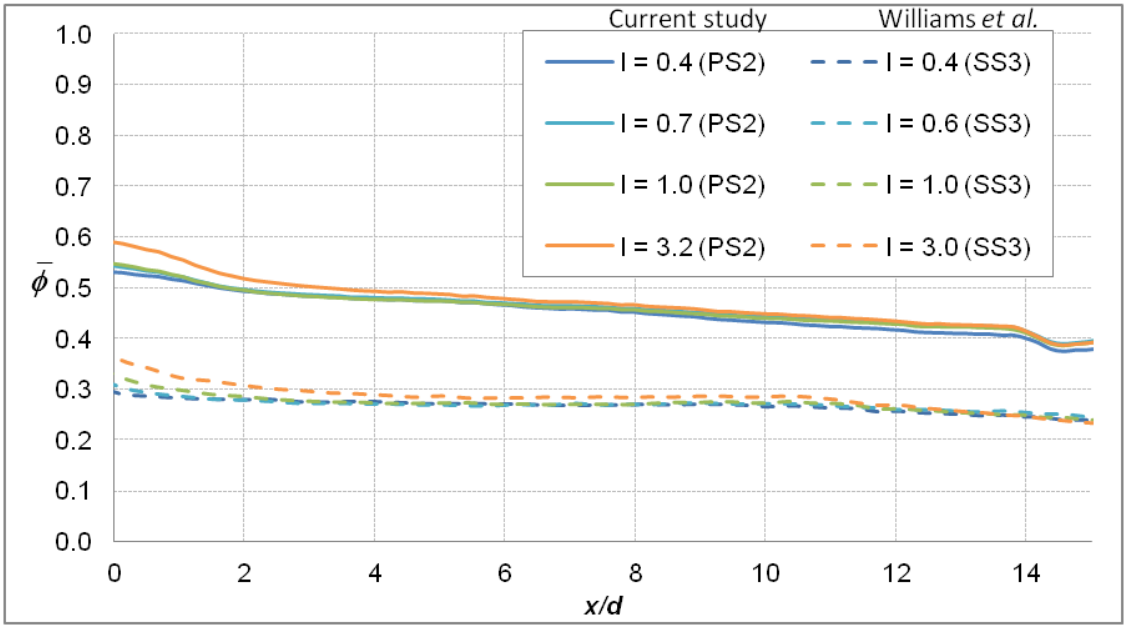

Figure 3.2.2: Comparison of the current study to the work of Williams *et al.* [21] for select momentum flux ratios

The contours of overall effectiveness, as shown in Fig. 3.2.3, more clearly show the impact of through-hole convective cooling. For the lowest momentum flux ratio, the region near the holes was nearly the same temperature as the surrounding wall and showed only small regions of decreased temperature near the holes. These regions progressively increased with momentum flux ratio until the area was nearly uniform in temperature.

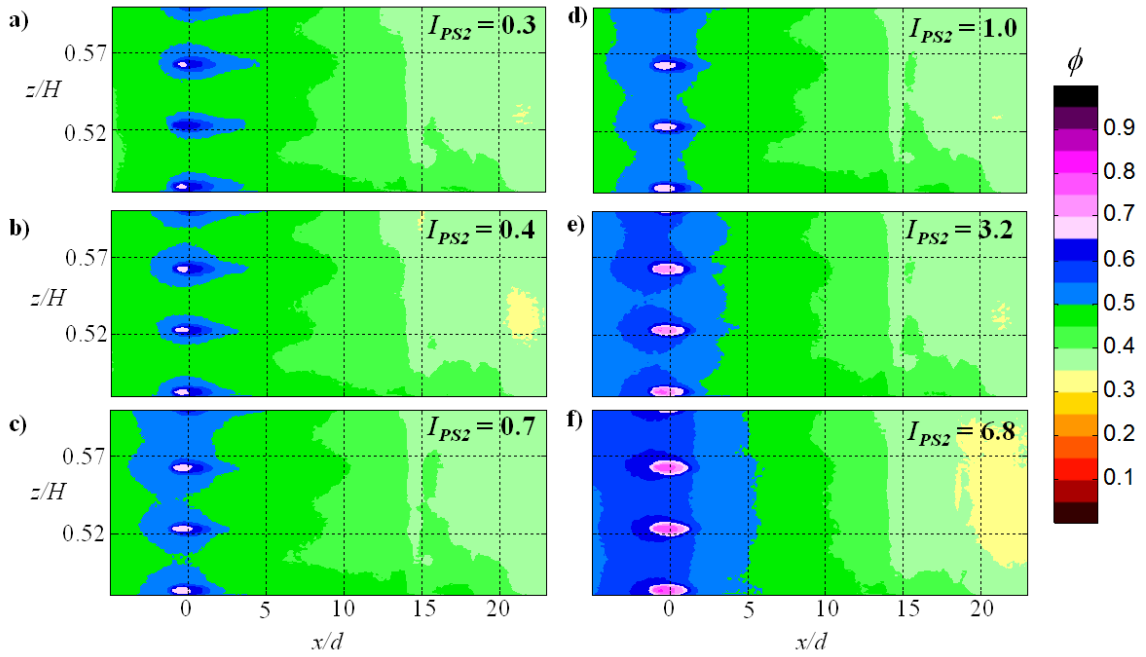

Figure 3.2.3: Contours of ϕ for the PS2 only configuration

Like previous studies (in particular, [21]), these measurements show a significant span-wise temperature gradient associated with the film cooling jets. The magnitude of the difference was too small to be very prominent in the contour plots, but Fig. 3.2.4 shows more clearly that even though the thermal gradient was much reduced, there was still approximately a 0.05 difference between the maximum and minimum ϕ at x/d = 5. This may seem like a small change, but at engine conditions this would be equivalent to approximately 75 K, which is considered enough to cut down part life for temperature driven failure modes by a factor of four [10]. For higher momentum flux ratios, the span-wise temperature was almost completely uniform.

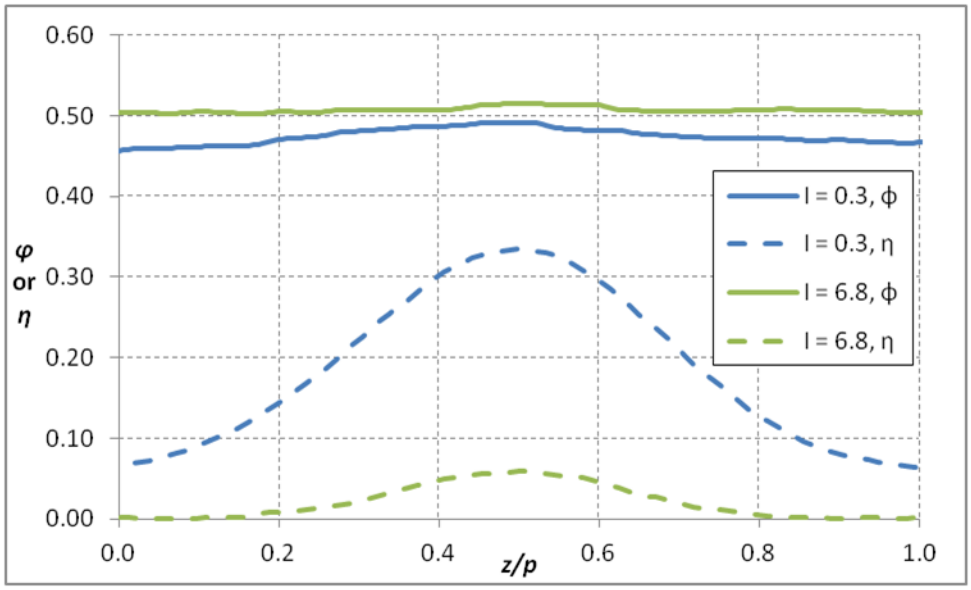

Figure 3.2.4: Span-wise profile of η (dashed lines) and ϕ (solid lines) for two momentum flux ratios at x/d = 5

Chapter 4 – Fully Cooled Configuration

This configuration represents the ultimate goal of the film cooling studies which began with Williams *et al.* [21] and Nathan *et al.* [33]: an experimental model with a realistic film cooling configuration. Both adiabatic and overall effectiveness measurements were collected for I^*_{SH} = 0.8, 1.9, 3.3, 5.2, and 7.5 (M^*_{SH} = 1.0, 1.5, 2.0, 2.5, and 3.0). The data also make for interesting comparisons to the simpler film cooling configurations, a superposition analysis using the showerhead data from Nathan *et al.*, and a simple model for the prediction of $\bar{\phi}$ from more easily measured values of η and ϕ_0.

4.1. Adiabatic effectiveness measurements

The laterally averaged η results for the complete range of visible surface are shown in Fig. 4.1.1. Generally, $\bar{\eta}$ improved with increasing momentum flux ratio in and immediately downstream of the showerhead, while jet separation reduced $\bar{\eta}$ downstream of the other rows of holes. Note that the distinct peaks at the locations of the holes are due to the inclusion of the holes in the lateral average.

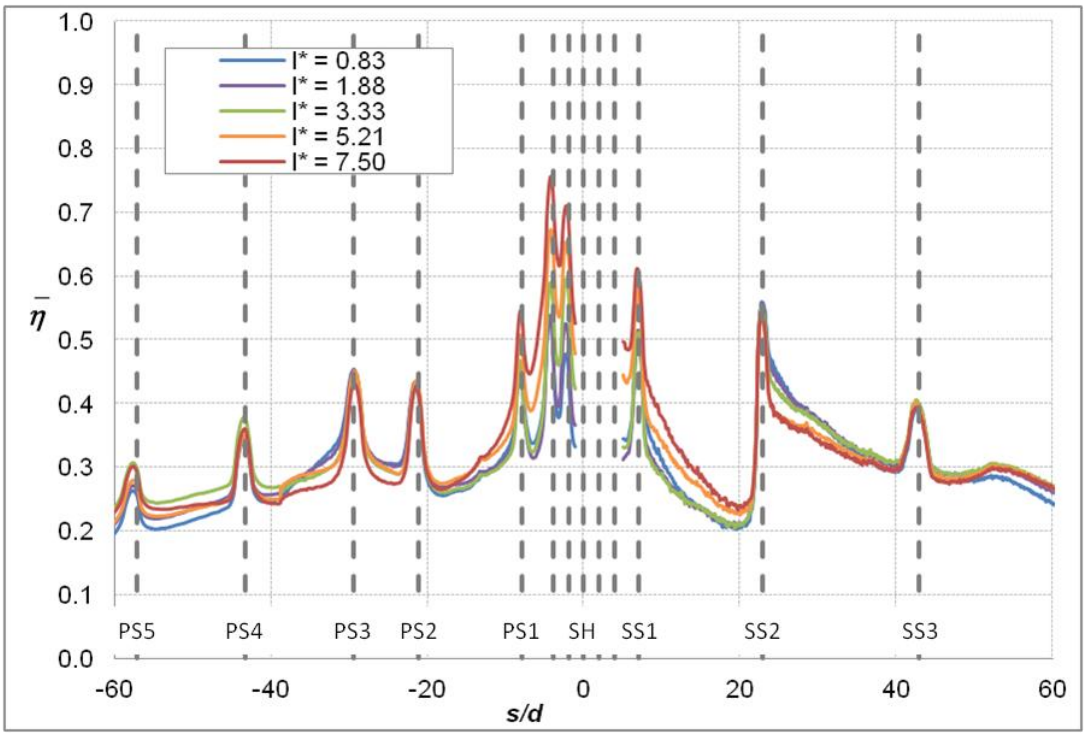

Figure 4.1.1: Laterally averaged adiabatic effectiveness over the complete measurement range for the fully cooled configuration. Dashed lines indicate the hole locations.

The behavior of $\bar{\eta}$ in the showerhead was consistent with the measurements of Polanka *et al.* [72] and Witteveld *et al.* [90], who showed that a "build-up" of coolant within the showerhead produced increasing coverage. The measurements may also be more directly compared to the work of Nathan *et al.* [33], who tested the same showerhead configuration without any downstream cooling. Figure 4.1.2 shows selected momentum flux ratios for both configurations. Agreement was good except downstream of the SS1 gill row of holes. The showerhead alone displayed adiabatic effectiveness levels between 0.05 and 0.08 higher than the current study. This could have been due to a change in the internal flow conditions. Gritsch *et al.* [81] showed that internal

cross-flow had an especially strong effect on span-wise oriented holes at low pressure ratios. The SH only configuration would have a much stronger cross-flow as coolant entering from downstream of the SS1 row moved upstream internally to exit in the showerhead region. The reduced C_d caused by stronger cross-flow would reduce the local blowing ratio of the SS1 row in the SH configuration compared to the current configuration, which would improve cooling performance by reducing jet separation. This effect would be less pronounced on the pressure side because the local momentum flux ratio there was much higher ($1.8 < I_{PS1} < 14$) so a slight reduction in local flow rate would have less effect.

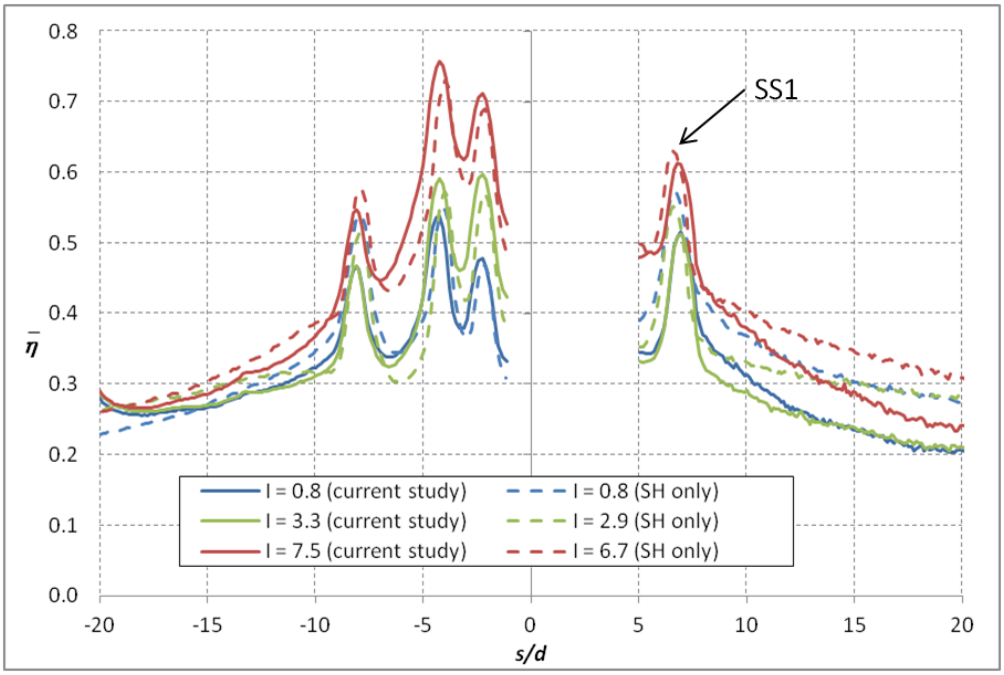

Figure 4.1.2: Comparison of $\bar{\eta}$ values between the current study and the work of Nathan *et al.* [33]

Figure 4.1.3 shows the contours of η for all the measured momentum flux ratios. The contour plots more clearly show the effect of jet separation on the downstream jets. The SS1 row of holes in particular shows a much reduced "blue" region immediately downstream as the momentum flux ratio increased. A comparison with the SH only data for the same momentum flux ratio in Fig. 4.1.4 shows that separation was increased downstream of SS1, which supports the idea that a change in the flow from SS1 was responsible for the change in η. The increase in η at the highest momentum flux ratios comes from coolant in the showerhead region, where the span-wise build-up of coolant has greatly improved effectiveness by blocking the mainstream from reaching the wall. These features are emphasized in Fig. 4.1.5, which shows a close-up view of the showerhead for three momentum flux ratios. Another behavior emphasized in Fig. 4.1.5 is the fact that the differing pitch between the showerhead holes and the SS1 row produced a span-wise variation in the performance as row-to-row interaction varied. Similar behavior was observed by Nathan *et al.* for the SH alone configuration. It was also evident that an increasing momentum flux ratio had an impact on the span-wise component of the velocity near the wall, as jet traces from downstream holes tended to move vertically. This was most apparent for the SS3 row of holes. Increasing momentum flux ratios also eliminated span-wise uniformity in the showerhead region. This was because there were only a limited number of holes in the showerhead to build up coolant prior to entering the field of view. This behavior is something that would be expected for a real engine part with very few, large showerhead cooling holes. Often, span-wise

periodicity is assumed, but clearly that was not the case for this design. Cutbirth and Bogard [91] explored the development of span-wise periodicity in more detail.

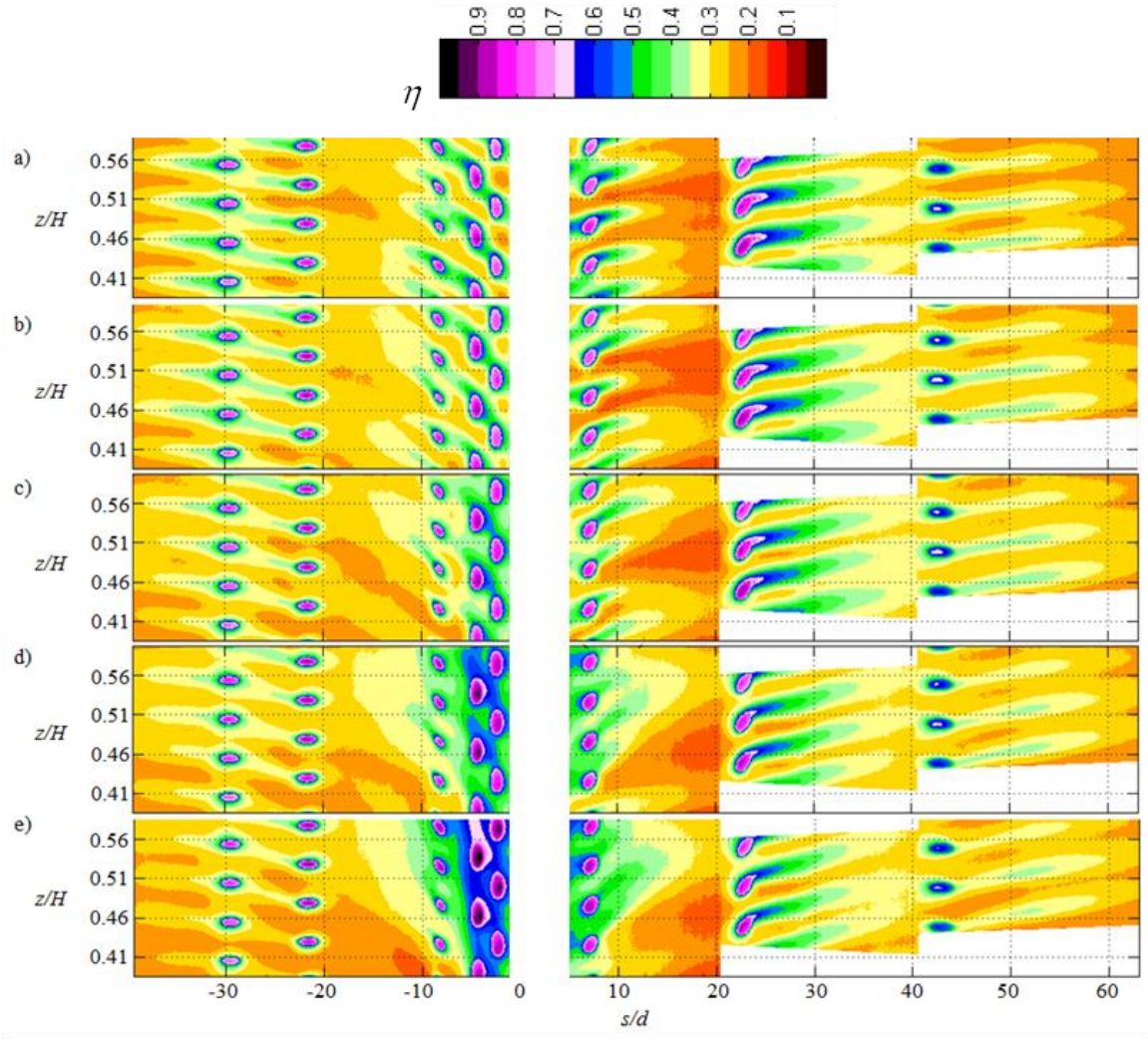

Figure 4.1.3: Contours of η for the fully cooled configuration for I^*_{SH} = a) 0.8, b) 1.9, c) 3.3. d) 5.2, and e) 7.5

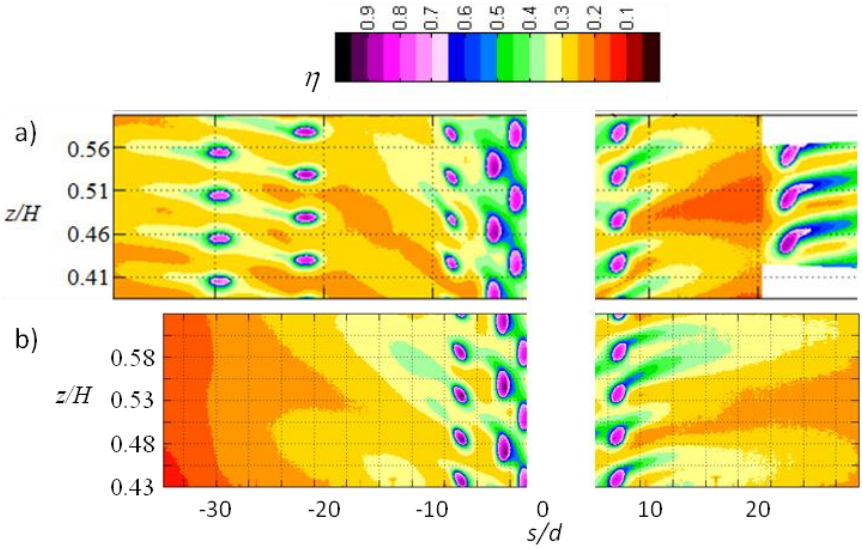

Figure 4.1.4: Contours of η for a) the fully cooled configuration at I^*_{SH} = 3.3 and b) the SH alone configuration of Nathan *et al.* [33] at I^*_{SH} = 2.9

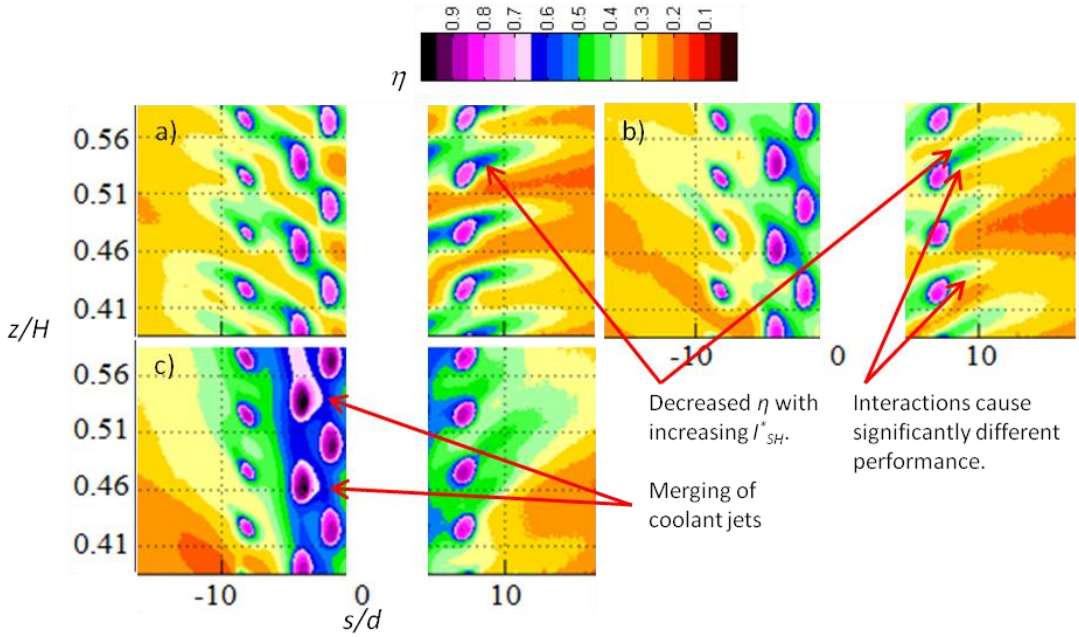

Figure 4.1.5: Close-up view of the showerhead region for the fully cooled configuration at I^*_{SH} = a) 0.8, b) 3.3, and c) 7.5

Figure 4.1.6 shows two examples of the contours from the far downstream region on the pressure side (-30 < *s/d* < -70). The coolant flow rate for these holes was varied from 0.6 < I_{PS4} < 1.2 and 0.9 < I_{PS5} < 2.0; however, very little change was observed. The change in the cooling contributed from the PS3 row of holes was evident, as separation reduced the performance for the higher momentum flux ratio. The work of Albert and Bogard [32], who employed the same vane profile with a reduced showerhead and a single row of holes at approximately the PS2 position, showed an improvement at high blowing ratios on the pressure side caused by reattachment of detached jets for *s/d* < ~ -30. This behavior was not observed for this configuration, possibly because further injection from downstream holes prevented reattachment.

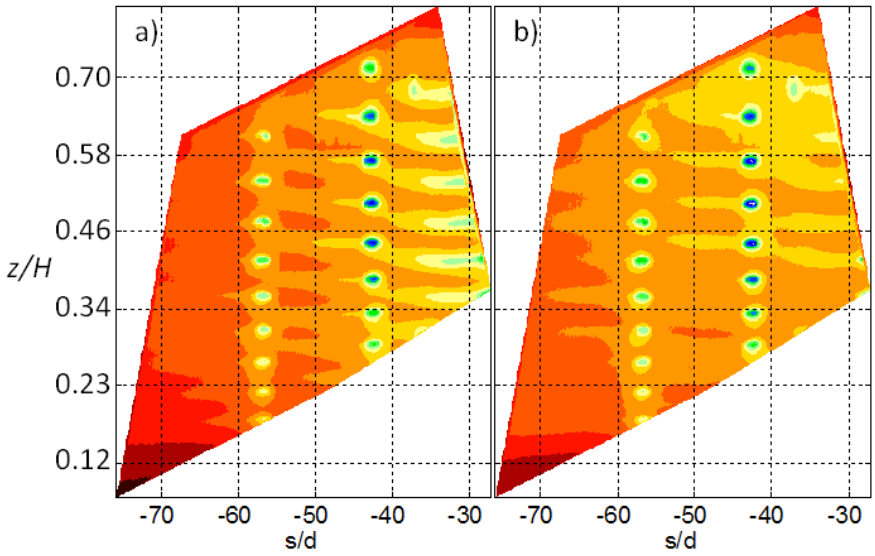

Figure 4.1.6: Contours of η for the downstream portion of the PS for the fully cooled configuration at I^*_{SH} = a) 0.8 and b) 7.5

4.2. Overall effectiveness measurements

The overall cooling effectiveness was measured for the same conditions as those used for the adiabatic effectiveness measurements. Additionally, some holes were blocked in the mid-span region, which allowed the measurement of overall effectiveness without film cooling, ϕ_0.

4.2.1. Overall effectiveness with film cooling

Unlike $\bar{\eta}$, the laterally averaged overall effectiveness improved with increasing *I* virtually everywhere on the surface of the vane, as shown in Fig. 4.2.1.1. Even locations where $\bar{\eta}$ was reduced (*e.g.*, downstream of the SS2 row of holes) saw improved overall effectiveness, which can be attributed to enhanced internal cooling. The sharp dip in overall effectiveness at *s/d* = -13 was due to a hatch seam that had been sealed using the low conductivity spackle normally employed on the foam vane. Also note the dramatic reduction in overall effectiveness downstream of the PS3 row of holes was due to the transition from impingement cooling to channel flow in the aft passage. The change at the highest flow rate for the *s/d* < -40 region was probably from the uncertainty in measuring the aft flow rate more than anything else. Bafflingly, the pressure side did not show any significant change in performance with varying *I* for -30 < *s/d* -10. A possible explanation for this behavior can be obtained with comparison to the ϕ_0 data presented later.

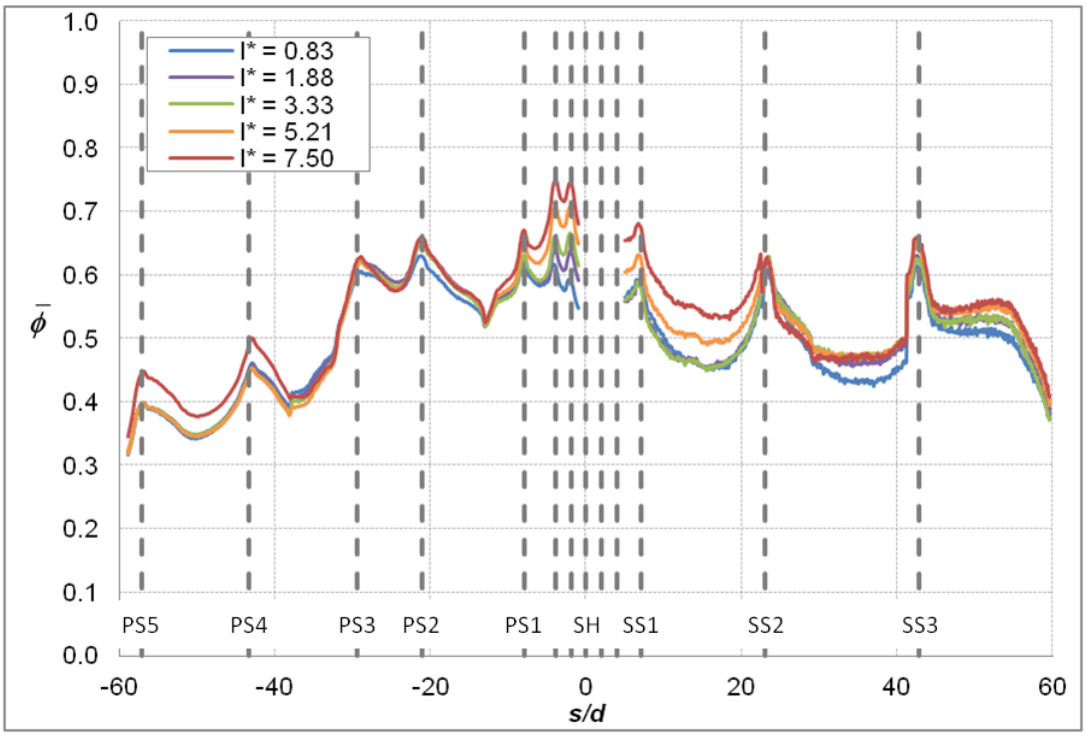

Figure 4.2.1.1: Laterally averaged overall effectiveness over the complete measurement range for the fully cooled configuration

The effect of coolant build-up previously seen in the adiabatic effectiveness results was very evident in the contour plots of ϕ, as shown in Fig. 4.2.1.2. It was also interesting that the overall effectiveness in the $10 < s/d < 20$ region did not improve until $I^*_{SH} = 5.2$, at which point it improved more than the adiabatic effectiveness for the same conditions. The expectation had been that the overall effectiveness would improve continuously with momentum flux ratio, as had been seen in the same region for SH cooling alone in Nathan *et al.* [33]. Also notable was the lack of distinct coolant jets on the pressure side while the suction side still showed distinct jets. This uniformity indicated that the internal cooling was playing a larger part in the total cooling for this part of the vane.

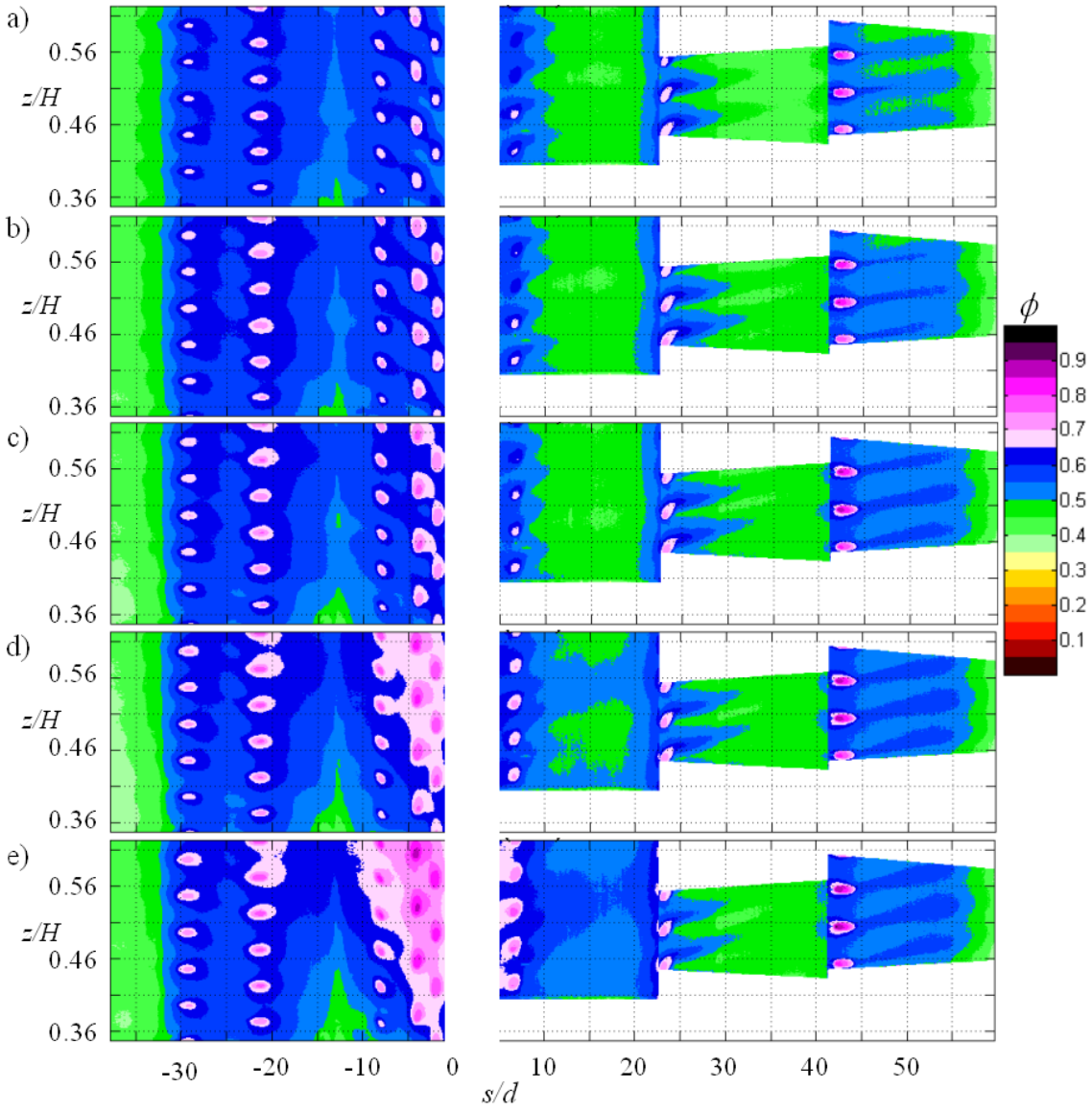

Figure 4.2.1.2: Contours of ϕ for the fully cooled configuration for I^*_{SH} = a) 0.8, b) 1.9, c) 3.3. d) 5.2, and e) 7.5

The ϕ contours for the s/d < -35 region were identical for the lowest momentum flux ratios. Recall that for I^*_{SH} = 0.8, 1.9, and 3.3 the aft passage was

maintained at the same flow rate, so the lack of sensitivity was not surprising when it was observed that η was not affected much by upstream cooling. However, Fig. 4.1.6 shows that at the highest momentum flux ratio – where the aft flow rate was approximately double the condition used for the other showerhead flow rates – the overall effectiveness was improved. The improvement was most significant upstream of the holes, indicating that this change was primarily from through-hole convection.

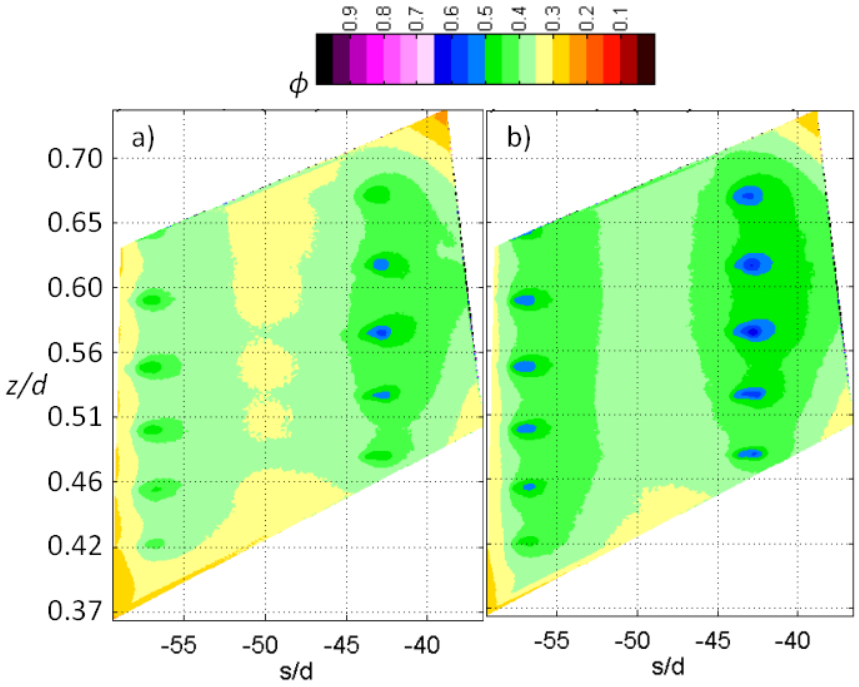

Figure 4.2.1.3: Contours of ϕ for the downstream portion of the PS for the fully cooled configuration at I^*_{SH} = a) 0.8 and b) 7.5 (I_{PS4} = 0.6 and 1.2)

4.2.2. Overall effectiveness without film cooling

Internal cooling was measured for coolant flow rates equivalent to those used for the film cooling portion of the study. There was an assumption that the strength of the impingement jets was not greatly affected by blocking some of the film cooling holes with tape. This assumption was supported by the span-wise temperature uniformity visible in Fig. 4.2.2.1. Note that the cold spots near s/d = -28 at high coolant flow rates were the result of active upstream holes. Even with some holes blocked, the presence of unblocked holes limited the places where good measurements of ϕ_0 could be obtained, as shown by the gaps in the data in Fig. 4.2.2.2. As expected, the internal cooling improved continuously with increasing coolant flow rate. The ϕ_0 levels were also much higher on the pressure side than the suction side, which was due to the much reduced h_0 values there (see Fig. 9.2.2). The effect of transition on the suction side (which greatly increases h_0) was also visible as a sharp decline in ϕ_0 around s/d = 23, where Dees *et al.* [29] determined that transition occurred for high mainstream turbulence. The decline in ϕ_0 for s/d > 55 was from the lack of impingement cooling in the aft passage.

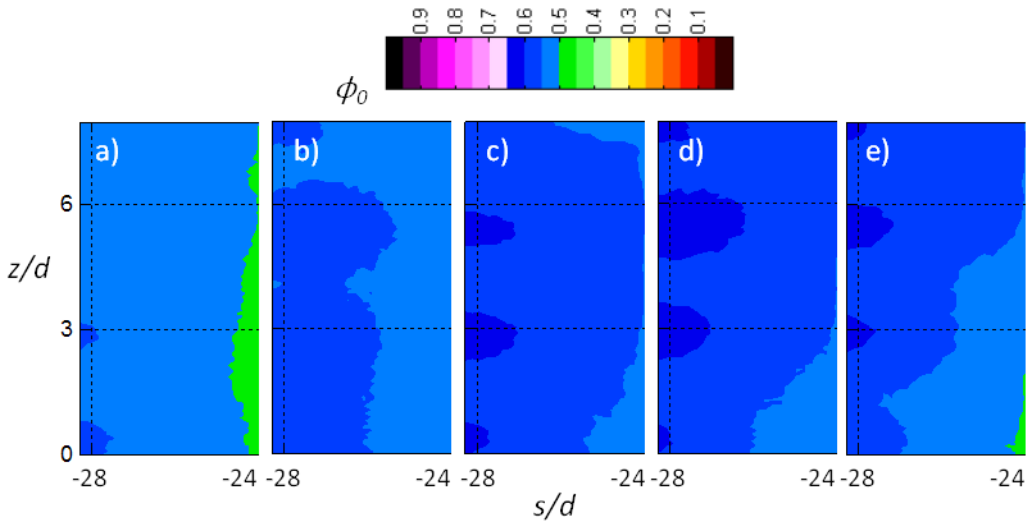

Figure 4.2.2.1: Contours of ϕ_0 for internal coolant flow rates equivalent to *I*SH* = a) 0.8, b) 1.9, c) 3.3, d) 5.2, and e) 7.5

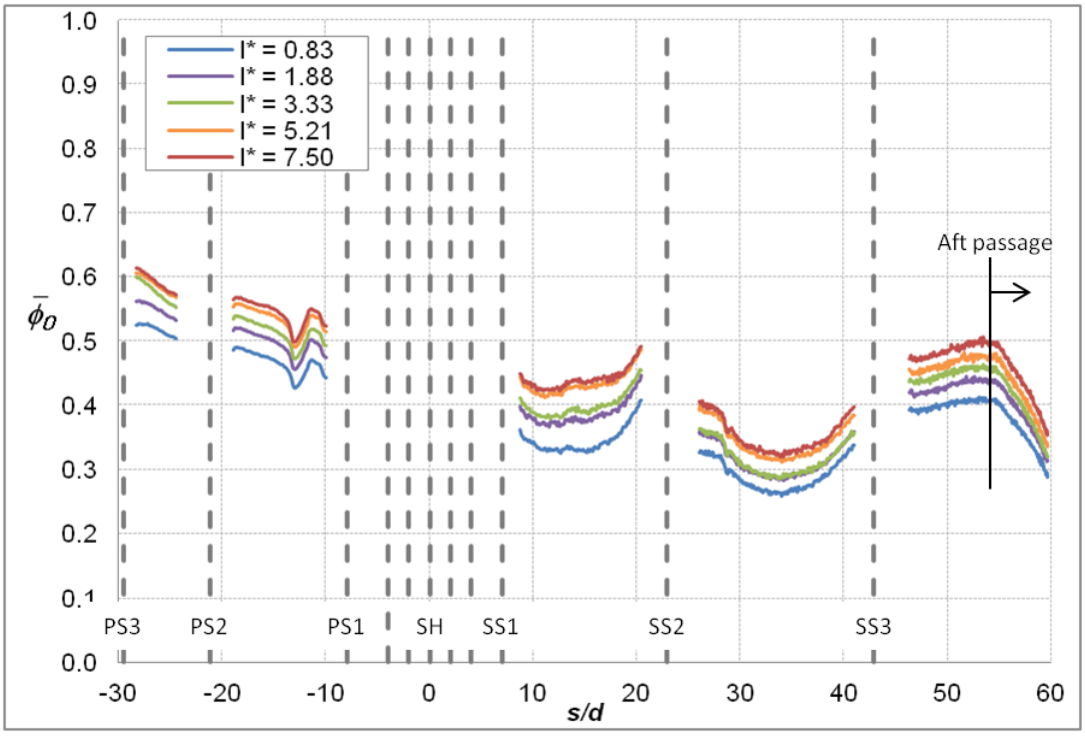

Figure 4.2.2.2: Overall effectiveness without film cooling

A direct comparison between $\bar{\phi}$ and $\bar{\phi}_0$ (Fig. 4.2.2.3) shows the contribution of internal cooling to the overall effectiveness. Though the internal cooling was clearly improving for *s/d* < -10, $\bar{\phi}$ remained approximately the same. At the same time, $\bar{\eta}$ increased slightly for -20 < *s/d* < -10 and decreased for *s/d* < -20, but remained close to 0.3. Normally effectiveness levels of 0.3 would provide significant protection from the hot mainstream, but film injection significantly disturbs the boundary layer. The flow field for this region of the vane was laminar or near laminar for h_0 [64] but would be expected to be turbulent following film injection. Increasing levels of coolant flow would further increase h_f and further reduce the overall effectiveness [35]. The suction side of the vane may have been affected similarly (for the portion prior to transition at least), but strong acceleration over the 0 < *s/d* < 10 region ($K > 3.5 \times 10^{-5}$, double what was seen on the PS) would reduce the impact of augmentation form the showerhead, so film cooling was still providing a substantial benefit. This behavior helps to illuminate why the pressure side values of $\bar{\phi}$ did not display any sensitivity to coolant flow rate; enhanced augmentation eliminated the benefit of film cooling but internal cooling compensated for the loss.

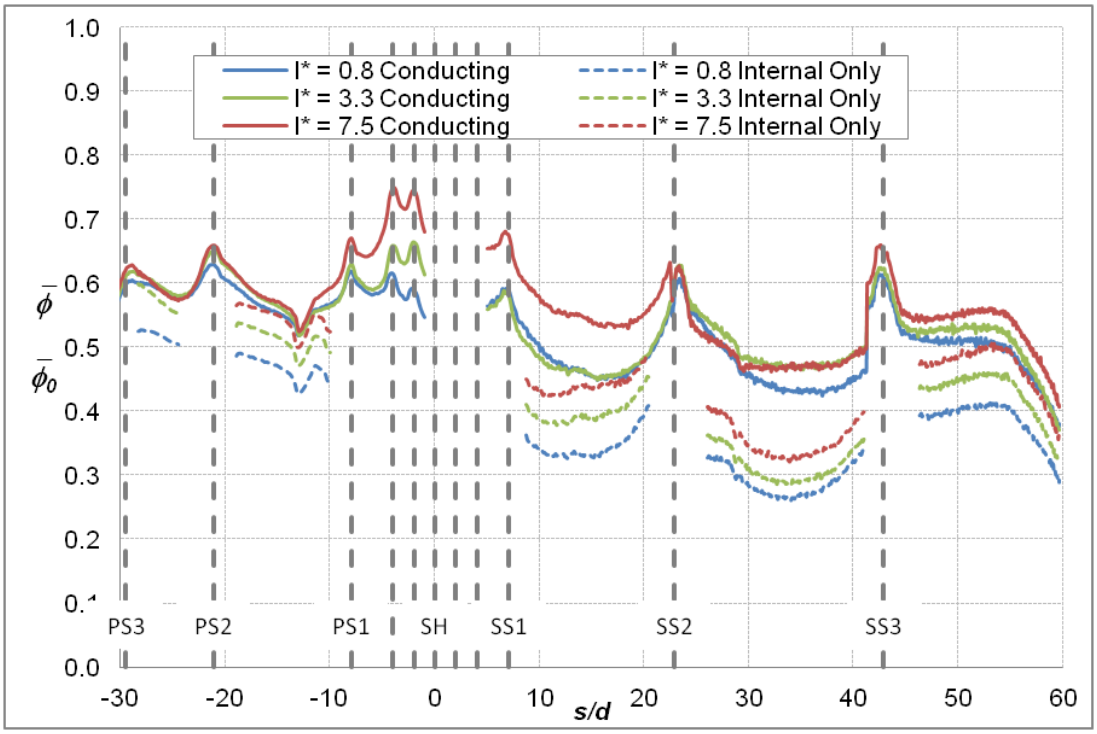

Figure 4.2.2.3: Comparison of laterally averaged ϕ and ϕ_0 for selected values of l^*_{SH}

4.3. Additional comparisons and superposition analysis

This configuration was already compared to adiabatic effectiveness data from the showerhead alone configuration of Nathan *et al.* [33], which showed similarity for the pressure side and the showerhead itself, but a substantial change in the suction side cooling performance. It is instructive to extend this comparison to the overall effectiveness, as well as to the SS3 alone data of Williams *et al.* [21] and the PS2 only configuration presented in chapter 3. Also, because data were available for the showerhead alone, the PS2 alone, and a combination of both, it was possible to perform a superposition analysis for that portion of the vane. Lastly, a simple method for prediction of the overall

effectiveness using more easily measured quantities (η and ϕ_0) was compared to experimental data.

4.3.1. Comparison to the showerhead alone

Because the adiabatic effectiveness was nearly identical in the showerhead region, the improvement in the overall effectiveness for the current configuration compared to the showerhead alone – shown in Fig. 4.3.1.1 – was due to improvement in the internal cooling. It was also interesting to see that although $\bar{\eta}$ was reduced by over 0.05 for the fully cooled configuration compared to the showerhead alone near *s/d* = 15 (discussed previously), the overall effectiveness was improved, especially at the highest flow rate (though the momentum flux ratio was not matched as well). This was at least partially due to conduction from the through-hole convective cooling from the SS2 row at *s/d* = 23, as was the improvement on the pressure side. Though the coolant flow rate through the showerhead was nominally the same for both cases, the total coolant flow rate for the fully cooled model was 74-133% greater than the showerhead alone to feed the downstream holes. This means that for the showerhead alone case, some of the coolant feeding the holes was warmed through interaction with uncooled parts of the vane prior to exiting the showerhead.

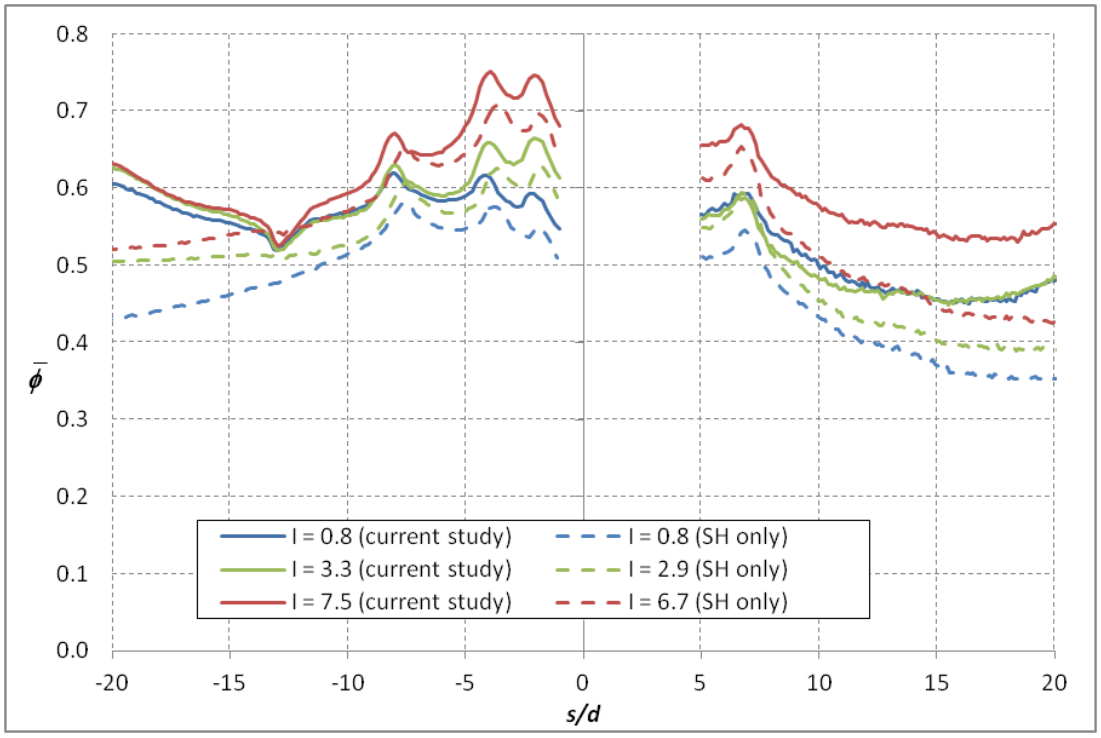

Figure 4.3.1.1: Comparison of laterally averaged ϕ for the current study to the showerhead alone data of Nathan *et al.* [33]

4.3.2. Comparison to SS3 alone

The presence of upstream cooling had a significant impact on the adiabatic effectiveness distribution downstream of the SS3 row of holes, as shown in Fig. 4.3.2.1, which compares contours of η at I_{SS3} = 0.4 from the current study to the SS3 alone data of Williams *et al.* [21]. The upstream cooling clearly imparted significant span-wise momentum to the near-wall flow, which caused the jets to turn. A portion of the upstream data was included to show that the SS2 row of holes was providing significant cooling immediately upstream of the SS3 row. Note that the contour data from the fully cooled configuration have not been

corrected for conduction effects while the SS3 alone data were corrected, so this figure serves for qualitative comparison only (conduction correction data were only available for *s/d* > 47).

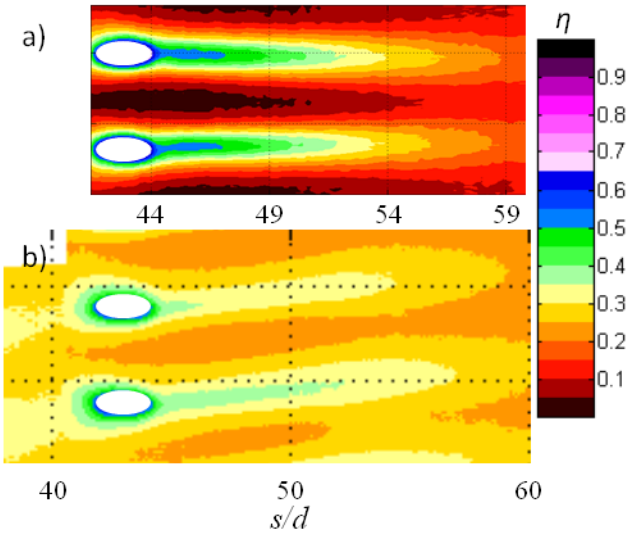

Figure 4.3.2.1: Adiabatic effectiveness comparison at I_{SS3} = 0.4 for a) SS3 alone [21] and b) fully cooled configurations

Even though the data were only qualitative, it was clear that the upstream cooling reduced the effectiveness directly downstream of the SS3 holes, though there was improved cooling between the jets. Laterally averaged data corrected for conduction are shown in Fig. 4.3.2.2. The performance very near the holes was compromised by the presence of upstream cooling at the lowest flow rate, possibly because of increased jet separation caused by reduced momentum in the flow over the SS3 row of holes (the results of chapter 5 further illustrate this point). However, for the higher flow rate the improved coverage compensated for

the increased separation. Farther downstream, the improved coverage was beneficial for both flow rates, producing a substantial improvement of 0.1 for the higher momentum flux ratio, actually reversing the usual trend in $\bar{\eta}$ with increasing momentum flux ratio.

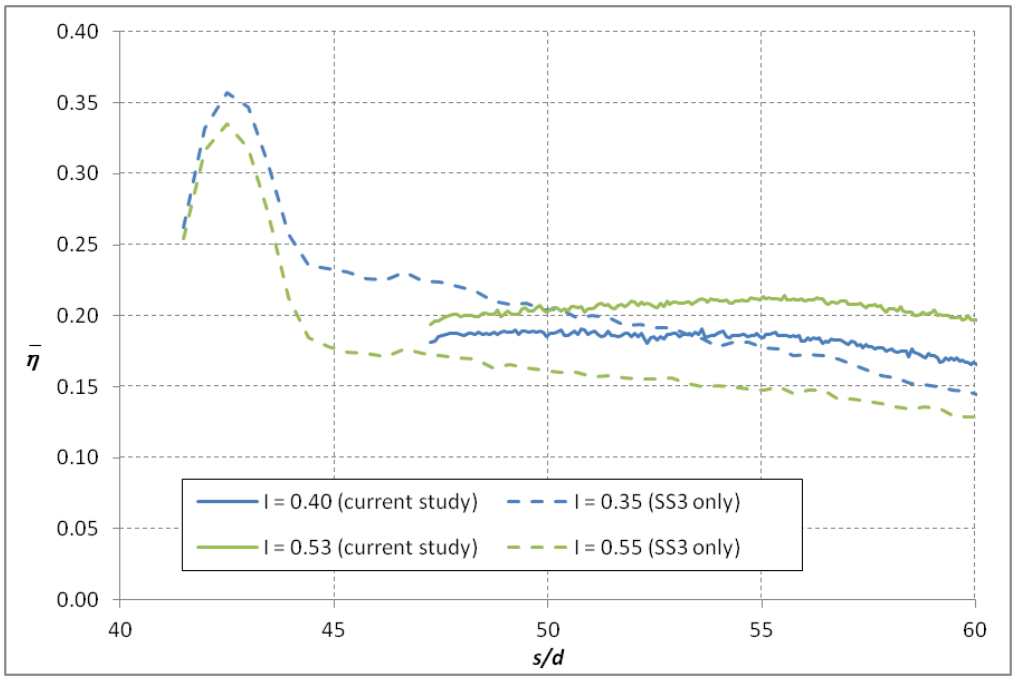

Figure 4.3.2.2: Laterally averaged η for the current study and the SS3 alone data of Williams *et al.* [21]

Comparison of the overall effectiveness was more problematic because of the different internal cooling. Figure 4.3.2.3 shows using ϕ_0 that internal cooling was substantially improved for the fully cooled case. As with the showerhead alone, the coolant for the SS3 alone case entered through impingement holes all over the vane. Though the majority of the coolant entered from the impingement

holes nearest to the film cooling holes, some of the coolant came from the pressure side and passed through the stagnation region.

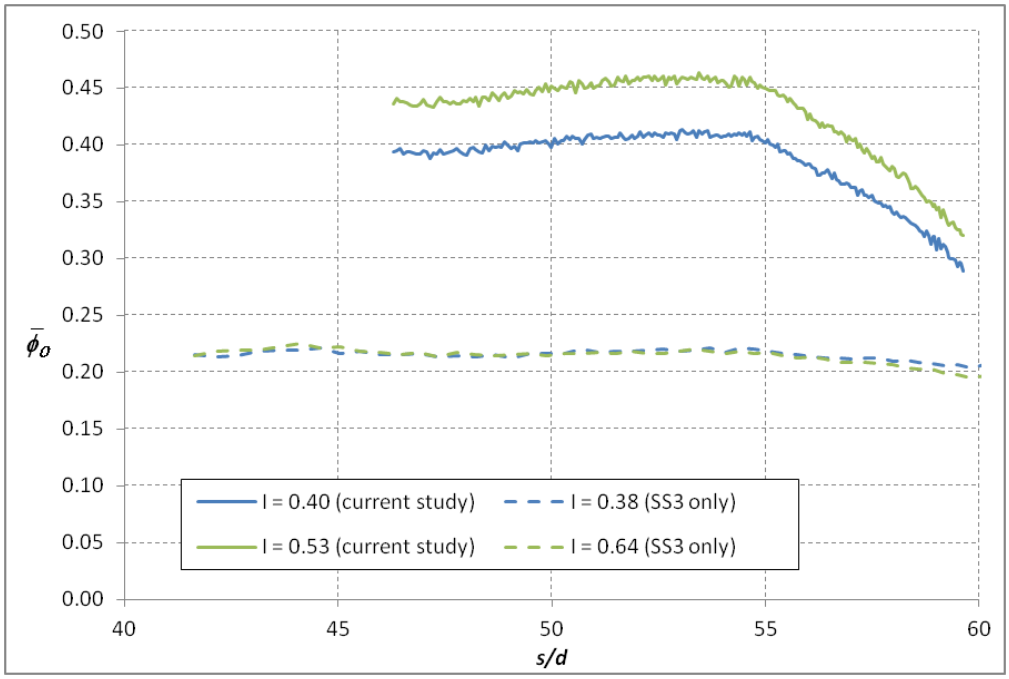

Figure 4.3.2.3: Comparison of ϕ_0 between the fully cooled and the SS3 alone data of Williams *et al.* [21]

The relative performance of the two configurations may be compared by observing the ratio $\bar{\phi}/\phi_0$, which shows the relative benefit of film cooling. Using this metric, the two configurations agreed within uncertainty, as shown in Fig. 4.3.2.4. Because the adiabatic This showed that the change in overall effectiveness for the fully cooled configuration was entirely due to internal cooling effects and the slight change in $\bar{\eta}$ had no impact on the results. The improved adiabatic effectiveness for the fully cooled configuration was apparently counteracted by increased h_f from the additional turbulence introduced by

upstream blowing (it is shown in chapter 5 that upstream blowing continues to affect turbulence levels even after subsequent injection).

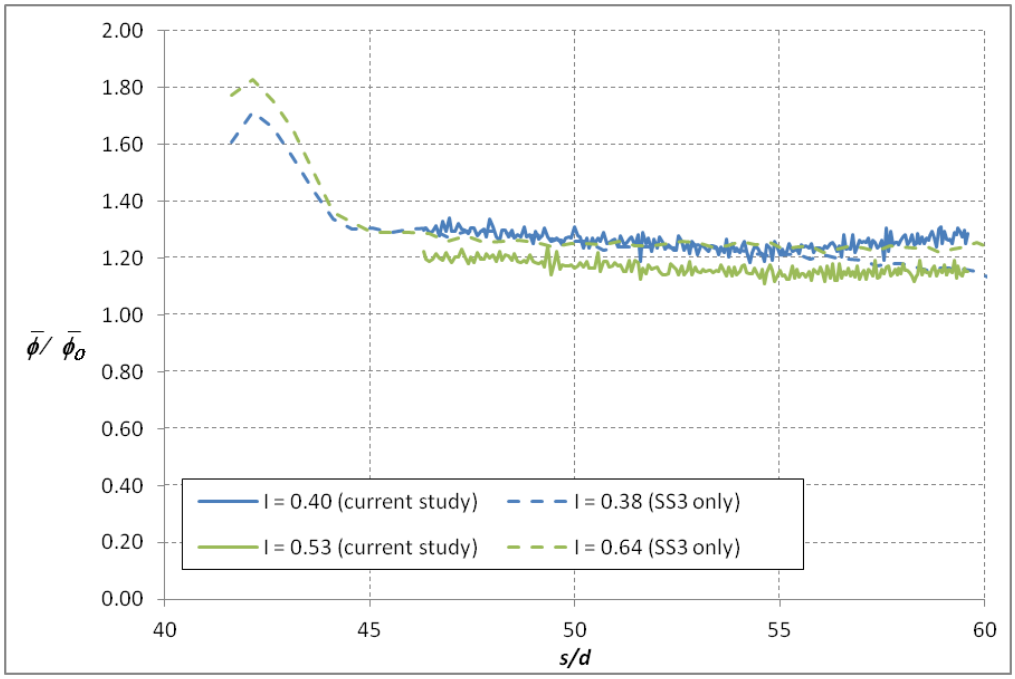

Figure 4.3.2.4: Comparison of the relative performance of film cooling (ϕ/ϕ_0) for the fully cooled configuration and the SS3 alone data of Williams *et al.* [21]

4.3.3. Comparison to the PS2 alone configuration and superposition analysis

A convenient method for predicting the performance of a design is to combine data from simpler configurations using superposition. With the adiabatic effectiveness data from Nathan *et al.* [33] and the data from the fully cooled and PS2 alone cases, the data are available to test the accuracy of superposition for this design. The same analysis could not be performed on the suction side because no measurements of the performance for the showerhead alone were

collected. Before use in this analysis, the SH alone and fully cooled data had the conduction correction from the PS2 only case applied to them. These values were likely representative for the SH case, but no data were available for comparison. The limited conduction correction data from the fully cooled case were very similar to the values from the PS2 only configuration, but there was difficulty with blocking the showerhead so the PS2 data were of better quality and covered a larger range. The superposition analysis used:

$$\bar{\eta}_{sp} = \bar{\eta}_{SH} + \bar{\eta}_{PS2}(1 - \bar{\eta}_{SH}) \qquad (4.3.3.1)$$

to combine the data. This process is illustrated in Fig. 4.3.3.1, which shows the component effectivenesses and the final result. The use of the slightly mis-matched momentum flux ratios was justified by the very good agreement between the showerhead alone and the fully cooled case on the pressure side.

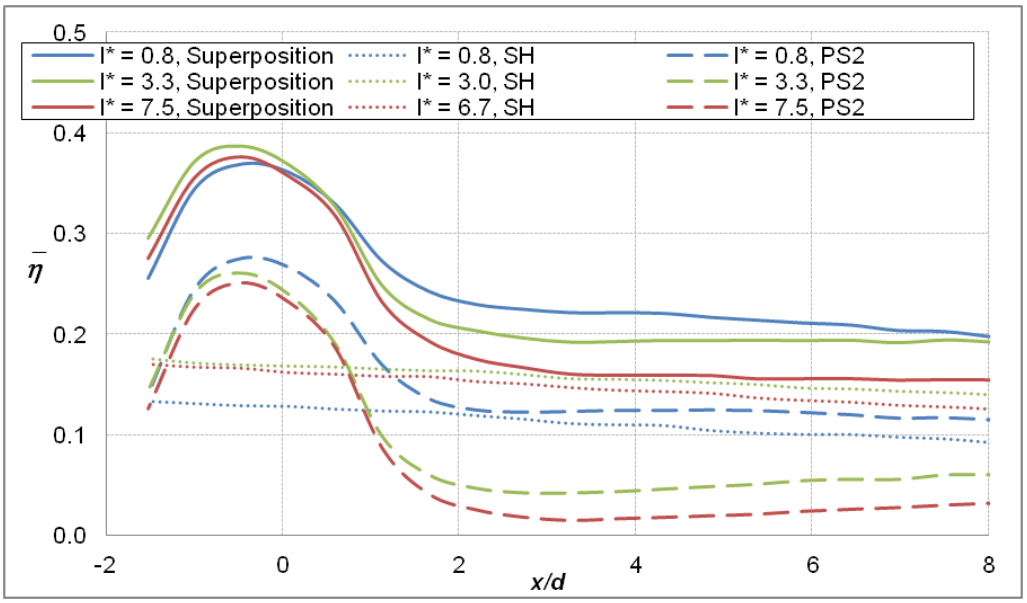

Figure 4.3.3.1: Components used for the superposition analysis compared to the result of Eqn. 4.3.3.1

When compared to the experimental measurements, as shown in Fig. 4.3.3.2, agreement was only seen for the lowest momentum flux ratio. The predictions were progressively worse for the higher coolant flow rates. This could be an effect of the increased turbulence produced by the showerhead injection. Cutbirth and Bogard [37] demonstrated that high levels of turbulence (from the mainstream or from upstream injection) greatly increased jet dispersion for a row of holes on the pressure side. For lower momentum flux ratios, this was very detrimental to performance, but for higher momentum flux ratios the increased dispersion kept more coolant from a “separated” jet nearer to the wall. This interaction is not accounted for by superposition, which is why it under-predicted the performance relative to the measured values of $\bar{\eta}$ for higher momentum flux ratios. Note that the increasing trend for $x/d > 8$ in the measured values may be

due to the conduction correction for the fully cooled data not including the effect of an active row of PS3 holes.

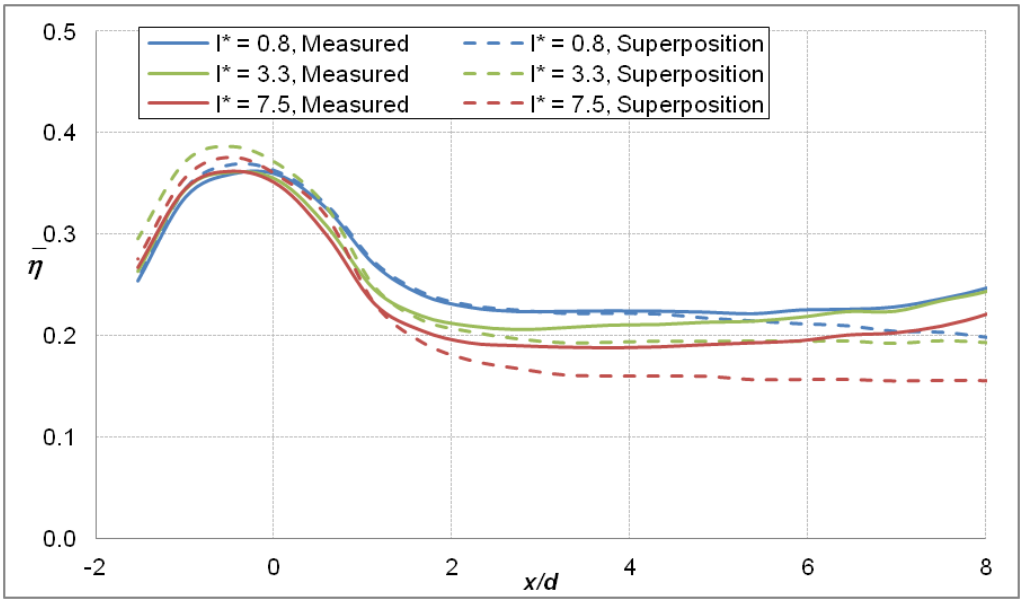

Figure 4.3.3.2: Comparison between the measured values of η and the predictions using superposition downstream of the PS2 holes

The combined effect of coolant from the showerhead and the improved performance of the PS2 row due to the added turbulence produced substantial gains in adiabatic effectiveness, which can be more clearly seen by the direct comparison in Fig. 4.3.3.3. It was also evident that upstream blowing moderated the effect of jet separation, reducing the sensitivity to coolant flow rate.

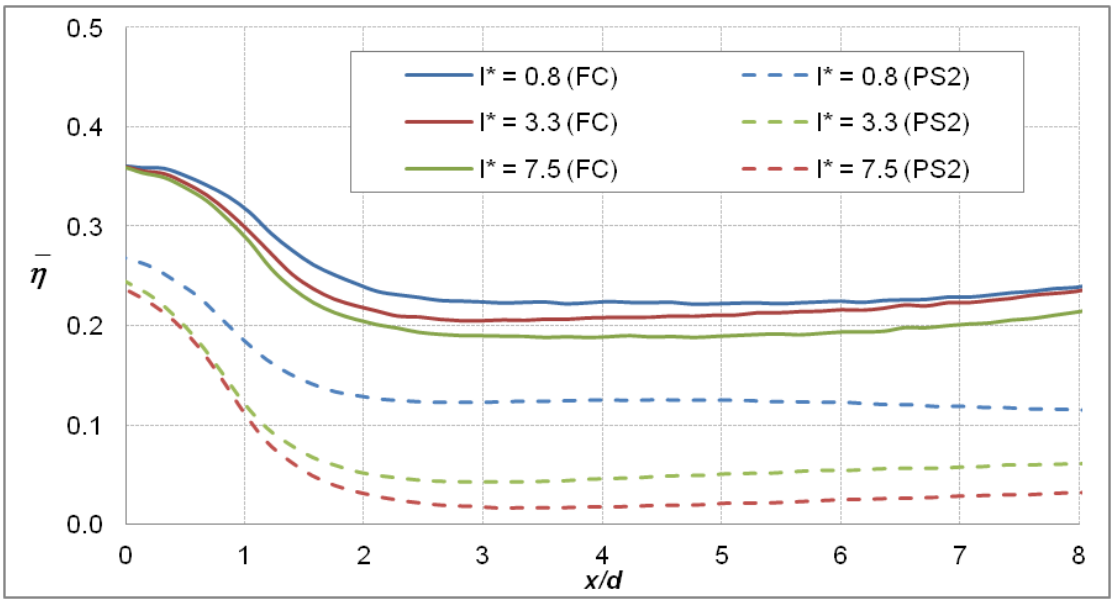

Figure 4.3.3.3: Comparison of laterally averaged η for the fully cooled and PS2 only configurations

No ϕ_0 data were available for the PS2 only case, so a comparison of the overall effectiveness ratio similar to that used for the SS3 configuration could not be made. Figure 4.3.3.4 shows that while the overall effectiveness was improved for the fully cooled case, it was not nearly as large a difference was seen for the SS3 region. In part this is because for the PS2 configuration, the SS holes were left open to keep the overall coolant flow rate high and to prevent coolant from the suction side from mixing internally with the pressure side coolant. Previously, a possible explanation for the lack of ϕ sensitivity to coolant flow rate in this region was that the increased turbulence increased h_f and offset the internal cooling. This could still be the case, but this comparison shows that the augmentation would have to be primarily a result of showerhead injection because the PS2 only case was still affected by increasing coolant flow rate in

the expected manner (*i.e.*, continuous improvement with increasing *I* due to strengthened internal impingement jets.).

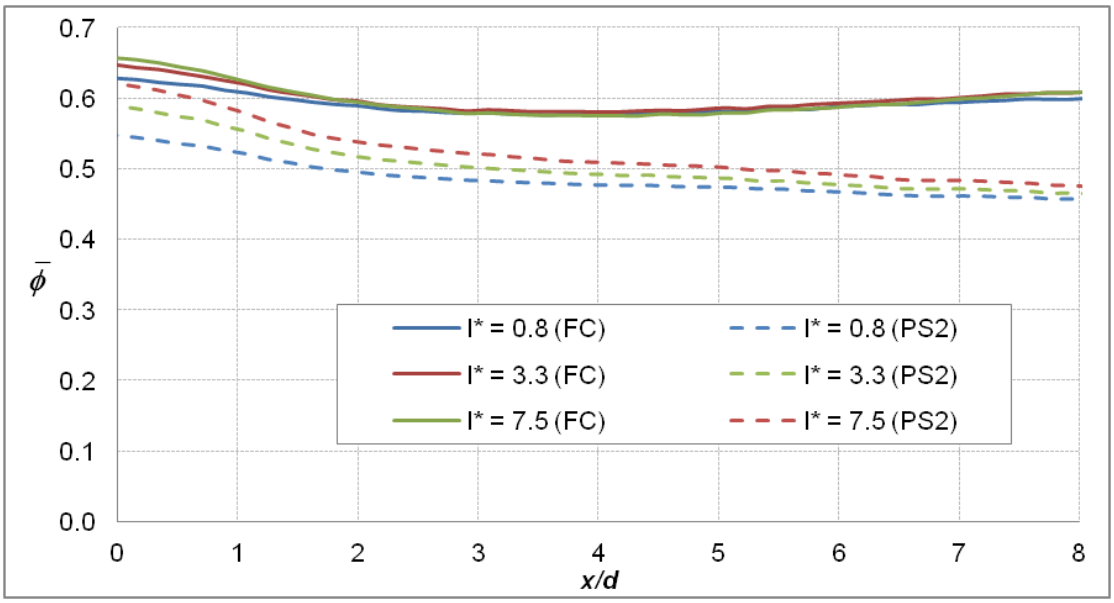

Figure 4.3.3.4: Laterally averaged ϕ comparison for the PS2 and fully cooled configurations

4.3.4. Overall effectiveness prediction with a 1D model

Dees *et al*. [31] proposed a means of predicting the overall effectiveness given the adiabatic effectiveness and ϕ_0. Their analysis relies on the same 1D analysis used to produce the scaling parameters for ϕ, with the realization that a special case exists without film cooling:

$$\phi_0 = \frac{1}{1 + Bi + {}^{h_0}/_{h_i}} \qquad (4.3.4.1)$$

If one assumes that h_0/h_i is similar to h_f/h_i (a tenuous assumption except downstream of transition on the SS), the ϕ equation becomes:

$$\phi_p = \phi_0(1 - \chi\eta) + \chi\eta \qquad (4.3.4.2)$$

The warming factor, χ, was not included in Dees *et al.*'s original analysis, but was added as a refinement by Williams *et al.* [21] to account for the different coolant temperatures used in the definitions of η and ϕ. The motivation for pursuing this model is that large databases of η data exist, as well as correlations and other tools designed to predict effectiveness for many configurations. If a model for combining these databases with a single measurement of ϕ_0 could be applied, it would make predicting ϕ – often the ultimate goal of the designer – much easier.

Dees *et al.* showed that this simple model worked well for an attached jet, but failed in the case of a separated jet. However, Williams *et al*. showed the opposite; detached jets showed reasonable agreement but an attached jet had questionable performance. Given the inconsistent performance it was not surprising that the model performed poorly for the fully cooled configuration, as shown in Fig. 4.3.4.1. Generally predicted values were 10-15% greater than the measured values, with the exception of $I^*_{SH} = 0.8$ in $8 < s/d < 21$.

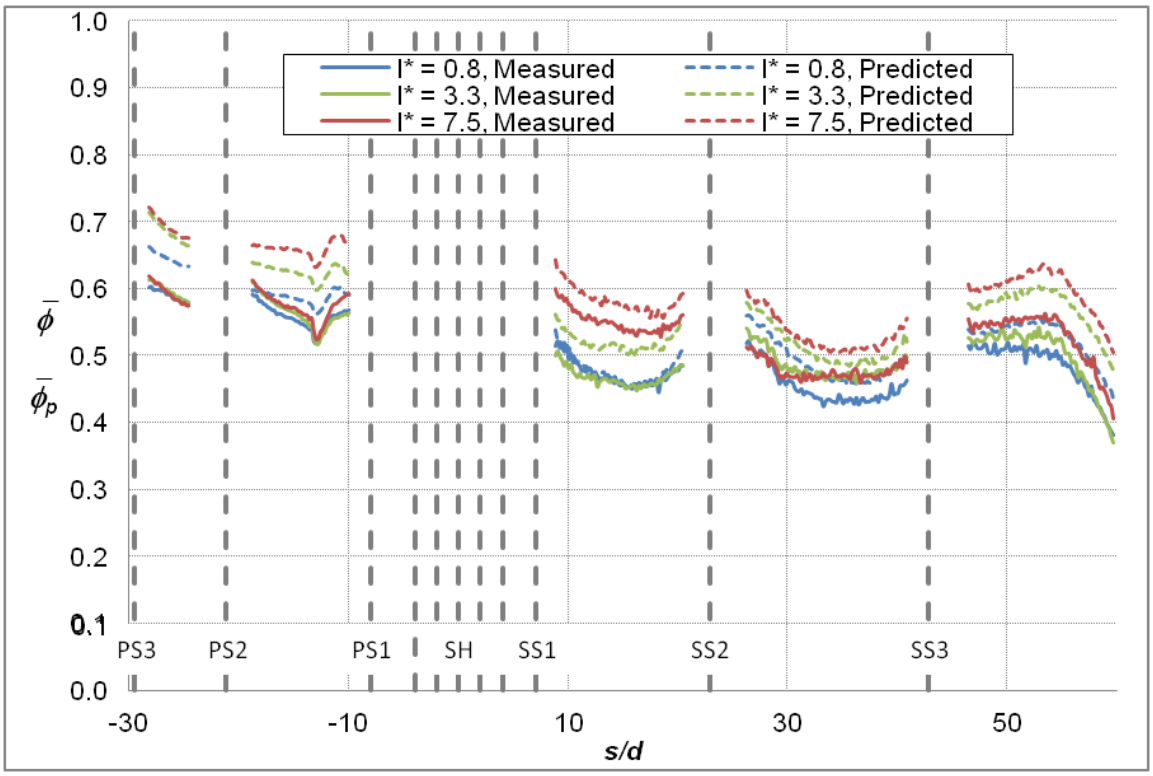

Figure 4.3.4.1: The predictions of Eqn. 4.3.4.2 compared to the measured values of ϕ for the fully cooled configuration

There are many reasons why this model fails. One of these is that the effect of heat transfer augmentation due to film injection was neglected. For laminar regions of on the vane, this is a poor assumption. If this assumption is not taken, Eqn. 4.3.4.2 becomes:

$$\phi_p = \frac{\phi_0(1-\chi\eta)}{\phi_0\left(1-\frac{h_f}{h_0}\right)+\frac{h_f}{h_0}} + \chi\eta \qquad (4.3.4.3)$$

However, no measurements of hf/h0 were available. Instead, measured values of $\bar{\phi}$, $\bar{\phi}_0$, and $\bar{\eta}$ were used to calculate the values of h_f/h_0 necessary to correct the

results to conform to the experimental measurements. Figure 4.3.4.2 shows that to correct the prediction h_f/h_0 would need to be between 1.5 and 2.0. For the -20 < *s/d* -10 region, this was very similar to the measurements of Ames [35] for a C3X with multiple rows injecting onto the PS. However, in regions where augmentation is expected to be small (*i.e.*, where the boundary layer was already turbulent) the augmentation was unrealistic and there was very little augmentation for 10 < *s/d* < 20. An additional source of error for the ϕ prediction was that there was some uncertainty in the correct value to use for χ. No direct measurement was made of the level of cooling between the inlet and exit of the film cooling holes, so an assumption was made that approximately 10% additional warming of the coolant would take place as the coolant passed through the holes. This assumption was based on the work of Terrel *et al.* [92], who measured the temperature rise through the holes in a matched Biot number leading edge model. This additional warming was added to the available measurement of the warming between the exit of the impingement holes and the inlet of the film cooling holes. It should be noted that the prediction was not very sensitive to the exact value of χ because the adiabatic effectiveness was low over much of the surface. There was also the 1D assumption use to formulate Eqn. 1.2.2.10, which was likely to be a poor approximation over large portions of the vane due to the density of film cooling holes.

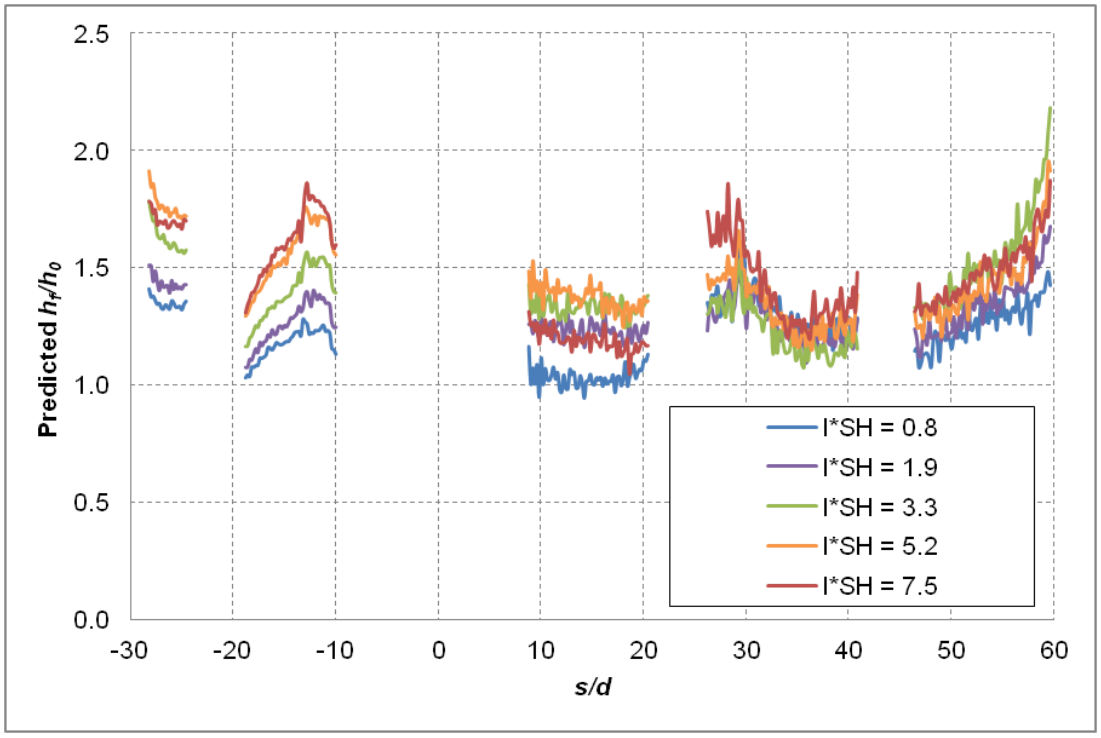

Figure 4.3.4.2: Heat transfer augmentation necessary to correct Fig. 4.3.4.1

However, the 1D analysis did generally show the correct shape of the resulting profiles, so it may be used as a means of gauging the relative contributions of ϕ_0 and $\bar{\eta}$ to $\bar{\phi}$. Figure 4.3.4.2 clearly shows how the internal cooling was generally much more important to the overall effectiveness. The exception was the SS2 < *s/d* < SS3 region, where film cooling and internal cooling contributed approximately equally to the overall effectiveness.

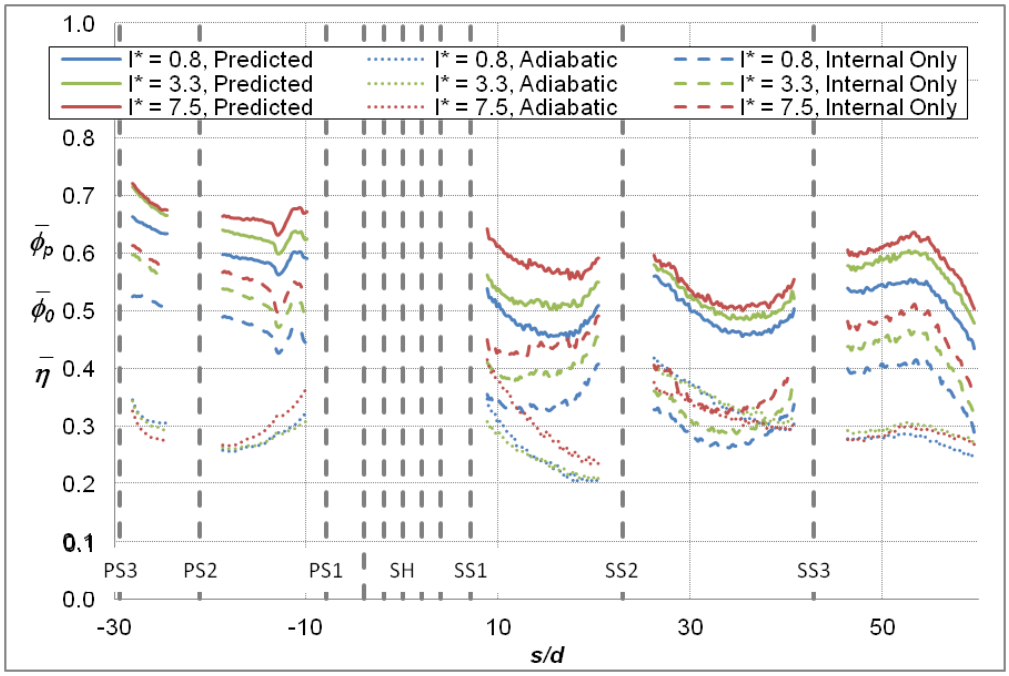

Figure 4.3.4.2: The results of the 1D analysis with the component laterally averaged η and ϕ_0 values

Chapter 5 – Velocity Measurements on the Suction Side of the Vane

The impact of the turbulence generated by upstream blowing on downstream cooling holes has been mentioned several times in prior chapters. The general effect of turbulence on film cooling is to reduce adiabatic effectiveness through increased jet diffusion, provided that the jet was close to the wall. For cases where the jet would normally be interacting with the wall minimally – or even not at all – increased turbulence tends to bring some coolant back to the wall, improving the adiabatic effectiveness. Though these general trends are well known, precise measurements of the approach flow for holes located on the suction side had not been made. The strong acceleration downstream of the stagnation point around the suction side can dramatically affect turbulence. For that reason, measurements were made at locations on the suction side of the C3X vane corresponding to the positions of the SS2 and SS3 rows of holes (s/c = 0.28 and 0.49). Multiple blowing conditions were evaluated for each case, as well as the effect of high (Tu = 20%) and low (Tu = 0.5%) mainstream turbulence. Comparisons were made to data collected without any blowing.

5.1. Boundary layers without blowing

These data served as the baseline condition for the various blowing conditions measured. Both high and low turbulence conditions were measured, as shown in Fig. 5.1.1. A profile for a laminar boundary layer exposed to a

pressure gradient was computed using a Pohlhausen method [38] and another was computed using the 1/7th power law. Though the Pohlhausen method is not appropriate for comparison to the *Tu* = 20% data, the low and high *Tu* data had roughly the same profile shape, which fell between the laminar and turbulent profiles. This indicates that the boundary layer was transitional. This was confirmed for the high *Tu* case by observing that the turbulence increased near the wall, but displayed a peak value near y/δ = 0.1 as shown in Fig. 5.1.2. A fully turbulent profile from Dees *et al.* [64] shows that a turbulent boundary layer has no u_{rms}/U peak. The distinction for the *Tu* = 0.5% case was less clear. The turbulence levels did increase slightly toward the wall, but the same was also true for a laminar profile from Dees *et al.* However, the Dees *et al.* data matched a Pohlhausen profile nearly exactly. This suggests that the low turbulence case was also transitional, but at a much earlier stage.

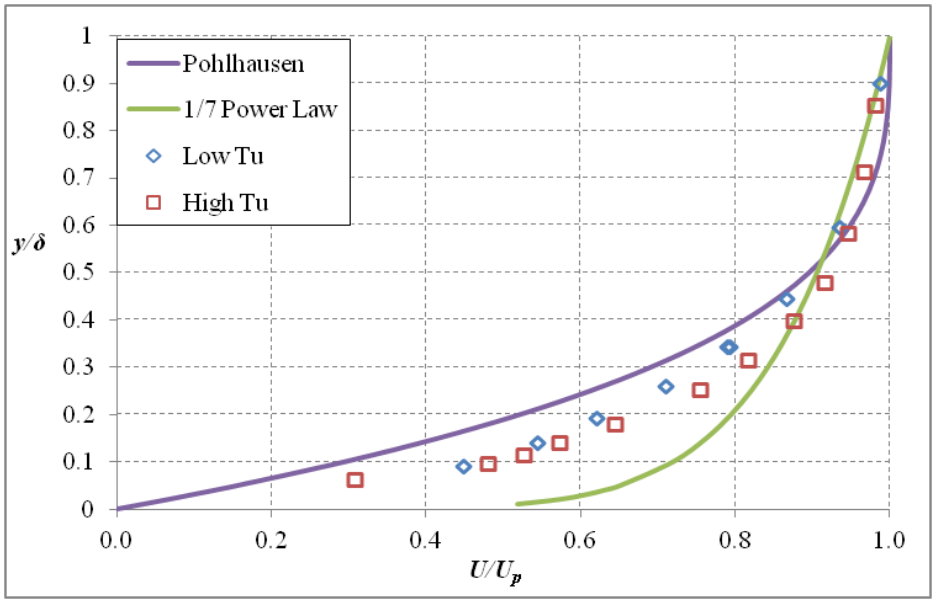

Figure 5.1.1: Boundary layer profile at the SS2 position compared to canonical profiles

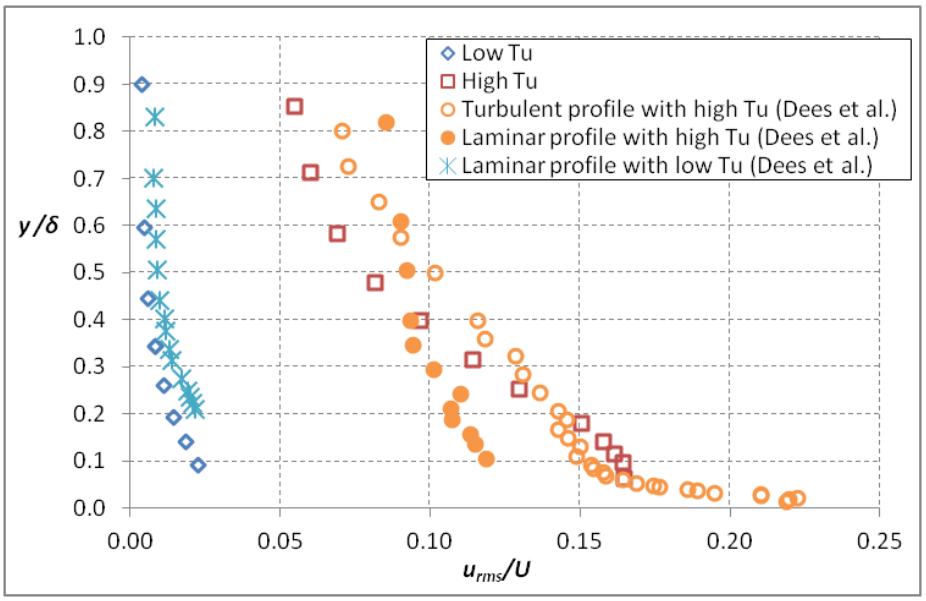

Figure 5.1.2: Turbulence data for the SS2 position without blowing compared to the data for laminar and turbulent profiles form Dees *et al*. [64]

Dees *et al.* [64] also made mean velocity measurements similar to those in the current study at several locations on a C3X vane. Figure 5.1.3 shows the velocity profiles for upstream (*s/c* = 0.19) and downstream (*s/c* = 0.38) locations. These profiles bracketed the new data, indicating that the boundary layer was progressively thickening toward transition (which occurred prior to *s/c* = 0.38), as expected. Also note that this figure uses *c* to normalize the wall normal coordinate. This was chosen because the differences between boundary layers were sometimes masked by using δ and a film cooling hole was not always present. The boundary layer thicknesses for the low and high *Tu* cases were 0.75 and 1.1 mm, respectively.

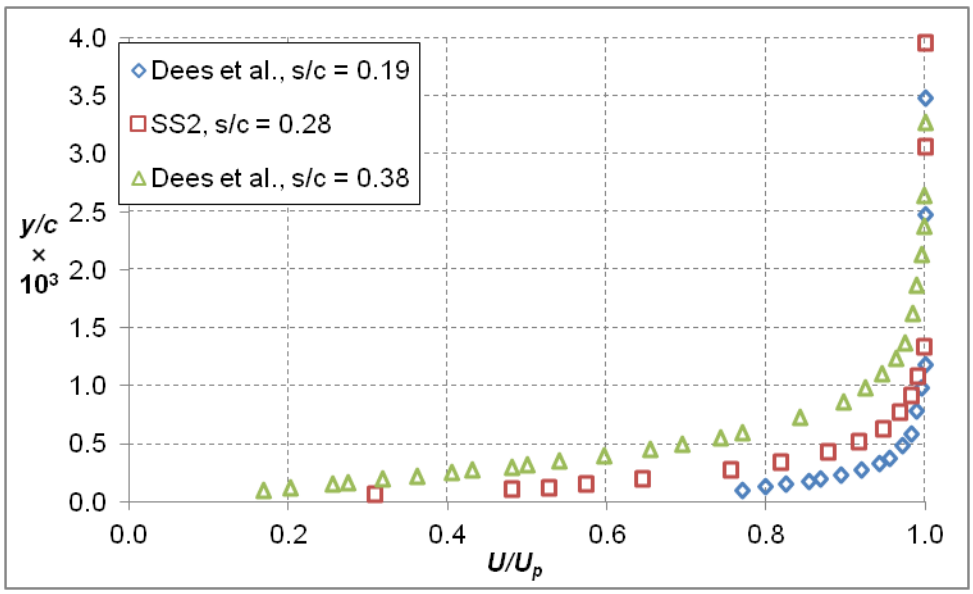

Figure 5.1.3: Comparison to data collected by Dees et al. [64] upstream and downstream of the SS2 position

The SS3 position was expected to be downstream of transition, which was confirmed by a comparison to the 1/7th power law, shown in Fig. 5.1.4. Both high and low mainstream turbulence profiles exhibited turbulent profiles. A comparison of the SS3 and SS2 u_{rms} profiles is depicted in Fig. 5.1.5. This figure shows that the effect of mainstream turbulence was to uniformly increase the turbulence level in the turbulent boundary layer at SS3, but the transitional profile at SS2 was advanced more toward a turbulent boundary layer (*i.e.*, $u_{rms,high} > u_{rms,low} + u_{rms,mainstream}$). This phenomenon is more clearly seen in Fig. 5.1.6, which shows the same data nondimensionalized using the predicted inviscid velocity. At this position, the boundary layer thicknesses for Tu = 0.5 and 20% were 3.5 and 6.0 mm, respectively.

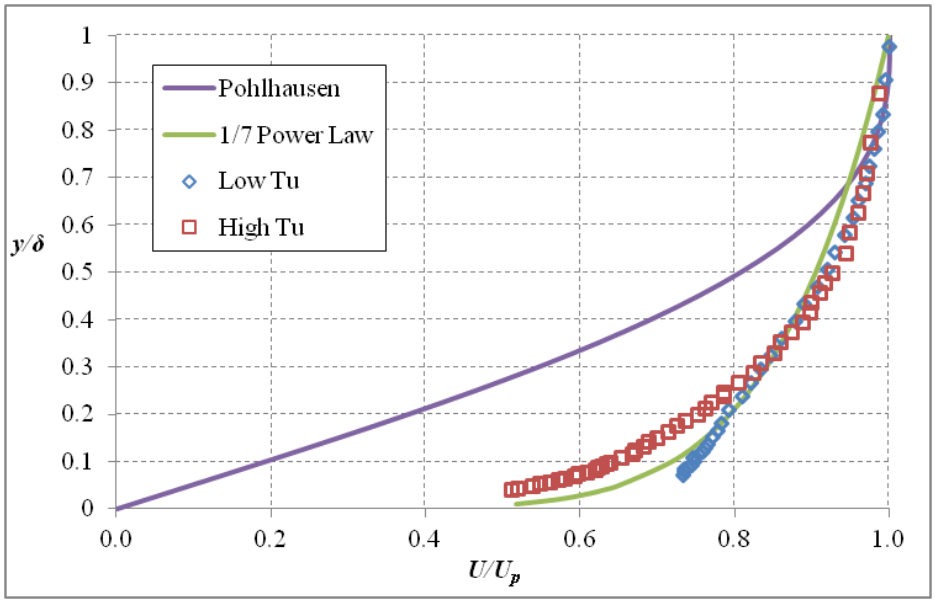

Figure 5.1.4: Boundary layer profile at the SS3 position compared to canonical profiles

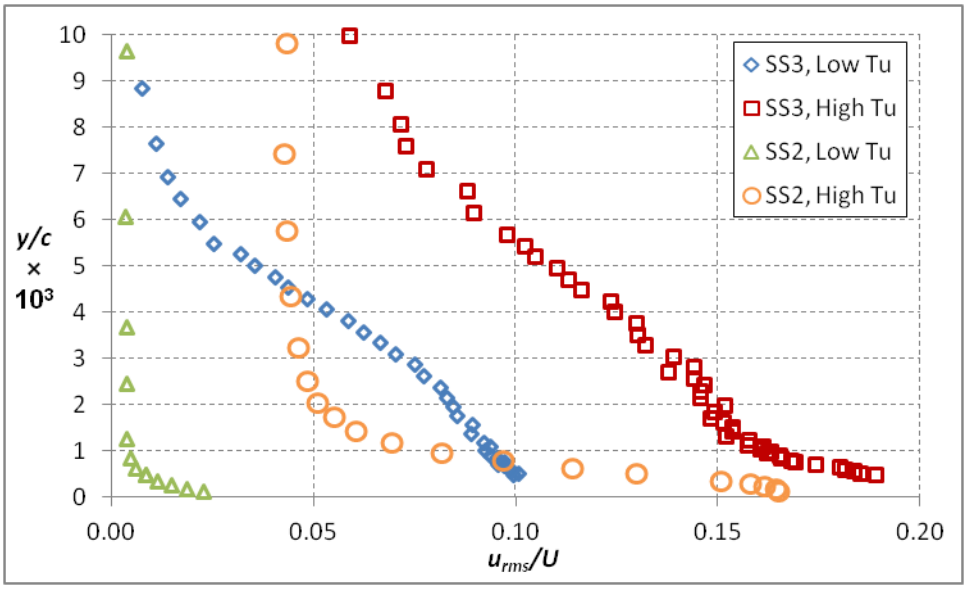

Figure 5.1.5: Turbulence data for both SS2 and SS3 positions without blowing

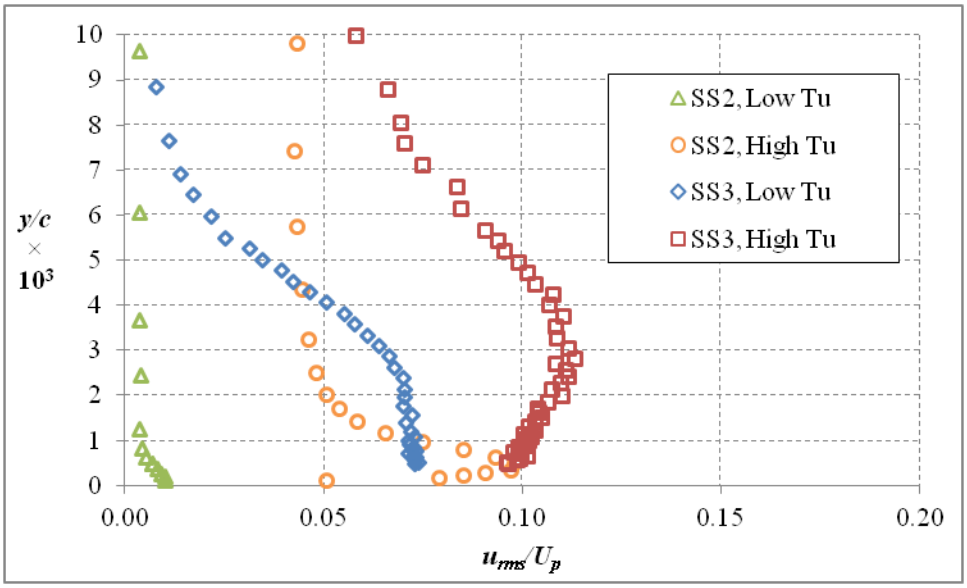

Figure 5.1.6: Turbulence data for both SS2 and SS3 positions without blowing using U_p

Integral length scales were also measured for the no flow condition. As expected for a low turbulence condition, the length scales very large at the SS2 position, as shown in Fig. 5.1.7. These length scales were considerably larger than the 47 *d* of the low *Tu* approach flow due to the acceleration around the vane; however, they are not expected to impact the film cooling flow because of their low energy. The *Tu* = 20% case (shown with better detail in Fig. 5.1.8) had length scales slightly higher than the approach flow's Λ/d = 5.8 with a Λ/d ~ 6.5 peak just above the wall. Eddies with a length scale larger than the film cooling jet have been shown by Cutbirth and Bogard [37] to rapidly displace the cooling jet laterally, which produces an apparent diffusion in time-averaged results.

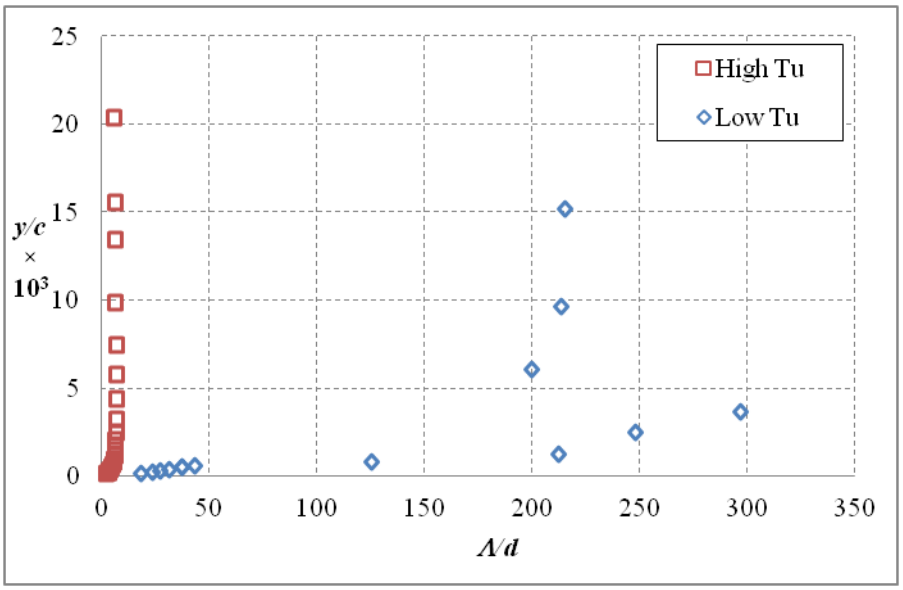

Figure 5.1.7: Integral length scale measurements at SS2 without blowing

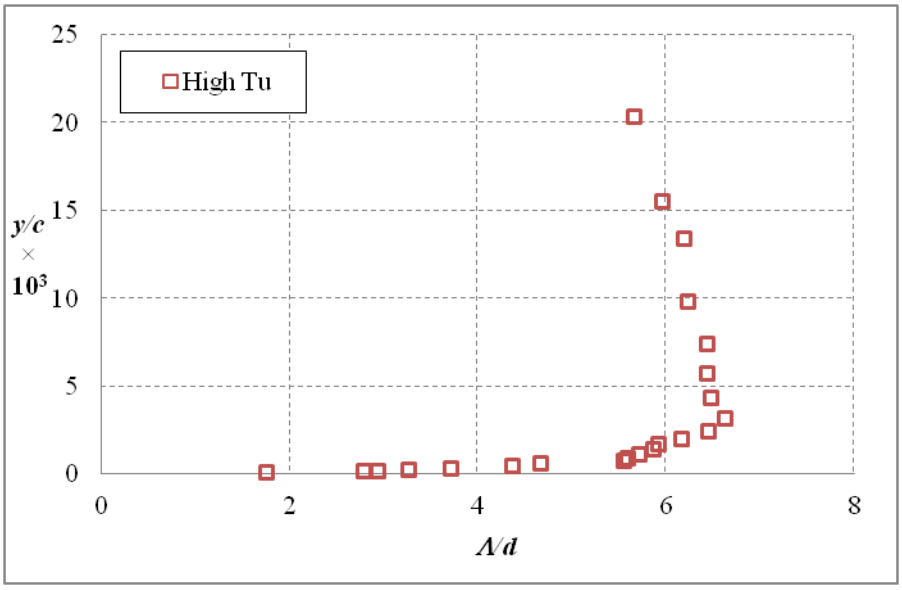

Figure 5.1.8: Integral length scale measurements for *Tu* = 20% at SS2 without blowing

At the SS3 position, Λ was decreased compared to the SS2 position, as shown in Fig. 5.1.9. This was expected because of the deceleration in the mainstream between SS2 and SS3. The low turbulence case saw very small scale turbulence within the turbulent boundary layer, and retained extremely large length scales (not shown) farther away.

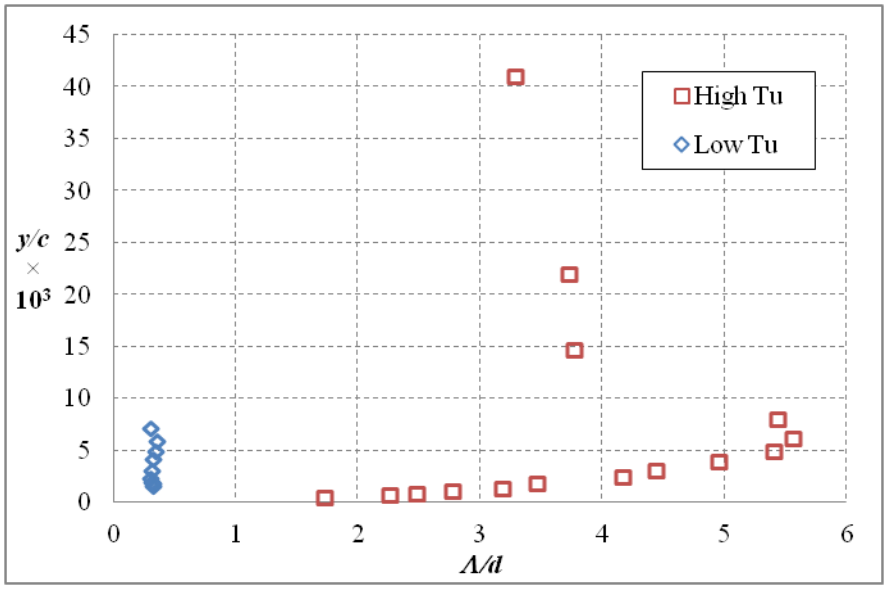

Figure 5.1.9: Integral length scale measurements at SS3 without blowing

5.2. Effect of showerhead injection at the SS2 position

Data were collected at two span-wise positions for multiple showerhead flow rates at *Tu* = 0.5% and 20%. The mean and RMS velocity profiles for the upper positions, where flow rates were measured, are shown in Figs. 5.2.1 and 5.2.2. Film injection clearly caused an increase in the boundary layer thickness, but was not a direct function of momentum flux ratio. However, increasing *I** did progressively increase the turbulence levels for *y/c* > 0.0005. The increased turbulence from blowing extended more than two hole diameters off the wall (Fig. 5.2.3), so it would have a substantial impact on film cooling jets injected at this location.

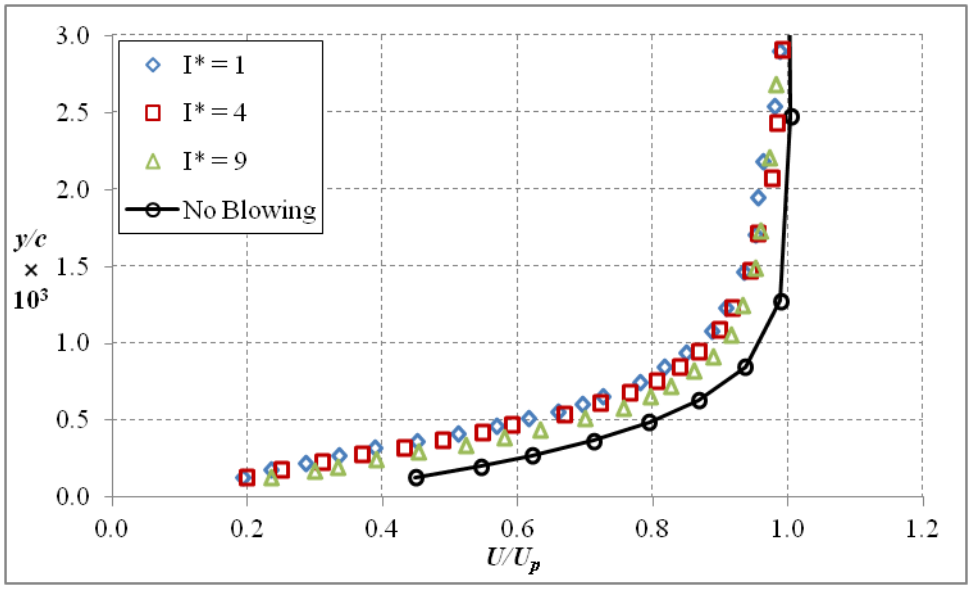

Figure 5.2.1: Mean velocity profiles at SS2 with showerhead blowing at *z/H* = 0.58 and *Tu* = 0.5%

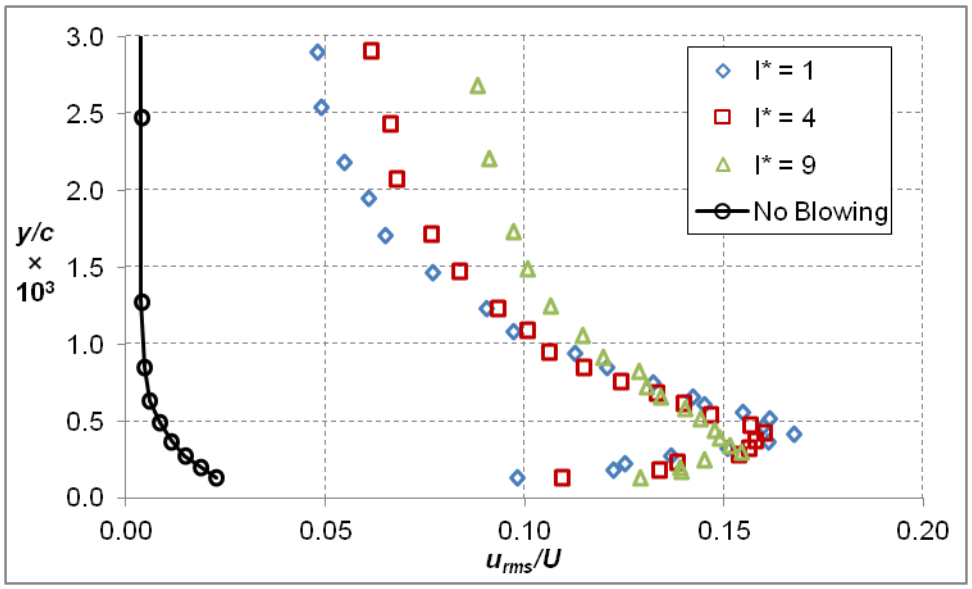

Figure 5.2.2: RMS velocity profiles for the SS2 position with blowing at *z/H* = 0.58 and *Tu* = 0.5%

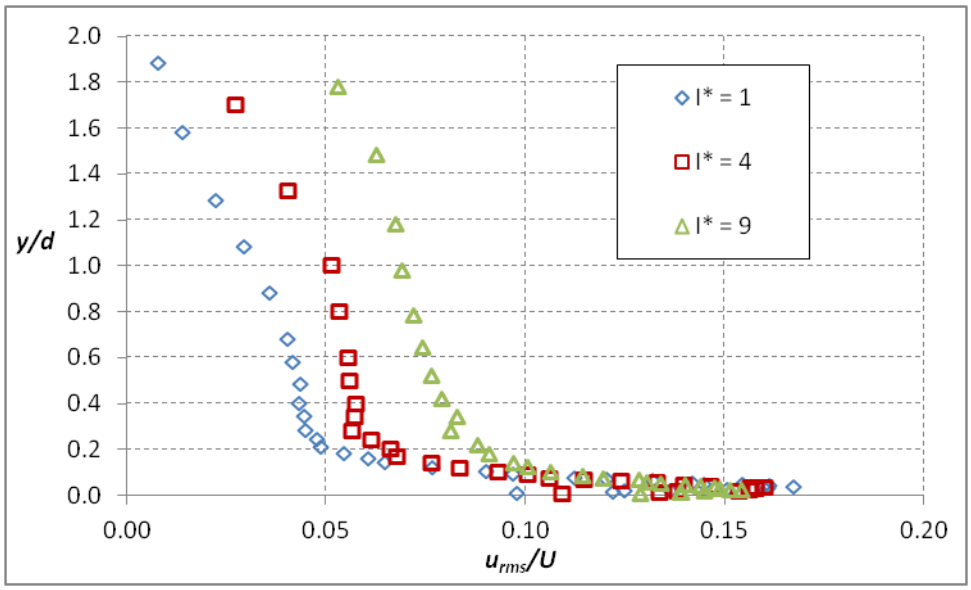

Figure 5.2.3: RMS velocity profiles for the SS2 position with blowing using a *y/d* scale extending further off the wall at *z/H* = 0.58 and *Tu* = 0.5%

There was an expectation that the boundary layer thickness would be a function of coolant flow rate. However, δ_{99} for I^* = 1, 4, and 9 was 1.8, 1.5, and 1.8 mm, respectively. This can be explained by looking back to the contour plots presented in Fig. 4.1.3, which shows the adiabatic performance here. The coolant flow from the showerhead merges into a large stream the position of which was determined by the momentum flux ratio. The measurements taken for a single position on the vane will then move in and out of this coolant stream, which will affect the velocity profiles. At a lower position on the vane, *z/H* = 0.49, δ_{99} values for I^* = 4 and 9 were 1.5 and 1.1 mm, respectively, showing that the span-wise position relative to the coolant stream was important. Figure 5.2.4 shows the associated velocity profiles. The span-wise dependence was also

visible for the RMS profiles, which are shown in Fig. 5.2.5. The high turbulence levels (~ 6%) as far as *y/c* = 0.02 (*y/d* = 1.7) off the wall indicate that for *z/H* = 0.49 the measurements were within the coolant stream for *I** = 4, but not at *I** = 9, and the opposite was true for *z/H* = 0.58.

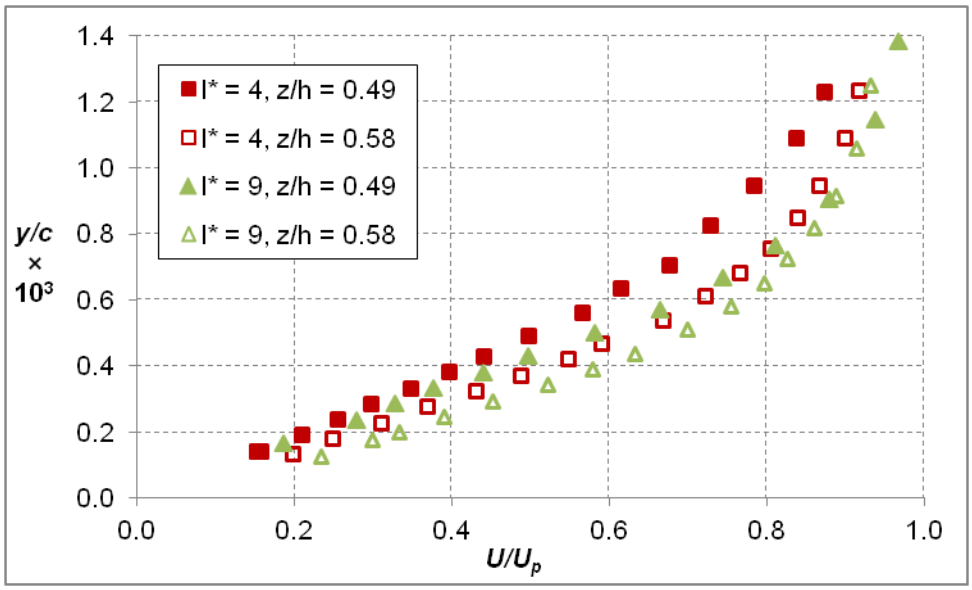

Figure 5.2.4: Mean velocity dependence on *z/H* for *Tu* = 0.5%

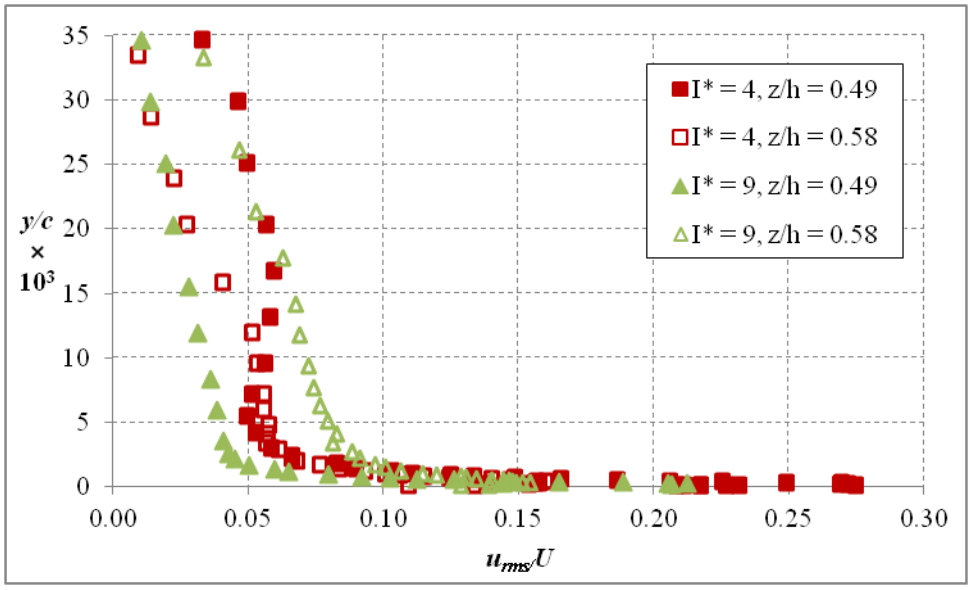

Figure 5.2.5: SS2 RMS velocity profile dependence on *z/H* for *Tu* = 0.5%

Increasing the mainstream turbulence to 20% did not have a strong effect on the mean velocity profiles, as shown in Fig. 5.2.6. The boundary layer thicknesses were nearly identical, with δ_{99} = 1.6 and 2.0 mm for *I** = 4 and 9 respectively. However, the u_{rms} profiles were strongly affected even close to the wall, as shown by Fig. 5.2.7. The effect of mainstream turbulence was approximately the same for both span-wise positions.

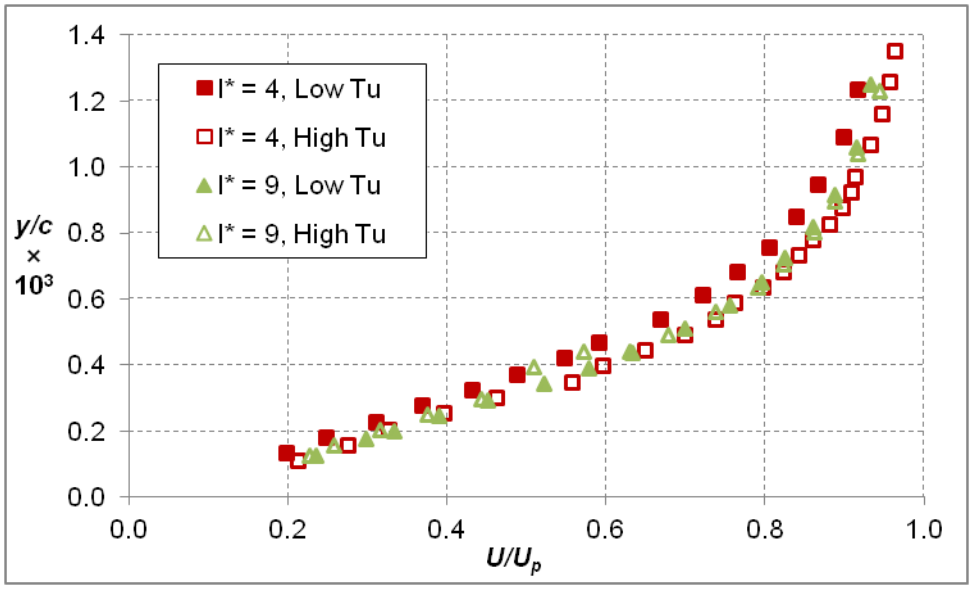

Figure 5.2.6: SS2 mean velocity profiles for *Tu* = 0.5 and 20% at *z/H* = 0.58

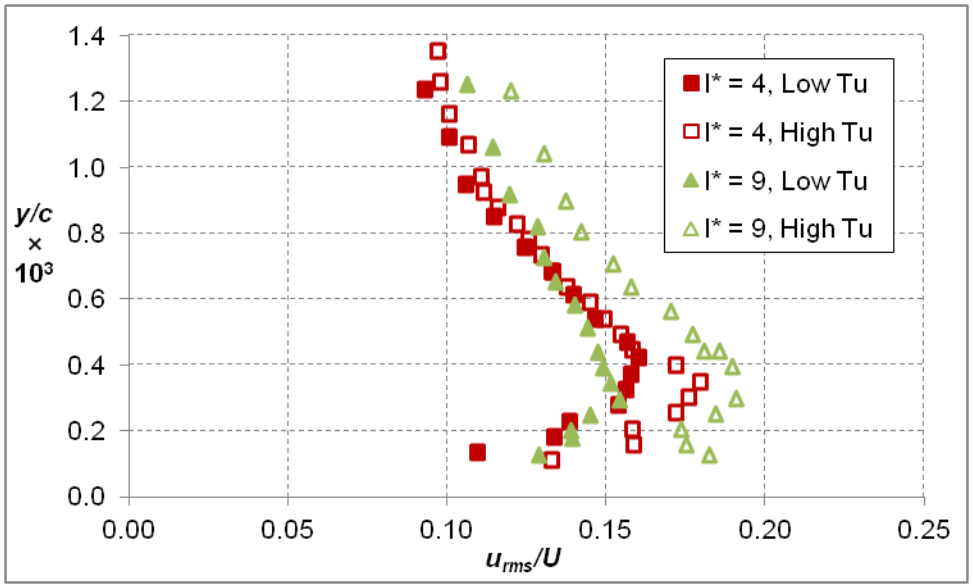

Figure 5.2.7: SS2 RMS velocity profile dependence on *Tu* at *z/H* = 0.58

Film injection acted to reduce the integral length scale. Figure 5.2.8 shows that for $y/c > 0.005$ ($y/d > 0.4$) Λ was halved for the Tu = 20% case. Film cooling

holes do not generally produce turbulence with a length scale greater than *y/d* = 1, so it follows that the small scale turbulence generated by the film injection combines with the larger scale turbulence in the mainstream to produce smaller eddies on average. This hypothesis was also supported by the low turbulence case, because the low energy residual eddies from the mainstream were completely wiped out by the film cooling turbulence. In both cases, these eddies were considerably larger than the film cooling hole diameter near the wall, so they would be expected to strongly affect the film cooling holes.

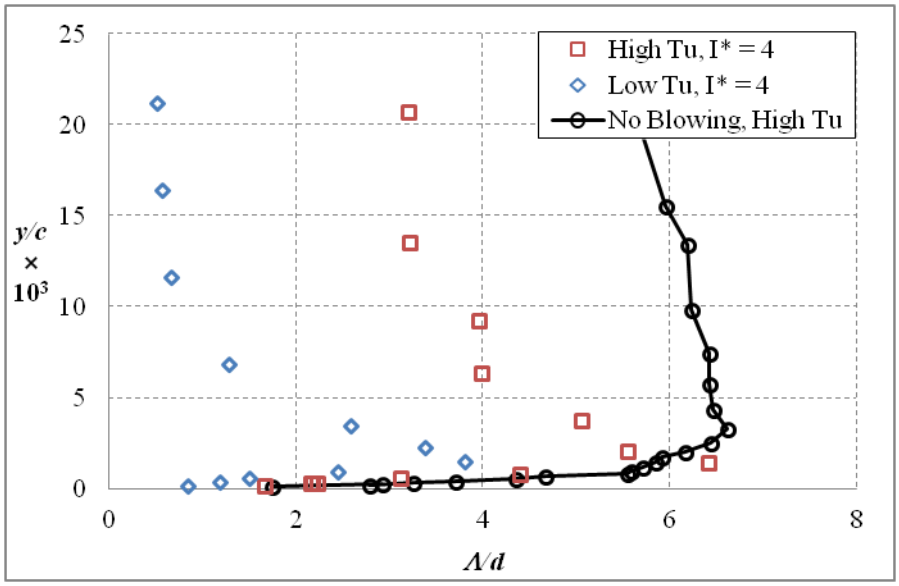

Figure 5.2.8: Measurements of *Λ* at SS2 for *I = 4 at *z/H* = 0.49**

Increasing the coolant flow rate further reduced the integral length scale, as shown by Fig. 5.2.9 for the mid-span position. This indicates that as the coolant flow rate increased, the turbulence generated by the film injection

became the dominant effect. This could also be a factor in the increase of u_{rms} values with increasing *I**.

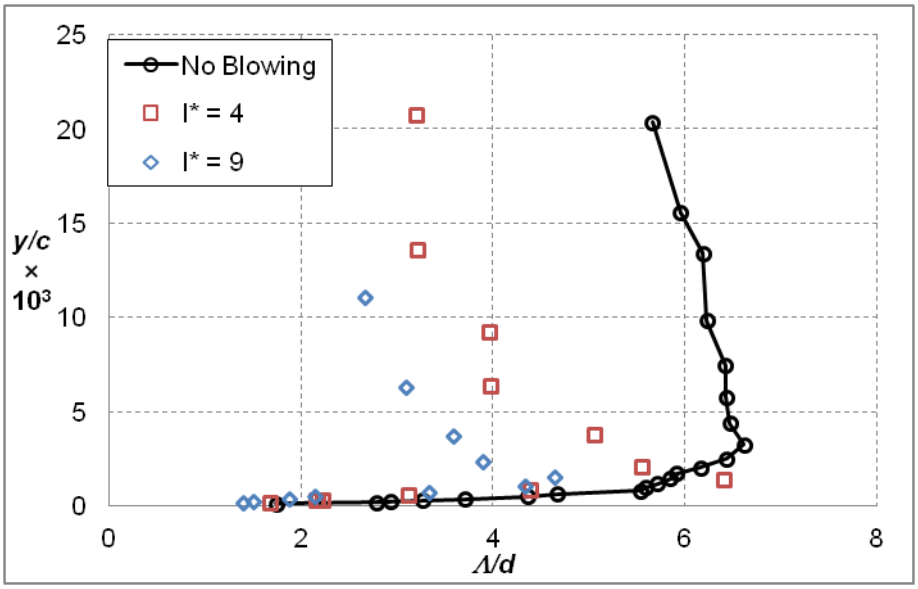

Figure 5.2.9: SS2 integral length scale dependence on *I at *z/H* = 0.49**

5.3. Effect of film injection at the SS3 position

Three blowing conditions were tested at this position: the showerhead alone, the SS2 row alone, and both showerhead and SS2 together. The investigation used only the high *Tu* condition. When the SS2 row was active, it had a coolant flow rate equivalent to what it would have had when the showerhead was active with *I** = 4 and 9.

Unlike the SS2 position, the coolant from the showerhead had little impact on the mean and RMS velocity profiles at the SS3 position. Figure 5.3.1 shows that the mean velocity profile with the showerhead active was nearly identical to

the profile without blowing, and in fact δ_{99} was 5.4 mm, which was 0.6 mm thinner (double the combined uncertainty bands for these measurements) than the without blowing condition. It was also observed that the mean velocity was very similar for the SS2 alone and SH + SS2 case. The case with all upstream holes blowing did have a thicker boundary layer (12 mm vs. 9.4 mm for the SS2 alone). Increasing *I** to 9 still did not remarkably affect the mean profile, as shown in Fig. 5.3.2, though the boundary layer thickness was increased to 8.4 mm. Because the effect of *I** on the boundary layer thickness at the upstream position was more a function of the position of the periodic coolant stream from the showerhead, this change indicates that even at *s/c* = 0.49 this stream remained coherent enough to impact the local flow field (increased boundary layer thickness has a negative impact no local coolant flow).

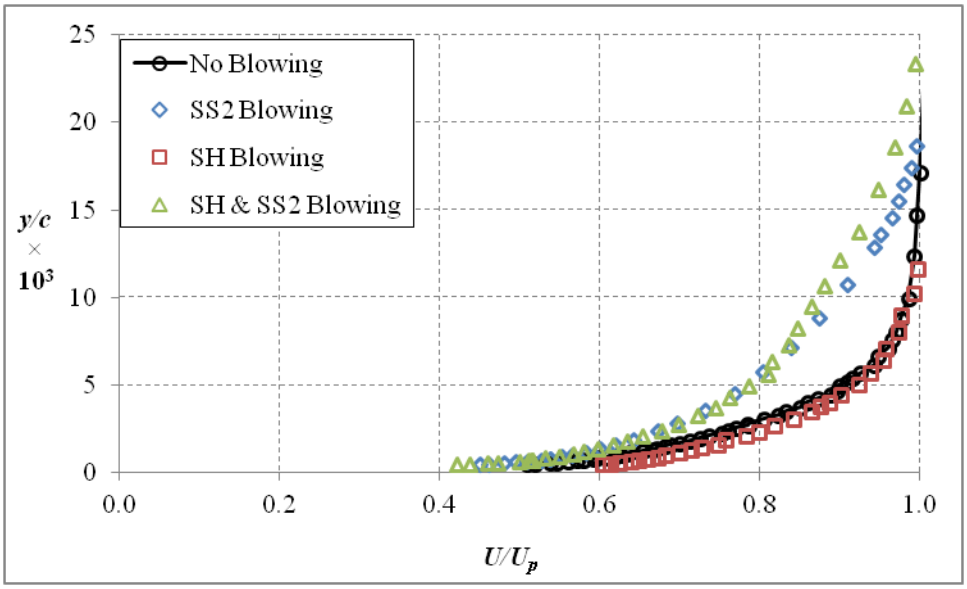

Figure 5.3.1: Mean velocity profiles at SS3 for different blowing conditions and *I = 4**

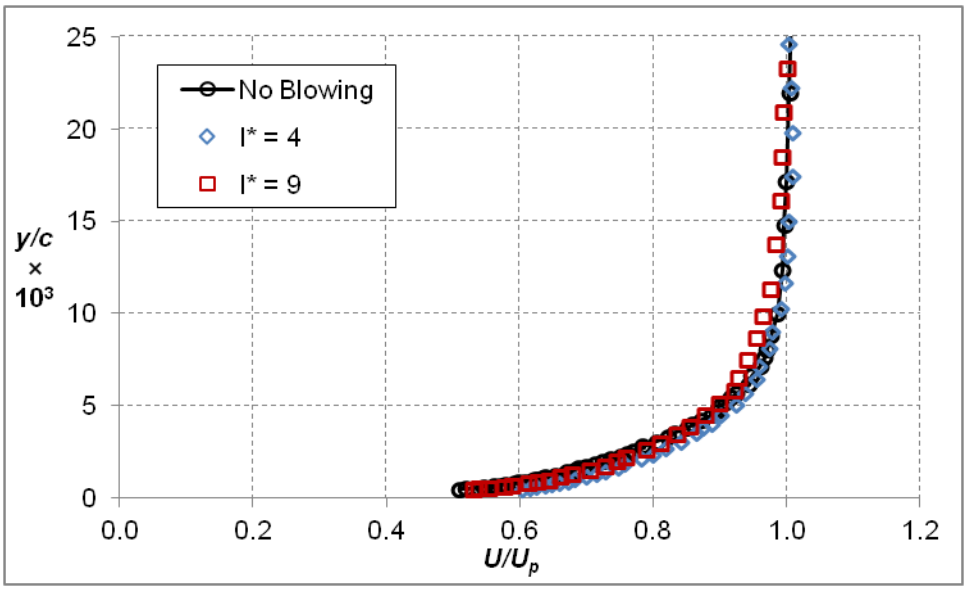

Figure 5.3.2: Effect of coolant flow rate variation on *U* for the SH alone case at SS3

Active film injection from the showerhead did have some impact on the u_{rms} profile. Figure 5.3.3 shows that near the wall (y/c < 0.005) there was no change in the turbulence levels compared to the case without blowing, but farther from the wall the turbulence levels were increased approximately 2%. This level of change would only minimally affect coolant jets injected at this location. In contrast, the SS2 film injection dramatically increased turbulence levels all the way to the wall, where they were elevated to over 22%. The increased turbulence remained above 10% even as far as 2 *d* from the wall, so the enhanced mixing would noticeably affect the coolant jets. The SH + SS2 condition behaved similarly, but the enhanced turbulence extended even farther from the wall. Increasing the momentum flux ratio for the showerhead alone did increase the turbulence away from the wall significantly, as shown in Fig. 5.3.4. This was

another indication that the location of the coolant stream from the showerhead was important. The same comparison for the SH + SS2 case is depicted in Fig. 5.3.5, which shows that the coolant flow rate had less impact when the SS2 row was active. This indicates that the residual turbulence from the showerhead was overwhelmed by the injection of coolant at SS2.

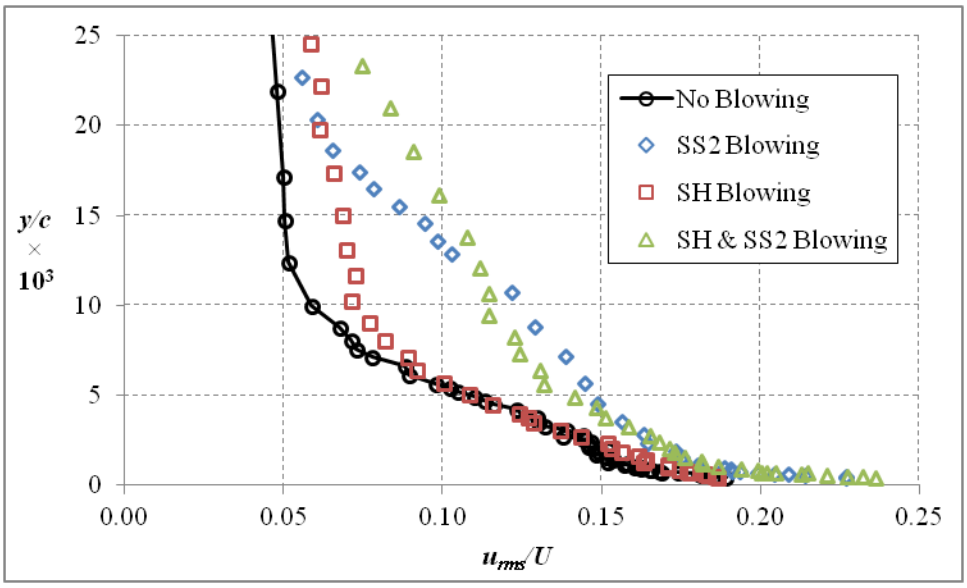

Figure 5.3.3: RMS velocity profiles at SS3 for different blowing conditions and *I = 4**

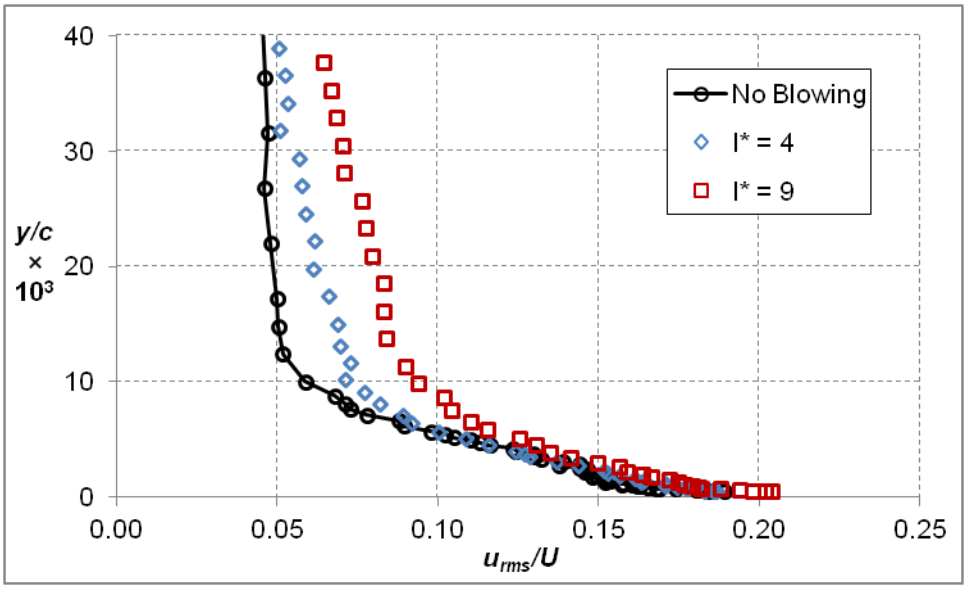

Figure 5.3.4: Effect of SH coolant flow rate variation on u_{rms} at SS3

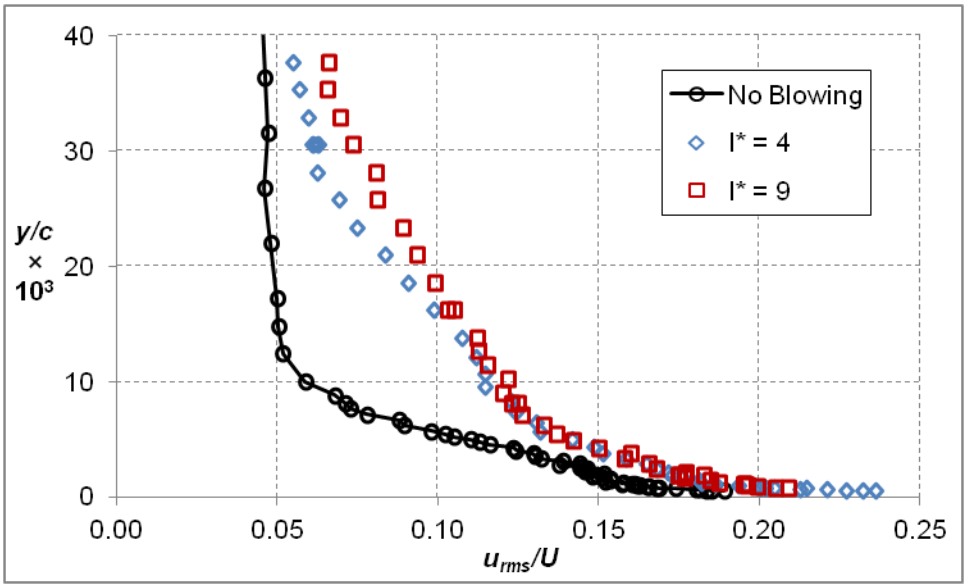

Figure 5.3.5: Effect of SH +SS2 coolant flow rate variation on u_{rms} at SS3

Like the SS2 position, coolant injection tended to decrease the integral length scale, as shown in Fig. 5.3.6. This effect extended more than 3 *d* off the

wall. Unlike the U and u_{rms} profiles, the source of the coolant did not have a clear impact on the length scale, though the change in length scale did approach the wall more closely when the SS2 row was active.

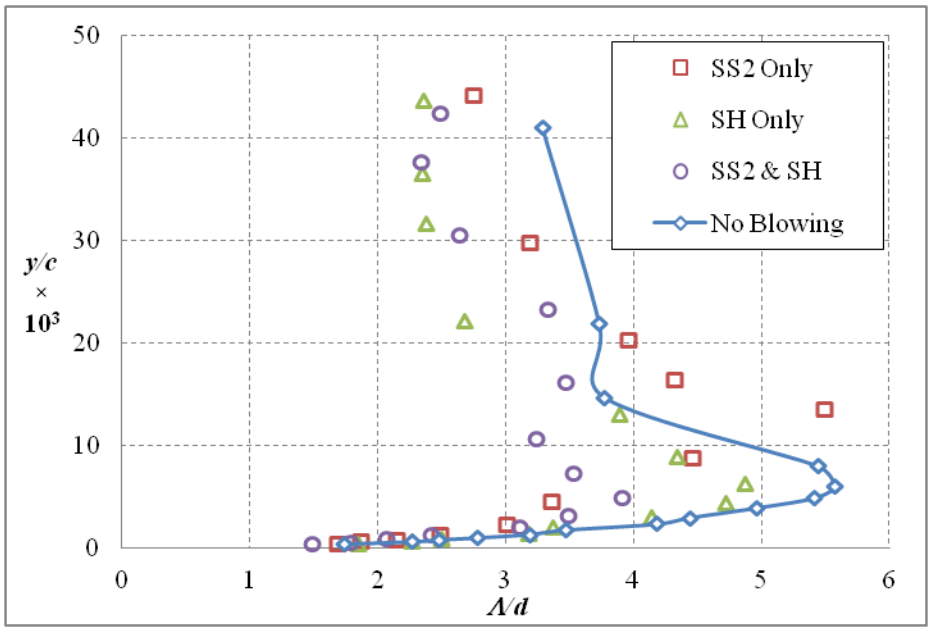

Figure 5.3.6: Effect of coolant injection on Λ at SS3 for I^* = 9

COMPUTATIONAL SIMULATIONS

The following chapters describe the simulations that were performed as part of this work. Two film cooling configurations are examined in detail, and the results are presented and compared to experimental data from other studies. Additionally, a comparison of several RANS turbulence models on a thermal boundary layer basis is made.

Chapter 6 – Computational Methods

In the course of this study three different simulated geometries were used. The first was a representation of the experimental vane without any additional features. This configuration was used to refine the prism layer and to evaluate turbulence models through comparison with the data of Dees *et al*. [64]. The second was a simulation of the geometry used in the film cooling study of Williams *et al.* [21], who used a single row of holes on the suction side. This configuration is referred to as “SS3 Only”. Lastly, a simulation was constructed using the geometry of Nathan *et al.* [33], who used a showerhead identical to that used in the full coverage configuration described in Ch. 3, but no additional film cooling. This configuration is referred to as the “Showerhead” or “SH”. Though each case was treated similarly, there were different challenges associated with each geometry.

With the exception of the turbulence model comparison, all the simulations made use of the *k-ω* SST turbulence model with low Reynolds number corrections. This model was selected because it had been shown to have the

best performance for prediction of separation [41], which was expected to play an important part in correctly predicting film cooling. All simulations were carried out using ANSYS® FLUENT™ 13 or 14. The pressure based solver was employed with 2nd order discretization for every parameter except pressure. Pressure was solved using the "standard" discretization, which is described in [93]. The SIMPLE algorithm was used for pressure-velocity coupling, and the ideal gas law was used to compute density.

For all simulations, a constant C_p was used, because it changes much less than 1% over the range 230 K < T < 330 K. Thermal conductivity for air would change approximately 20% over the same range. However, no single simulation covered the whole range, so the most variation from the constant that was used would be approximately 10%. For the film cooling simulations, Sutherland's model was used to compute viscosity, because it would change more than 10% over the range of temperatures encountered. The thermal field evaluation used a constant viscosity. This was done in part to better match the experimental data; hot wire measurements were made in an isothermal flow while temperature data were collected in a separate experiment. The simulations extracted both velocity and temperature from the same simulation, so changes to the velocity field due to property variation would alter the results. It should also be noted that the maximum temperature change through the boundary layer was approximately 25 K, so viscosity would change less than 10%, and most of the surface had less temperature variation. Density was still allowed to vary with the ideal gas law, but a simulation using a "cold wall", shown in Fig. 6.1, revealed

that this had very little impact on the results. Note that the thermal boundary layer is represented in terms of θ, a non-dimensional temperature defined so that it is zero at the wall and one in the freestream:

$$\theta = \frac{T_w - T}{T_w - T_\infty} \tag{6.1}$$

This normalization for the temperature was used for all temperature profiles in chapter 9.

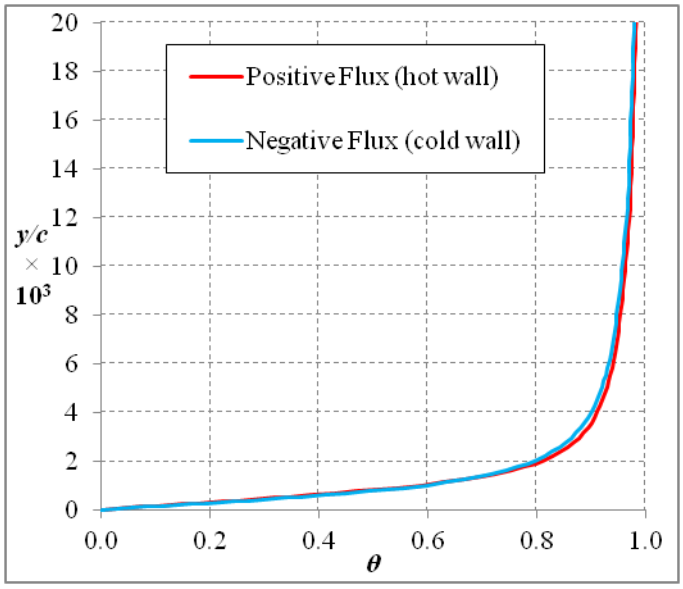

Figure 6.1: Comparison of thermal profiles from simulations using positive and negative wall fluxes

Another important assumption used for the data reduction in chapter 9 was that the theta profile at each position would not be strongly affected by changing the boundary condition between a constant wall heat flux and the more realistic condition (varying surface temperature) used in the experiments. To

confirm that this was the case, a separate simulation using a constant wall temperature boundary condition was carried out. For positions near the leading edge, there was no measurable difference. Farther downstream, there was a minimal change between the two boundary conditions, as shown by Fig. 6.2 for the PS3 position. Though the experimental condition was neither constant wall temperature nor constant heat flux, a simulation using the correct boundary condition would likely fall in between these two cases.

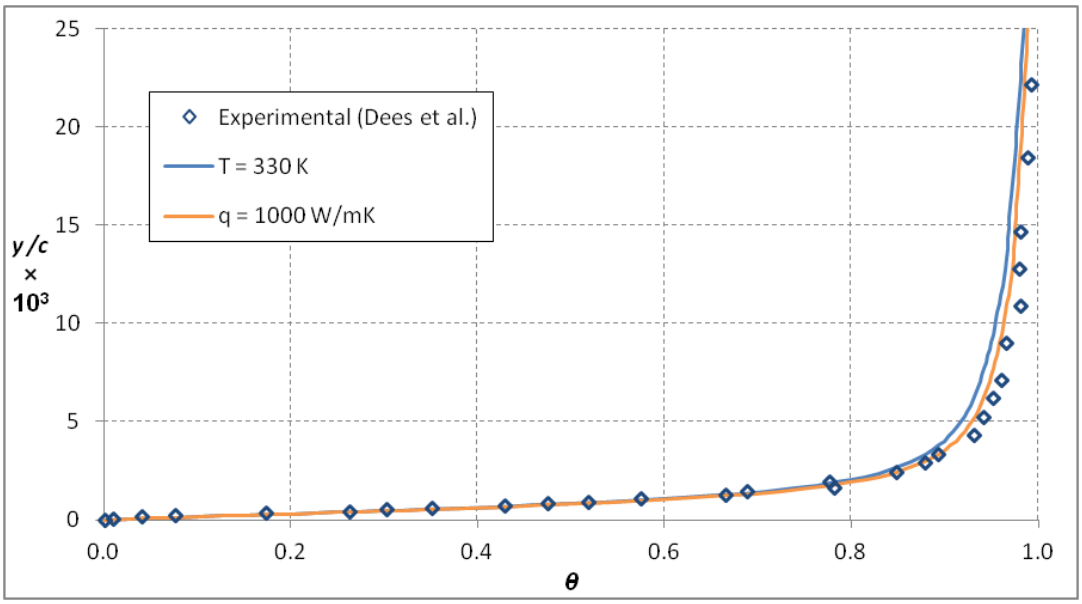

Figure 6.2: Comparison of the thermal profiles from Transition SST simulations using q'' = 1000 W/m·K and T_w = 330 K at PS3

The simulations of the matched Biot number models had k = 1.0 W/m·K for the solid body to match the experiment. The other properties for Corian® were C_p = 1382 J/kg·K [75] and ρ = 1700 kg/m^3 [94]. The conductivity for the "foam" used for the showerhead simulation was set to be k = 0.048 W/m·K, because that

was the value reported in many past results (*e.g.*, [30]). However, the manufacturer's spec for the material used in the current study had k = 0.044 W/m·K [74]. This is only an 8% difference, so the simulated value was likely within the (unreported) experimental uncertainty.

6.1. Mesh Specifications

A different basic mesh was used for each portion of this study. However, each mesh was constructed using the same techniques. All the meshes were built using ANSYS® ICEM™ 13. An unstructured tetrahedral mesh was selected. This type of mesh has been shown to offer reduced cell count (and therefore, computational cost) compared to block-structured meshes without any compromise in solution quality as long as a prism layer is selected with enough elements to resolve the boundary layer [95]. Considerable thought was put into the proper specification of the prism layer. To reduce the size of the mesh, a section of the vane 12 *d* tall (two impingement or showerhead hole pitches and three gill or SS3 row pitches) was modeled with periodic boundaries in the span-wise and cascade-wise directions. The result was a simulation of an infinite cascade with infinitely tall vanes. In all cases, the mainstream flow included regions 0.5 *c* axially up- and downstream of the vane.

6.1.1. Specification of an Appropriate Prism Layer

The best practice for creating a well resolved prism layer is to construct a mesh such that 15 or more nodes cover the boundary layer region [96]. This presents a challenge for a simulated vane with dramatically different boundary

layer thickness at different surface locations. The selection of a single prism layer specification that could produce good predictions for the whole vane was desired for practical mesh construction. In all cases, the first grid point was positioned so that $y^+ \leq 1$ for all but a small region near the tail of the vane. Prism layer thicknesses of 1, 2, and 6.6 mm were used. It was noted that thin prism layers that met the guidelines at locations where the boundary layer was thin produced severe discontinuities in the velocity profile at downstream locations, as shown in Fig. 6.1.1.1, which compares the predictions to the experimental data of Dees *et al*. [64]. The edge of the prism layer for the 1 mm (y/d = 0.16) and 2 mm (y/d = 0.31) cases are clearly visible as sharp changes in the profile. Unfortunately, creation of a prism layer that could encompass the entire boundary layer for the entire vane proved impractical. The 6.6 mm thickness (the experimentally measured thickness at SS3) was approximately the thickest specification that could produce a mesh without unacceptable quality problems at the tetra-prism interface. Better than 95% of the velocity change was still captured even for the thicker boundary layer at SS4, so this 6.6 mm prism layer was used. The prism layer was composed of 33 layers employing a growth rate of 1.1 with an initial height of 0.03 mm. It was verified during initial simulations that with the exception of a portion near the tail on the suction side (outside the region measured experimentally) this height produced first node heights of $y^+ < 1$. This specification was used for all the film cooling cases as well.

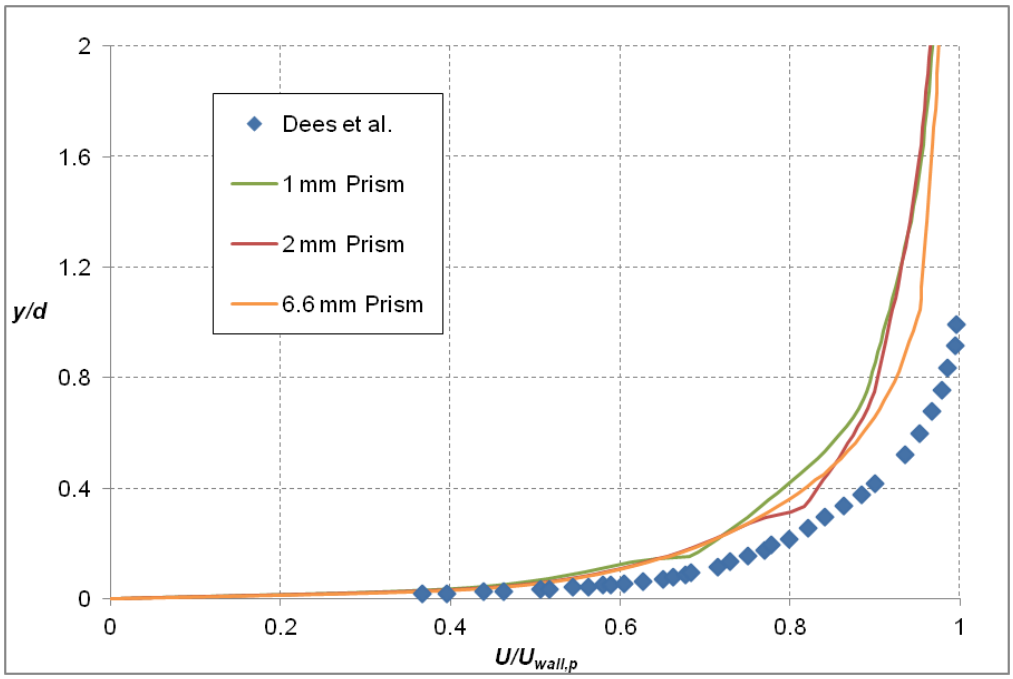

Figure 6.1.1.1: Predictions of the boundary layer using *k-ω* SST and several prism layers compared to experimental data at the SS3 position

6.1.2. Vane Without Film Cooling

Even though the geometry for this configuration was 2D in nature, a 3D mesh was produced for several reasons. The first was a practical reason: it was easier to develop the meshing parameters that would produce a good mesh without the complicating factor of film cooling holes. It was also found that for low turbulence conditions, the use of a 3D mesh allowed the prediction of Taylor-Görtler instabilities on the pressure side of the vane. This well-known instability forms vortices on concave surfaces that are stable as long as the boundary layer remains laminar, so RANS codes should be able to predict their formation. Toé *et al*. [97] showed that these vortices can significantly augment heat transfer, so

their presence must be accounted for when attempting to model a concave surface. The simulations that made use of low mainstream turbulence showed the influence of Taylor-Görtler vortices, as shown in Fig. 6.1.2.1a. Higher mainstream turbulence levels apparently wiped out these structures, producing a uniform span-wise temperature. This behavior was consistent with the data of Dees *et al.* [30]; however, the span-wise variation of surface temperature was approximately 10% for the low turbulence case, indicating that the models were greatly over-predicting the impact of these structures.

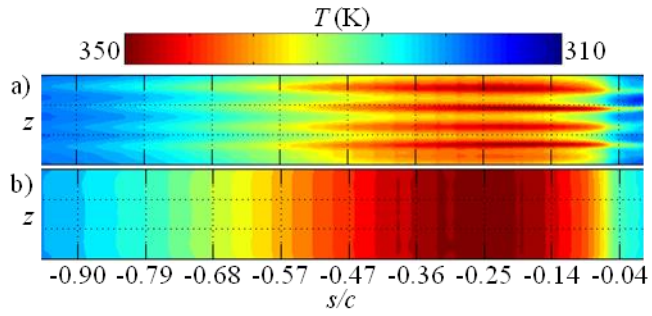

Figure 6.1.2.1: Temperature contours from the realizable *k-ε* case using a) *Tu* = 0.5% and b) *Tu* = 20%

The mesh used for the majority of the cases without film cooling made use of a mesh totaling 10 million elements. A mesh refinement study was carried out by using FLUENT's mesh adaption tool to refine the mesh near temperature gradients. Figure 6.1.2.2 shows that even though the mesh was more than doubled in size, there was no impact on the temperature profiles.

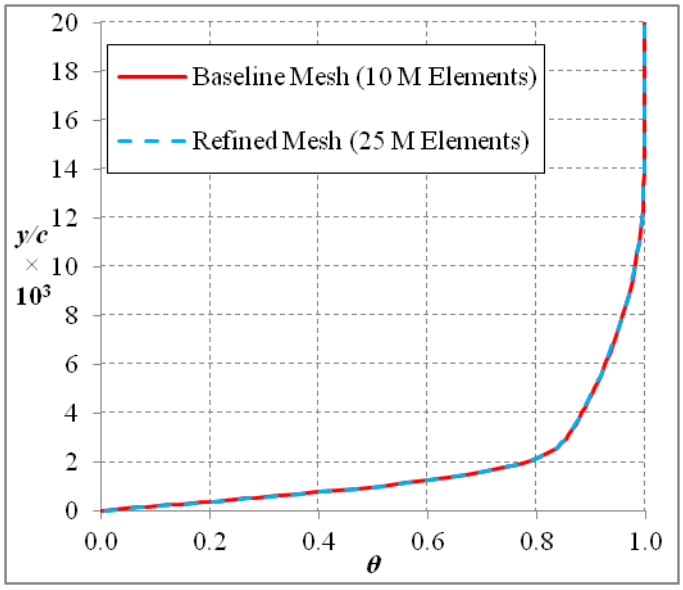

Figure 6.1.2.2: The temperature profile at the PS3 position for the original and refined meshes

However, the Transition SST case had an unusual problem with the turbulence levels predicted downstream of transition using the original mesh at low turbulence. Figure 6.1.2.3 shows that the turbulence levels were unusually low, which lead to a dramatic under-prediction of heat transfer coefficient. This case also displayed convergence problems that were not seen for other cases. A refinement to 18 M-elements resolved the problem, and subsequent refinement did not significantly affect the results. Because this was the only case affected by this problem, all other cases used the 10 M-element mesh.

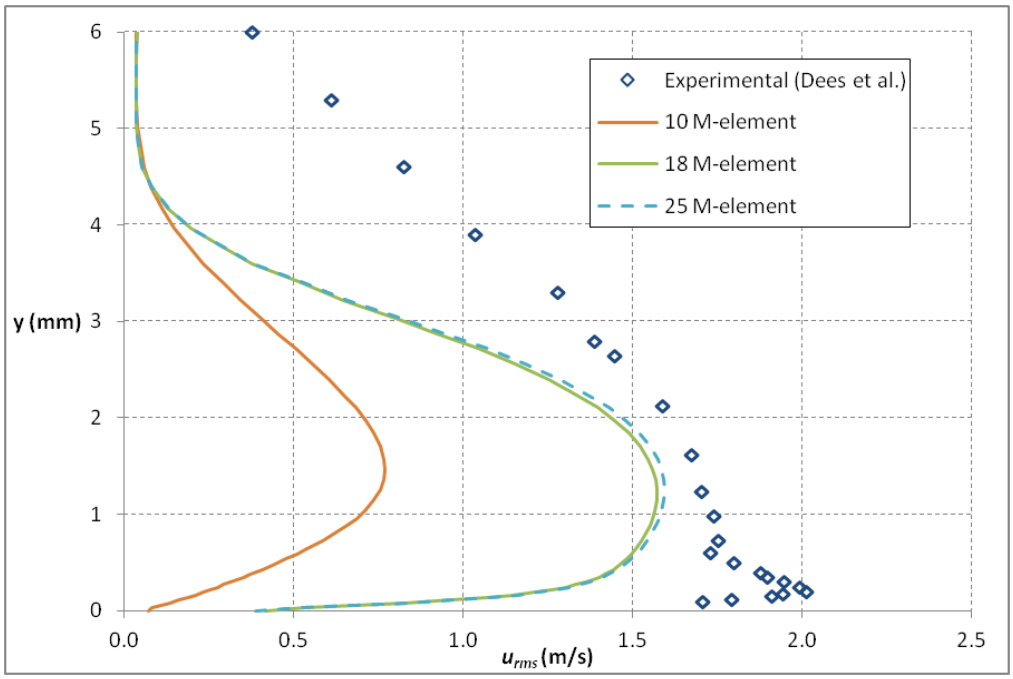

Figure 6.1.2.3: Turbulence levels at the SS3 position for Transition SST and *Tu* = 0.5% at different mesh densities

6.1.3. SS3 only configuration

Because this configuration contained film cooling holes and the internal cooling geometry used in the experiments, it made use of a considerably larger mesh than the plain C3X vane. To improve the predictions of internal cooling, a thin (1 mm) prism layer was placed on the internal surface, which was subjected to impingement cooling. A very thin (0.2 mm) prism layer was placed inside the film cooling holes. Three zones (coolant, solid, and mainstream) were meshed separately and joined prior to use in FLUENT. Figure 6.1.3.1 shows an example of the mesh used for this configuration with the different regions highlighted. Grid points were very dense in the vicinity of the holes. For the simulations of

adiabatic effectiveness, the portion of the mesh representing the solid wall was deactivated.

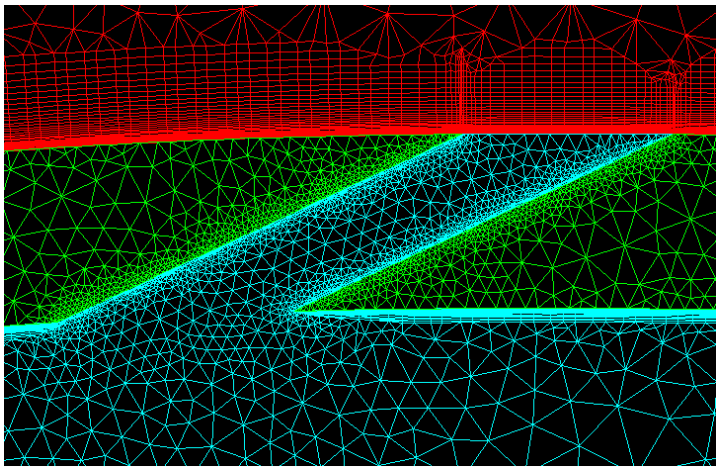

Figure 6.1.3.1: An example of the mesh used for the SS3 Only configuration with blue indicating the coolant mesh, green the solid mesh, and red the mainstream mesh

The total mesh consisted of 23 million elements. A grid refinement study was carried out for one of the flow rates. The grid was refined using FLUENT's refinement tool using gradients of temperature and turbulence to concentrate the new elements around the film cooling jets. The resulting mesh was 43% larger at 33 million total elements. Comparison of the overall effectiveness contours for both cases, shown in Fig. 6.1.3.2, revealed only negligible changes for the refined case.

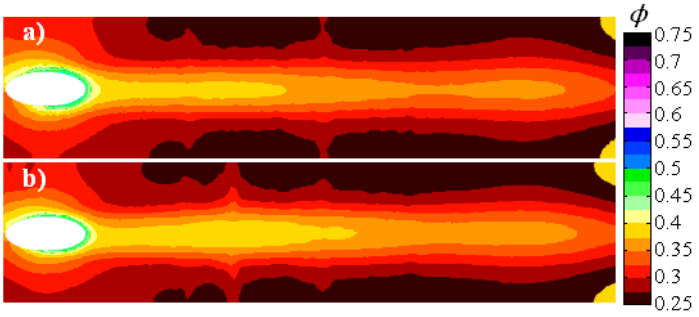

Figure 6.1.3.2: Overall effectiveness for a) 23 M-element and b) 33 M-element meshes

6.1.4. Showerhead configuration

The inclusion of the showerhead holes made this the largest mesh used for any configuration. As with the SS3 Only mesh, a thin prism layer was included on the inner surface to improve the prediction of internal heat transfer. Unfortunately, cutting the domain for the periodic boundary through the holes (as shown in Fig. 6.1.4.1) created problem areas for the mesh quality. This meant that including a prism layer inside the holes always created an unusable mesh. Because the mesh within the holes was already fairly dense, the expected benefit of prism layers was small. Also like the SS3 Only case, the mesh was constructed from separately generated coolant, solid, and mainstream meshes. For the simulations of true adiabatic effectiveness, the solid zone was deactivated.

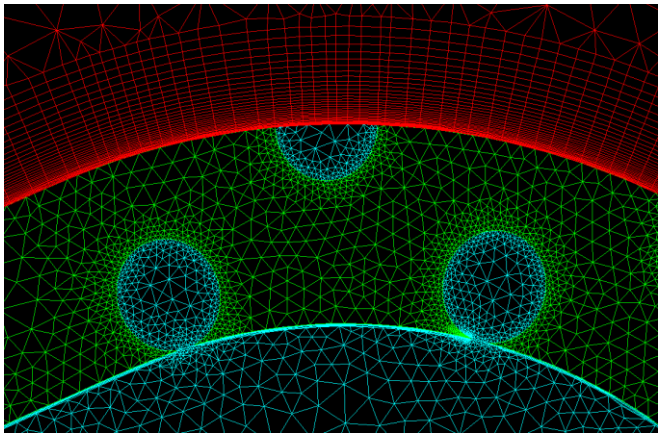

Figure 6.1.4.1: An example of the mesh used for the SH configuration with red for mainstream, blue for coolant, and green for solid

The initial mesh used for this configuration was 32 million elements. This large size was due to the large number of elements concentrated around the film cooling holes. Grid independence was verified by using FLUENT's refinement tool to create new elements concentrated in regions where film cooling jets were interacting with the mainstream. The refined mesh consisted of 42 M-elements. Figure 6.1.4.2 shows that the effect of mesh refinement was minimal.

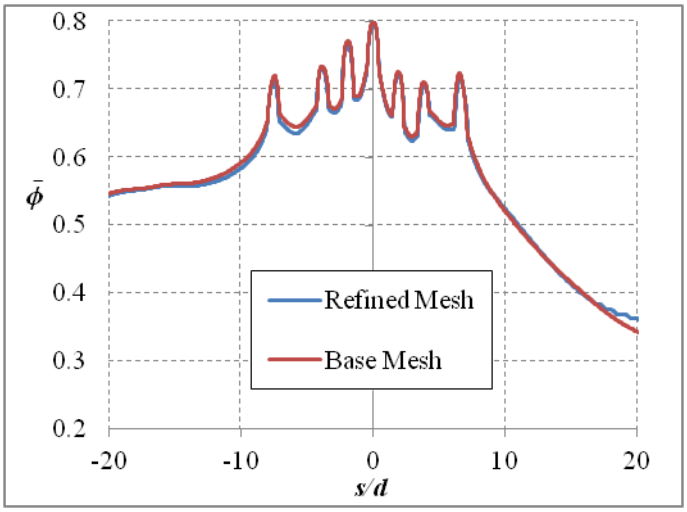

Figure 6.1.4.2: Laterally averaged overall effectiveness for the 32 and 42 M-element meshes used for the SH simulations

6.2. Common Boundary Conditions

All the configurations had inlet and outlet conditions in common. The inlet was a “pressure inlet” with a temperature of 305 K and a pressure of 101 kPa. The outlet was a “pressure outlet” with a target mass flow rate that was adjusted depending on film cooling conditions such that the inlet flow averaged 5.8 m/s, which matched the experiment. Another important inlet condition was the turbulence level. For the film cooling studies, the inlet turbulence was set to match the high levels of turbulence expected downstream of a combustor. As mentioned in chapter 2, the experimental level of turbulence was set using a passive grid upstream of the vane and verified with measurements taken x/c = -0.27 upstream of the vane position, as shown in Fig. 6.2.1.

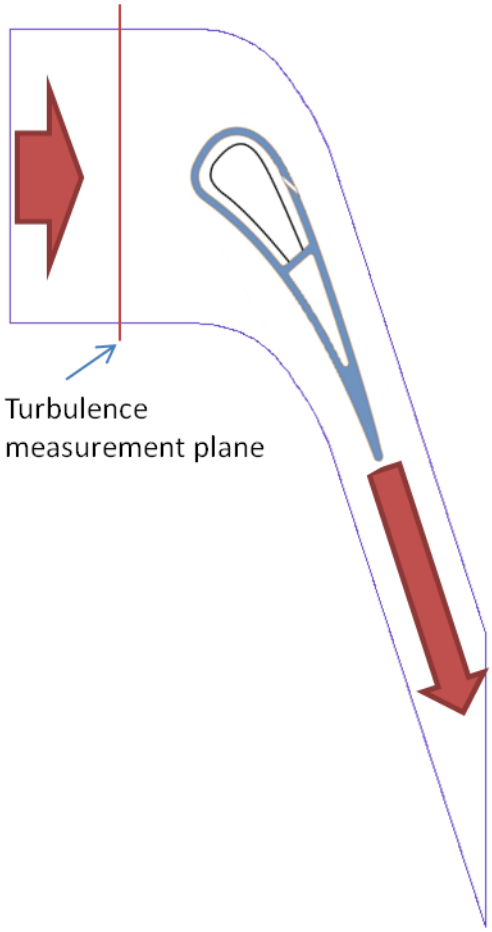

Figure 6.2.1: Computational domain showing the mainstream inlet and outlet along with the plane where mainstream turbulence was measured

Computationally, the turbulence level can easily be set to whatever desired level. However, to match the experiment at the measurement plane, the inlet conditions needed to be very high. Some trial and error found that, with the *k-ω* SST model (which is essentially the standard *k-ε* model in the free-stream) the turbulence decayed to the experimental values of Tu = 20% and Λ_∞ = 37 mm at x/c = 0.27 when the inlets were set to Tu = 47% and Λ_∞ = 18.8 mm (note that FLUENT uses something close to (but not quite) Λ_{EI} (the scale of the largest

“energy containing” eddy defined as $\Lambda/6$ [98], where Λ is the integral length scale) as the turbulent length scale, so the actual inlet condition was 3.082 mm). There was some concern that, though the experimental measurement was matched, the turbulence was not matching the expected decay rate and would produce unrealistic results. To examine this, the decay rate was compared to the experimental data of Polanka *et al.* [99]. As shown in Fig. 6.2.2, even though the absolute values of the turbulence were not matched, the decay rate was well matched. Note that though the same turbulence grid was used at roughly the same position for both Polanka *et al.* and Pichon [70], the more recent data show significantly reduced turbulence. Also note that the values selected worked well for all of the models with the exception of the RNG k-ε model. This model was low compared to the others, with only Tu = 17% at the measurement plane. The boundary conditions were not adjusted to account for the differing decay rate of the RNG k-ε model.

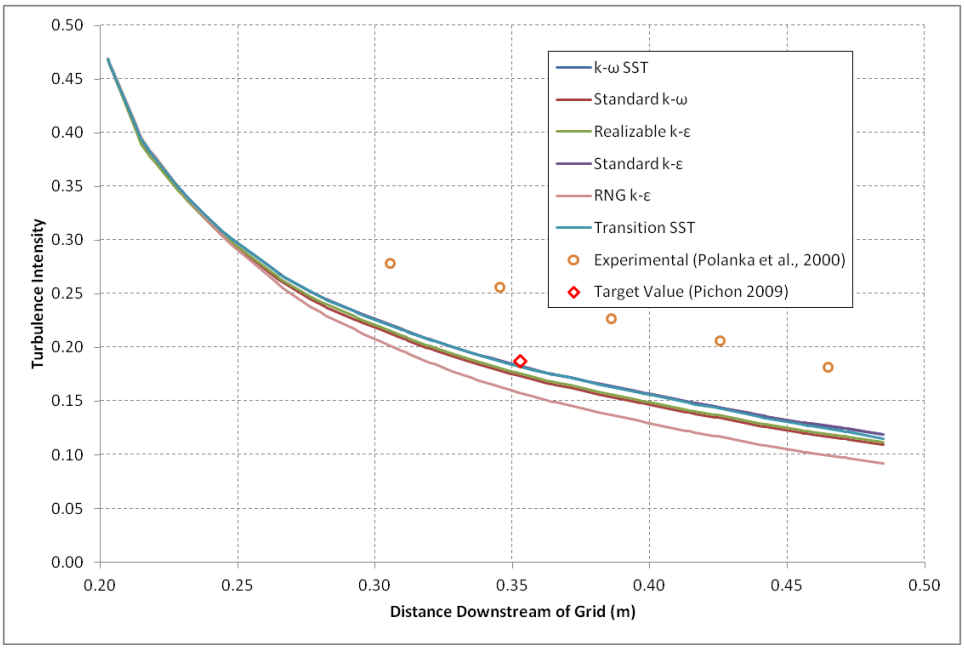

Figure 6.2.2: Comparison of the decay rates of many turbulence models to experimental data

The boundary conditions for the coolant inlets and internal cooling were shared between the film cooling configurations. To maintain a periodic condition the coolant entered the vane through the impingement holes rather than the base of the vane. The temperature of the coolant was set at these “pressure inlet” boundaries to match the experimental density ratio, and the pressure was adjusted to match the desired mass flow rate. The adjustment process usually required several iterations to achieve the correct pressure to match each flow rate within 0.001 of the target *M*. The impingement plate itself was considered a “convective” boundary with a plate thickness matching the steel impingement plate and a back-side *h* value set using a correlation for fully developed channel flow [100]. It was recognized that this correlation was a poor approximation, but

the normalized internal gas temperatures matched reasonably well with the experimental values. The aft passage was modeled using the same correlation despite the fact that the Reynolds number fell outside the appropriate range. Because neither film cooling study was particularly interested in the performance over the aft passage, this was considered acceptable.

6.3. Determining convergence

There is no universal standard for convergence that can be applied to all cases. The most often used metric for convergence is the value of the residuals for energy, velocity, and the continuity equation, along with other parameters such as ω. For all cases considered in this body of work, the residuals for velocity and continuity typically were reduced to ~ 10^{-5} while energy was reduced to ~ 10^{-7}, though often times values in the ~ 10^{-6} and ~ 10^{-8} ranges were achieved. Turbulence parameters did not typically drop below ~ 10^{-4}, though the study without film cooling managed ~ 10^{-6}. However, low residuals were considered a necessary but insufficient means of determining convergence. It was found that even when residuals had reached very low levels, important parameters such as mass flow rate through the film cooling holes were not yet steady. Several monitors were created for each configuration to verify that values of surface temperature at selected positions and coolant flow rate were steady. The temperature monitors were points on the leading edge and at s/d = 9, which were chosen based on examination of the output of solutions which had “converged” using residuals alone but failed to achieve steady temperature

values. The standards used to judge convergence based on these monitors varied for each configuration. For the without film cooling configuration, it was possible to achieve surface temperatures that did not vary at all within the precision of the output (five significant figures) for several hundred iterations, at which point the solution was considered converged. However, the film cooling cases were not so steady. The SS3 Only case was considered converged when the mass flow rate varied by less than 0.5% and the temperature varied by less than 0.1 K for over 500 iterations. The SH configuration was considered converged when the temperature varied by less than 0.02 K and the mass flow rate varied by less than 0.1% for 1000 iterations. Unfortunately, even by very relaxed standards of convergence no flow rate other than I^*_{SH} = 0.77 would converge for the SH case.

6.4. Conversion of Dees data

Part of the RANS model study was the comparison of RMS turbulence data from the experimental measurements to the computational simulations. Because RANS models assume isotropic turbulence as part of their formulation, comparison of u_{rms} data may not be the best method for evaluating predictions of the turbulence profile. However, the available data were for u_{rms} only, making comparison of k problematic. The u_{rms} contribution to k in a turbulent boundary layer has been well explored for a flat plate, so an approximation of k can be made by assuming that the ratio of u_{rms} to the other fluctuating velocity components was the same as that for a flat plate. The DNS data of Spalart [101]

were used to compute the ratios v_{rms}/u_{rms} and w_{rms}/u_{rms} through the boundary layer. Spalart showed that the turbulence profile had some Reynolds number dependence when using y/δ instead of y^+, but this was confined primarily to a region near the wall (*i.e.*, $y/\delta < 0.3$, there were at most eight points in this region). The y/δ data were used because y^+ was not available for the experimental data for most positions. The use of the ratios from $Re_\theta = 300$ (the closest available for the majority of the measurement positions) was considered acceptable for the majority of the vane, but $Re_\theta = 670$ was used for the SS3 and SS4 positions, where the measured values of Re_θ were approximately 800. Comparisons using different Re_θ values did not change the conclusions drawn in this study. For the lower Re_θ positions, isotropic turbulence was also considered as a method for comparison. The difference between the $Re_\theta = 300$ conversion and a method using isotropic turbulence throughout did not appreciably affect the results. This approximation does not account for possible effects from curvature or pressure gradients on the turbulence; however, comparison of the data of Alving *et al*. [102] for a boundary layer subjected to a strong (*i.e.*, 90°) convex curvature to a flat plate boundary layer shows that although the turbulence profiles are strongly affected, the relative contribution to k from each component was almost unaffected.

Chapter 7 – Suction Side Only Simulations

A representation of the configuration using a single row of holes on the suction side was simulated using a RANS approach with the *k-ω* SST model. The results of these simulations were compared to the experimental measurements of Williams *et al.* [21]. Seven momentum flux ratios were simulated for both adiabatic and conducting (matched Biot number) cases. The data were also used to investigate off-the-wall temperature fields to show that T_{aw} was inappropriate as the driving temperature for heat transfer.

7.1. Overall and adiabatic effectiveness predictions

Typically, validations of CFD results have looked to laterally averaged values as a means of comparison. However, many studies have shown that while laterally averaged values for η and/or ϕ may be well predicted, the local values may have considerable disagreement (*e.g.*, [40], [44], and [41]). For this reason, the comparison of these simulations to experimental data used contour plots exclusively. A miscalculation of the DR for the overall effectiveness experiment meant that the momentum flux ratios were slightly higher than intended, but for the most part they were within experimental uncertainty of the desired value.

Only overall effectiveness measurements were collected at the lowest momentum flux ratio (I_{SS3} = 0.06). However, it was the only simulation which matched a coolant flow rate for an attached jet. The peak effectiveness for a flat plate (similar to this case) normally lies between I = 0.4 and 0.6, but separation has already begun at that point. Figure 7.1.1 shows the results of the simulations

for this low momentum flux ratio. It should be noted that the experimental results for this condition were not included in the Williams *et al.* study because of problems with the data, but they can still serve for a qualitative comparison. The simulations showed extremely high adiabatic effectiveness along the path of the coolant jets for x/d < 5. The overall effectiveness also strongly showed the influence of the jets, which were also seen experimentally. However, the experiments were a full contour level warmer than the predictions, indicating a poor match to the real performance of the coolant jets. Between the jets the predicted temperature was well matched, which indicated that the internal and external h_f was well predicted.

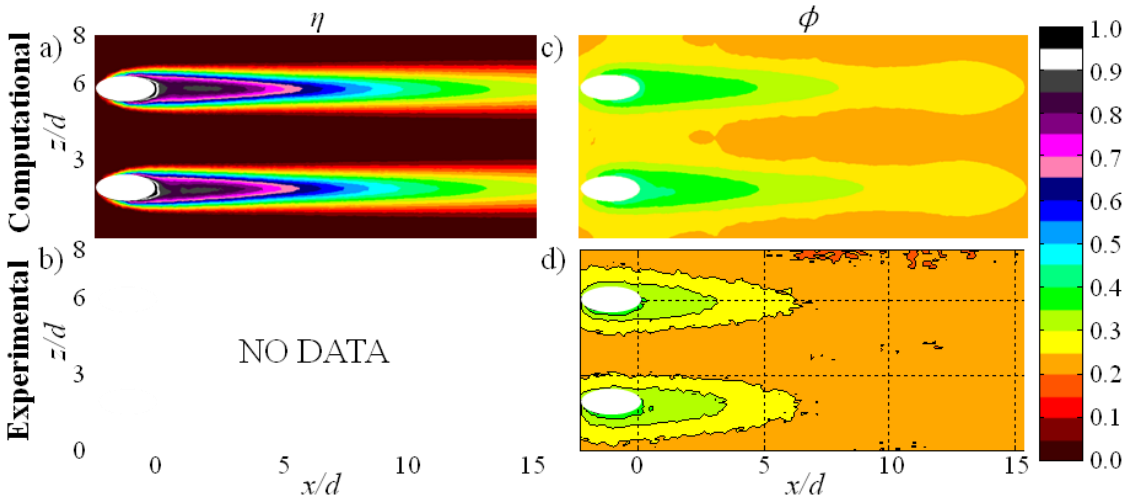

Figure 7.1.1: Contours of η for a) simulated I = 0.06 and ϕ for c) simulated I = 0.06 and d) experimental I = 0.06

Similar behavior was also seen for I_{SS3} = 0.35, as shown in Fig. 7.1.2. Here, the simulated values of η showed reasonable agreement very near the

holes, but displayed a characteristic problem with RANS models: lack of jet diffusion. Farther downstream of the film cooling holes, the coolant remained in a concentrated streak near the wall, which produced η values that were too high compared to the experiment. This carried over to the simulated ϕ values, which showed a strong effect of the jet much farther downstream than the measurements, and over-predicted ϕ under the jets. Once again, the values between the jets were very near the measured values, which indicated that the internal cooling was well matched. Identical behavior was also observed for I_{SS3} = 0.58, which is shown in Fig. 7.1.3. The effect of increasing jet separation can be seen in both the experimental and simulated η values.

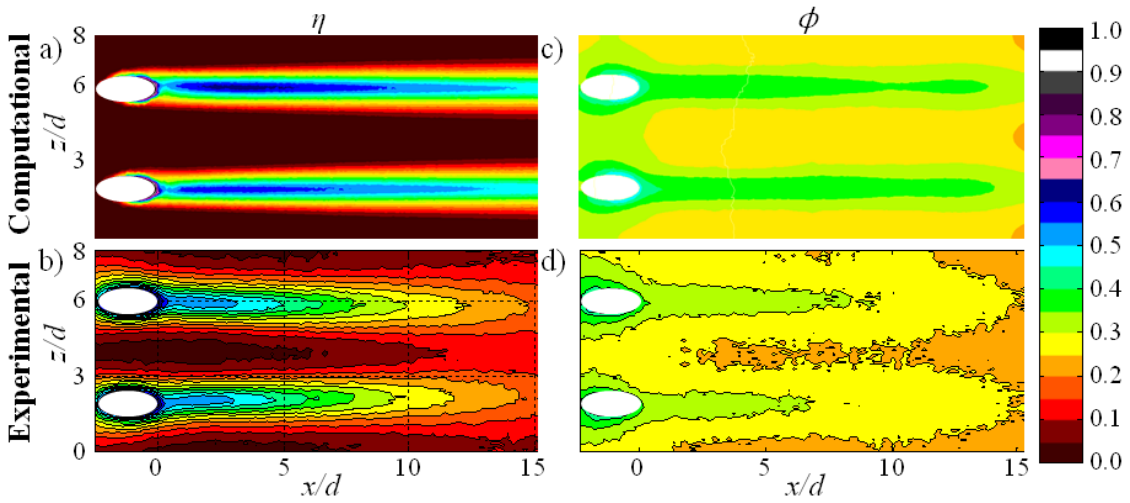

Figure 7.1.2: Contours of η for a) simulated I = 0.35 and b) experimental I = 0.34 and ϕ for c) simulated I = 0.35 and d) experimental I = 0.38

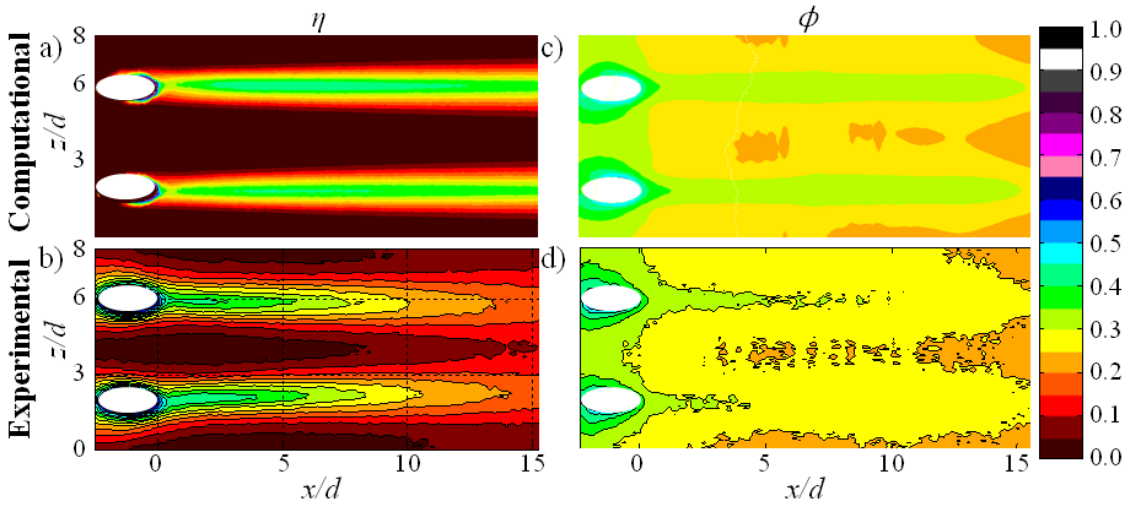

Figure 7.1.3: Contours of η for a) simulated I = 0.58 and b) experimental I = 0.55 and ϕ for c) simulated I = 0.58 and d) experimental I = 0.62

The performance trend seen for the lower momentum flux ratios reversed as the jets lifted farther off the surface at I_{SS3} > 0.6. Figure 7.1.4 shows the contours for I_{SS3} = 1.03. At this flow rate, the adiabatic effectiveness was under-predicted by the simulations. This was likely another consequence of poor prediction of the level of jet diffusion. Because of high mainstream turbulence (the approach flow measurements are reported in section 5.1), some coolant from the jet was brought back toward the wall, increasing the effectiveness. If this turbulent diffusion process was not properly simulated, the effectiveness levels would be too low because the coolant jet would be "over-separated" because the jet diameter would be too small. This can be more clearly seen for I_{SS3} = 2.85, which is shown in Fig. 7.1.5. At this momentum flux ratio, the simulations predicted that η was very near zero, but the experimental measurements still showed jet traces with η ~ 0.15. There was some visible asymmetry in the

experimental jets due to the internal impingement cooling jet pitch having a different pitch than the film cooling holes. The simulation was not able to fully capture this effect, though there was some asymmetry in the simulated jets.

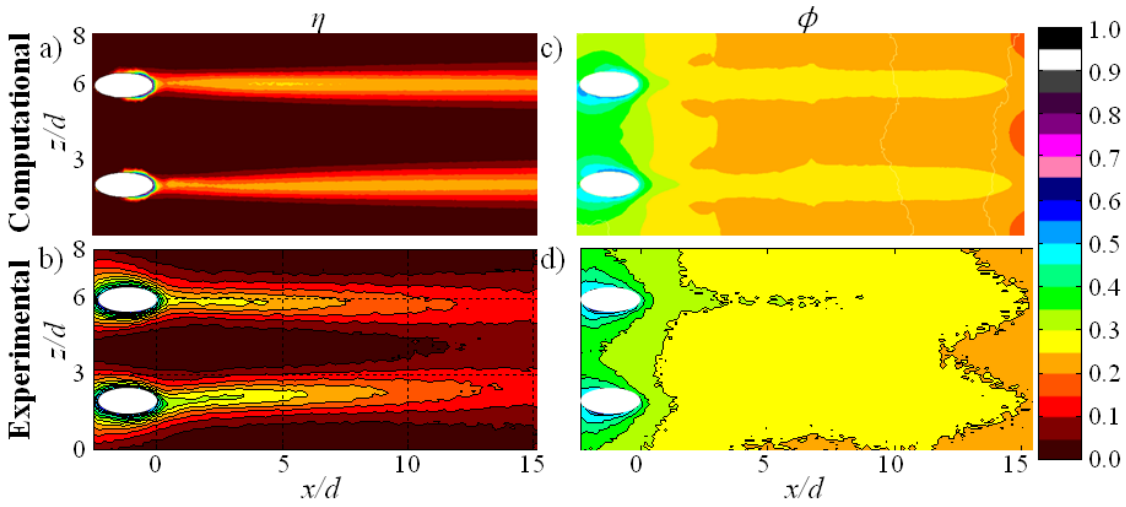

Figure 7.1.4: Contours of η for a) simulated I = 1.03 and b) experimental I = 0.98 and ϕ for c) simulated I = 1.03 and d) experimental I = 1.09

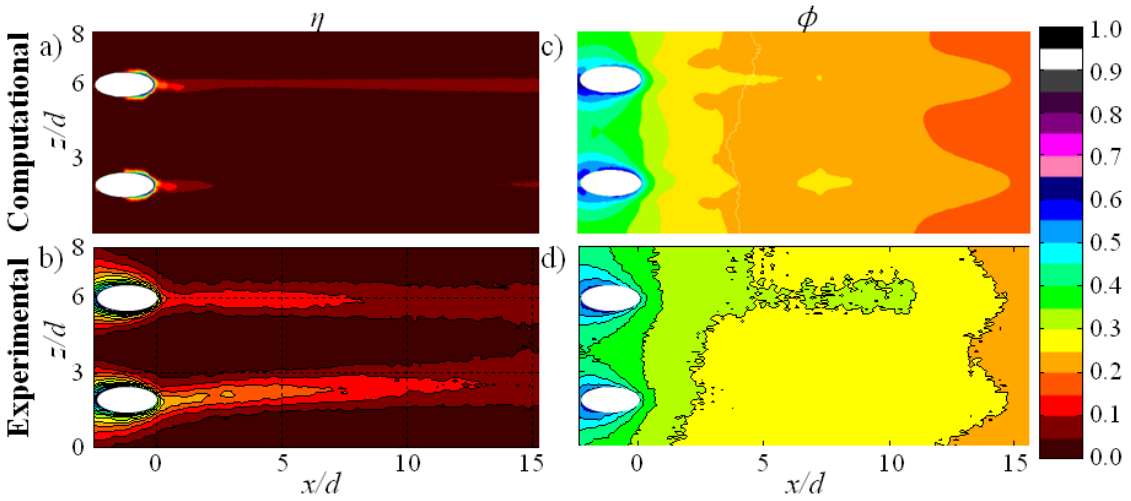

Figure 7.1.5: Contours of η for a) simulated I = 2.85 and b) experimental I = 2.75 and ϕ for c) simulated I = 2.85 and d) experimental I = 2.98

As the coolant jets separated from the surface, the impact of the poorly predicted η values were reduced. The resulting ϕ predictions were slightly low, but were within 0.04 of the experimental value over most of the surface for I_{SS3} = 1.0 and above. Interestingly, the overall effectiveness measurements and predictions continued to show a distinct effect of the jets even when the coolant jets were lifted completely off the surface (*i.e.*, η ~ 0). This was true even for the highest momentum flux ratio of I_{SS3} = 4.83, shown in Fig. 7.1.6. Unfortunately, there were no experimental measurements of η at this momentum flux ratio, but there was no reason to expect that jets with 60% greater momentum of those seen in Fig. 7.1.5b for I_{SS3} = 2.85 would produce any adiabatic effectiveness.

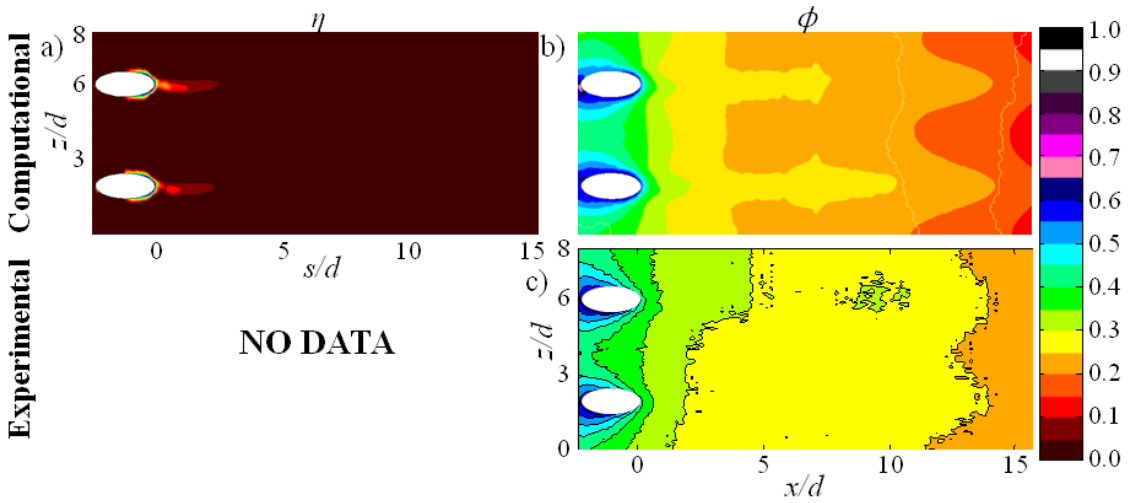

Figure 7.1.6: Contours of η for a) simulated I = 4.83 and ϕ for b) simulated I = 4.83 and d) experimental I = 5.01

The sinusoidal pattern for 10 < x/d < 15 was present in the experimental measurements as well as the simulations. This suggested that the simulations may be able to provide some insight into the physical behavior that caused the film cooling jets to provide some protection from the mainstream in the absence of coolant in direct contact with the wall. This investigation is the subject of the following section.

7.2. Off-the-wall jet cross-sections

To see how the over-lying jet was protecting the wall even though η was effectively zero, cross-sections of the gas temperature off-the-wall were collected at x/d = 5 and 10. These cross-sections were normalized using:

$$\theta = \frac{T_\infty - T_{gas}}{T_\infty - T_{c,exit}} \tag{7.2.1}$$

Note that η is a special case of θ at $y = 0$ for an adiabatic wall. This normalization was also applied to the conducting case, which made comparison simpler because through-hole warming of the coolant could be discounted. If conjugate effects can be ignored, the profiles should theoretically be identical when normalized in this way.

The highest momentum flux ratio that provided the impetus for looking at the off-the-wall performance is shown in Fig. 7.2.1. It was evident that the gas temperature profiles were identical for the conducting and adiabatic wall cases except for a small region near the wall ($y/d < 0.3$). For the adiabatic case, the jet was completely off the wall and there was no interaction by the coolant (*i.e.*, $\eta = \theta = 0$). However, for the conducting case there was a region where the thermal boundary layer was interacting with the coolant jet. This may have been a function of the counter-rotating vortex pair that forms along-side stream-wise injected jets drawing fluid from the nearby thermal boundary layer into the region beneath the jet. Regardless of the cause, the result was that at no point between the wall and the jet was $T_{gas} = T_{aw}$. The maximum temperature that was observed was 299 K, while T_{aw} was 305 K. Because T_w was 293 K directly beneath the jet, any heat transfer analysis using T_{aw} as the driving temperature for heat transfer would predict that q'' was double the actual value.

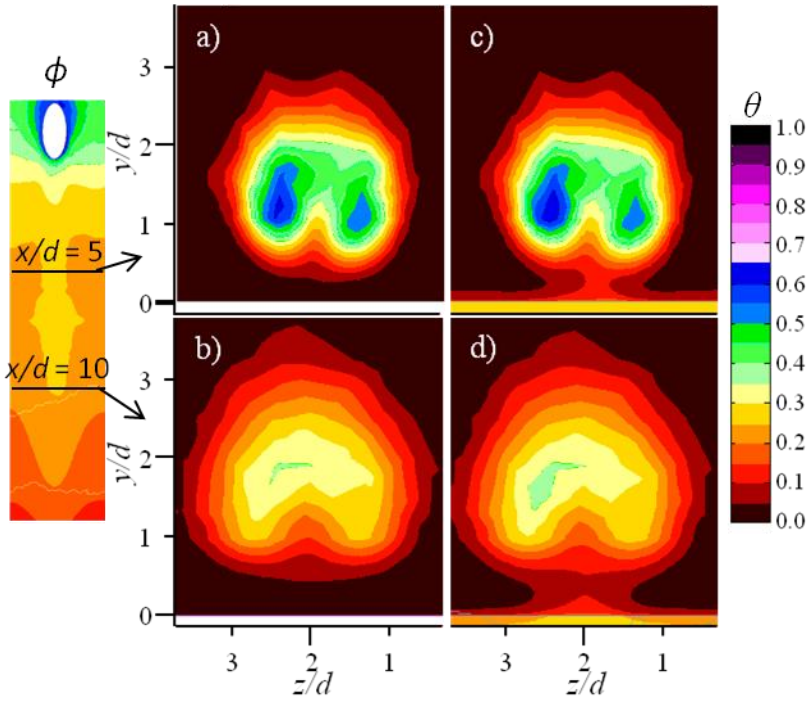

Figure 7.2.1: Simulated cooling jet cross-sections of θ at I_{SS3} = 4.83 for an adiabatic wall at *x/d* = a) 5 and b) 10 and for a conducting wall at *x/d* = a) 5 and b) 10

The interaction with the thermal boundary layer for a separated jet explained why the overall effectiveness still displayed streaks beneath the jets. The observation that T_{aw} was not the correct driving temperature also bore further investigation. The data of Dees *et al.* [103] suggested that this behavior would occur for separated jets in a region of high surface curvature. However, their data were limited and the uncertainty for many of the cases made drawing firm conclusions for lower momentum flux ratios (*i.e.*, attached jets) impossible. Figure 7.1.4 shows that even for the case of a partially attached jet at I_{SS3} = 1.03, the same behavior was present. There was no location between the wall and the core of the jet that was as warm as T_{aw}.

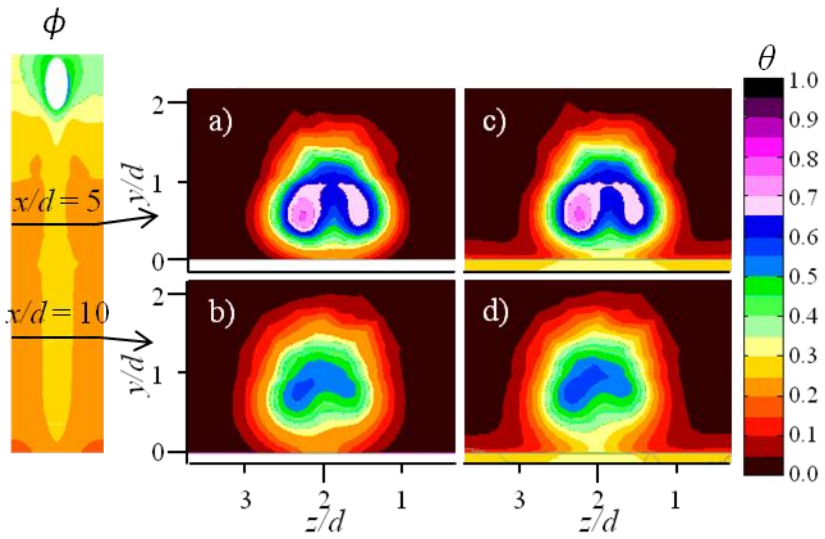

Figure 7.2.2: Simulated cooling jet cross-sections of θ at I_{SS3} = 1.03 for an adiabatic wall at x/d = a) 5 and b) 10 and for a conducting wall at x/d = a) 5 and b) 10

These cases both represent unusually high momentum flux ratio. As was shown in chapter 4, even at very high coolant flow rates from the showerhead (I^* = 7.5) the momentum flux ratio from the SS3 row was only I_{SS3} = 0.75. This would likely be the case for real designs. For a more moderate value of I_{SS3} = 0.35 (approximately equivalent to that which was achieved from this row of holes when the showerhead had I^*_{SH} = 1.0) T_{aw} appeared as the temperature immediately above the wall, as shown in Fig. 7.2.3. This supports the idea that T_{aw} would serve as the correct driving temperature for many real-world flow rates. However, investigation of the I_{SS3} = 0.06 case revealed that T_{aw} was too cold compared to the real temperature above the wall, which can be seen by comparing Figs. 7.2.4a and 7.2.4c. This affect appeared to be confined to the region immediately downstream of the film cooling holes, because by x/d = 10

the jet temperatures were more-or-less identical between the conducting and adiabatic cases (Figs. 7.2.4b and 7.2.4d).

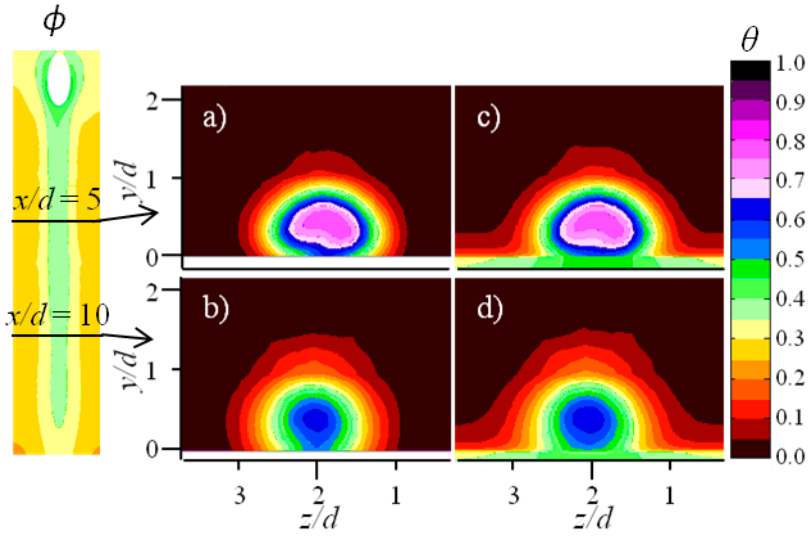

Figure 7.2.3: Simulated cooling jet cross-sections of θ at I_{SS3} = 0.35 for an adiabatic wall at *x/d* = a) 5 and b) 10 and for a conducting wall at *x/d* = a) 5 and b) 10

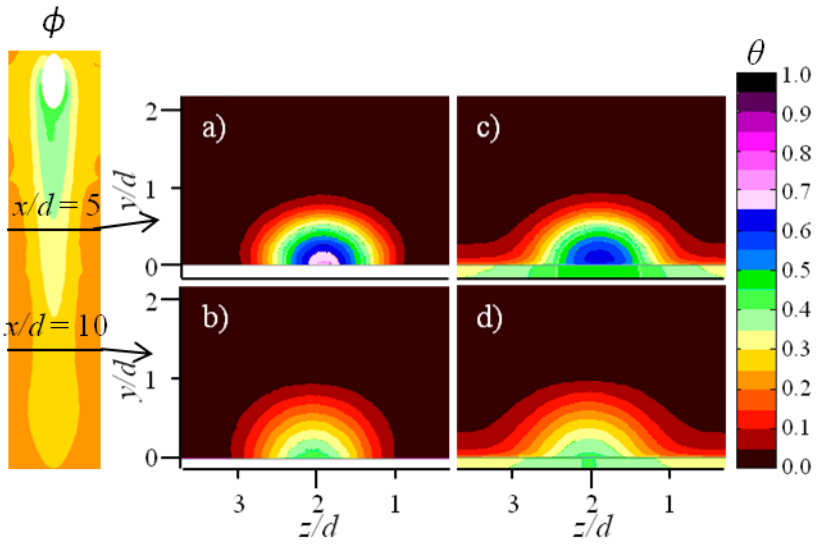

Figure 7.2.4: Simulated cooling jet cross-sections of θ at I_{SS3} = 0.06 for an adiabatic wall at *x/d* = a) 5 and b) 10 and for a conducting wall at *x/d* = a) 5 and b) 10

Chapter 8 – Showerhead Simulations

A computational model of the SH alone configuration used by Nathan *et* al. [33] was run for a single momentum flux ratio, I^*_{SH} = 0.77, using the *k-ω* SST RANS turbulence model. Both overall and adiabatic effectiveness were simulated. Because there was no way to experimentally correct for the conduction in the showerhead region, the results were not truly adiabatic. Therefore, the “adiabatic” simulation used a wall with conduction matched to the experimental material. Of particular interest to this study was the computation of h_f/h_0, which cannot be easily measured in the showerhead region. As mentioned in chapter 6, higher flow rates were attempted but convergence problems prevented their use.

8.1. Adiabatic effectiveness

The laterally averaged adiabatic effectiveness for the experimental and computational results is compared in Fig. 8.1.1. It was evident that the CFD over-predicted the performance by as much as $\Delta\eta$ = 0.2 for most of the measured range.

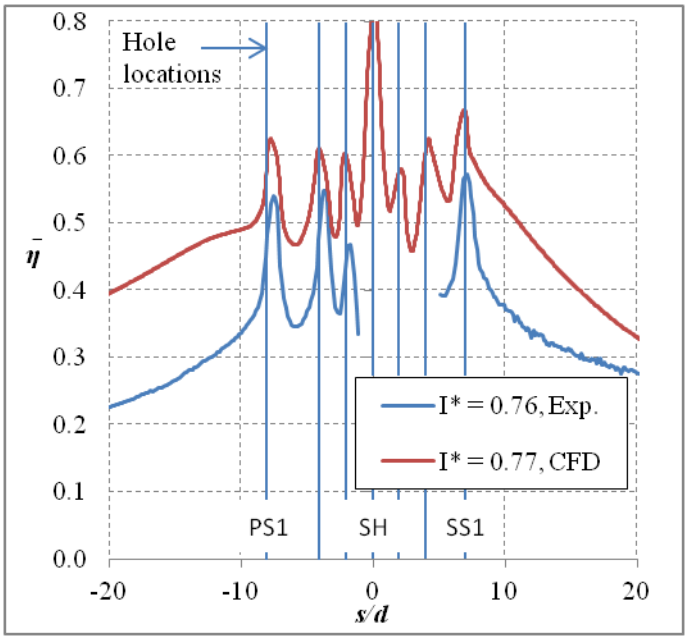

Figure 8.1.1: Laterally averaged η for both the experimental measurements of Nathan *et al.* [33] and CFD simulations

To better understand why the simulation was so far off from the measurements it is instructive to look at the contour plots in Fig. 8.1.2. Immediately downstream of the coolant holes the simulations showed much higher effectiveness than the measurements ($\Delta\eta$ = 0.4!), which indicated that coolant jet separation was not even close to correctly predicted. It was also evident that the coolant jets did not exhibit the correct level of diffusion, retaining very high levels of effectiveness even very far downstream from the holes (30 or more hole diameters), while the experimental measurements saw effectiveness levels rapidly fall off within 10 *d* of the last row of holes. The compounding effect of multiple rows of holes with over-predicted effectiveness levels lead to the dramatic over-prediction for the lateral averages. However, many flow features

were predicted. In particular, the periodic merging of the coolant jets from the last row on either side of the showerhead and the gill rows was predicted.

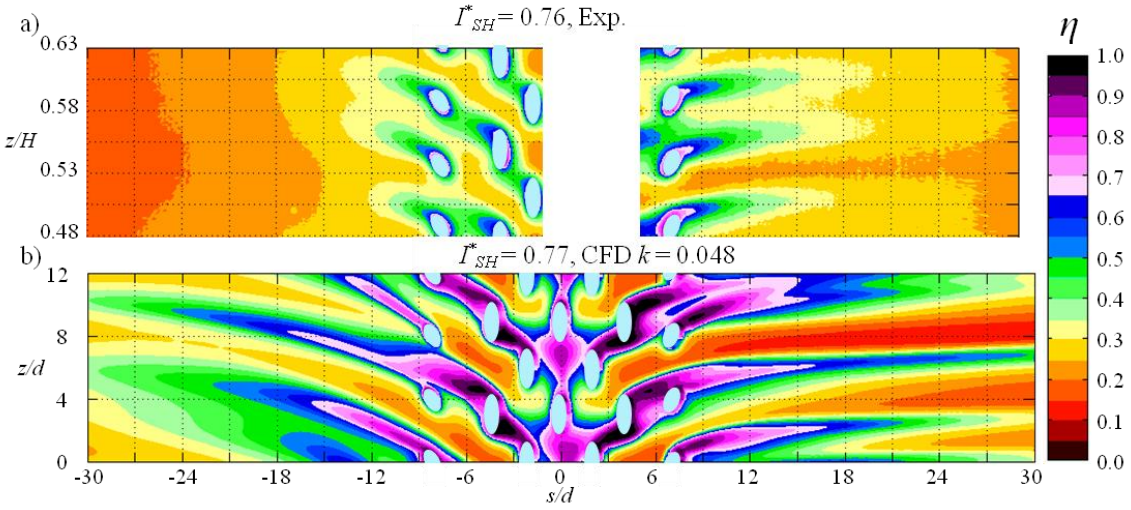

Figure 8.1.2: Contours of *η* from a) experimental measurement of Nathan *et al*. [33] and b) CFD simulation using *k* = 0.048 W/m·K

A useful capability of the computational model was the simulation of a case with a truly adiabatic wall. This simulation was used to predict the conduction error that the showerhead alone experiments of Nathan *et al.* [33] may have had because a conduction correction could not be measured. Figure 8.1.3 shows a portion of the showerhead from a truly adiabatic wall and the case more similar to the uncorrected experimental results. These simulations showed that the error was small for most positions, but very near the holes it was 0.1 or greater. This was why the results from the experiments were compared to the low conductivity data.

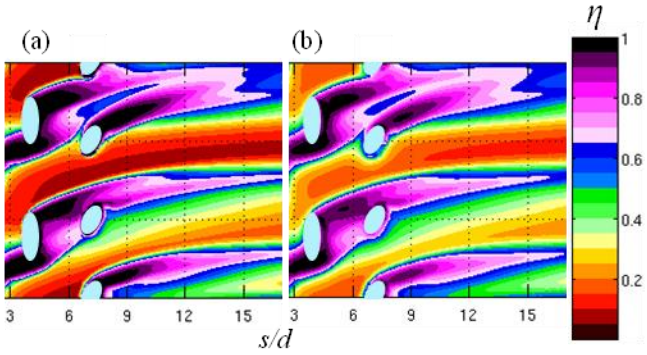

Figure 8.1.3: Comparison between simulations using a) adiabatic walls and b) *k* = 0.048 W/m·K walls similar to those used experimentally

8.2. Overall effectiveness

Given the dramatic over-prediction of the adiabatic effectiveness, the over-prediction of the overall effectiveness was expected. The laterally averaged overall effectiveness predictions are compared to the experimental measurements in Fig. 8.2.1. The level of over-prediction was not as great as for $\bar{\eta}$, though $\Delta\phi$ was still 0.1 or more for much of the measured *s/d* range.

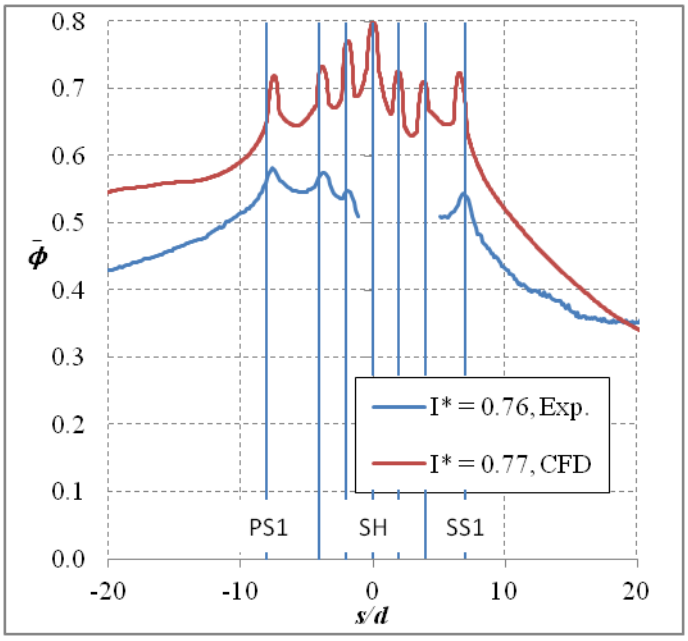

Figure 8.2.1: Laterally averaged ϕ for both the experimental measurements of Nathan *et al.* [33] and CFD simulations

Another potential reason why the simulations were considerably off from the measurements can be seen in Fig. 8.2.2, which shows the contour plots. The experimental results displayed a span-wise gradient in temperature on the pressure side. This was a result of the fact that the experimental vane had only a few (two or three) film cooling holes to "build-up" a layer of coolant prior to the measurement region. As was shown in chapter 4 for the fully cooled configuration, this can become a significant factor in the coolant distribution on the surface. Cutbirth and Bogard [91] showed that it took at least five pitches to achieve periodic flow over the stagnation line (for I^*_{SH} = 1.9, and for a slightly shorter pitch). However, the current simulations were of a periodic section one overall pitch (two showerhead, three gill holes) tall (*i.e.*, and infinitely tall vane).

Any span-wise effects due to incomplete build-up would not be captured by the simulation (incidentally, this was one of the reasons that higher momentum flux ratios were not simulated). The effect of the distinct coolant jets on the overall effectiveness were also visible in the simulations; where the experiments were mostly uniform in temperature, the jets were visible even far downstream.

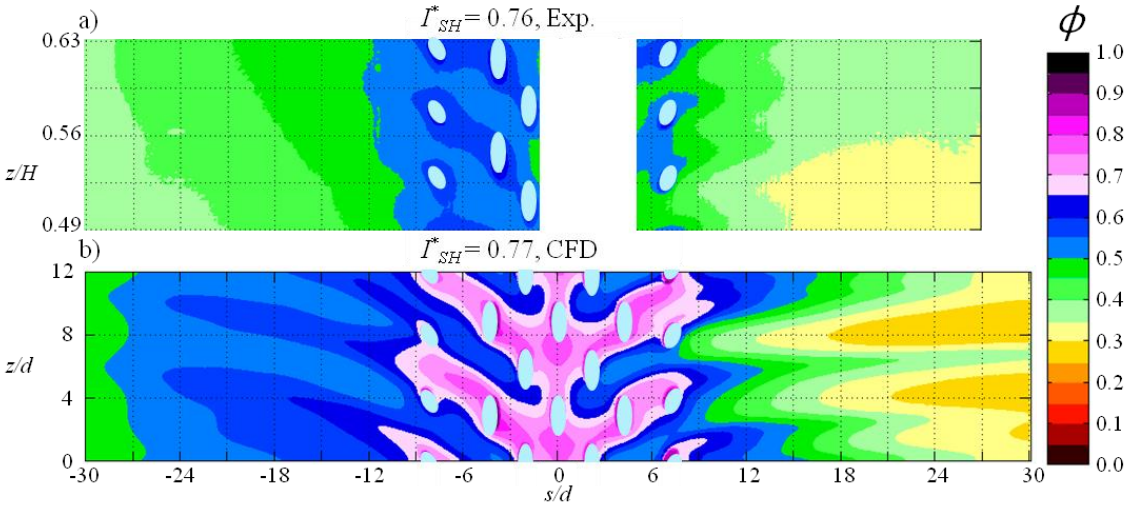

Figure 8.2.2: Contours of ϕ from a) experimental measurement and b) CFD simulation

8.3. Thermal fields

Even though the predictions of η and were poor, these simulations could provide another source of data for the evaluation of T_{aw} as the driving temperature for heat transfer. A comparison of the non-dimensional temperature profiles for the true adiabatic case and the conducting wall is shown in Fig. 8.3.1. The jets were seen to separate immediately downstream of the hole and to reattach to the wall before reaching the next hole. Cutbirth and Bogard [91]

showed separation similar to this, but for I^*_{SH} = 0.77 they showed that the core of the jet extended to 1.7 *d* off the wall, while the simulations here had at most 0.5 *d* of separation. This much reduced separation helps to explain the over-prediction along the stagnation line. A direct comparison between the adiabatic case (Fig. 8.3.1a) and the conducting case (Fig. 8.3.1b) shows that for the most part, the temperature profiles were identical, which was much like what was shown in chapter 7 for the SS3 alone case. Also like the SS3 alone case, there was a notable difference in temperature beneath the jets. For example, at *z/d* ~5 the adiabatic case had $\eta = \theta_w$ = 0.75, but the maximum temperature between the wall and the core of the jet for the conducting wall was θ = 0.8. Even this small difference could lead to a significant change in the predicted heat load were T_{aw} used as the driving temperature.

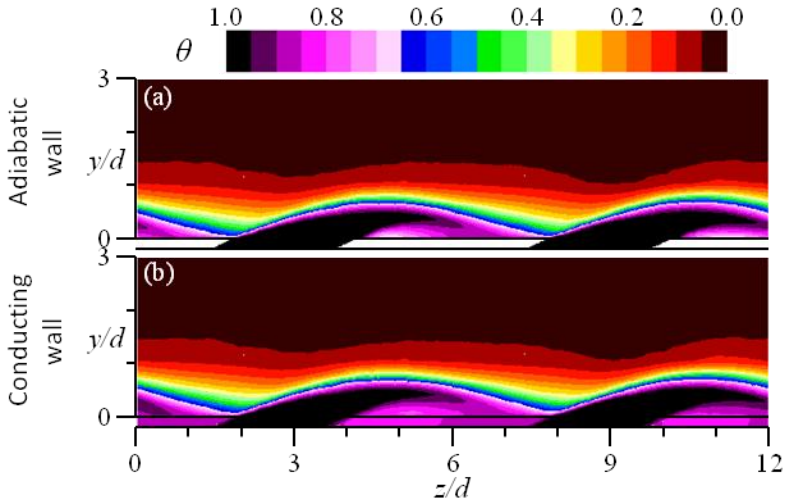

Figure 8.3.1: Gas temperature profile at *s/d* = 0 for a) true adiabatic wall and b) conducting wall

There was also interest to see if T_{aw} would work in a region where the jets were more mixed together, such as s/d = 9. Figure 8.3.2 shows the cross-section of θ at this position. Four regions were recognizable as coolant jets, though each was distorted toward the "left" (low z/d) by interaction with the mainstream. As the jets turned, the outer part of the jet was accelerated first, pushing it to lower z/d because of the orientation of the upward orientation of the jets. Like the other θ profiles, the temperature fields are mostly very similar for the conducting and adiabatic cases. However, some locations showed significant warming of the coolant for the conducting case (*e.g.*, 0.8 < z/d < 2 and 9 < z/d < 10). This indicates that the action of cooling the wall has reduced the jet temperature so that $\theta_{aw} < \theta_w$, which means that the adiabatic wall temperature would be inappropriate for use as the driving temperature.

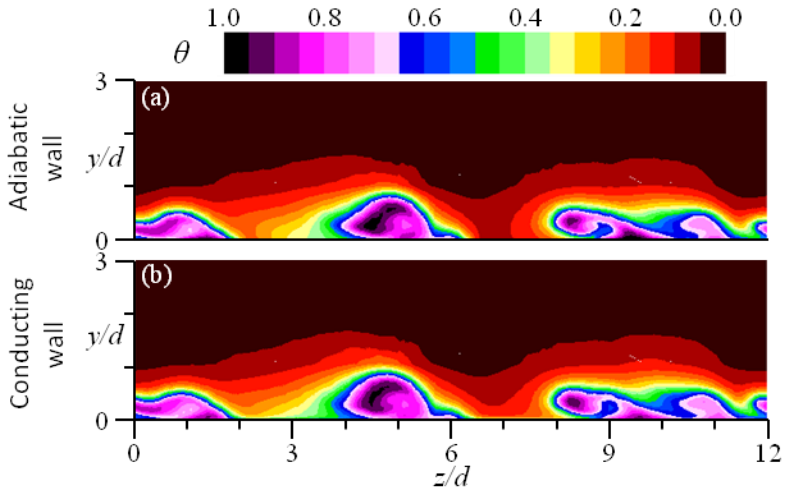

Figure 8.3.2: Gas temperature profile at *s/d* = 9 for a) true adiabatic wall and b) conducting wall

8.4. Heat transfer coefficient augmentation

The benefits of adiabatic effectiveness in the showerhead region may be significantly degraded by increasing the local heat transfer coefficient. No experimental measurements have been made for a realistic showerhead, but experiments using leading edge models (*e.g.*, [104] and [105]) have shown that h_f/h_0 = 2 or more could be expected. The difficulty of accurately measuring the heat transfer coefficient in a region of tightly spaced holes means that CFD predictions are particularly useful for investigating heat transfer augmentation in the showerhead.

Heat transfer coefficient augmentation was computed by using:

$$h_f = q_f'' / (T_{aw} - T_w) \tag{8.4.1}$$

where T_{aw} was pulled from the adiabatic simulation and T_w and q_f'' from the conducting simulation. The heat transfer coefficient without film cooling, h_0, was computed in a separate simulation without film cooling holes. Figure 8.4.1 shows the predictions for the heat transfer augmentation. There were regions of very high augmentation ($h_f/h_0 > 2$) downstream of the coolant jets consistent with the formation of a span-wise oriented vortex on the leeward side of the coolant jet. This is caused by the interaction of the mainstream with the coolant jet, which can be seen to some extent in Fig. 8.3.2. The augmentation from the jets can also be seen in Fig. 8.4.2, which shows the lateral distribution of η and h_f/h_0 at s/d = 9. Note that the highest values of augmentation were at low η positions "below" the jets corresponding to the location of the leeward side of the jet as it

turned. There were also regions of reduced heat transfer coefficient (*i.e.*, $h_f/h_0 < 1$) beneath the jets.

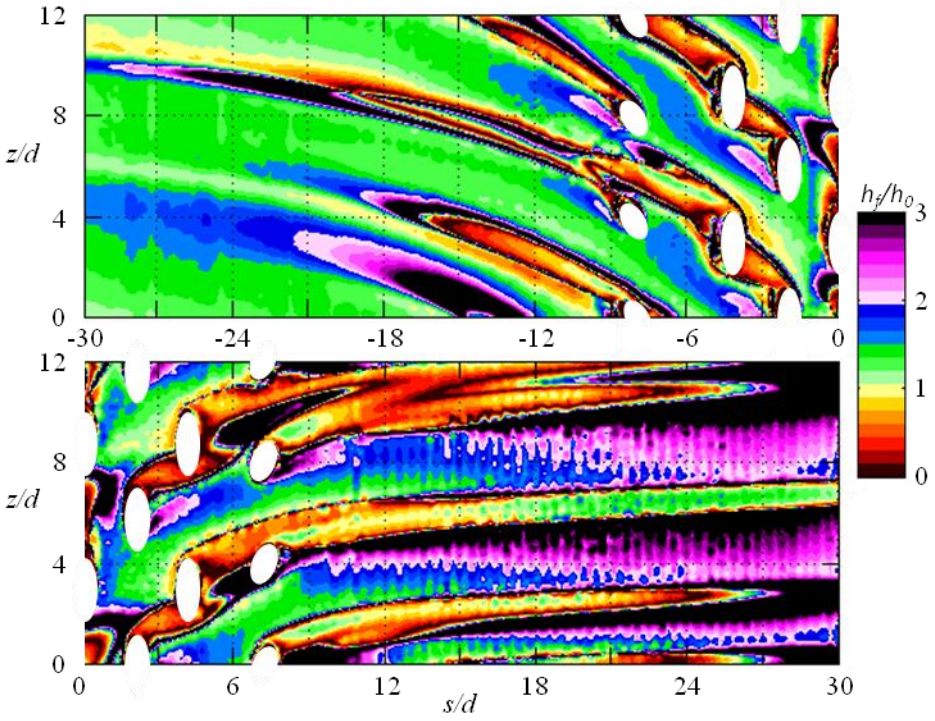

Figure 8.4.1: Heat transfer coefficient augmentation from the CFD simulation

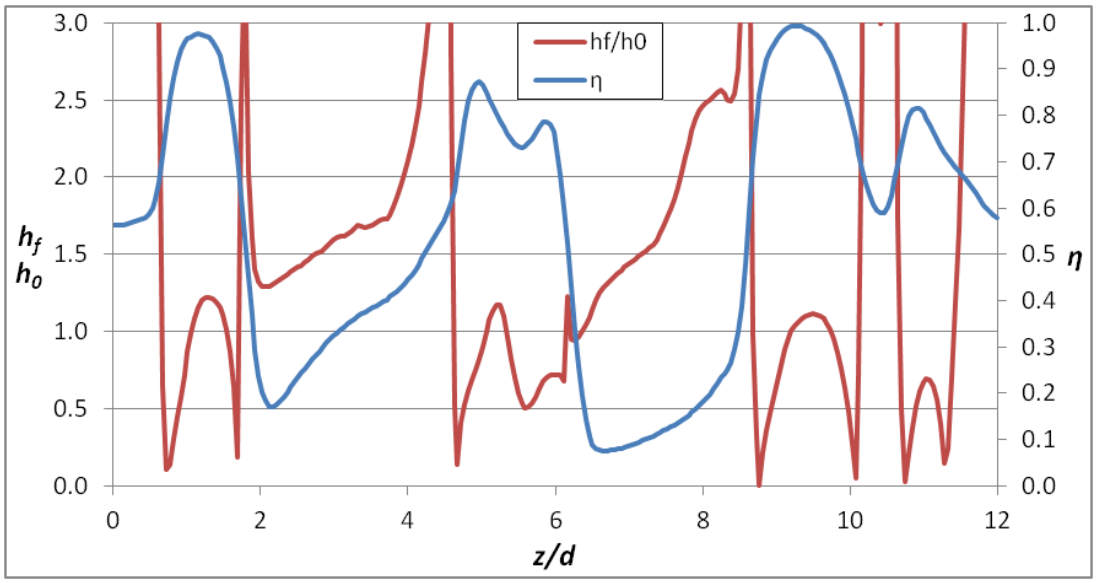

Figure 8.4.2: Lateral distribution of simulated h_f/h_0 and η at s/d = 9

The regions of reduced heat transfer coefficient may be due to T_{aw} being an inappropriate driving temperature. The simulations show that at these locations the heat flux was reversed, as shown in Fig. 8.4.3. This shows that the wall was heating the jets, which was what produced the problem with T_{aw} shown in Fig. 8.3.2. However, experimental jets were separated more than the simulations so this behavior would not necessarily be expected for a real part. Additionally, the heat flux figure shows that the portions of the vane where $h_f/h_0 >$ 3 far downstream on the vane (s/d > 24) were exposed to q'' ~ 1 kW/m^2, but an examination of the contours of η and ϕ shows that $T_{aw} - T_w$ ~ 0. This was another indication that T_{aw} may not be the correct driving temperature.

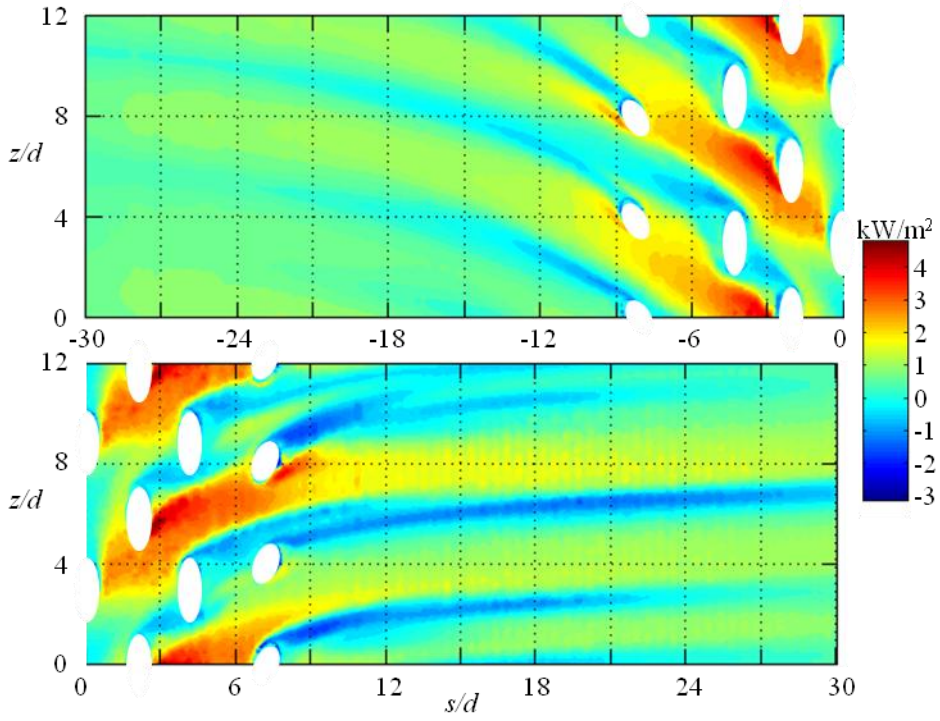

Figure 8.4.3: Contours of heat flux from the CFD simulation

The most common method to find heat transfer augmentation experimentally is to impose a constant wall heat flux and use unit density ratio jets for coolant. When the "coolant" jets are the same temperature as the mainstream, it eliminates the ambiguity of what temperature to use as the driving temperature because Eqn. 8.4.1 reduces to:

$$h_f = q_f'' / (T_\infty - T_w) \tag{8.4.2}$$

However, this method is difficult to apply for a showerhead because if holes are cut into the metal heat flux foil the energy distribution would no longer be uniform. Computational simulations are not subject to such a restriction, so this method was applied to the current simulations. Figure 8.4.4 shows the predicted heat flux

augmentation using this method. The strong augmentation in the lee of the jets was still present, but the extremely high values following the jets on the pressure side were not present, which reinforces the idea that these high augmentation region were an artifact of using T_{aw} as the driving temperature. The regions under the jets still had augmentation < 1, which may indicate that this phenomenon was a result of unrealistic levels of jet detachment. On the SS there were still high levels of augmentation in the 24 < *s/d* < 30 region, but the "jet following" augmentation was eliminated. The resulting levels of augmentation were consistent with tripping the laminar boundary layer to turbulent.

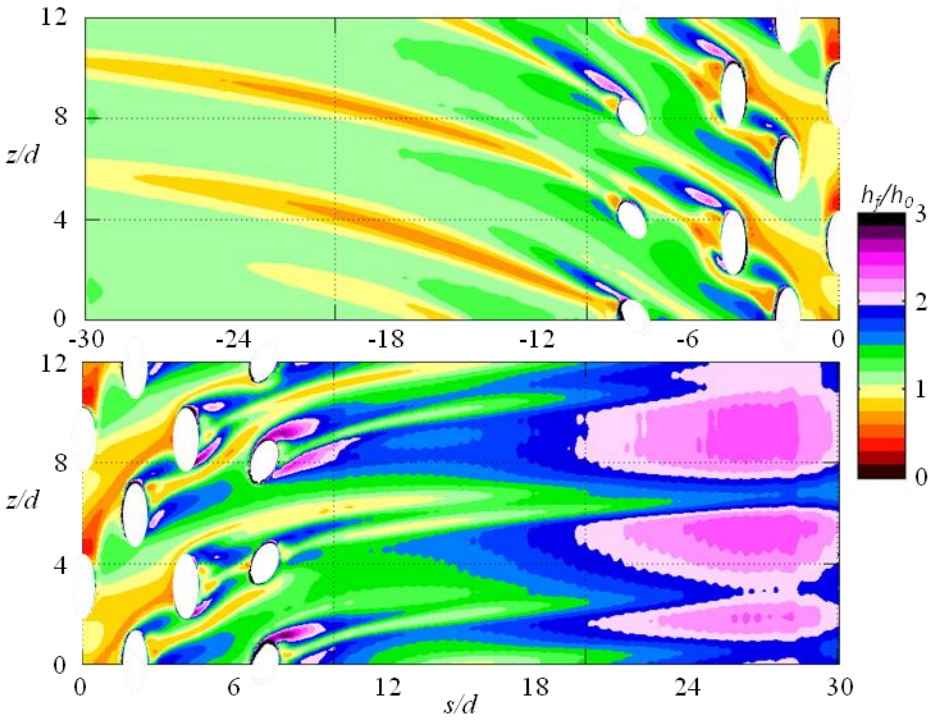

Figure 8.4.4: Heat transfer augmentation using *q"* = 1000 W/m·K and DR = 1

Chapter 9 – Turbulence Model Evaluations

A C3X vane without film cooling was modeled computationally and compared to the data of Dees et al. [64] for three locations on the PS and four locations on the SS. Figure 9.1 shows the relative positions around the vane profile and Table 9.1 depicts the exact locations in both *s/c* and *s/d*. The focus of the study was the comparison of the performance of several RANS turbulence models with respect to their prediction of the hydrodynamic and thermal boundary layer development. While previous studies have evaluated the performance of various models in terms of their capability to predict momentum boundary layer development, there was a surprising dearth of studies that investigate thermal performance. The standard k-ε and k-ω models, k-ω SST, RNG k-ε, realizable k-ε (RKE), and the Transition SST model of Menter *et al.* [106] were evaluated. The k-ω SST model used the low Reynolds number corrections, which acted as a limited transition model. Because the development of the thermal boundary layer is tied to the development of the momentum boundary layer, the performance of each model for predicting mean and RMS velocity profiles was also investigated. The models were evaluated for high (Tu = 20%) and low (Tu= 0.5%) mainstream turbulence. Note that while the experimental measurements were collected for a realistic vane surface temperature profile, the simulations imposed a constant wall heat flux.

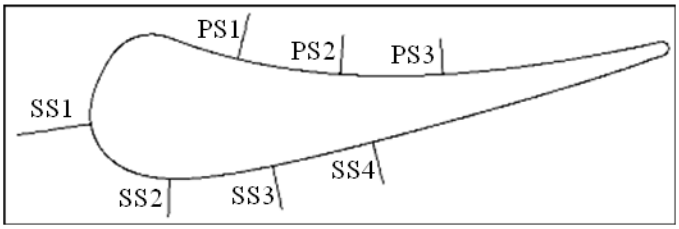

Figure 9.1: Locations on the C3X measured by Dees *et al.* [64]

Table 9.1: Measured positions on the vane in *s/c* and *s/d*

Position	*s/c*	*s/d*
PS1	-0.19	-16
PS2	-0.38	-31
PS3	-0.57	-47
SS1	0.19	16
SS2	0.38	31
SS3	0.57	47
SS4	0.75	63

9.1. Low mainstream turbulence

A well-known limitation of the standard *k-ω* model is its sensitivity to turbulence conditions in the freestream [107]. Therefore the standard *k-ω* model could not make useful predictions for the *Tu* = 0.5% case because it would produce unreasonable turbulence conditions even far from the wall. The standard *k-ε* model produced spurious turbulence generation in the passage, so it was not used for this condition either. This turbulence generation was not expected behavior for the *k-ε* model. Because of this unusual behavior, an investigation

using a simple channel flow model was performed. The mainstream turbulence generation was not observed for the standard k-ε model, so the generation was likely case dependent, but investigation into the cause was inconclusive.

Dees *et al*. [64] showed that all the PS locations and SS1 and SS2 were laminar for the low *Tu* condition. The location of transition can be seen clearly in Fig. 9.1.1, which shows measurements of *Nu* made by Dees *et al.* [30] in a prior study on the same vane. Note that the pressure side was laminar because acceleration prevented transition to a turbulent boundary layer. Therefore, even the "fully turbulent" k-ε models could potentially predict reasonable velocity profiles because all models start with a laminar profile, though the turbulent kinetic energy was far too high (shown later), which was not consistent with the laminar profile shape. Figure 9.1.1 also shows the relative performance of the turbulence models for predicting h_0. On the PS, all the turbulence models over-predicted the heat transfer, which was possibly due to the over-prediction of the strength of the Taylor-Görtler vortices (see Fig. 6.1.2.1). Dees *et al.* [108], who used the standard k-ω with a production limiter and the k-ω SST model with an unspecified "γ-θ" transition model to simulate a complete vane, did not show over-prediction in this region. However, Navarro-Martinez and Tutty [109] showed that the Taylor-Görtler vortices occupy most of the boundary layer thickness, so the thin prism layer (*i.e.*, prism layer thickness < boundary layer thickness) used by Dees *et al.* could have inhibited the formation of these structures. Navarro-Martinez and Tutty also noted that numerically generated vortices would not necessarily be expected to match those found in an

experiment because the factors which govern the wavelength (and therefore the strength of the span-wise variation) of Taylor-Görtler vortices may depend on many factors including imperfections in the leading edge and wind tunnel specifications. The SST models were the closest to matching the experimental data on the PS, but they over-predicted by over 40%.

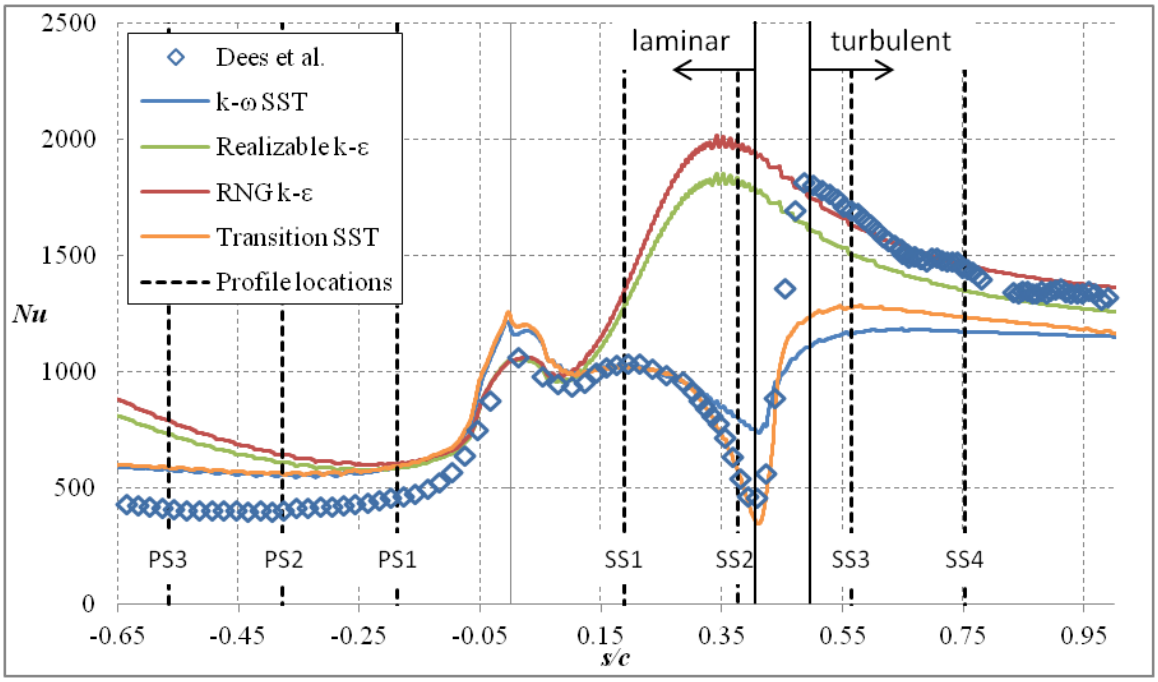

Figure 9.1.1: Heat transfer predictions compared to the experimental data of Dees *et al.* [30] for *Tu* = 0.5%

In the leading edge region (-0.05 < *s/c* < 0.05) the *k-ε* models were the best – both predicting *Nu* almost exactly – while the *k-ω* models over-predicted *Nu* by about 10%, which shows that at least initially the "fully turbulent" models may have matched the experimental boundary layer. For *s/c* > 0.1 however, the *k-ε* models diverge because they lacked any sort of transition model, as

expected. The *k-ω* SST model made use of Wilcox's [110] low *Re* corrections to the model constants, which matched *Nu* very well until *s/c* = 0.35. The Transition SST model matched the experimental data almost exactly all the way up to transition at *s/c* = 0.41. After transition, the *k-ω* models did not accurately capture the level of augmentation from the turbulent boundary layer, under-predicting by over 20%. The previously discussed work of Dees *et al.* [108] showed a similar under-prediction of the heat transfer coefficient for this region of the C3X vane. Menter *et al.* [111] – the originators of Transition SST – showed a similar under-prediction of h_0 downstream of transition on a compressor blade using low mainstream turbulence. However, they also showed a dramatic over-prediction for a higher mainstream turbulence case. Given a turbulent boundary layer, the *k-ε* models matched well, with the RNG *k-ε* model matching the experimental data almost exactly.

One would expect that the widely varying performance downstream of transition would carry over to prediction of the wall shear. For the SS3 and SS4 positions it was possible to determine shear velocity using the Clauser method. It was found that u_τ = 1.13 and 1.11 m/s for the SS3 and SS4 positions, respectively. The computational models uniformly near approximately 0.90 m/s – despite differences of over 20% for *Nu* – and in fact the best match was from Transition SST, one of the worst performers for *Nu*. The ratios of the computational to experimental measurements of u_τ are given in Table 9.1.4.1.

Table 9.1.4.1: Ratio of computational to experimental values of u_τ for Tu = 0.5%

Position	*k-ω* SST	RKE	RNG *k-ε*	Transition SST
SS3	0.78	0.79	0.80	0.84
SS4	0.78	0.78	0.78	0.81

9.1.1. Pressure side performance

Figure 9.1.1.1 shows the mean velocity profiles for the PS1 position. All the models performed reasonably well. Interestingly, this was true even for the fully turbulent *k-ε* models that are not generally recommended for use where laminar profiles exist. In fact, a simulation run using a laminar solution matched the *k-ω* models exactly. This would indicate that the turbulence models were not producing any turbulence in the boundary layer, but this was only true for the *k-ω* models (discussed later). The laminar profile matched the *k-ω* profiles for all the laminar positions (PS1-3 and SS1), so they are not shown in subsequent figures. The thermal boundary layers for PS1 (shown in Fig. 9.1.1.2) did not match as well far from the wall. The near-wall gradient for this and nearly all other cases was matched almost exactly as required by the heat flux boundary condition, but the for $y/c > 0.002$ thermal diffusion was too strong compared to the experiments, which produced much thicker boundary layers (60-90%) compared to the experiments, which had a profile that was almost exactly the same as the velocity

profile. Because the laminar profile also showed this behavior, it may be a consequence of the Taylor-Görtler vortices present in simulations.

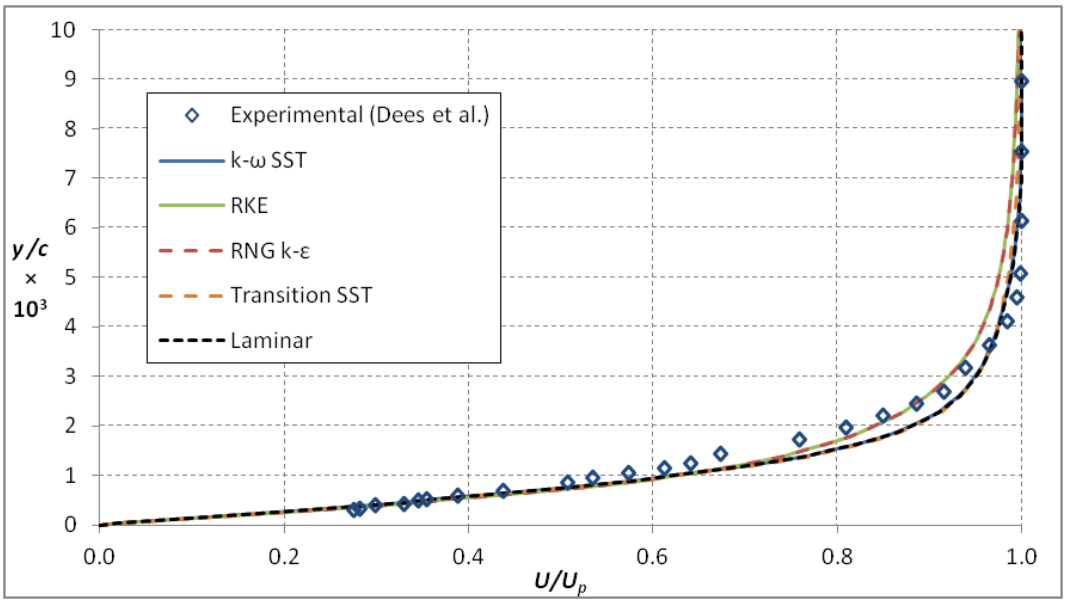

Figure 9.1.1.1: Computed mean velocity profiles at the PS1 position compared to the experimental data of Dees *et al*. [64] at *Tu* = 0.5%

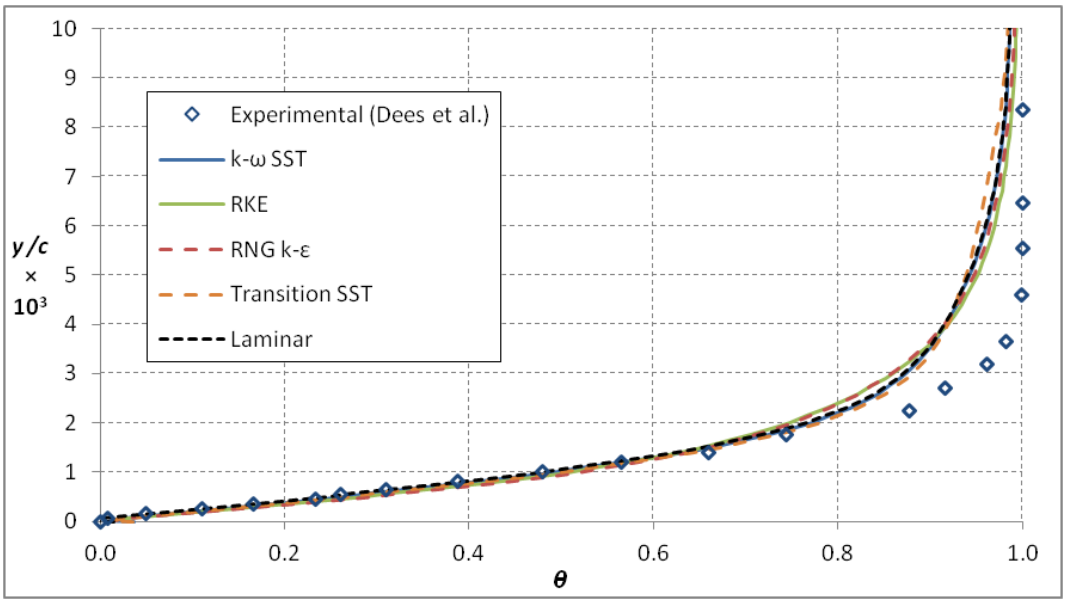

Figure 9.1.1.2: Computed thermal profiles at the PS1 position compared to the experimental data of Dees *et al*. [64] at *Tu* = 0.5%

At the PS2 position, the turbulence models had better agreement with the mean velocity profile near the wall, but diverged further from the wall, as shown in Fig. 9.1.1.3. Note that the divergence occurred far enough out for the *k-ω* models that the δ_{95} values were only off from the experimental measurements by 3%, but that δ_{99} was off by almost 100%. This emphasizes that the boundary layer thickness alone represents a poor metric for comparison. The *k-ε* models began to diverge from the experimental measurements earlier, which was consistent with turbulent kinetic energy levels that were excessively high (shown later).

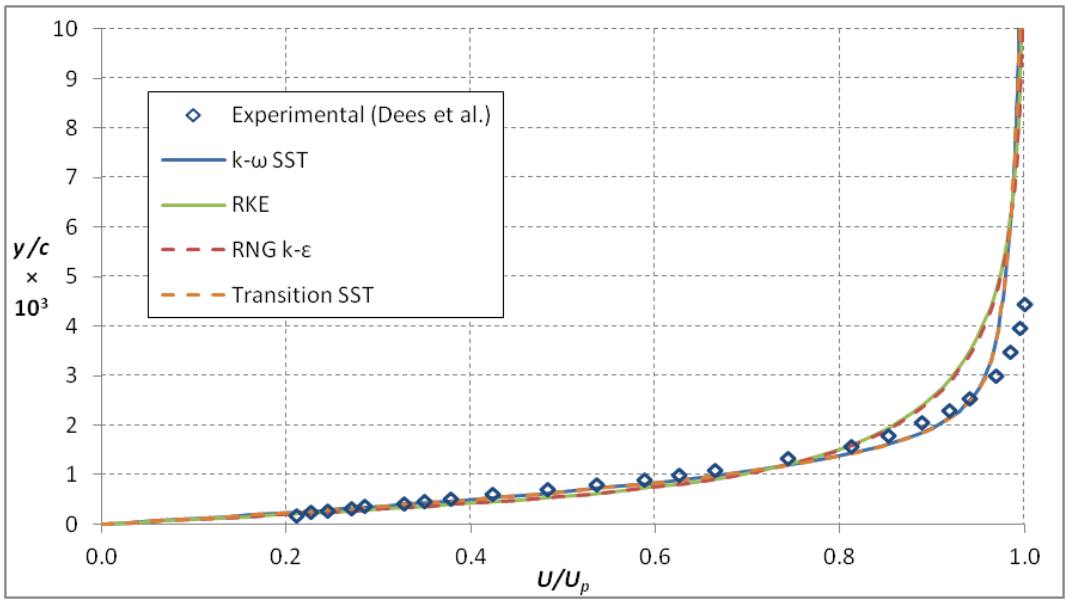

Figure 9.1.1.3: Computed mean velocity profiles at the PS2 position compared to the experimental data of Dees *et al*. [64] at *Tu* = 0.5%

The thermal profiles for PS2 are shown in Fig. 9.1.1.4. Like the PS1 position, the turbulence models had excellent agreement with the measurements for $y/c < 0.002$, but began to diverge where and over-prediction of thermal diffusion increased the rate of thermal boundary layer growth compared to the experiment. The disagreement with the experimental measurements was much worse. It should be noted that though they had similar levels of error in terms of the thermal boundary layer thickness, the *k-ω* models maintained the correct profile further from the wall.

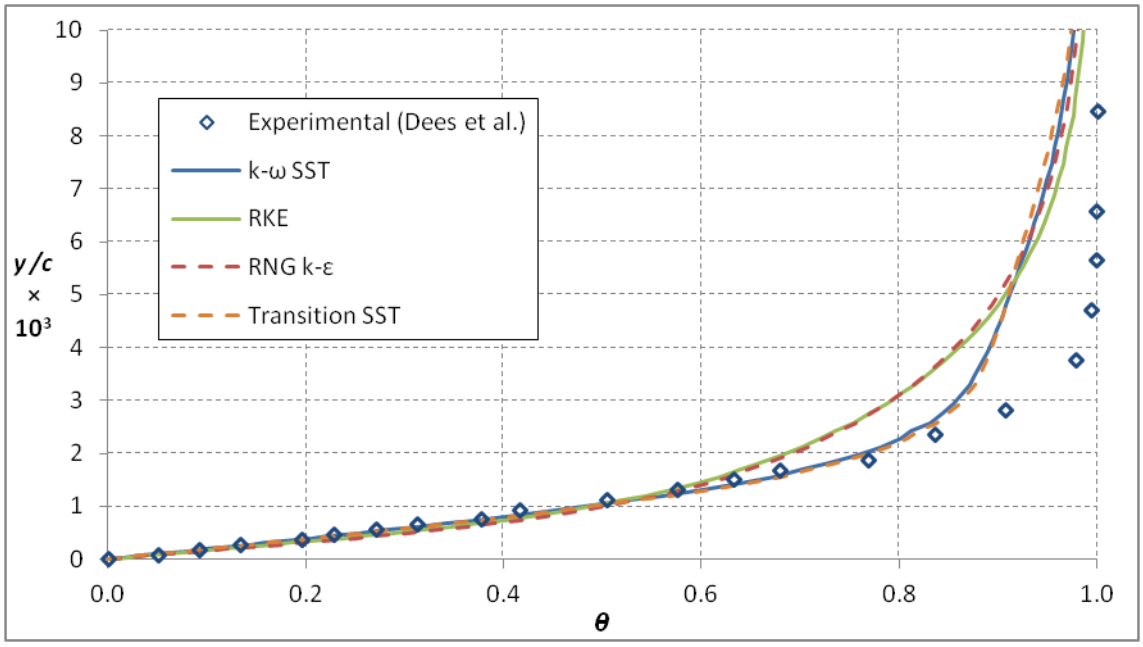

Figure 9.1.1.4: Computed thermal profiles at the PS2 position compared to the experimental data of Dees *et al*. [64] at *Tu* = 0.5%

At the PS3 position, the mean velocity profile was almost exactly predicted by the *k-ω* turbulence models, which can be seen in Fig. 9.1.1.5. For this position the prediction of the boundary layer thickness was under-predicted by 10%, like the PS1 position. The *k-ε* models showed apparent improvement over the PS2 location in terms of the mean velocity profile. Even though the velocity profile was improved, the performance for the thermal boundary layer was approximately the same as for the PS2 position, as shown in Fig. 9.1.1.6. Note that the "kink" in the thermal profile near *y/c* = 0.002 became sharper for each position.

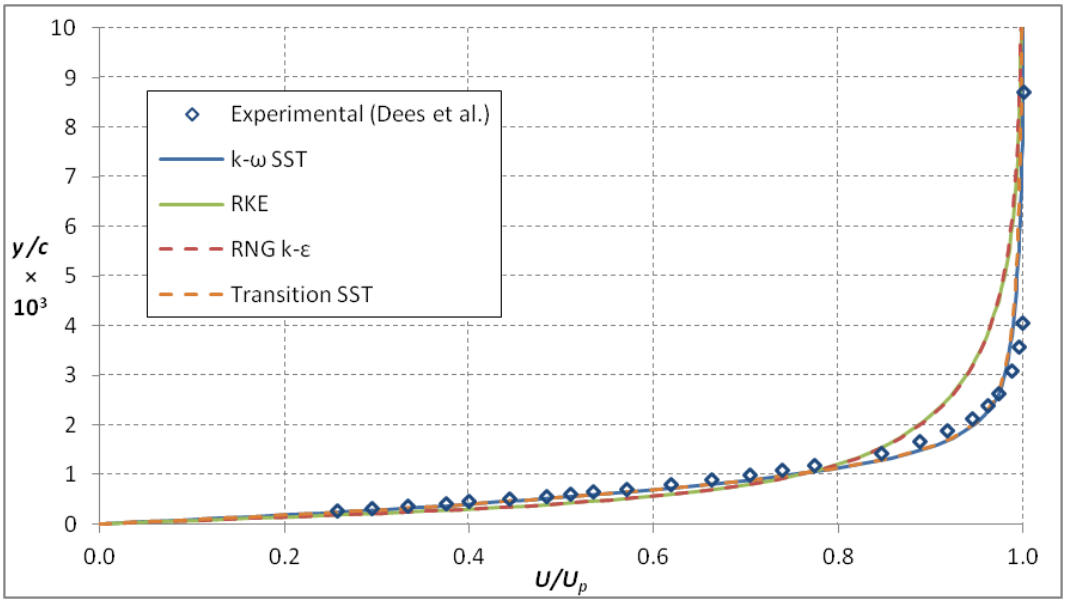

Figure 9.1.1.5: Computed mean velocity profiles at the PS3 position compared to the experimental data of Dees *et al*. [64] at *Tu* = 0.5%

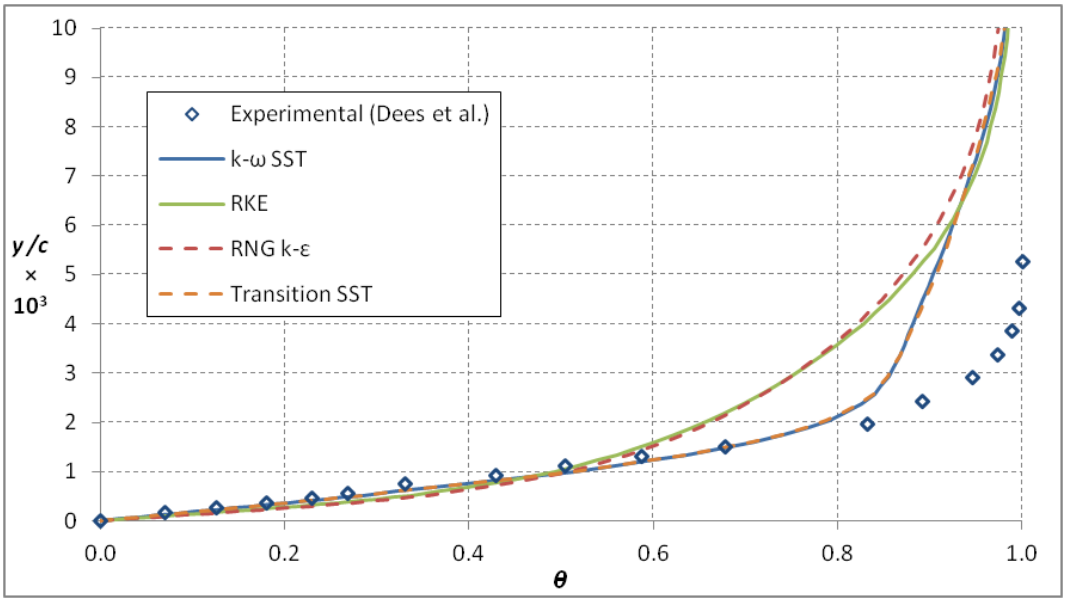

Figure 9.1.1.6: Computed thermal profiles at the PS3 position compared to the experimental data of Dees *et al*. [64] at *Tu* = 0.5%

The reason that the models were off of the measurements for the PS2 and PS3 positions may not be due to the action of Taylor-Görtler vortices. The experimental measurements showed that these structures created a 10% variation in the span-wise surface temperature difference while the turbulence models all predicted 30% or more, which shows that the turbulence models were greatly over-predicting the strength of the Taylor-Görtler vortices. However, these vortical structures should also affect the velocity profiles, which were well matched. The poor predictions for the thermal profiles were therefore more likely to stem purely from an over-prediction of thermal diffusion.

9.1.2. Suction side performance

Because the SS1 position was laminar, the performance there was similar to that which was seen at PS1. This was also one of the locations where the "fully turbulent" models were expected to produce poor predictions based on recommended practice. Figure 9.1.2.1 shows that the *k-ω* models matched the data nearly exactly for the entire boundary layer. As expected, the *k-ε* models matched less well, showing a more turbulent shape. Note that velocity profiles on the SS were nondimensionalized using the maximum velocity instead of the predicted zero viscosity line. This eliminated some ambiguity in proper selection of points for determination of the line, which was mainly an issue for the positions where $\delta_{boundary\ layer} > \delta_{prism\ layer}$.

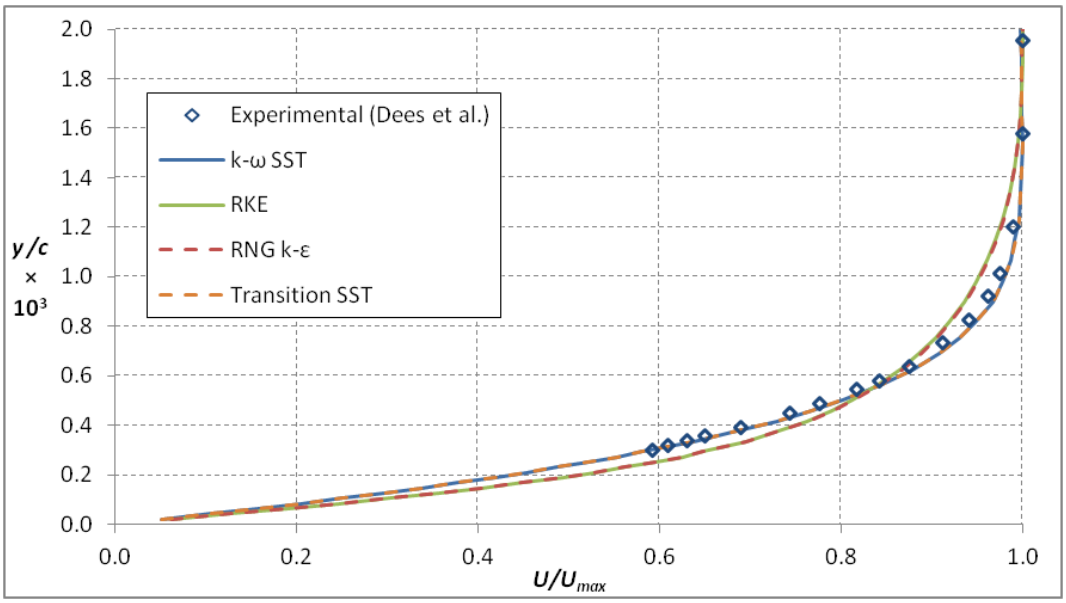

Figure 9.1.2.1: Computed mean velocity profiles at the SS1 position compared to the experimental data of Dees *et al*. [64] at *Tu* = 0.5%

Unlike the PS1 position, the thermal profiles predicted by the *k-ω* turbulence models were nearly identical to the measurements, which can be seen in Fig. 9.1.2.2. The estimates for δ_{95T} were within experimental uncertainty at only 5% high. The *k-ε* models were not as well matched; though given that they were not expected to perform particularly well, a ~ 30% miss on the thickness was reasonable.

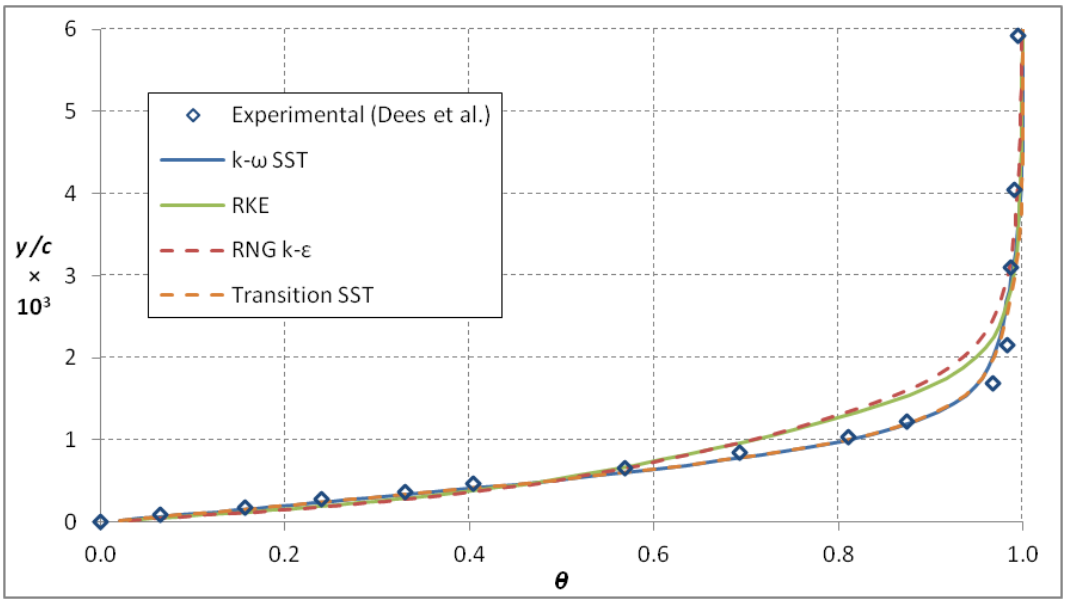

Figure 9.1.2.2: Computed thermal profiles at the SS1 position compared to the experimental data of Dees *et al*. [64] at *Tu* = 0.5%

An interesting feature of the thermal boundary layer at SS1 was that it was nearly twice as thick as the momentum boundary layer. Figure 9.1.2.3 shows this more clearly by directly comparing the thermal and velocity profiles. This was because of the fact that under prolonged acceleration the suppression of the hydrodynamic boundary layer by pressure gradients (which do not affect the thermal field) creates a region where thermal diffusion is the dominant means of transport. This region ($\delta_T > y > \delta$) was coined the "thermal superlayer" by Launder and Lockwood [111], who hypothesized that it should exist based on a theoretical analysis. Subsequent measurements by Kays *et al.* [112] proved its existence. Because regions of high acceleration exhibit a thicker thermal boundary layer, the heat transfer coefficient is reduced compared to a zero pressure gradient reference. Refined versions of Launder and Lockwood's

integral analysis have been used to successfully predict this reduction in heat transfer coefficient on highly accelerated portions of an airfoil (*e.g.*, [113]). The action of the thermal superlayer was clearly captured even by the turbulence models that did not match the laminar result because they produced thermal boundary layers much thicker than the hydrodynamic boundary layers.

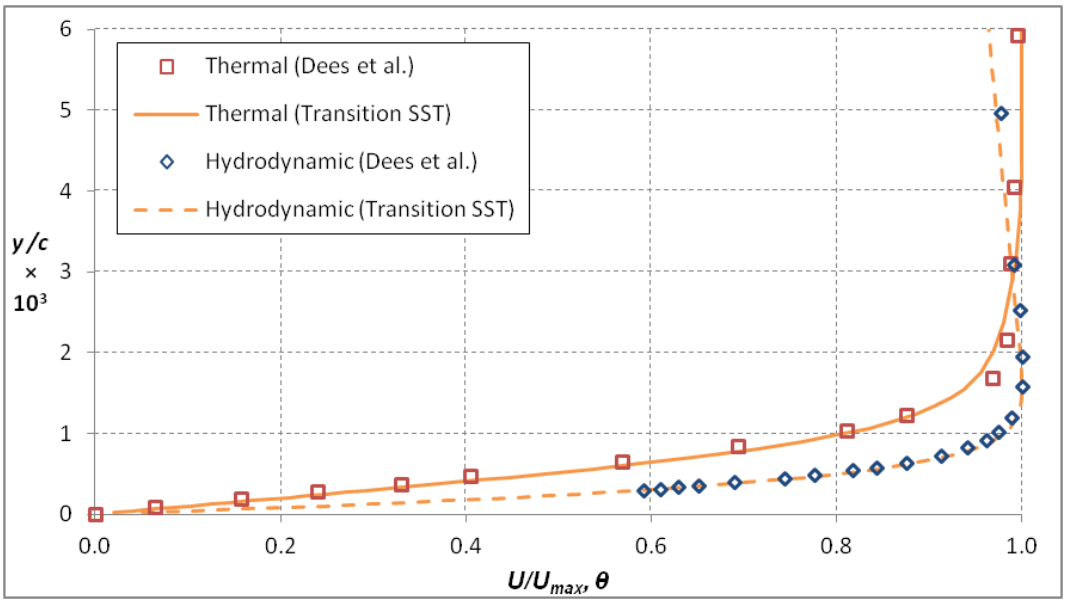

Figure 9.1.2.3: Comparison of the mean velocity and thermal profiles at the SS1 position at *Tu* = 0.5%

At the SS2 position the measurements indicated that the boundary layer was still laminar. However, the velocity profiles predicted by the turbulence models were very far from the measurements, as shown in Fig. 9.1.2.4. The poor performances for the *k-ε* models were expected, because at this position they were predicting a fully turbulent boundary layer flow (Fig. 9.1.1 shows that the *k-ε* models had completed transition). The shape of the Transition SST profile

indicates that it was predicting a much stronger impact of the adverse pressure gradient than was seen experimentally.

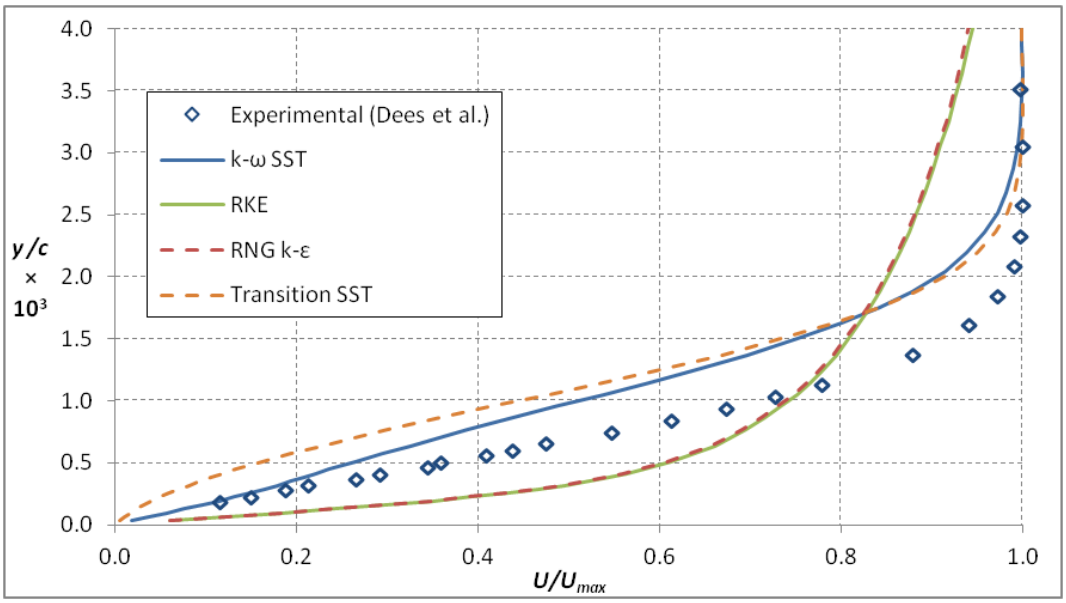

Figure 9.1.2.4: Computed mean velocity profiles at the SS2 position compared to the experimental data of Dees *et al*. [64] at *Tu* = 0.5%

Even though the velocity profiles were substantially off from the measurements, the thermal profiles predicted by the *k-ω* models were matched extremely well. The Transition SST model was within experimental uncertainty for δ_{95T} (6% over), while k-ω SST over-predicted only 11%. The thermal profiles predicted by the *k-ε* models were similar to the velocity profiles at this position. Note that this position was the only location where the near-wall thermal gradient was substantially different from the experiment for any model. This was due to a very large difference in T_w between the various cases; *dT/dy* was still matched as required by the heat flux boundary condition. Like the SS1 position, the thermal

boundary layer was thicker than the velocity boundary layer, but less so than at SS1. All the turbulence models successfully captured this trend.

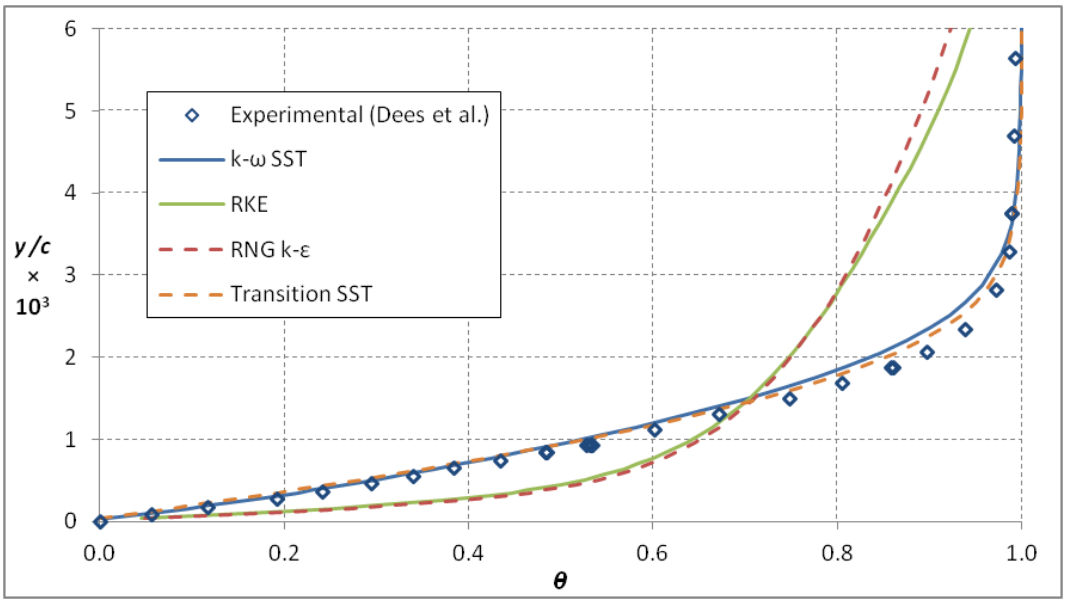

Figure 9.1.2.5: Computed thermal profiles at the SS2 position compared to the experimental data of Dees *et al*. [64] at *Tu* = 0.5%

After transition, none of the models predicted the velocity distribution very well. Figure 9.1.2.6 shows the mean velocity profiles for the SS3 position. The *k-ω* models produced very oddly shaped velocity profiles not representative of a turbulent profile. The reasons for this shape were not clear and similar problems have not been reported before (Dees *et al.* included a simulation using *k-ω* SST which did not have this difficulty, though their profile was an order of magnitude thicker). Even with this unusual shape, the *k-ω* models were actually within experimental uncertainty of the correct δ_{95} (7% low), once again highlighting the problem with using boundary layer thickness as a metric for comparison. The *k-ε*

models continued to predict boundary layers far thicker than the measurements because their early prediction of transition meant that the boundary layer had much more development length.

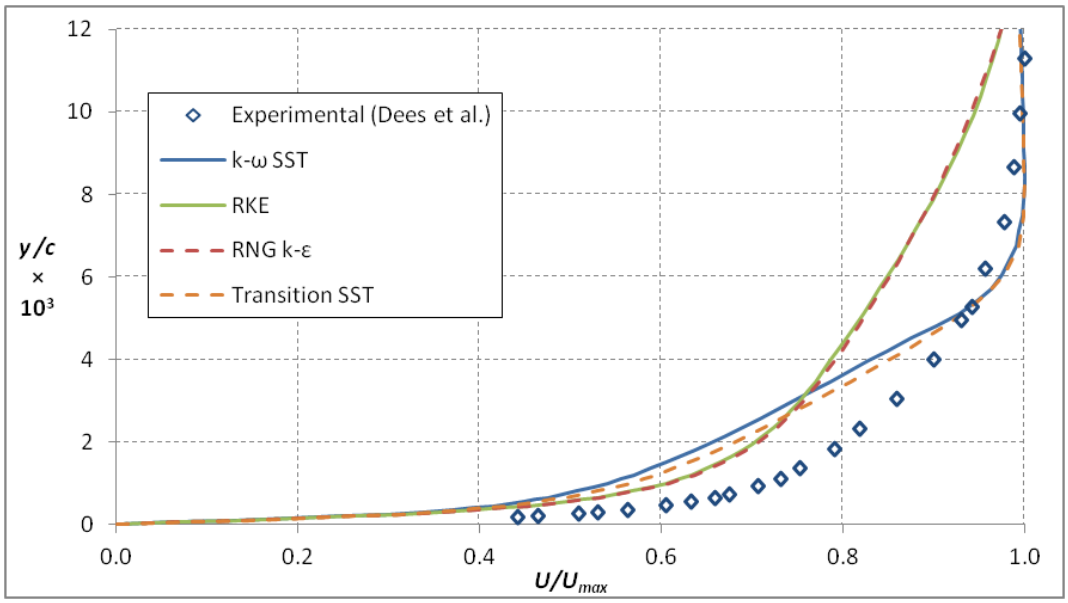

Figure 9.1.2.6: Computed mean velocity profiles at the SS3 position compared to the experimental data of Dees *et al*. [64] at *Tu* = 0.5%

The corresponding thermal profiles for the *k-ε* models were near the experiment, as shown in Fig. 9.1.2.7. The RKE model matched particularly well for $y/c > 0.004$, producing a predicted δ_{95T} within experimental uncertainty. The *k-ω* models both produced very unrealistic profiles with shapes informed by the velocity profile and thermal boundary layer thicknesses under-predicted by 40% or more. At this position there was also the first evidence that the prism layer used was not thick enough to capture the whole boundary layer. It ended at *y/c* =

0.012, where the *k-ε* models both show a slight kink as the mesh transitioned from prisms to tetrahedral elements.

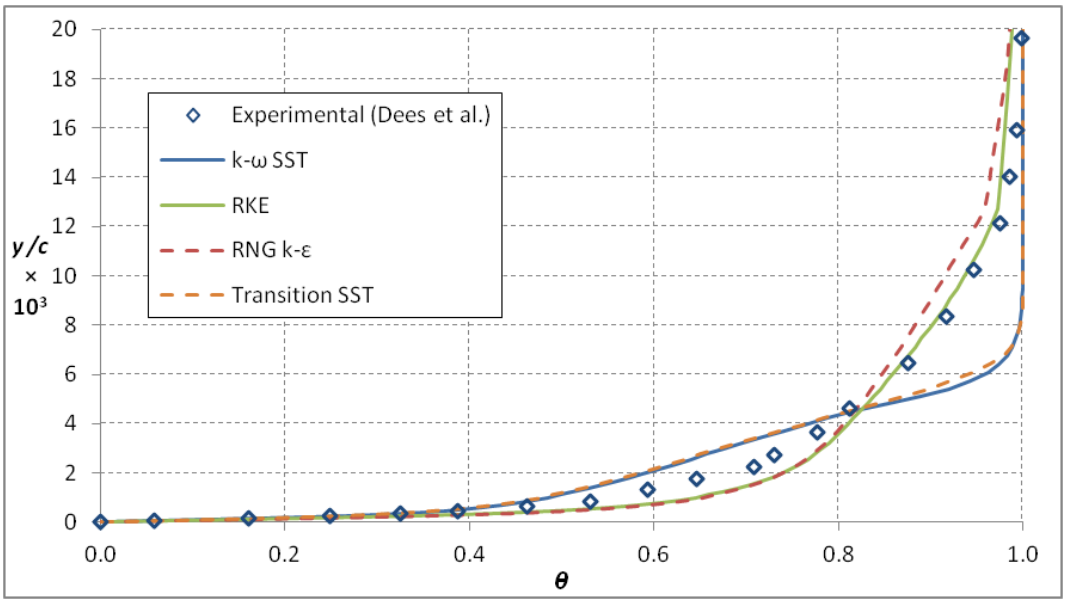

Figure 9.1.2.7: Computed thermal profiles at the SS3 position compared to the experimental data of Dees *et al*. [64] at *Tu* = 0.5%

At the farthest downstream position the velocity boundary layer was thick enough that the predicted velocity profiles were expected to be affected by the transition from prisms to tetrahedral elements. The *k-ε* models did show a kink in the profile at *y/c* = 0.012, but the *k-ω* models were both still predicting a boundary layer thinner than 6.6 mm, so they were unaffected. Figure 9.1.2.8 shows that the prism to tetrahedral transition had little effect on the overall boundary layer shape, which was too thick for the *k-ε* models (40%) and too thin for the *k-ω* models (20%). The performance for the corresponding thermal profiles (shown in

Fig. 9.1.2.9) was similar to the SS3 position, but the *k-ε* models were further off from the measurements.

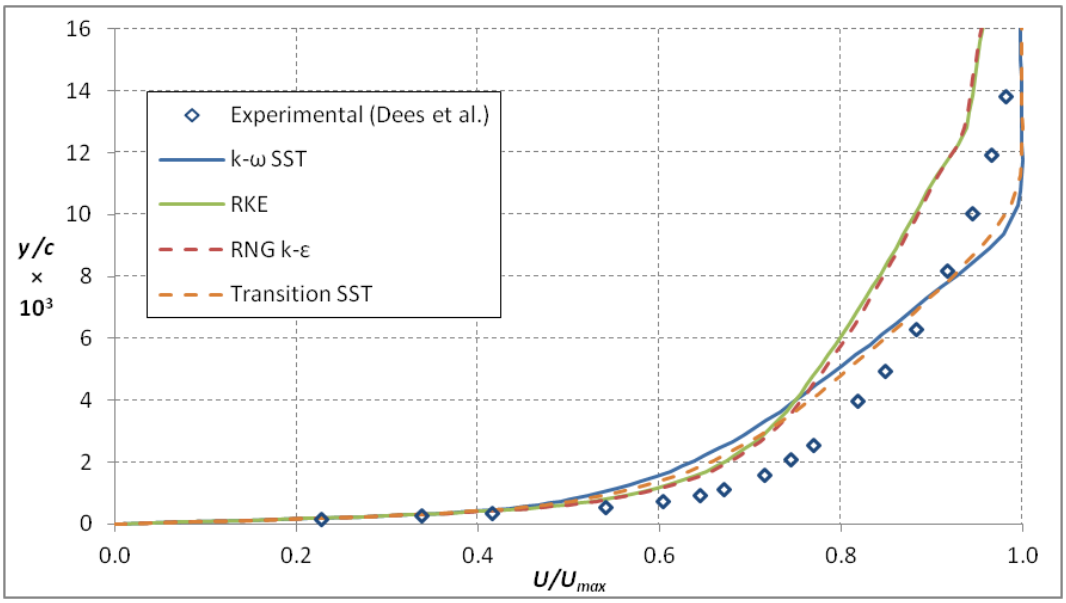

Figure 9.1.2.8: Computed mean velocity profiles at the SS4 position compared to the experimental data of Dees *et al*. [64] at *Tu* = 0.5%

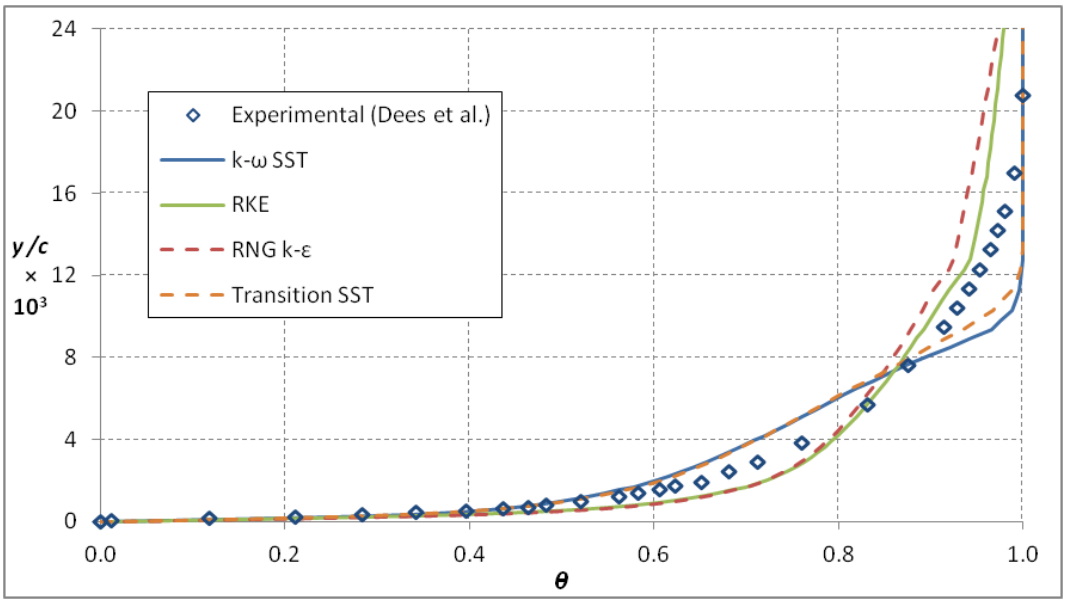

Figure 9.1.2.9: Computed thermal profiles at the SS4 position compared to the experimental data of Dees *et al*. [64] at *Tu* = 0.5%

9.1.3. Velocity and thermal performance summary

Though it was repeatedly shown that a well matched boundary layer thickness did not necessarily mean that the velocity or thermal profile had been well matched, δ_{95} still serves as a convenient means of summarizing the performance of the models. Table 9.1.3.1 shows the experimentally measured values of δ_{95} and δ_{95T}, while Tables 9.1.3.2 and 9.1.3.3 show the ratio of the computationally predicted thickness to the experimental values (*i.e.*, $\delta_{95,\text{computed}}/\delta_{95,\text{measured}}$) for the hydrodynamic and thermal boundary layers, respectively.

Table 9.1.3.1: Thermal and momentum boundary layer thicknesses measured by Dees *et al.* [64] for Tu = 0.5%

Position	δ_{95} (mm)	δ_{95T} (mm)
PS1	1.80	1.64
PS2	1.40	1.80
PS3	1.20	1.60
SS1	0.49	0.85
SS2	0.90	1.34
SS3	3.09	5.56
SS4	5.58	6.40

Table 9.1.3.2: Ratio of computational to experimental values of δ_{95} for Tu = 0.5%

Position	*k-ω* SST	RKE	RNG *k-ε*	Transition SST
PS1	0.89	1.10	1.10	0.88
PS2	1.03	1.45	1.42	1.03
PS3	0.90	1.49	1.48	0.91
SS1	0.89	1.07	1.06	0.89
SS2	1.36	2.47	2.58	1.30
SS3	0.94	1.77	1.80	0.93
SS4	0.81	1.41	1.44	0.84

Table 9.1.3.3: Ratio of computational to experimental values of δ_{95T} for Tu = 0.5%

Position	*k-ω* SST	RKE	RNG *k-ε*	Transition SST
PS1	1.73	1.60	1.66	1.88
PS2	2.12	1.93	2.06	2.26
PS3	2.44	2.36	2.61	2.48
SS1	1.04	1.25	1.36	1.05
SS2	1.11	2.48	2.84	1.06
SS3	0.56	1.04	1.16	0.59
SS4	0.75	1.18	1.51	0.81

The average deviations from 1.0 (*i.e.*, a perfect prediction) show that for the hydrodynamic boundary layer the Transition SST was the best in terms of the boundary layer thickness, with an average of only 13% error. The *k-ω* SST model was close behind, with only 14% average error. The *k-ε* models performed much worse on average, with 54 and 55% average error for the RKE and RNG *k-ε* models, respectively. Once again, the poor performance from the "fully turbulent" models was not unexpected, and in part their overall score was skewed by the extremely poor performance at the SS2 position and the fact that a longer development length meant that boundary layers on the suction side would always be thicker than the measurements. The same analysis for the thermal boundary layers shows that no model did particularly well, with the best performance

coming from the *k-ω* SST model at 59% average error. The remaining models had 62, 69, and 88% average error from the Transition SST, RKE, and RNG *k-ε*, respectively. Performance was typically much worse on the pressure side compared to the suction side, with thermal boundary layers over twice the thickness of the experimentally measured profiles.

9.1.4. Kinetic energy predictions

Another metric often used to compare the performance of various turbulence models is their ability to predict the correct profile for the turbulent kinetic energy off-the-wall. Dees *et al.* [64] also reported u_{rms} profiles for the same positions where velocity and temperature were measured. These data were converted to measurements of turbulent kinetic energy using a procedure described in section 6.4.

Even for laminar profiles such as PS1, there was a low level of turbulence in the boundary layer very near the wall, as shown in Fig. 9.1.4.1. This was attributed to the low level freestream turbulence penetrating to the wall. The *k-ω* turbulence models greatly over-predicted the turbulence present in the freestream, but performed very well in comparison to the *k-ε* models, which are visible in Fig. 9.1.4.2 because it makes use of a much larger $k/U_{w,p}^2$ axis. The over-prediction in the boundary layer was expected given that the *k-ε* models were “fully turbulent”; however, the fact that the *k-ε* models were predicting ~ 5% turbulence in the freestream was entirely unrealistic (measurements had ~ 0.5% and the *k-ω* models ~ 0.7%). Also note that the data were normalized based on $U_{w,p}^2$ (the predicted inviscid velocity at the wall) instead of the more common u_τ^2;

it was not possible to compute experimental values of u_τ because there was no clearly defined log region for the laminar positions.

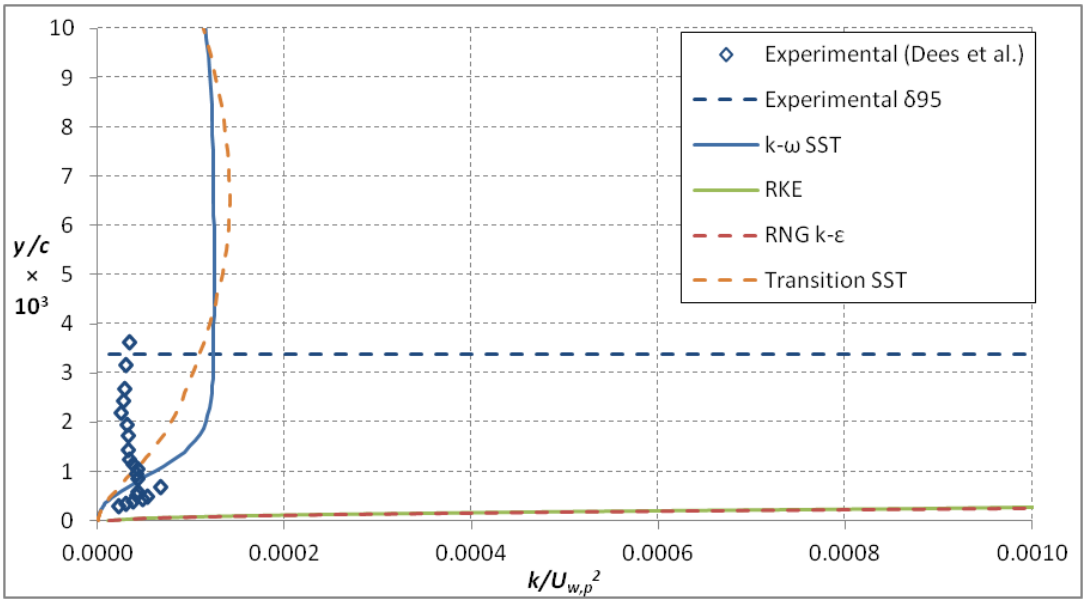

Figure 9.1.4.1: Computed turbulent kinetic energy profiles at the PS1 position compared to the experimental data of Dees *et al*. [64] at *Tu* = 0.5%

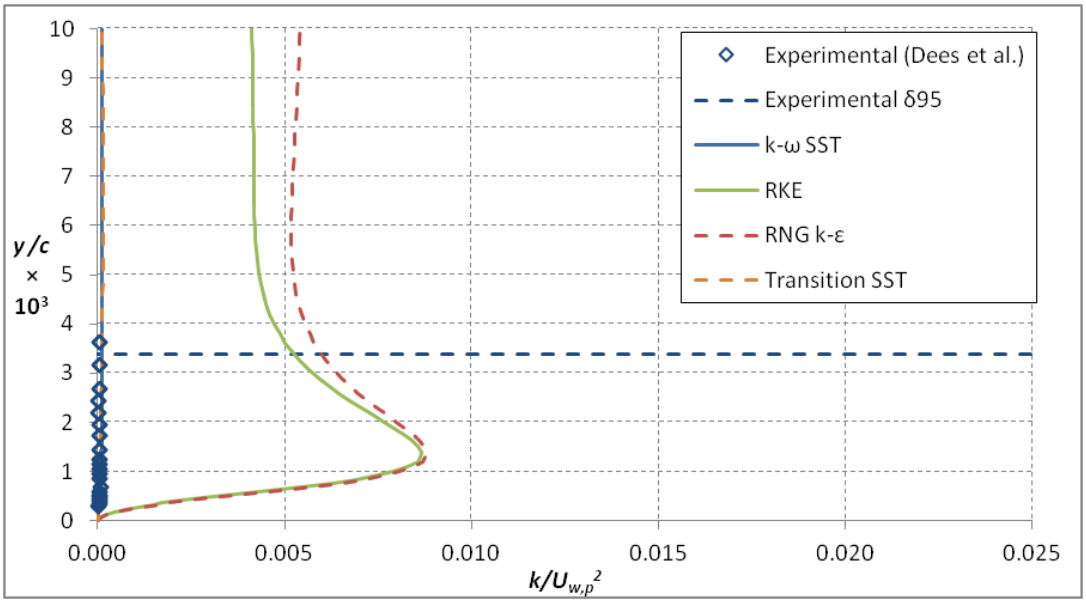

Figure 9.1.4.2: Computed turbulent kinetic energy profiles at the PS1 position compared to the experimental data of Dees *et al*. [64] at *Tu* = 0.5% with a large *x* scale

Turbulence levels increased slightly at the PS2 position, which was not captured by the *k-ω* models. As shown in Fig. 9.1.4.3, while the *k-ω* did predict that absolute levels of *k* increased at this position, the local $U_{w,p}$ increased more quickly. The result was $k/U_{w,p}^2$ values that were actually nearer the experimental values. Figure 9.1.4.4 shows that this performance trend continued at PS3. At both positions the *k-ε* models are not visible because these models predicted fully turbulent levels of *k* in the boundary layer. It should be noted though that the experimentally measured near-wall *k* peak was reproduced only by the *k-ε* models.

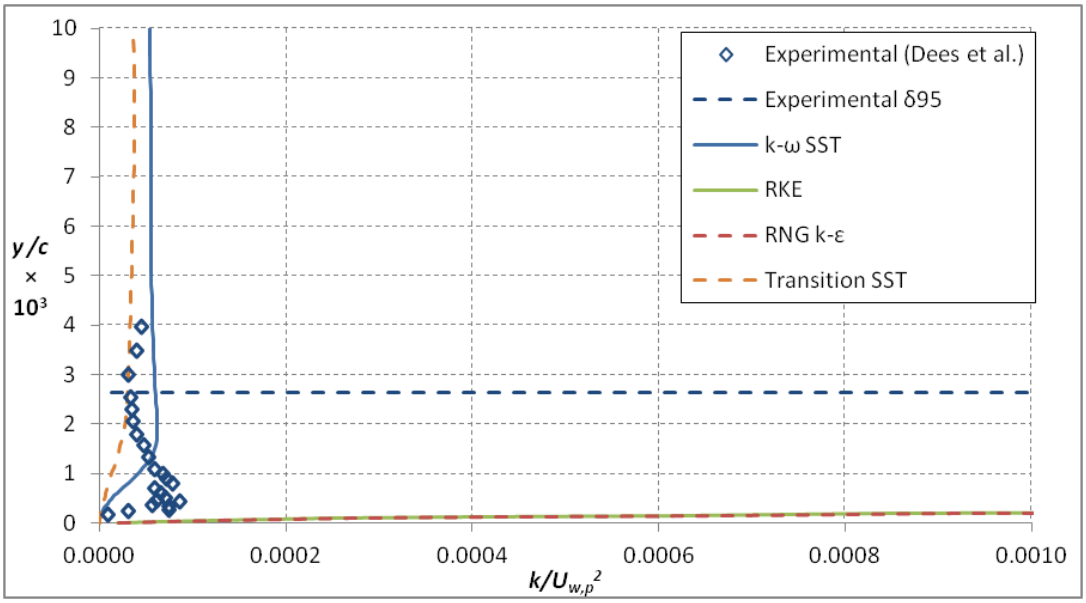

Figure 9.1.4.3: Computed turbulent kinetic energy profiles at the PS2 position compared to the experimental data of Dees *et al*. [64] at *Tu* = 0.5%

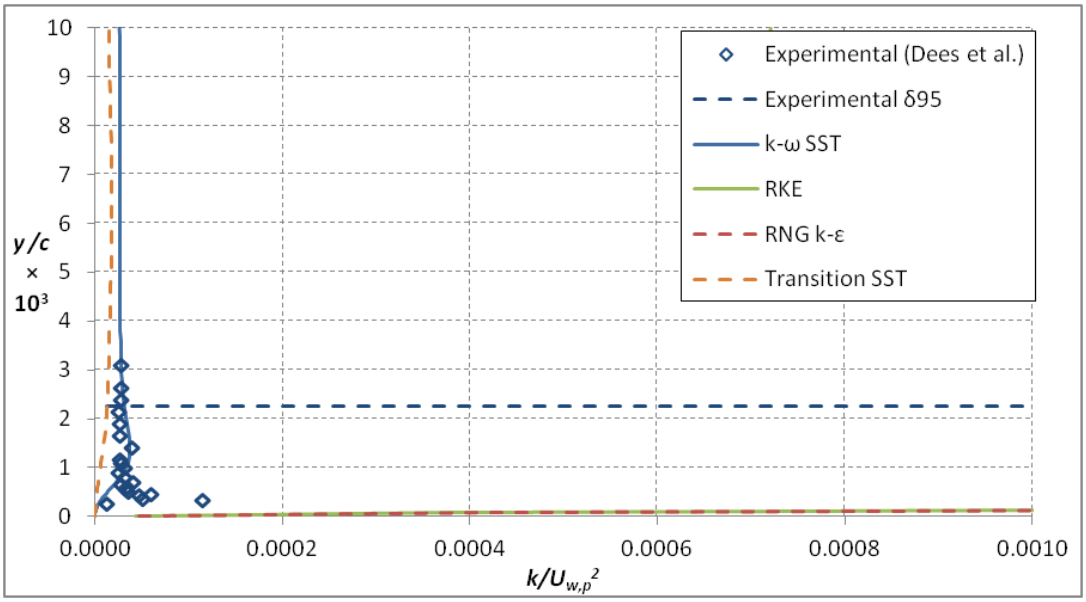

Figure 9.1.4.4: Computed turbulent kinetic energy profiles at the PS3 position compared to the experimental data of Dees *et al*. [64] at *Tu* = 0.5%

The performance of the models at SS1 was similar to that on the PS, which can be seen in Fig. 9.1.4.5. Here, the *k-ω* SST model matched the turbulence levels exactly for *y/c* > 0.0004.

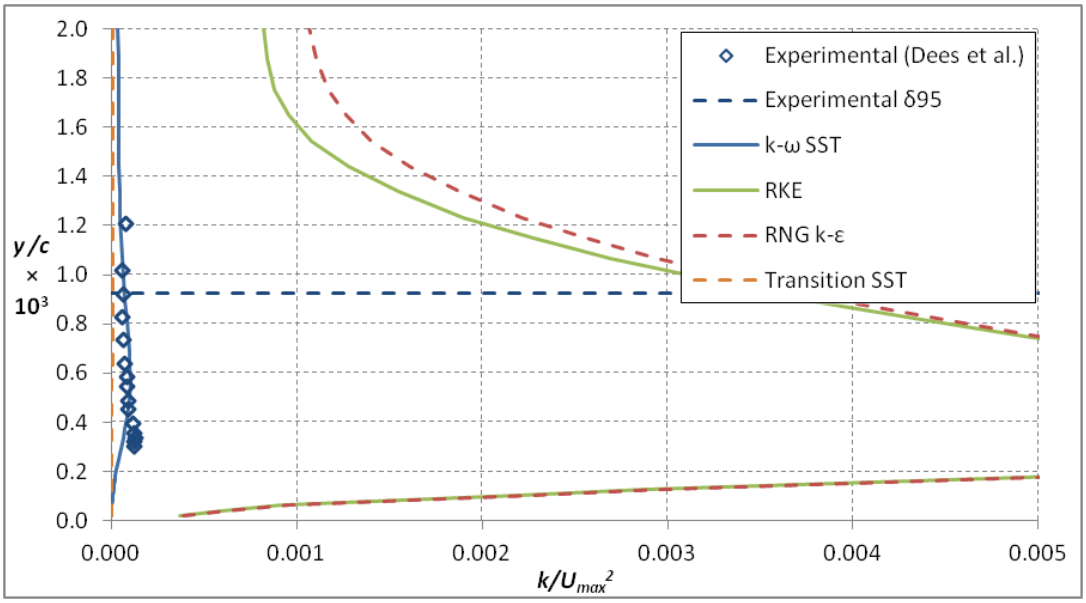

Figure 9.1.4.5: Computed turbulent kinetic energy profiles at the SS1 position compared to the experimental data of Dees *et al*. [64] at *Tu* = 0.5%

While the velocity profile at SS2 was still laminar, the increasing turbulence levels shown in Fig. 9.1.4.6 indicated that the onset of transition was not far away. Interestingly, the Transition SST model continued to predict essentially no near-wall turbulence even though it correctly predicted the location of transition. The *k-ω* SST model matched the experimental data well.

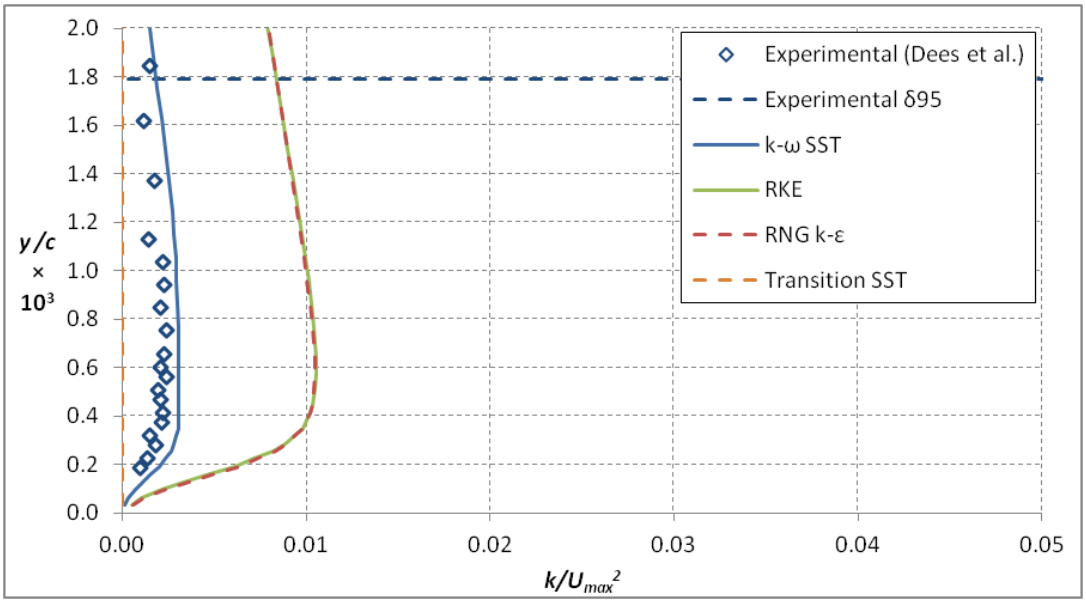

Figure 9.1.4.6: Computed turbulent kinetic energy profiles at the SS2 position compared to the experimental data of Dees *et al*. [64] at *Tu* = 0.5%

The fully turbulent profile at SS3 had two notable features: the near-wall peak and a broad region before turbulence levels fall off to freestream values. The experimental near wall peak was lower than the generally accepted value because hot wire measurements have difficult measuring the very fine scale turbulence very close to the wall. However, this should only affect the data for $y/c < 0.002$ (increasing effect closer to the wall). Figure 9.1.4.7 shows that the *k-ε* models, which matched the mean velocity profile better (Fig. 9.1.2.6), did not predict the correct shape for the *k* distribution. In contrast, the *k-ω* SST model, which predicted a very thin, oddly shaped boundary layer, predicted both features correctly even if the absolute levels were too high. The Transition SST model did not predict a near-wall peak. Performance at the SS4 position was very similar, as shown in Fig. 9.1.4.8.

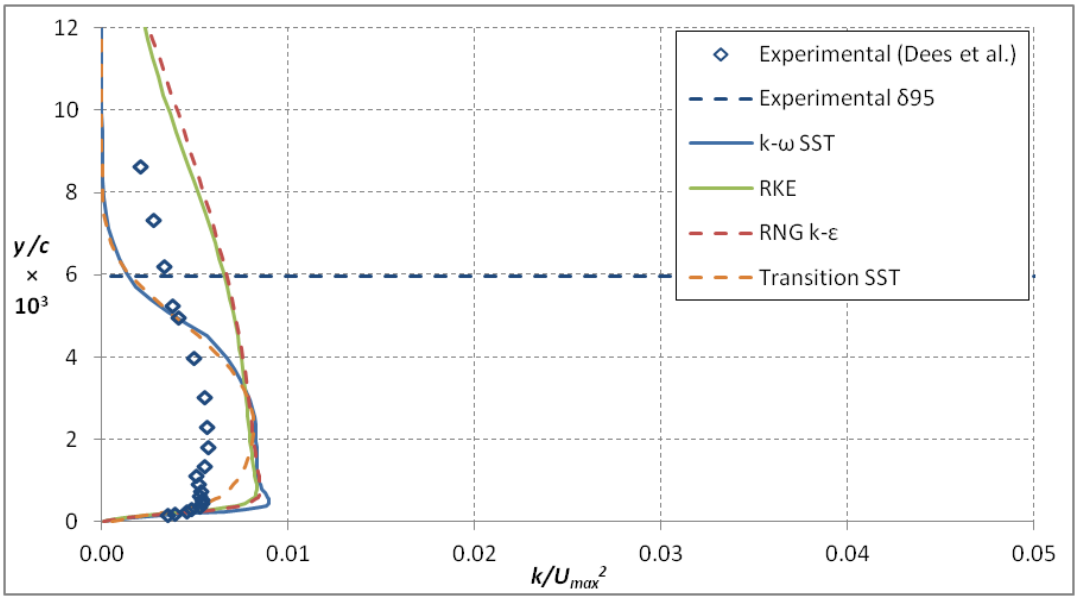

Figure 9.1.4.7: Computed turbulent kinetic energy profiles at the SS3 position compared to the experimental data of Dees *et al*. [64] at *Tu* = 0.5%

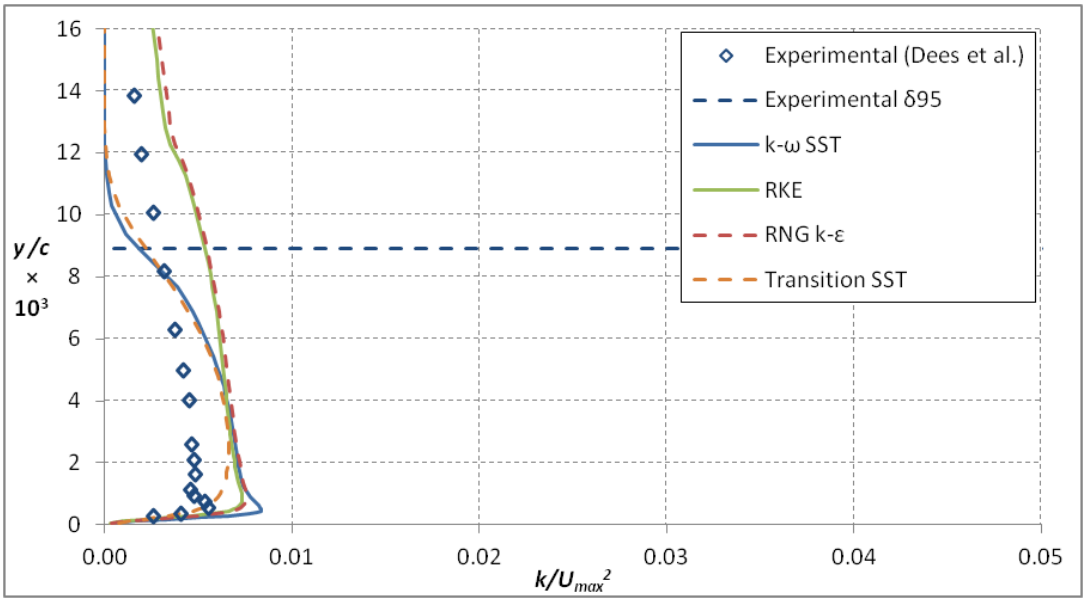

Figure 9.1.4.8: Computed turbulent kinetic energy profiles at the SS4 position compared to the experimental data of Dees *et al*. [64] at *Tu* = 0.5%

It should be noted that the broad region of nearly constant k was not something seen in the flat plate zero pressure gradient boundary layer that was used to convert the experimental data from u_{rms} to k. Figure 9.1.4.9 shows a comparison to the literature using the more conventional k/u_τ^2 scaling. The broadening of the higher k region was a result of the upstream pressure gradients.

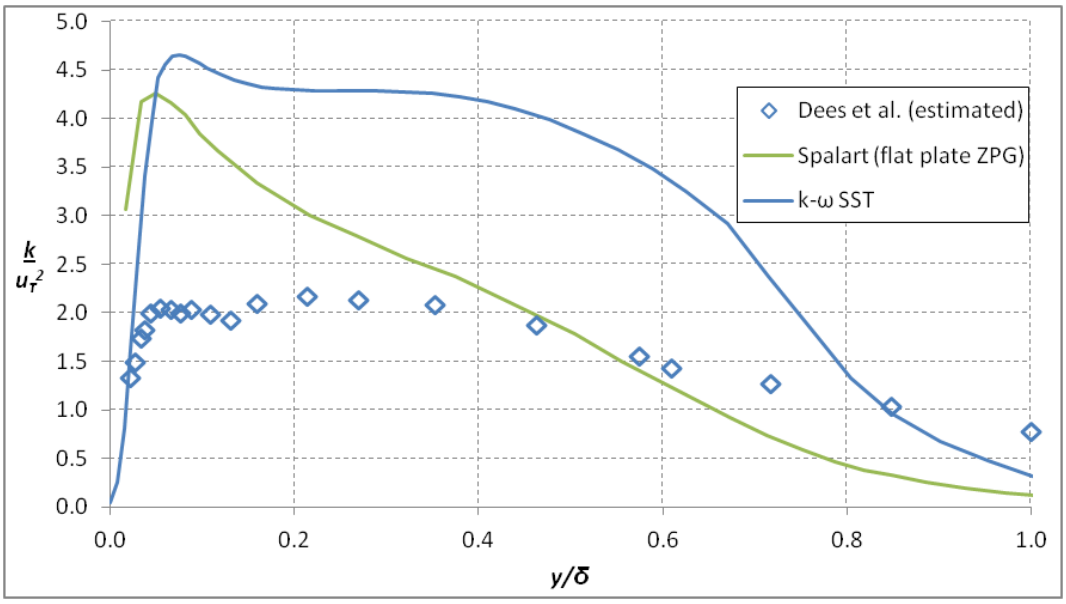

Figure 9.1.4.9: Turbulent kinetic energy compared to the DNS data of Spalart [101] using the conventional u_τ^2 nondimensionalization at SS3

9.2. High mainstream turbulence

Increased levels of mainstream turbulence promoted larger heat transfer coefficients over most of the vane surface, as shown in Fig. 9.2.1, which compares the Tu = 0.5 and 20% conditions. The turbulence models all captured

the increased level of heat transfer coefficient, though to differing degrees. Downstream of transition, mainstream turbulence levels had no impact on the heat transfer coefficient.

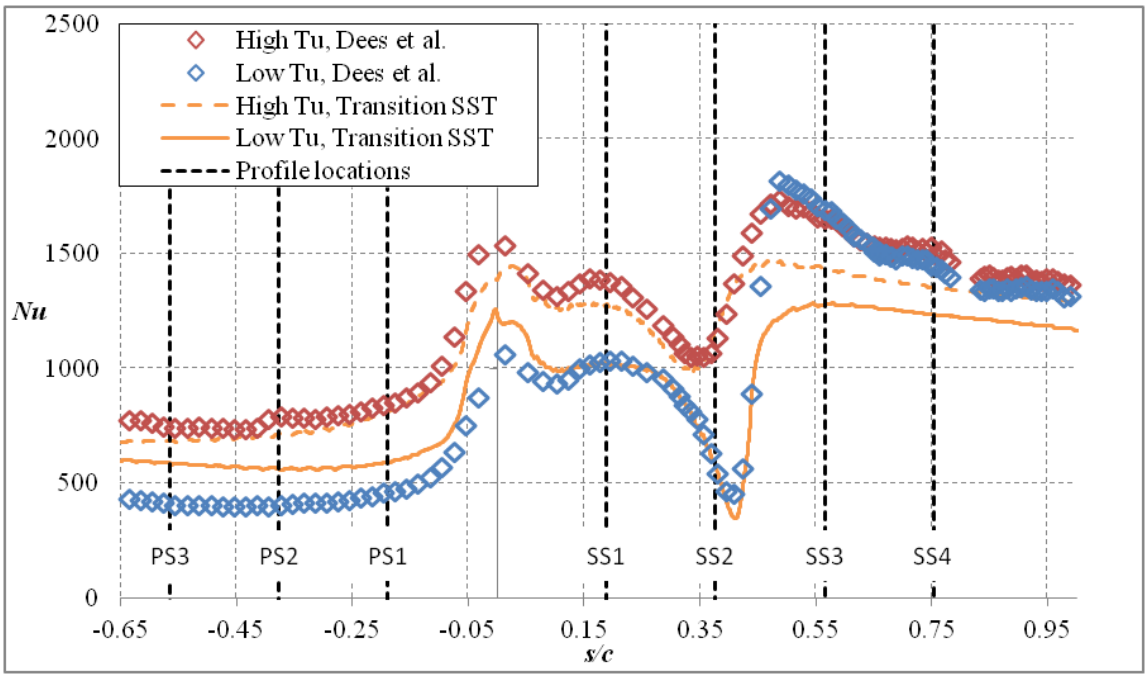

Figure 9.2.1: Heat transfer predictions for both mainstream turbulence conditions compared to the experimental data of Dees *et al.* [30]

Figure 9.2.2 shows the predictions for all of the turbulence models compared to experimentally measured values. The standard *k-ε* and *k-ω* models are not visible because they predicted identical *Nu* distributions to the RKE and *k-ω* SST models, respectively. Only the Transition SST model predicted the correct behavior on the PS, where it was within experimental uncertainty from just downstream of the stagnation point. All the other models predicted a continuously increasing *Nu* for *s/c* < -0.25. However, the *k-ω* SST model

matched well for -0.25 < *s/c* < 0, while the *k-ε* models predicted *Nu* values that were ~ 25% low. In the stagnation region (-0.05 < *s/c* < 0.05), only the *k-ω* SST model matched the experiments, though Transition SST was only 7% low, which was only just outside the experimental uncertainty of 5%. In contrast to its performance for the low turbulence case, the *k-ω* SST model produced a much worse prediction for *Nu* between stagnation and transition, though it was still better than the standard *k-ω*. This was probably because the low Re_t corrections were not formulated to deal with high mainstream turbulence, so *k-ω* models predicted an immediate transition much like the "fully turbulent" *k-ε* models, which also over-predicted *Nu*. The Transition SST model remained 5-8% low (near the margin of uncertainty), but captured the location of transition almost exactly. Note that the transition location had moved from *s/c* = 0.38 to 0.35 because of the higher levels of turbulence, and that Transition SST captured the location correctly in both cases. However, like the low *Tu* case, Transition SST was unable to properly predict the level of *Nu* enhancement produced by the transition to a turbulent boundary layer giving a ~ 15% low prediction. The other models were all within the experimental uncertainty downstream of transition.

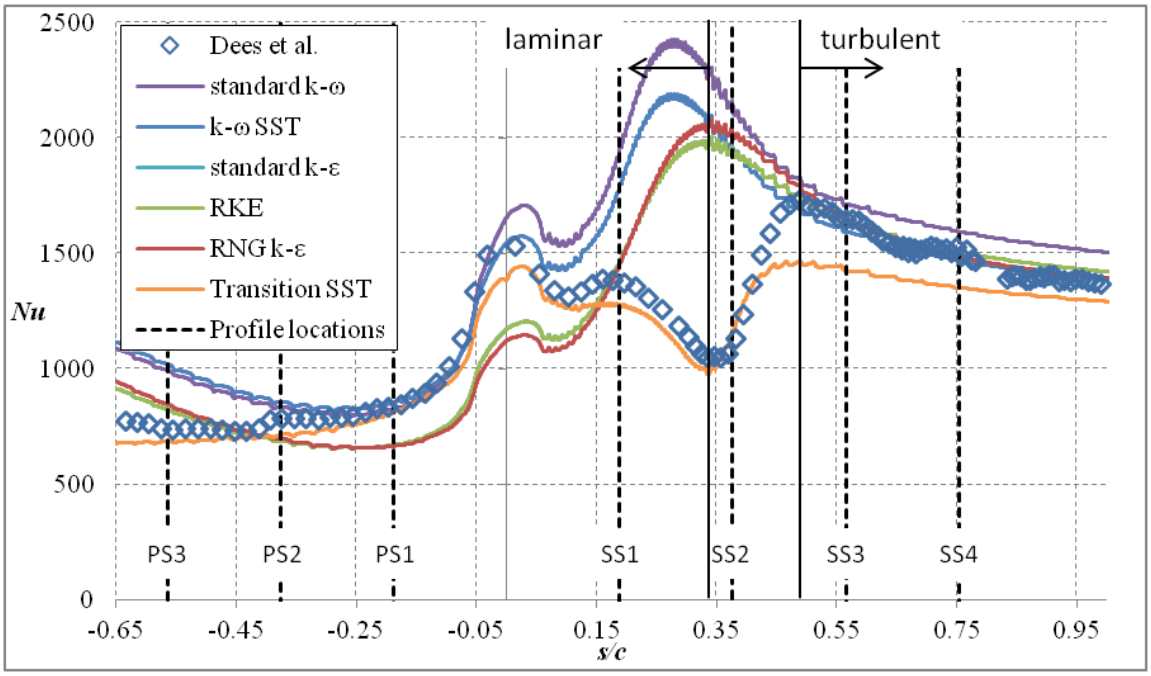

Figure 9.2.2: Heat transfer predictions compared to the experimental data of Dees *et al.* [30] for *Tu* = 20%

The shear velocity at SS3 and SS4 did not change much from the low turbulence condition; it was estimated as u_τ = 1.07 and 1.10 m/s from the experimental data at SS3 and SS4, respectively. The turbulence models' performances were similar to the low *Tu* condition (*i.e.*, u_τ ~ 0.90 m/s). Table 9.2.4.1 gives the ratio of each turbulence model to the experimental measurement.

Table 9.2.4.1: Ratio of computational to experimental values of u_τ for *Tu* = 20%

Position	*k-ω*	*k-ω* SST	*k-ε*	RKE	RNG *k-ε*	Transition SST
SS3	0.84	0.85	0.82	0.84	0.83	0.84
SS4	0.82	0.82	0.79	0.80	0.78	0.80

9.2.1. Pressure side performance

Dees *et al.* [64] showed that increased mainstream turbulence did not have a strong effect on the boundary layer thickness for the laminar portions of the vane, including all locations on the PS. However, the shape of the velocity profile was affected; the high turbulence condition had sharper near-wall gradients. Figure 9.2.1.1 shows that at the PS1 position, the turbulence models were all in agreement with the measurements for $y/c < 0.002$, indicating that they had predicted the change in the profile. Farther from the wall there was some deviation, which resulted in the boundary layer thickness predictions being off from the experimental value. All the models predicted a hydrodynamic boundary layer thicker than the measurements, but there was disagreement between the models, with predictions ranging from the standard k-ω model, which was only 16% high in terms of δ_{95}, to the RNG k-ε model, which was 35% high.

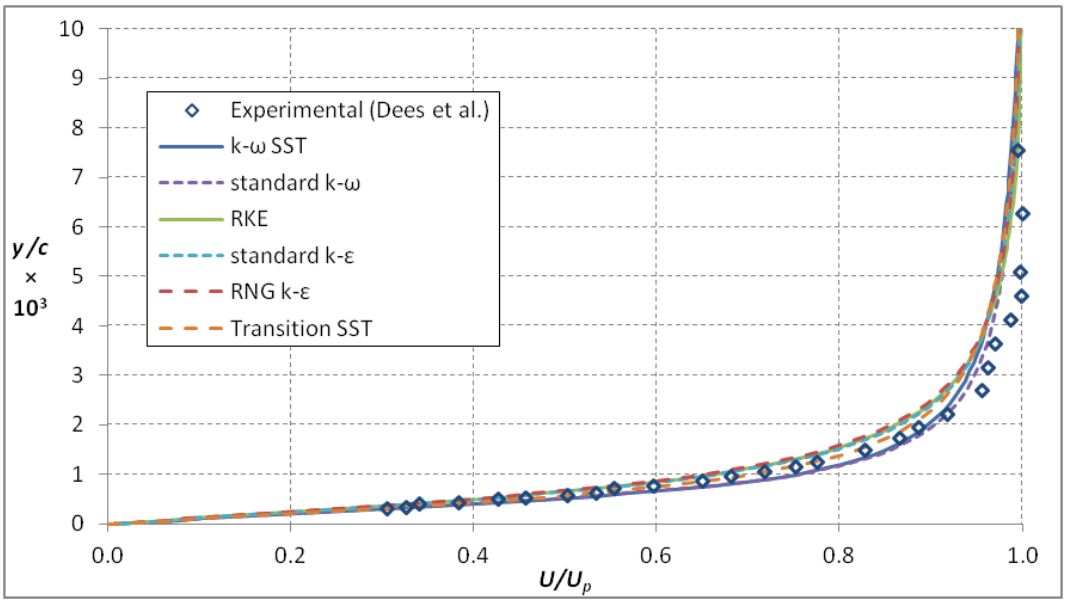

Figure 9.2.1.1: Computed mean velocity profiles at the PS1 position compared to the experimental data of Dees *et al*. [64] at *Tu* = 20%

Unlike the hydrodynamic boundary layer, the thermal boundary layer was substantially thickened by the action of mainstream turbulence. Because of this, Fig. 9.2.1.2, which shows the predicted thermal profiles, uses a larger *y/c* scale. The models mostly captured the effect of turbulence here, but the *k-ω* models over-predicted the thickness increase (21% for the standard and SST *k-ω* models and 13% for Transition SST). The *k-ε* models performed better overall, with closer matches to the temperature profile and better estimates of the boundary layer thickness (14%, 9%, and 3% below the measurement for the RKE, standard, and RNG *k-ε* models, respectively).

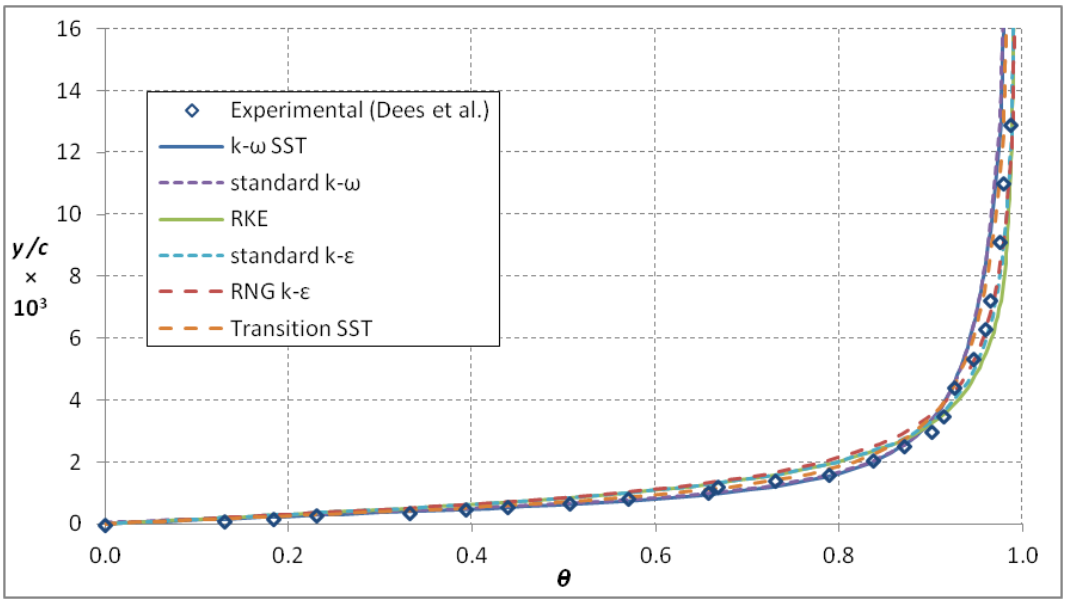

Figure 9.2.1.2: Computed thermal profiles at the PS1 position compared to the experimental data of Dees *et al*. [64] at *Tu* = 20%

The change in the thermal boundary layer without a corresponding change in the velocity profile can be attributed to a strengthening of the mixing in the superlayer. If the thermal boundary layer is represented using the similarity variable defined by Launder and Lockwood [111] as:

$$\eta \equiv \frac{yU\sqrt{K}}{\nu} \tag{9.2.1}$$

where K is the acceleration parameter at the measurement location (1.04×10^{-5}), Launder and Lockwood showed that there should be a distinct change in the curvature in the θ profile near the edge of the hydrodynamic boundary layer. However, the β value at PS1 was small enough that this was difficult to observe directly or in the first derivative. However, Fig. 9.2.1.3 shows using the second derivative that there was a change in the behavior of the thermal boundary layer

near the edge of the hydrodynamic boundary layer. This change was stronger in the high turbulence case, indicating that the superlayer, which normally is a region where molecular diffusion dominates, was enhanced due to turbulent mixing. Unfortunately, the experimental measurements were not detailed enough this far out from the wall to confirm this behavior, but close match of the RNG k-ε model to the experimental θ profile means that it was probably representative (at least for high Tu; recall that for low Tu it was considerably off. Because no model matched well for both cases on the pressure side, this analysis will be revisited later).

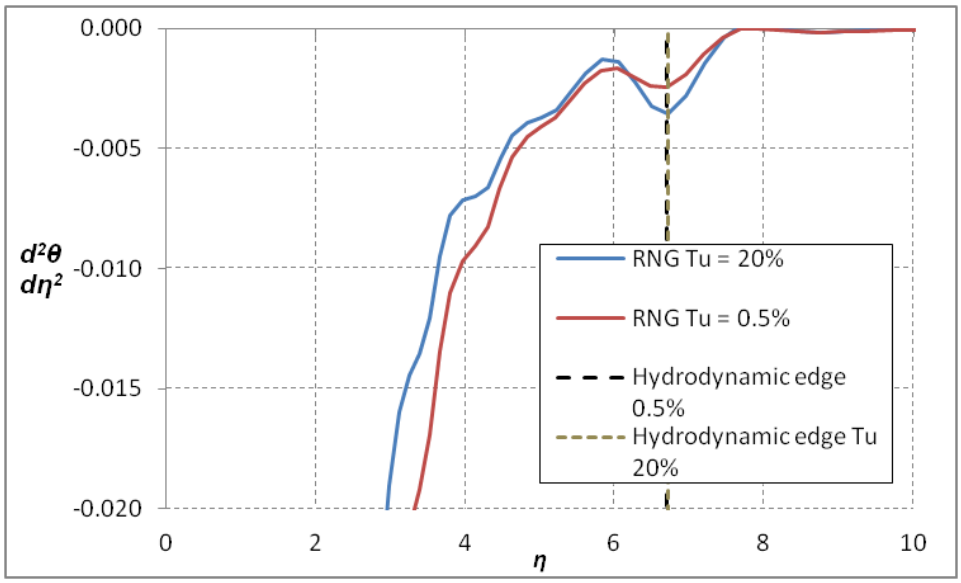

Figure 9.2.1.3: Comparison of the second derivative of θ with respect to Launder and Lockwood's similarity variable at PS1 for high and low mainstream turbulence using the RNG k-ε model

Farther downstream at PS2, the measurements once again showed little effect of mainstream turbulence on the hydrodynamic boundary layer. Figure 9.2.1.4 shows that the turbulence models were all close to each other and the experimental measurements, though agreement near the wall was not as good as for the PS1 position. All the *k-ω* models were within experimental uncertainty of δ_{95}, but the *k-ε* models all over-predicted the boundary layer thickness somewhat. The standard and realizable *k-ε* models were not far off at 12 and 14%, respectively, but the RNG *k-ε* model was off by 17%. Given how closely all the profiles resembled each other, this much variation in the boundary layer thickness highlights the problem in using δ as a performance metric.

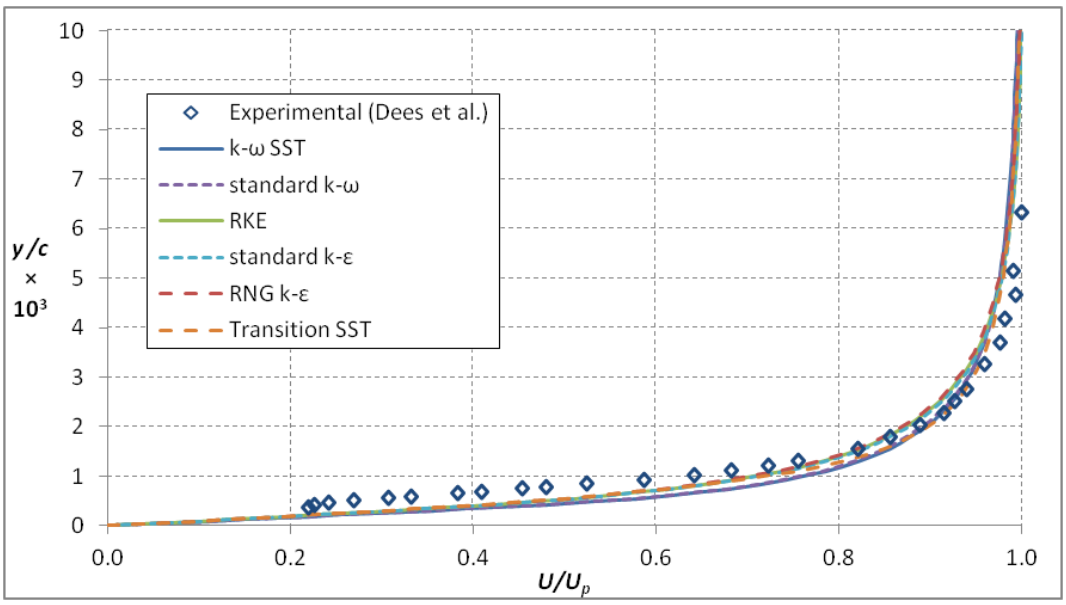

Figure 9.2.1.4: Computed mean velocity profiles at the PS2 position compared to the experimental data of Dees *et al*. [64] at *Tu* = 20%

The corresponding thermal profiles at PS2 are shown in Figure 9.2.1.5. The turbulence models all produced slightly different profiles, none of which were particularly well matched, though the shape of the profile was roughly matched. This was in contrast to the *Tu* = 0.5% condition, where there were unrealistic thermal profile shapes. All the models over-predicted the boundary layer thickness at this location, ranging from 18% (RKE) to 73% (standard and SST *k-ω*) high. With the exception of *k-ω* SST, the turbulence models also did not predict a thicker thermal boundary layer at this position compared to the low turbulence condition, due to poor prediction for the low *Tu* case.

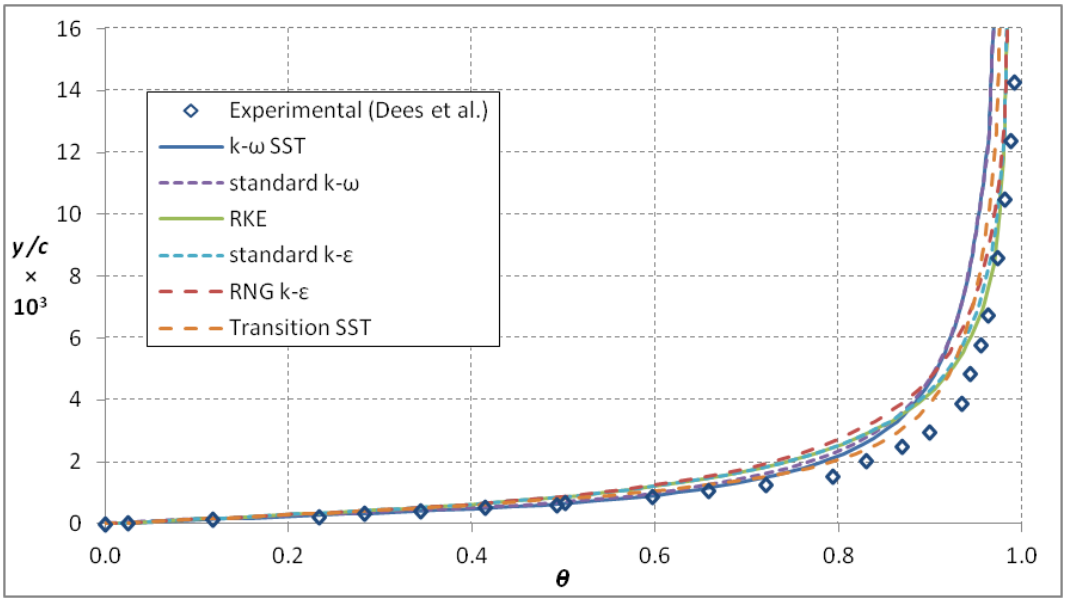

Figure 9.2.1.5: Computed thermal profiles at the PS2 position compared to the experimental data of Dees *et al*. [64] at *Tu* = 20%

The hydrodynamic performance at the PS3 position was very similar to the PS2 position, as shown in Fig. 9.2.1.6, with the exception of the Transition SST

model. Transition SST was the only model to under-predict the boundary layer thickness; however, it was also the closest to the experimental measurements in the $y/c < 0.001$ region. Also like the PS2 position, the k-ω SST model was the only one that predicted an increase in the thermal boundary layer thickness compared to the low turbulence case. However, as can be seen in Fig. 9.2.1.7, the models generally matched the data well. The primary difference between the low and high *Tu* cases on the PS was the action of Taylor-Görtler vortices. The high *Tu* case did not show any span-wise variation in the surface temperature, indicating that the mainstream turbulence had wiped out these structures. This was consistent with the experimental data, which also showed very uniform temperatures. As was pointed out in the low turbulence section, the action of Taylor-Görtler vortices cannot account for everything because the velocity profiles were apparently unaffected.

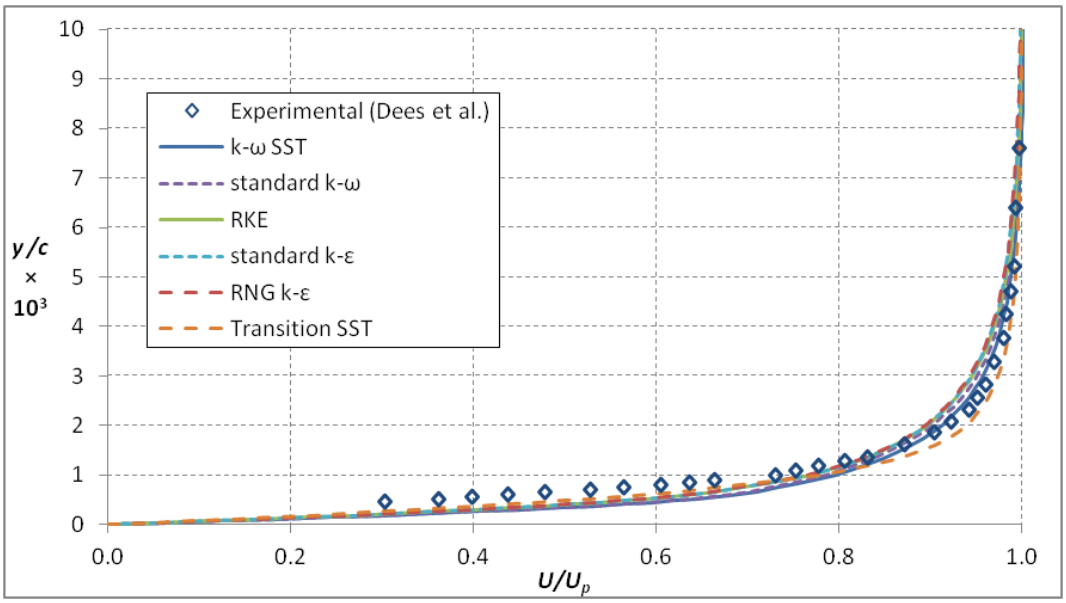

Figure 9.2.1.6: Computed mean velocity profiles at the PS3 position compared to the experimental data of Dees *et al*. [64] at *Tu* = 20%

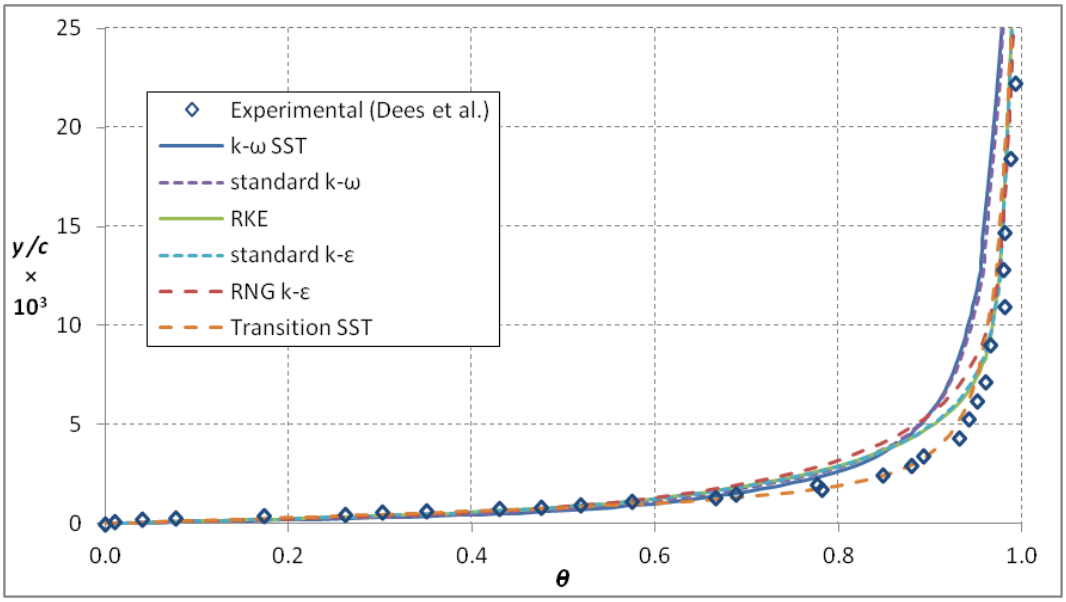

Figure 9.2.1.7: Computed thermal profiles at the PS3 position compared to the experimental data of Dees *et al*. [64] at *Tu* = 20%

9.2.2. Suction side performance

Experimentally, the SS1 position was shown to be pushed to a much different velocity profile even though the thickness remained the same (< 0.5 mm). None of the turbulence models were able to accurately predict this profile, which can be seen in Fig. 9.2.2.1. All of the turbulence models predicted a much fuller profile than was measured. This laminar position was expected to be the most difficult for turbulence models to match.

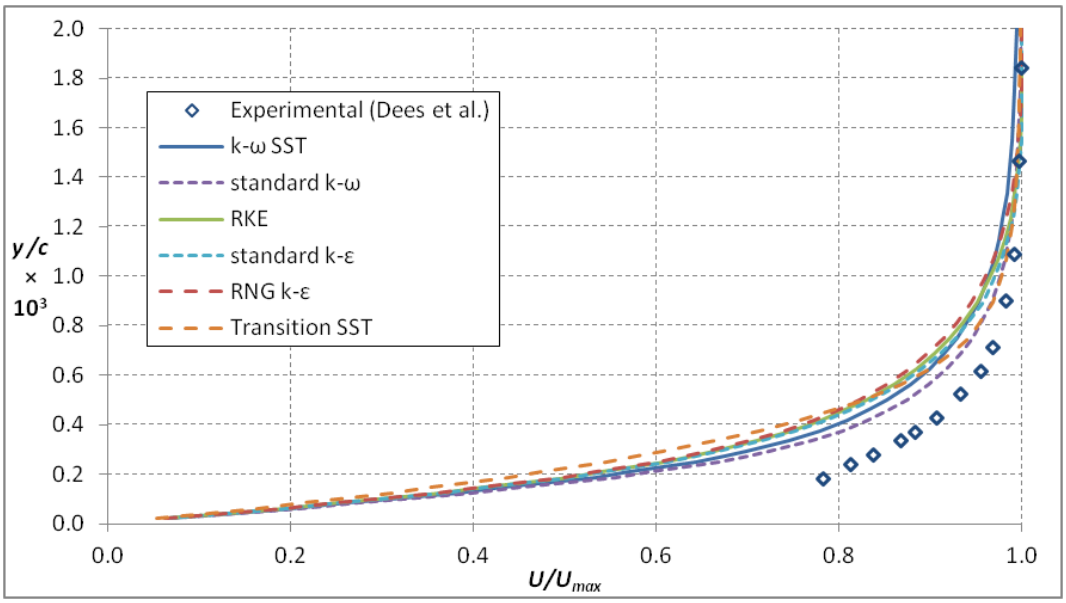

Figure 9.2.2.1: Computed mean velocity profiles at the SS1 position compared to the experimental data of Dees *et al*. [64] at *Tu* = 20%

Given its poor performance predicting the hydrodynamic boundary layer, it was somewhat surprising that the models were able to reasonably predict the thermal profile. Transition SST was able to almost exactly match the thermal profile, as shown in Fig. 9.2.2.2. The *k-ε* models also performed very well,

matching the experimental data for $y/c < 0.003$. In terms of δ_{95T}, Transition SST was within experimental uncertainty while the k-ε models were 10, 13, and 14% low for the RNG k-ε, standard k-ε, and RKE models, respectively.

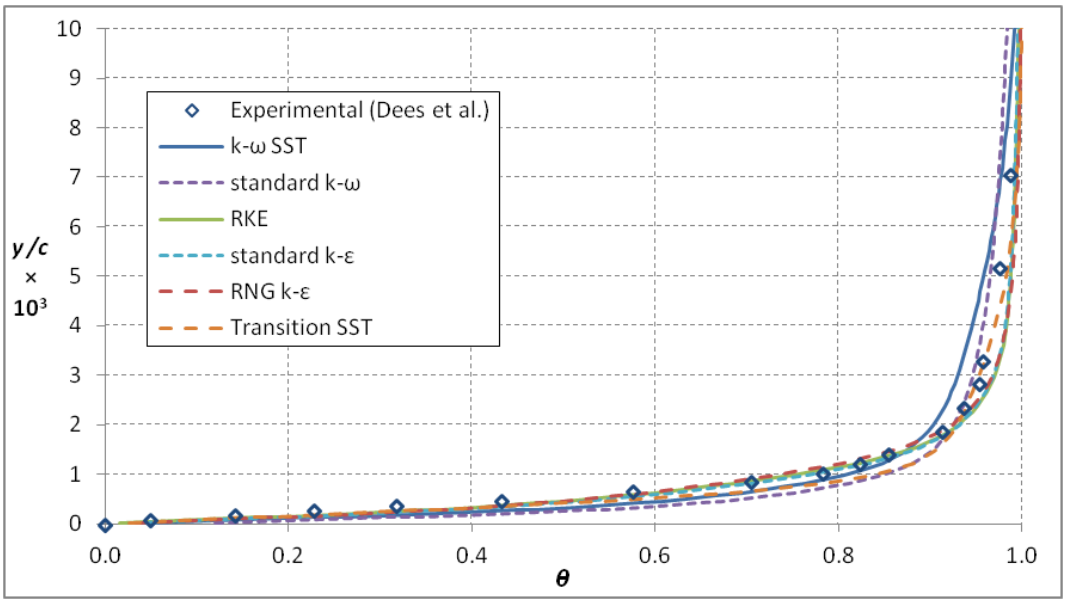

Figure 9.2.2.2: Computed thermal profiles at the SS1 position compared to the experimental data of Dees *et al*. [64] at *Tu* = 20%

The SS1 position possessed the largest proportional thermal superlayer of any position, with the thermal boundary layer coming in at over four times the thickness of the hydrodynamic boundary layer. Even though the hydrodynamic boundary layer was very thin, this makes it a good location to evaluate the superlayer effect further. Because the Transition SST model matched the θ profile very closely for both high and low Tu cases, it was used to evaluate the profile near the edge of the hydrodynamic boundary layer, as shown in Fig. 9.2.2.3. Both turbulence cases showed a change to constant curvature at the

edge of the hydrodynamic boundary layer, but the high turbulence case was much flatter and stayed below zero much longer (until η ~ 20). This indicates that the high mainstream turbulence greatly spread out the mixing zone which was previously dominated by molecular diffusion. Even prior to the edge of the hydrodynamic boundary layer, the mainstream turbulence affected the boundary layer significantly.

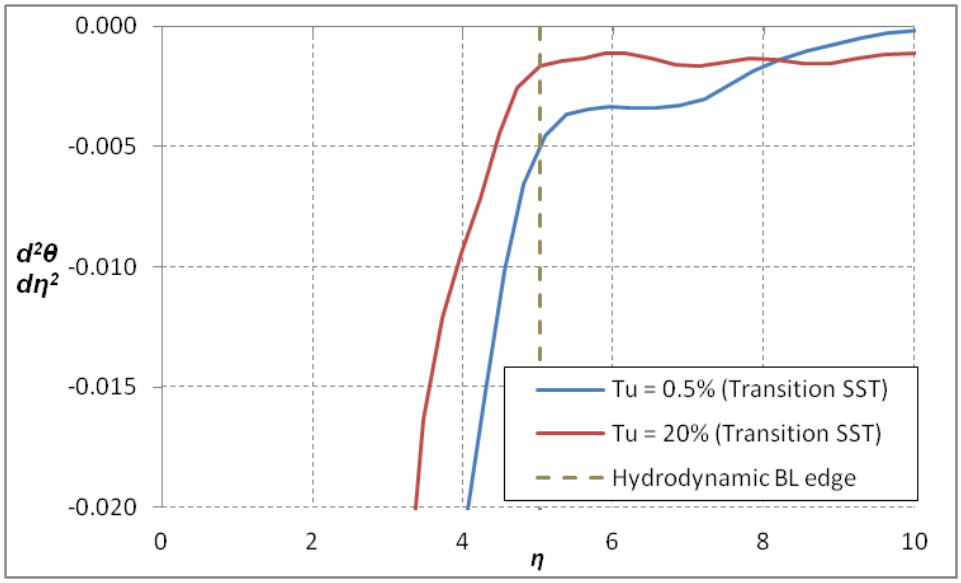

Figure 9.2.2.3: Comparison of the second derivative of θ with respect to Launder and Lockwood's similarity variable at SS1 for high and low mainstream turbulence using the Transition SST model

At the SS2 position, the profile was transitional. It was no surprise that only the Transition SST model was able to accurately capture the boundary layer at this position; it matched the experimental data very well while all the "turbulent" models predicted much fuller profiles, as seen in Fig. 9.2.2.4. It is noteworthy that

the Transition SST model was the only model to accurately predict *Nu* at this location as well.

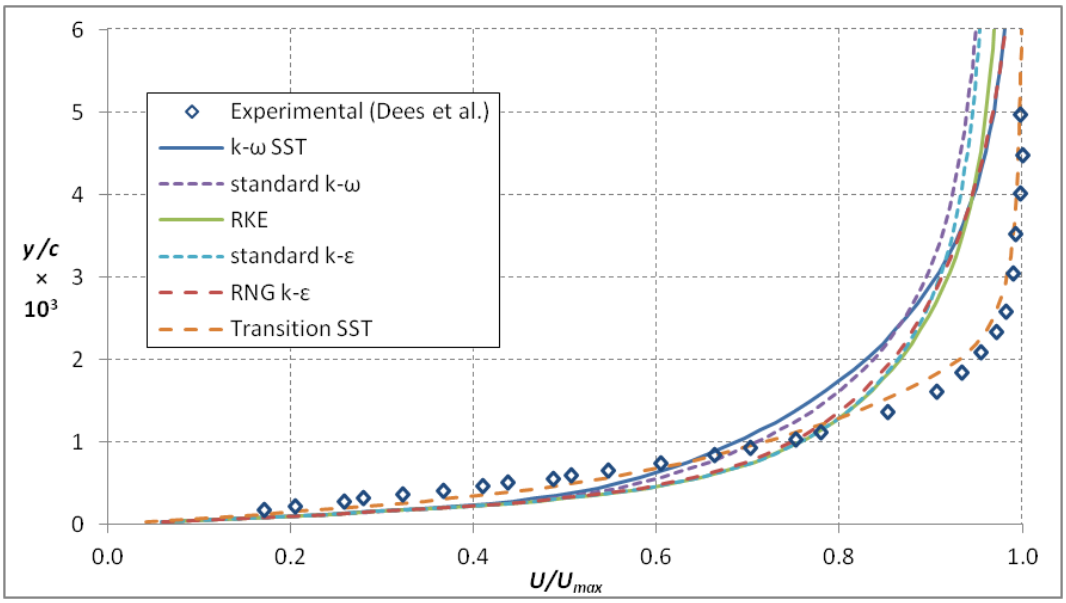

Figure 9.2.2.4: Computed mean velocity profiles at the SS2 position compared to the experimental data of Dees *et al*. [64] at *Tu* = 20%

The thermal performance at SS2 reflected the hydrodynamic performance, as shown in Fig. 9.2.2.5. Transition SST's performance was very good here as well, though it diverged slightly from the measurements for $y/c > 0.003$. This was still far better than the other models, which greatly over-predicted thermal diffusion.

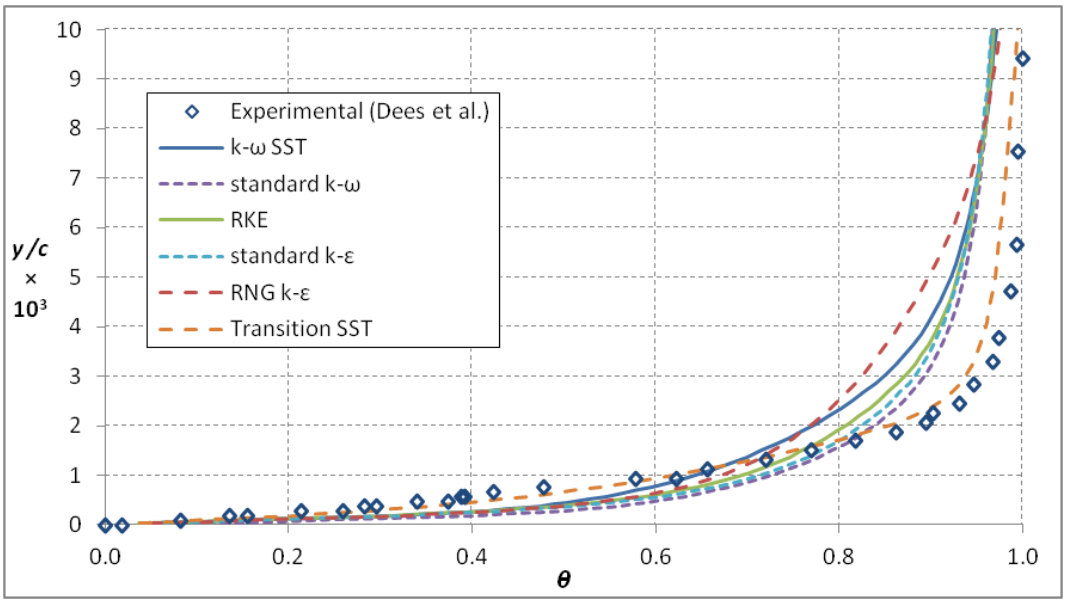

Figure 9.2.2.5: Computed thermal profiles at the SS2 position compared to the experimental data of Dees *et al*. [64] at *Tu* = 20%

Downstream of transition, all of the turbulence models predicted entirely different velocity profiles. Figure 9.2.2.6 shows that even with the variety of predicted profiles, no model matched the experimental profile. The best performance for $y/c < 0.002$ came from the RNG *k-ε* and RKE models, but farther from the wall only the Transition SST model was near the measurements. However, the Transition SST profile was not realistic; it had the same unusual profile shape that was seen at this position for the *Tu* = 0.5% case. The *k-ε* models were expected to be too thick because they had early transition, so their development length was too long. The *k-ω* models were similarly affected, but the SST model was still closer to the experimental data than the other models.

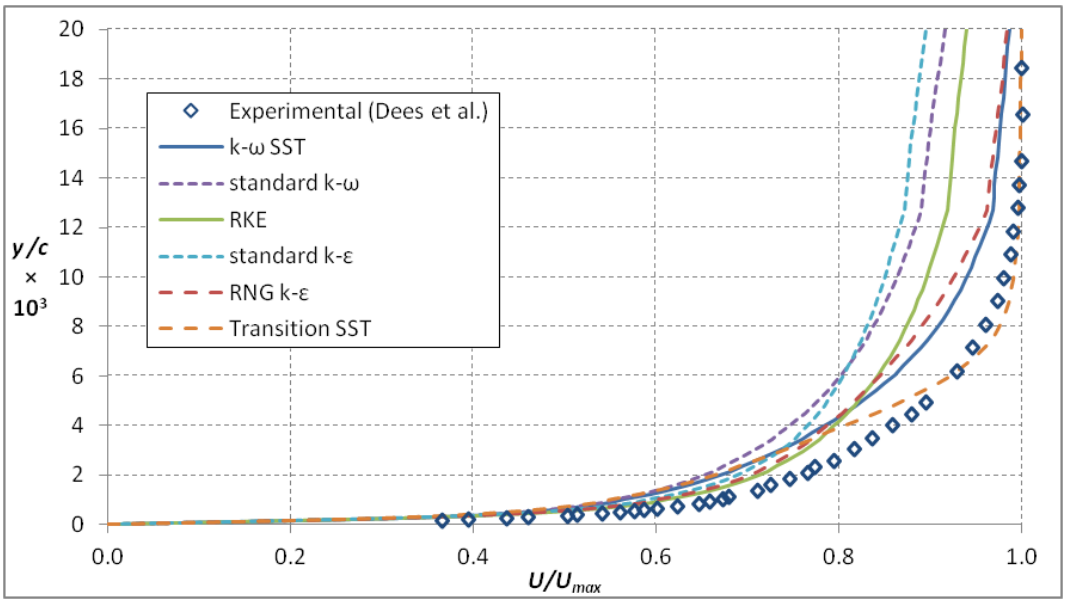

Figure 9.2.2.6: Computed mean velocity profiles at the SS3 position compared to the experimental data of Dees *et al*. [64] at *Tu* = 20%

The transition to turbulence and the reduced acceleration of the flow brought the thermal boundary layer closer to the same thickness as the hydrodynamic boundary layer, as can be seen in Fig. 9.2.2.7. Considering that all of the turbulence models except Transition SST correctly predicted *Nu* at this position, it was interesting that none of them were very close to the correct profile. The *k-ω* SST model was very close for $y/c < 0.006$, but otherwise the closest to the correct profile came from the Transition SST model – the only model that failed to predict *Nu*. In terms of δ_{95T}, Transition SST was within experimental uncertainty but the remaining models were more than 30% thicker. Considering that the hydrodynamic boundary layer was so greatly over-predicted, this meant that most of the models were predicting $\delta_{95T} < \delta_{95}$, which was completely unrealistic. The performance at the SS4 position was virtually the

same as for the SS3 position, as can be seen in Figs. 9.2.2.8 and 9.2.2.9 for the hydrodynamic and thermal profiles, respectively.

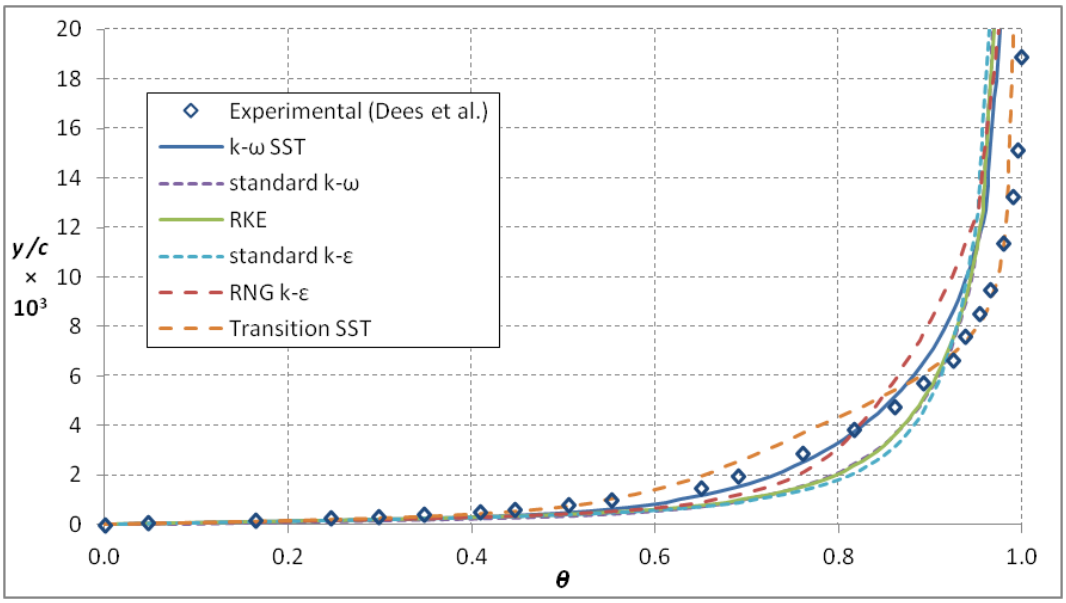

Figure 9.2.2.7: Computed thermal profiles at the SS3 position compared to the experimental data of Dees *et al*. [64] at *Tu* = 20%

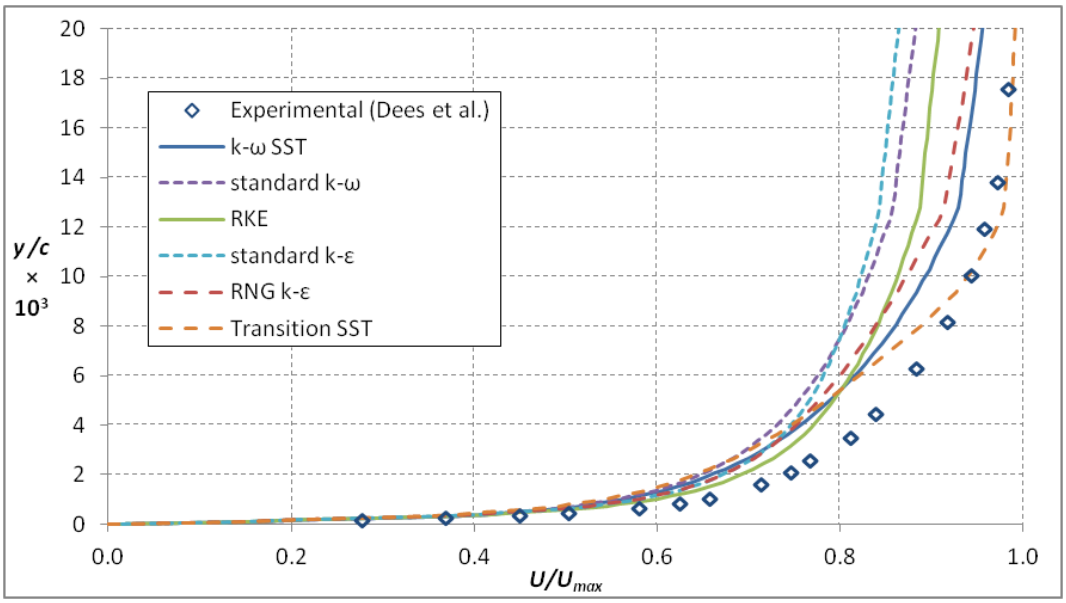

Figure 9.2.2.8: Computed mean velocity profiles at the SS4 position compared to the experimental data of Dees *et al*. [64] at *Tu* = 20%

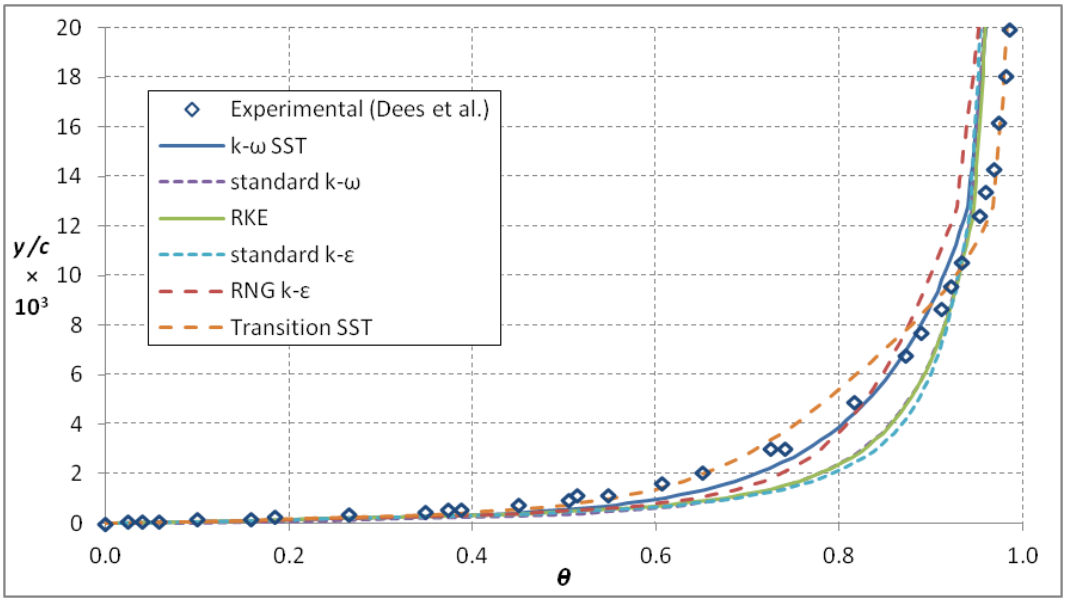

Figure 9.2.2.9: Computed thermal profiles at the SS4 position compared to the experimental data of Dees *et al*. [64] at *Tu* = 20%

9.2.3. Velocity and thermal performance summary

Perhaps even more than for the low turbulence condition the boundary layer thicknesses was not necessarily a good indicator of performance, but it still serves as an indicator of performance. For reference, Table 9.2.3.1 shows the experimentally measured values of δ_{95} and δ_{95T} at each position. Tables 9.2.3.2 and 9.2.3.3 show the ratios of the computational to experimental boundary layer thicknesses for the hydrodynamic and thermal boundary layers, respectively.

Table 9.2.3.1: Thermal and momentum boundary layer thicknesses measured by Dees *et al.* [64] for *Tu* = 20%

Position	δ_{95} (mm)	δ_{95T} (mm)
PS1	1.41	3.00
PS2	1.63	2.88
PS3	1.40	3.30
SS1	0.36	1.45
SS2	1.08	1.50
SS3	3.96	4.40
SS4	5.78	6.40

Table 9.2.3.2: Ratio of computational to experimental values of δ_{95} for Tu = 20%

Position	*k-ω*	*k-ω* SST	*k-ε*	RKE	RNG *k-ε*	Transition SST
PS1	1.16	1.28	1.34	1.34	1.37	1.35
PS2	1.08	1.07	1.12	1.14	1.17	1.01
PS3	1.13	1.06	1.21	1.20	1.23	0.84
SS1	1.15	1.30	1.27	1.31	1.37	1.17
SS2	2.96	2.01	2.69	2.08	2.05	1.08
SS3	4.00	1.46	4.91	3.13	1.57	0.91
SS4	3.58	1.69	4.55	3.18	1.93	0.97

Table 9.2.3.3: Ratio of computational to experimental values of δ_{95T} for Tu = 20%

Position	*k-ω*	*k-ω* SST	*k-ε*	RKE	RNG *k-ε*	Transition SST
PS1	1.21	1.21	0.91	0.86	0.97	1.13
PS2	1.73	1.73	1.25	1.18	1.37	1.39
PS3	1.77	1.89	1.22	1.18	1.36	1.18
SS1	1.20	1.60	0.87	0.86	0.90	1.05
SS2	2.27	2.46	2.45	2.39	2.63	1.22
SS3	1.32	1.35	1.46	1.34	1.50	0.96
SS4	1.31	1.34	1.44	1.22	1.61	0.95

The Transition SST model had the same performance for the high turbulence condition as for the low turbulence condition: 13% average error. However, no other model was even close, with 2nd place being *k-ω* SST at 41%.

The remaining models had 53, 91, 115, and 144% average error for the RNG k-ε, RKE, standard k-ω, and standard k-ε models respectively. In large part this poor average performance stems from the poor predictions on the suction side, where with the exception of Transition SST the models uniformly greatly over-predicted the boundary layer thickness for the SS2, SS3, and SS4 positions. If only the laminar positions are considered, the standard k-ω model turned in a 13% average error and even the worst performance (RNG k-ε) was within 30%.

In general, all the turbulence models over-predicted the thermal boundary thickness. The only exceptions were for PS1 and SS1, where the k-ε models predicted thinner than measured values for δ_{95T} (though the RNG k-ε model was within uncertainty). The poor performance on the pressure side could not be attributed to Taylor-Görtler vortices because they were not present for the high mainstream turbulence condition. The Transition SST model had the best overall performance, with 15% average error. The next closest was the RKE model with 37% average error. The remaining models had 43, 51, 55, and 65% average error for the standard k-ε, RNG k-ε, standard k-ω, and k-ω SST models, respectively. It was interesting that – with the exception of Transition SST – the hydrodynamic performance was not a good predictor of the thermal performance. It was also interesting to note that a good prediction for Nu seemed unrelated to the model's ability to predict the right θ profile, which was counter-intuitive.

9.2.4. Kinetic energy predictions

Dees *et al*. [64] showed that mainstream turbulence penetrated almost all the way to the wall, which increased turbulence levels even for the laminar

portions of the vane and resulted in deviation from an ideal laminar shape. Figure 9.2.4.1 shows that even the fully turbulent *k-ε* models captured this increase at PS1. Figure 9.2.4.2 shows all the models for *Tu* = 20%. The standard *k-ω* and *k-ω* SST models both matched very well near the wall (*y/c* < 0.001) but did not show the level of turbulence measured experimentally farther from the wall. This was common to all the models, which showed that the freestream turbulence at this position was only 10-12%, which was far below the measured values of 21%. Transition SST performed the worst, in contrast to its generally good performance predicting the mean velocity and thermal profiles.

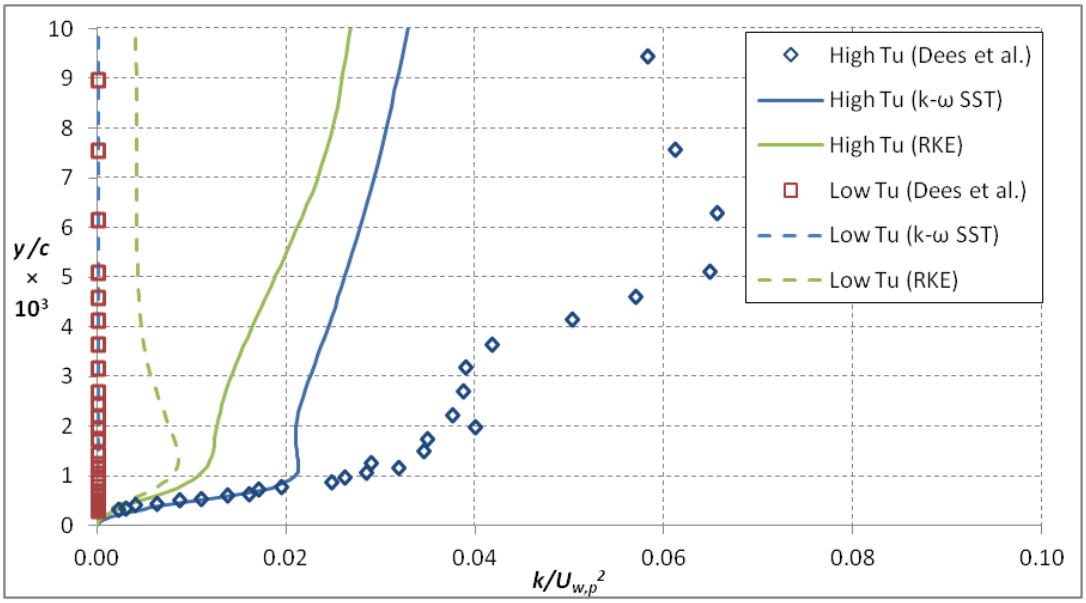

Figure 9.2.4.1: Comparison of *Tu* = 0.5 and 20% at PS1 for selected turbulence models and the experimental data of Dees *et al*. [64]

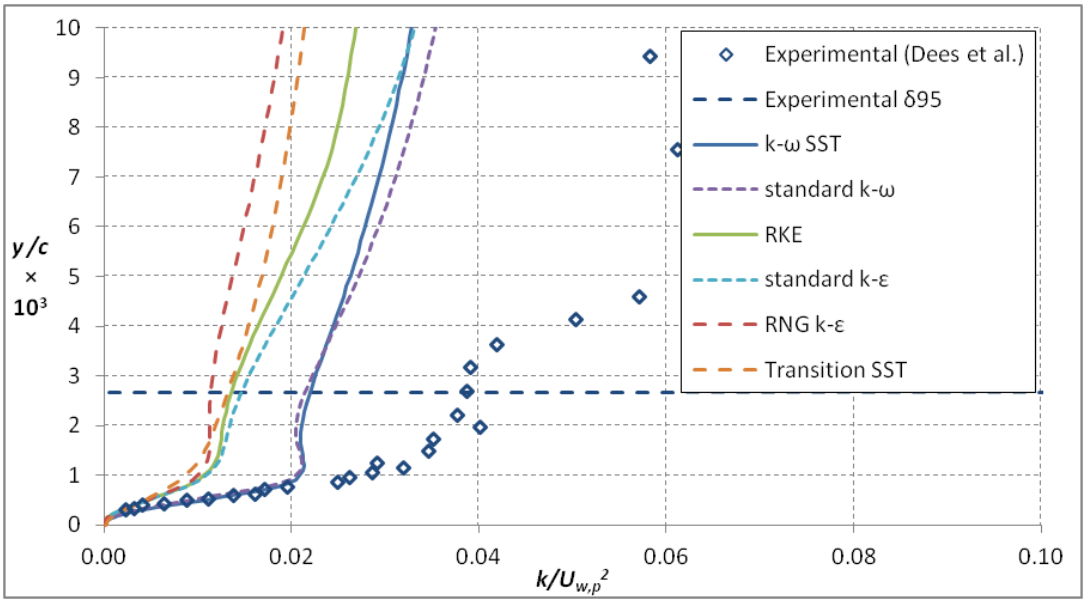

Figure 9.2.4.2: Computed turbulent kinetic energy profiles at the PS1 position compared to the experimental data of Dees *et al*. [64] at *Tu* = 20%

As shown in Fig. 9.2.4.3, predictions of k at PS2 were similar, though the models were somewhat closer to the measurements of freestream turbulence levels, and the k-ε models did better near the wall. Note that the measured and simulated turbulence $k/U_{w,p}^2$ values at PS2 decreased compared to PS1 because $U_{w,p}$ was increasing faster than k.

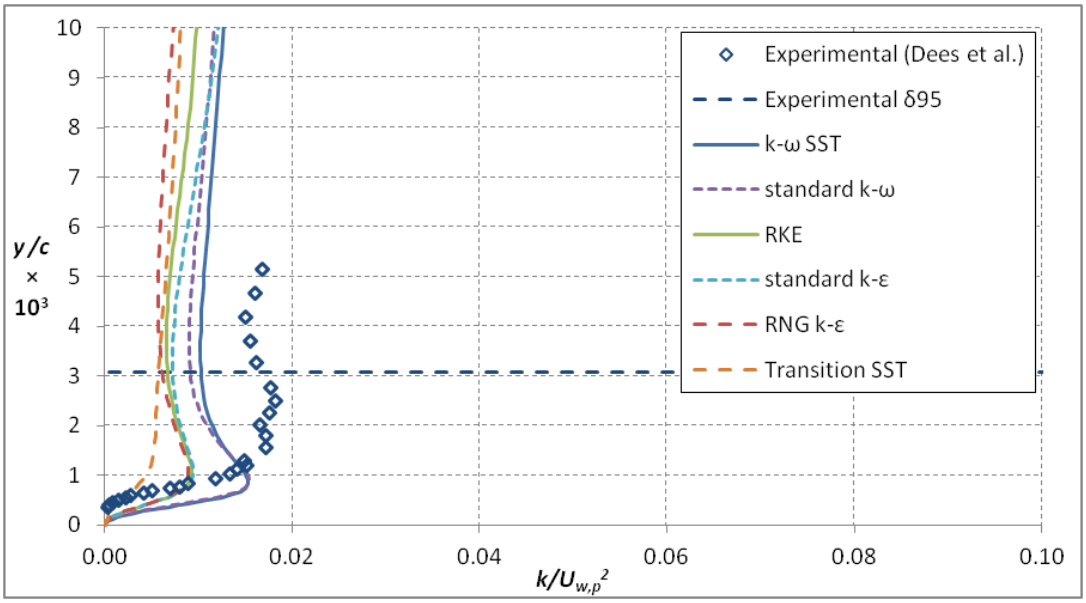

Figure 9.2.4.3: Computed turbulent kinetic energy profiles at the PS2 position compared to the experimental data of Dees *et al*. [64] at *Tu* = 20%

The trend of reduction in k/U_w^2 continued at PS3, which is shown in Fig. 9.2.4.4. At this position, all of the models except for Transition SST and *k-ω* SST were reasonably close to the measurements within the boundary layer, though *k-ω* SST performed the best outside the boundary layer. For all positions U_w was within 10% of the measurements, so the performance trend on the PS indicates that the turbulence decay rate in the freestream was too high for the region with strong acceleration, and too low for the downstream regions. This allowed the initially poor predictions of turbulence to “catch up” to the measured data.

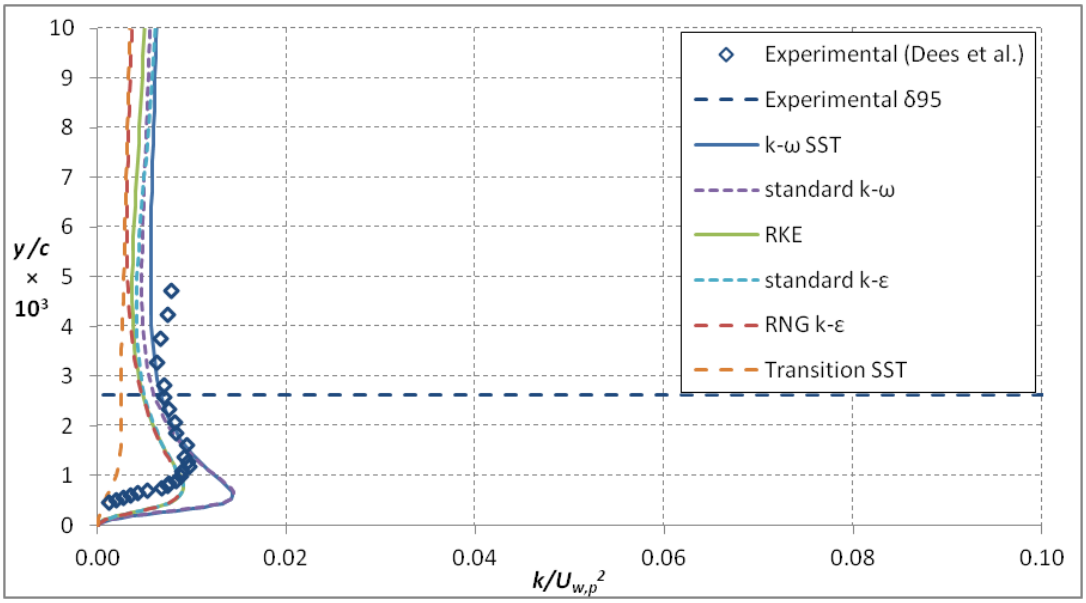

Figure 9.2.4.4: Computed turbulent kinetic energy profiles at the PS3 position compared to the experimental data of Dees *et al*. [64] at *Tu* = 20%

For the laminar SS1 position, the measurements showed that kinetic energy was constant throughout the boundary layer. Figure 9.2.4.5 shows that though the standard *k-ω* model was close to the measured turbulence levels outside the boundary layer, the turbulence models all predicted a peak *k* similar to what was observed on the PS. The exception was the Transition SST model, which predicted the right trend even if the absolute values of *k* were very low in comparison to the measurements. The implication of the peak *k* is that turbulence models were predicting a transitional boundary layer, which was consistent with the observed *Nu* behavior.

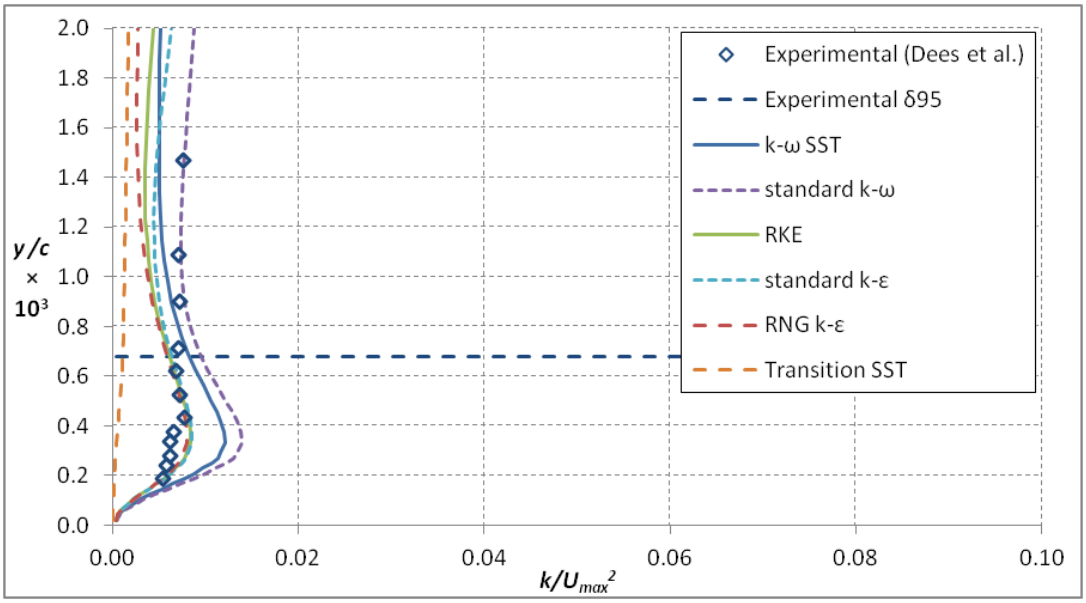

Figure 9.2.4.5: Computed turbulent kinetic energy profiles at the SS1 position compared to the experimental data of Dees *et al*. [64] at *Tu* = 20%

Unlike the pressure side, where continued high values of K suppressed turbulence generation in the boundary layer, after SS1 there was an adverse pressure gradient, promoting turbulence generation and transition, as shown in Fig. 9.2.4.6. This meant that turbulence levels greatly increased for the SS2 position, which can be seen in Fig. 9.2.4.7. The figure also shows that as the boundary layer approached transition, the turbulence models did better at predicting the levels of k. However, though the models were able to predict the correct trend (k/U_w^2 increasing to a peak before falling off), the absolute values were considerably off. It should be mentioned that for this position the method used to convert the experimental data was the most likely to be inappropriate (i.e., the ratios of u_{rms} to v_{rms} and w_{rms} taken from a fully turbulent boundary layer would not be expected to provide an accurate estimate). Transition SST

predicted the lowest level of *k* but best matched the shaped of the profile, with the *k* peak farther from the wall (representative of a transitional profile).

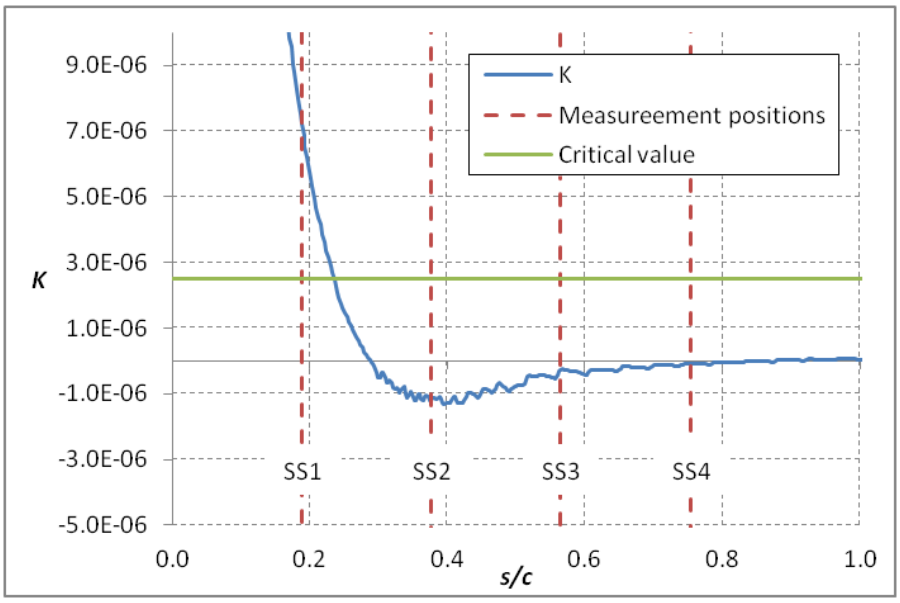

Figure 9.2.4.6: Acceleration parameter on the SS

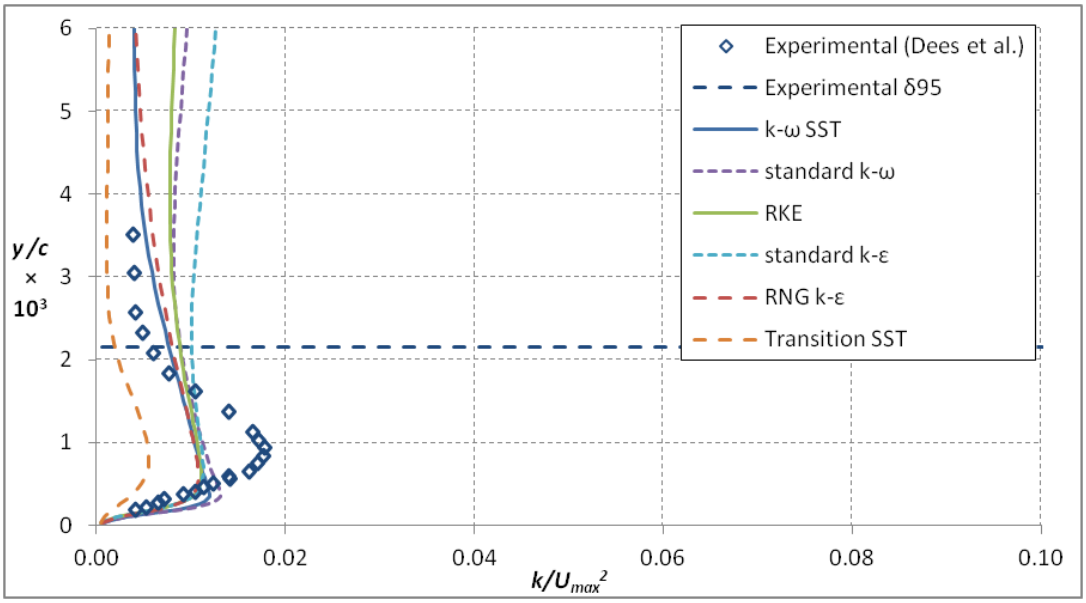

Figure 9.2.4.7: Computed turbulent kinetic energy profiles at the SS2 position compared to the experimental data of Dees *et al*. [64] at *Tu* = 20%

The turbulent boundary layer at SS3 showed lower peak levels of turbulence within the boundary layer, though there was a broad region of nearly constant k consistent with the production region found in turbulent boundary layers for $y/\delta < \sim 0.6$ [98]. Only the Transition SST model predicted this behavior, though it did not predict the near-wall peak, as seen in Fig. 9.2.4.8. However, all the turbulence models predicted slightly low turbulence levels for $0.002 < y/c < 0.006$. In the freestream, the standard k-ω, RKE, and standard k-ε models over-predicted the level of turbulence, while the RNG k-ε and k-ω SST models matched very closely.

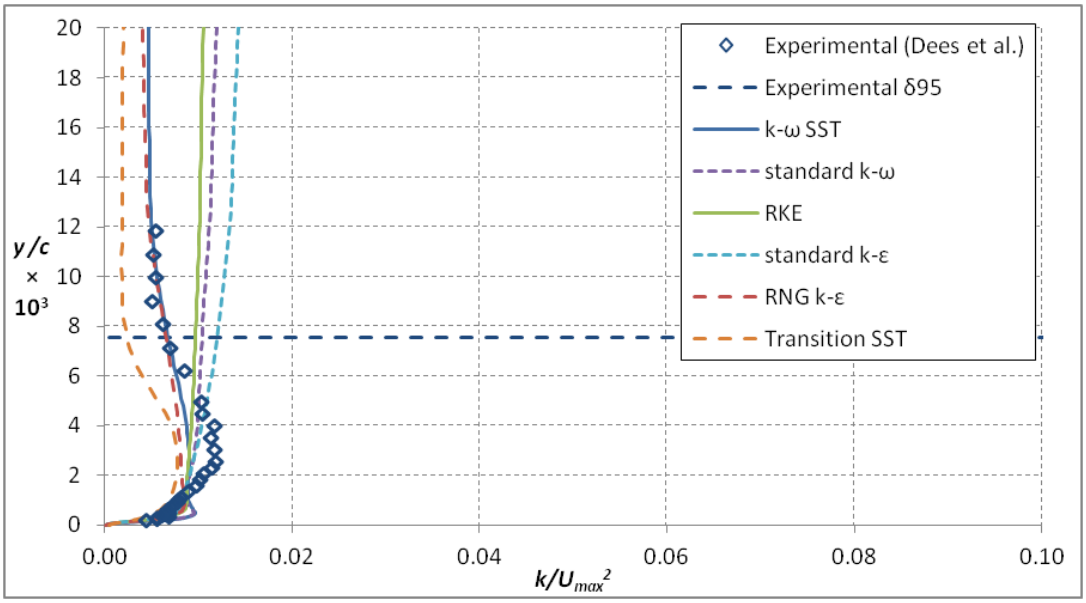

Figure 9.2.4.8: Computed turbulent kinetic energy profiles at the SS3 position compared to the experimental data of Dees *et al*. [64] at *Tu* = 20%

The production region was proportionally thicker at SS4, as shown in Fig. 9.2.4.9. The performance of the models was similar to that which was seen for the SS3 position. Interestingly, though Transition SST was predicting an unrealistic mean velocity profile shape at these positions, it matched the *k* profile almost exactly.

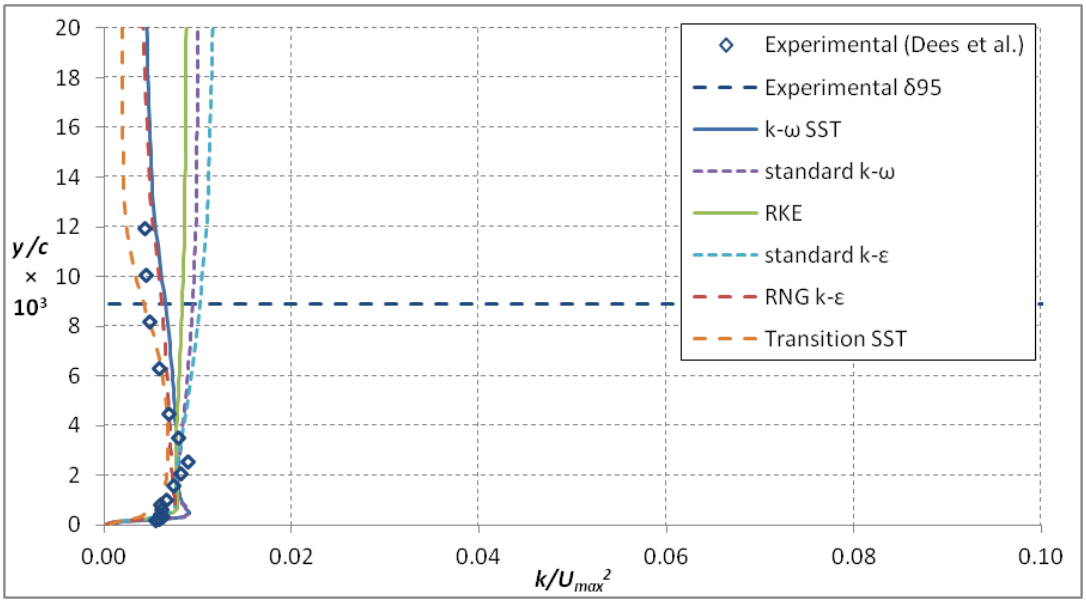

Figure 9.2.4.9: Computed turbulent kinetic energy profiles at the SS4 position compared to the experimental data of Dees *et al*. [64] at *Tu* = 20%

9.3. Turbulent Prandtl number variation

The turbulent Prandtl number, Pr_t, is among the most important parameters for the determination of heat transfer, especially when using RANS models. Therefore, it represents a good starting point for an attempt to improve the prediction of the thermal boundary layer.

While it is generally accepted that a constant $Pr_t = 0.85$ represents a good approximation of the real behavior, it is known that very near the wall ($y^+ < \sim 10$) Pr_t increases sharply, reaching values above 2. Because this region should be dominated by molecular conduction, the effect on the overall boundary layer for using a constant Pr_t should be minimal. To test this, a case was run using an experimental correlation for Pr_t from Kays and Crawford [114]. This correlation

was shown to fit the data very well [62]. Figure 9.3.1 shows that this model had virtually no effect on the thermal profile, even at the SS2 position. Therefore, a constant value for the turbulent Prandtl number should provide a reasonable model.

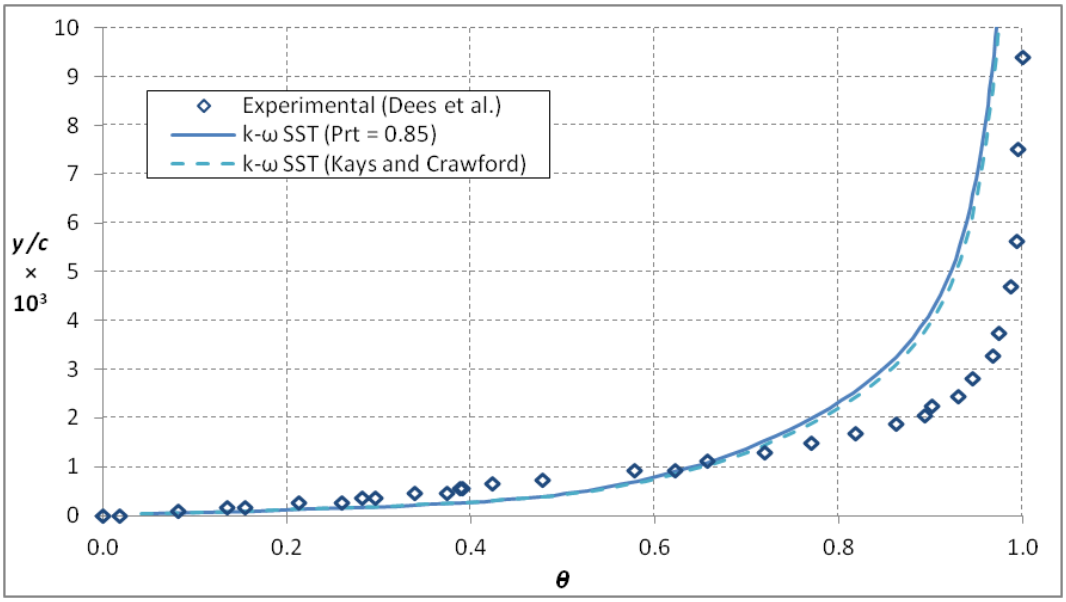

Figure 9.3.1: Computed thermal profiles at the SS2 position compared to the experimental data of Dees *et al*. [64] at *Tu* = 20% at differing Pr_t

Though Pr_t = 0.85 represents the best available experimental value for air, it remains to be seen if it is the optimal value for use with RANS models, which include additional approximations. The goal for adjusting the turbulent Prandtl number was not only to improve the thermal boundary layer prediction, but to better match the ratio of the hydrodynamic boundary layer thickness to the thermal boundary layer thickness. This ratio is proportional to the square root of Pr_t, so it was used as a guide for exploring the parameter space. Table 9.3.1

shows the experimentally measured δ_{95T}/δ_{95} ratio and the computed results relative to that ratio. It is clear that while the models were generally able to predict that the thermal boundary layer was thicker than the hydrodynamic boundary layer, they tended to over-predict that ratio on the PS and under-predict that ratio on the SS. However, over-predictions were usually worse, indicating that Pr_t was too small. Several larger values of Pr_t were compared using the Transition SST model, which had the best performance in terms of the boundary layer thickness ratio.

Table 9.3.1: Comparison of the simulated δ_{95T}/δ_{95} ratio to experimental measurements

Position	**Dees *et al.*** [64]		**Computational/Experimental**							
			k-ω SST		RKE		RNG *k-ε*		Transition SST	
Tu	20%	0.5%	20%	0.5%	20%	0.5%	20%	0.5%	20%	0.5%
PS1	2.13	0.91	0.94	1.94	0.64	1.45	0.71	1.51	0.84	2.13
PS2	1.77	1.29	1.61	2.05	1.04	1.33	1.17	1.45	1.37	2.20
PS3	2.36	1.33	1.79	2.72	0.98	1.59	1.10	1.77	1.40	2.73
SS1	4.03	1.73	1.23	1.17	0.66	1.17	0.65	1.28	0.90	1.18
SS2	1.38	1.49	1.22	0.82	1.15	1.00	1.28	1.10	1.13	0.81
SS3	1.11	1.80	0.93	0.60	0.43	0.59	0.95	0.64	1.05	0.56
SS4	1.11	1.15	0.80	0.92	0.38	0.84	0.83	1.04	0.97	0.91

Four different values were evaluated in addition to the default case (Pr_t = 0.85): 0.95, 1.0, 1.1, and 1.7. For all cases, the Prandtl number at the wall (a separate parameter in FLUENT) was set to Pr_t = 1.7, the value predicted by the Kays and Crawford model. This value was selected to better match the

experimental condition, but by itself it had no noticeable impact on the temperature distribution, as shown in Fig. 9.3.2, which depicts the thermal profiles for Pr_t = 0.85 with $Pr_{t,w}$ set to the default (0.85) and 1.7 using the Transition SST model. Only the high mainstream turbulence case was considered in this analysis.

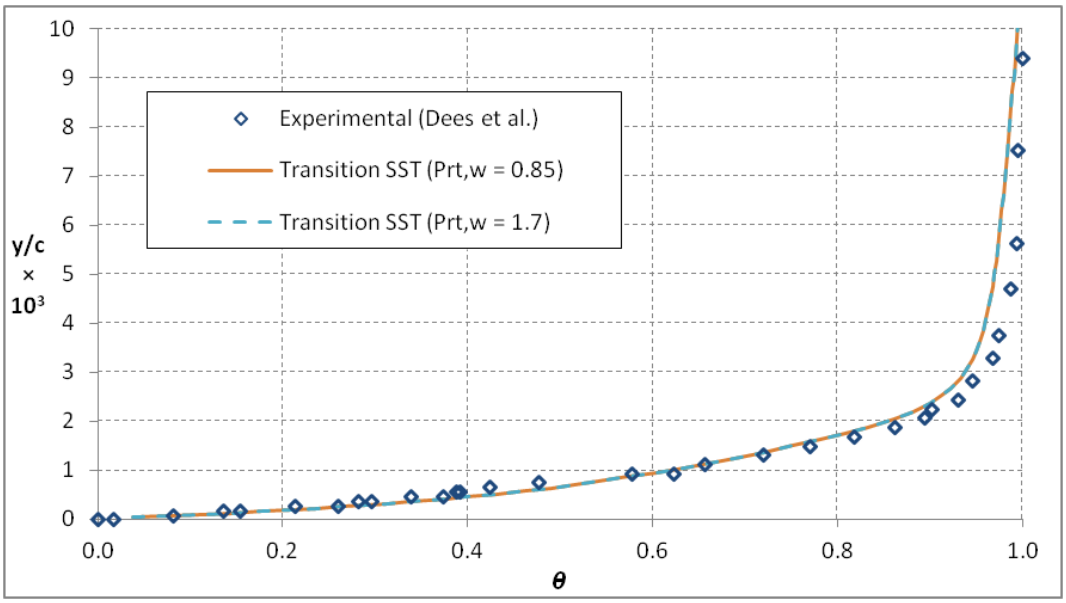

Figure 9.3.2: Computed thermal profiles at the SS2 position compared to the experimental data of Dees *et al*. [64] at *Tu* = 20% at differing $Pr_{t,w}$

As expected, the effect of increasing Pr_t was to decrease the thermal boundary layer thickness without affecting the hydrodynamic boundary layer. Figure 9.3.3 shows that for the PS2 position even doubling the turbulent Prandtl number did not thin the boundary layer enough to match the experimental data, though it was greatly improved in terms of the overall shape and the prediction of δ_{95T} (down to 13% error from 39%). However, Fig. 9.3.4 shows that at SS3 –

where the thermal boundary layer was already well matched – the variation in Pr_t produced a thermal boundary layer that was too thin. Note that the change in the boundary layer thickness required a refined θ scale.

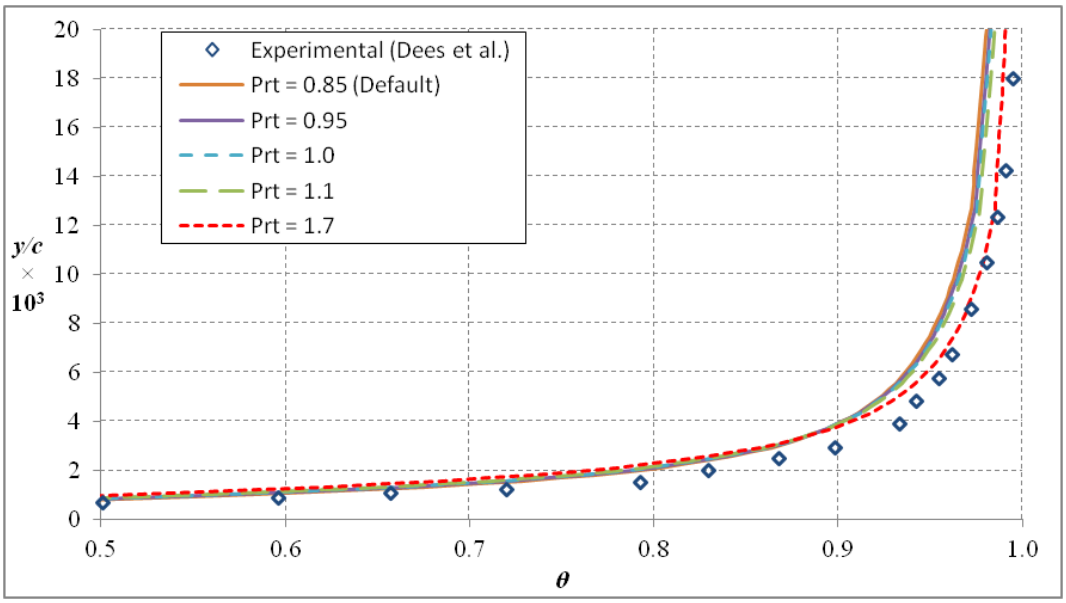

Figure 9.3.3: Variation in Pr_t using the Transition SST model and *Tu* = 20% compared to the experimental measurements of Dees *et al*. [64] at the PS2 position

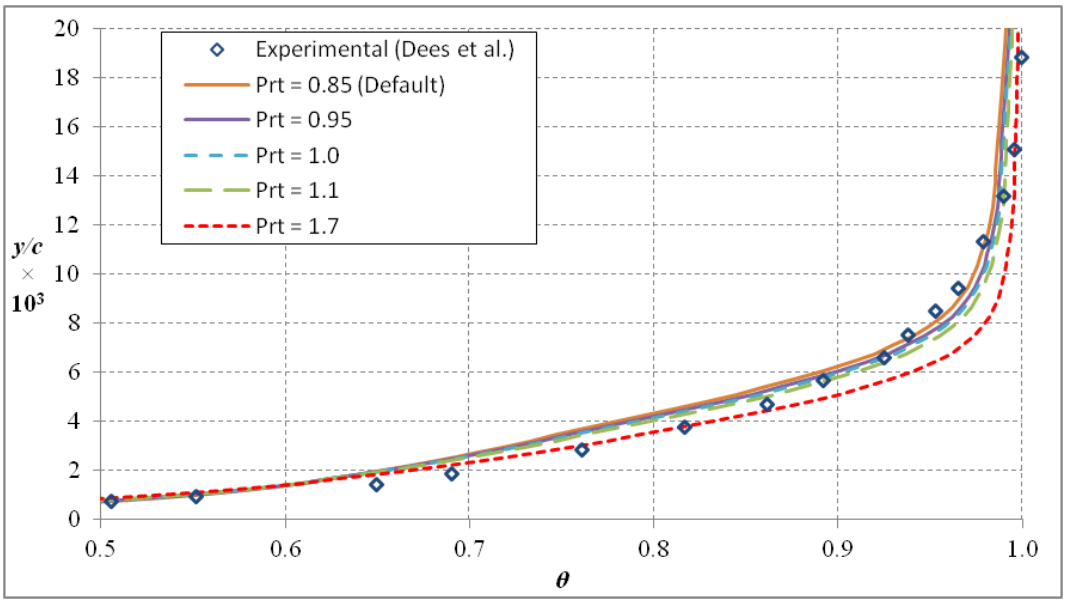

Figure 9.3.4: Variation in Pr_t using the Transition SST model and *Tu* = 20% compared to the experimental measurements of Dees *et al*. [64] at the SS3 position

Because matching one position was detrimental to others, there was no single Pr_t that could produce good predictions everywhere. When considering the SS alone, there was an apparent optimal value for Pr_t that produced the best average deviation from the experimental boundary layer ratio at Pr_t = 0.95. However, as shown in Fig. 9.3.5, the PS would require even an even greater increase in Pr_t to reach an optimal value, at substantial detriment to the SS performance.

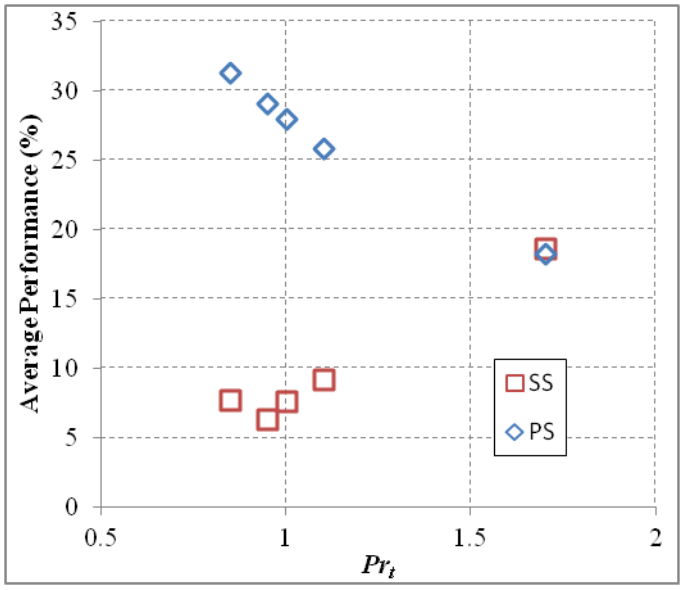

Figure 9.3.5: Average performance of the Transition SST model with variation of Pr_t for the SS and PS individually at Tu = 20%

Increasing Pr_t had an unexpected effect on Nu. Because the effect was to make the boundary layer thinner, the expectation was that it would slightly increase the heat transfer coefficient. However, it had more effect than predicted, and in the opposite direction. Figure 9.3.6 shows that increasing the turbulent Prandtl number to 1.7 decreased Nu by 10-25% over the vane surface. This means that using an elevated Pr_t value in an attempt to better match the thermal boundary layer would likely be detrimental to an overall effectiveness study, where h_0 is just as – if not more – important as matching the thermal fields off-the-wall. It should also be noted that based on the work of Liu *et al*. [65], increasing the turbulent Prandtl number may have a detrimental effect on the prediction of η.

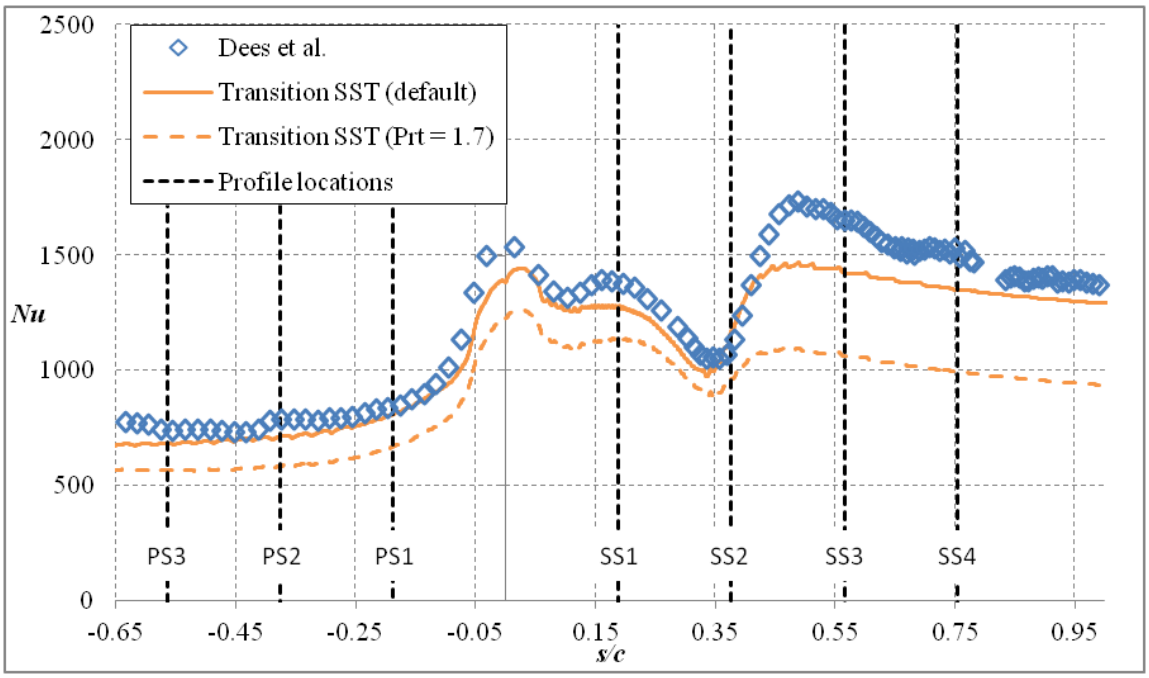

Figure 9.3.6: Effect of Pr_t variation on *Nu*

Chapter 10 – Conclusions

This study has approached the film cooling of gas turbine blades using both computational and experimental methods to improve the understanding of film cooling physics. The use of a new matched Biot number model with realistic internal and external cooling allowed new insight into the conjugate effects that impact the surface temperature. A configuration using a single row of holes on the pressure side and another which employed many film cooling holes over the entire vane surface were employed. Adiabatic effectiveness was also measured for both configurations, which allowed a superposition analysis to be performed for the pressure side.

The interaction of cooling jets with turbulence generated by upstream jets was seen to produce substantial changes in the adiabatic effectiveness. To better understand the flow conditions that caused these changes, the mean velocity, RMS velocity, and turbulence integral length scale were measured at two positions on the suction side immediately upstream of the cooling holes. While previous studies had investigated the effect of upstream cooling on downstream film injection, no such study had investigated this effect in conjunction with the strong acceleration imposed on the flow passing over the suction side of the vane.

Computational tools are increasingly important in the design of advanced gas turbine engines. Part of the process of integrating these tools into the design process requires validation of the simulation so that their reliability can be assessed and improvements can be made to the model. To that end, two

configurations were simulated and compared to past experimental work. Very few conjugate computational studies have the luxury of experimental backing, so each new study using the matched Biot number technique provides ideal data for conjugate code validation. Additionally, because CFD solves the entire domain, it can be used to investigate flow behavior that may be otherwise difficult to measure. The first part of the computational work focused on a single row of holes on the suction side of the vane. This configuration was used for validation, but it also lead to interesting insight into the interaction of the film cooling jets with the thermal boundary layer. The second configuration simulated the showerhead region.

Though there has been much work into the refinement of RANS models for use in gas turbines, there has been little work comparing their performance on the basis of predicting the correct thermal boundary layer. The final portion of this study sought to remedy this by comparing the performance of several different RANS models to experimental data. Additionally, the variation of the turbulent Prandtl number was explored as a possible means of improving the predictions.

10.1. PS2 only configuration

Typically, η values peak between $0.4 < I < 0.8$ for a flat plate (depending on injection angle and mainstream turbulence), but no peak was apparent in these measurements for measured values as low as $I = 0.3$. This was consistent with past studies performed with much stronger concave curvature and low mainstream turbulence. Increasing momentum flux ratio reduced adiabatic

effectiveness for the measured range. There was some evidence that the $I_{PS2} \times \cos^2(\alpha) > 1$ condition for the highest momentum flux ratios (3.2 and 6.8) was bringing the coolant back toward the wall as predicted by the analysis of Ito *et al.* [89]. It was unknown if these predictions would hold in the presence of high mainstream turbulence and with a more mild curvature.

The overall effectiveness results showed that the pressure side performance was relatively insensitive to coolant flow rate. This was because the reduction in adiabatic effectiveness was balanced by improved internal cooling, so the only notable changes occurred very near the holes. There, through-hole convective cooling provided increased cooling with flow rate. The overall effectiveness measurements also showed that there were substantial span-wise temperature gradients present. These gradients had been demonstrated for the suction side, but because h_f values are expected to be lower on the pressure side it was not known if it would remain true. Increasing the coolant flow rate eliminated the span-wise temperature gradient.

10.2. Fully cooled configuration

This portion of the study provided the first overall and adiabatic effectiveness results for a film cooling configuration representative of a 1st stage turbine vane. Five momentum flux ratios were measured, and the data were compared to the results of simpler film cooling configurations. The internal impingement cooling was tied to the total coolant flow rate because all the coolant entering the vane exited through the film cooling holes.

The adiabatic effectiveness performance was consistent with past results for the showerhead region of the vane with the exception of the SS gill row of holes. The current configuration displayed reduced adiabatic and overall effectiveness compared to the showerhead alone, probably because of changes to the internal flow feeding the holes. This change extended to the overall effectiveness measurements in the region. The showerhead displayed the characteristic “build-up” effect often seen for the stagnation region. The continued addition of coolant with span-wise momentum caused a portion of the vane to be protected from the mainstream almost completely, which resulted in very high effectiveness that improved continuously with momentum flux ratio. However, increased momentum flux ratio also showed that the vane lacked sufficient cooling holes to achieve span-wise periodicity. This showed that the usual assumption of span-wise uniformity was not accurate for vanes with fewer, large holes similar to the one used for this study.

Downstream holes showed separation at higher coolant flow rates, though the change in momentum flux ratio for the SS holes was small so they were not affected as strongly as the PS holes. The downstream holes also showed that the near-wall flow had a substantial amount of span-wise velocity imparted to it by the action of the showerhead. Even more than 30 hole diameters downstream subsequently injected holes displayed a span-wise component to their velocity. This was especially apparent on the SS where jet momentum flux ratios were lower.

The overall effectiveness results showed that the PS was insensitive to coolant flow rate, which was an unexpected result. The SS showed improved overall effectiveness with increasing momentum flux ratio, which was similar to past work using a single row of holes on the same vane that showed the internal cooling would more than compensate for loss of adiabatic effectiveness. The combined effect of through-hole convective cooling and the built up coolant flowing span-wise over the surface meant that the leading edge region had the lowest temperatures. Because this region typically has the highest heat load, this would not necessarily be expected.

Overall effectiveness was also measured without film cooling. This allowed the contribution of internal cooling to be evaluated separately. Because of the lower external heat transfer coefficients, the PS had much higher ϕ_0 values than the SS (0.5-0.6 vs. 0.3-0.5). These measurements also helped to explain why the pressure side overall effectiveness was insensitive to coolant flow rate. The internal cooling did improve continuously with coolant flow rate, as expected. Because the adiabatic effectiveness levels remained approximately the same, this meant that the culprit had to be increasing heat transfer augmentation due to film injection. An analysis of the increase in heat transfer augmentation required showed that $1.5 < h_f/h_0 < 2.0$ could produce the observed behavior, which was not unreasonable based on the data for multiple rows of injection on the PS of Ames [35], who measured the heat transfer augmentation for a C3X with showerhead and downstream film cooling.

Comparison to data for the SS3 row of holes alone showed that there was a significant effect of upstream cooling. The increased boundary layer thickness and turbulence levels apparently caused a reduction in performance near the holes. This was because fluid in the boundary layer has a lower momentum than the mainstream, so the flow injected by the film cooling holes penetrates farther from the wall before turning. However, the additional coolant from upstream holes meant that the fully cooled configuration out-performed the SS3 alone except for a small region near the holes at the lowest flow rate. For the overall effectiveness, it was shown that both cases had the same relative performance from film cooling by comparing the ratio ϕ/ϕ_0. This indicated that the changes in adiabatic performance were not important for the surface temperature.

A superposition analysis was performed using the pressure side data combined with the showerhead alone data from a past study. The analysis showed that because superposition does not account for the enhanced mixing from the turbulence generated by upstream injection, it was not able to properly predict the performance, and was increasingly off for increasing coolant flow rates.

Lastly, the 1D model proposed by Williams *et al.* [21] was applied to the fully cooled configuration. The predictions combined measurements of η and ϕ_0 to generate values for ϕ. This form of analysis would be highly beneficial because a single measurement of ϕ_0 could be applied to many different η configurations. However, the results of the analysis showed poor agreement with experimental results. This was in contrast to past studies that had shown that the model could

work for some limited circumstances (though these circumstances were conflicting). Other than the weakness of the 1D assumption, the model could have produced spurious results because it neglects the effect of heat transfer coefficient augmentation due to film cooling. There was also some uncertainty in the correct value of the coolant warming factor.

10.3. Velocity measurements on the SS

For the position directly upstream of the SS2 row of holes, film injection from the showerhead increased the boundary layer thickness 50-250%. This wide variation was a function of the position of coolant jets from upstream, not a direct effect of blowing ratio. This was shown by measuring multiple span-wise positions, which demonstrated a dependence on the position of a coolant stream from the showerhead. The boundary layer remained thinner than the cooling hole diameter, so alone this change would not dramatically affect the film injection from SS2. However, there was a clear effect on the RMS velocity. Near the wall (y/c < 0.0005) the increased turbulence was substantial, but not a function of coolant flow rate, so it was probably more a function of the transition to a turbulent boundary layer. Farther from the wall, the RMS levels were also greatly increased more than two hole diameters off the wall, which would substantially affect coolant injected at this position. The large increase in turbulence levels without a correspondingly large increase in the boundary layer thickness was an interesting and unexpected result. The level of turbulence augmentation and the height off-the-wall where it was measured increased with momentum flux ratio.

The effect of mainstream turbulence was shown to be a somewhat uniform increase in the RMS velocity throughout the boundary layer. Film injection was also shown to decrease the integral length scale. This was because of the small scale turbulence generated by film injection mixing with the larger scale eddies from the mainstream. However, even at the highest coolant flow rate the length scale remained substantially larger than the film cooling holes, so the large mainstream eddies would force oscillation of the jet, producing apparent jet diffusion (as demonstrated by Cutbirth and Bogard [91]).

At the position just upstream of the SS3 row of holes, it was shown that showerhead injection had no measureable effect on the mean velocity profile. This was probably because even without film injection, the boundary layer at this position was fully turbulent. There was a small effect on the RMS profile for $y/c > 0.01$ ($y/d > 0.8$), so there would be a small effect on the injected coolant. Much more important was the action of the SS2 row of holes. When this row was active, the boundary layer was greatly thickened (by about 50% or 0.5 d). Probably because of the increased separation from the wall, when the SH was active in addition to the SS2 row of holes the boundary layer was even thicker. The injection of coolant from SS2 also strongly affected the RMS profile, and like the upstream position, the RMS levels increased with momentum flux ratio. Here, the enhanced turbulence levels extended more than 3 d off the wall. The turbulence length scales were affected similarly to the upstream position, though there was no dependence on the source of the upstream injection. For all cases the length scales remained larger than the film cooling hole diameter.

10.4. Suction side only simulations

Adiabatic and overall effectiveness results were simulated using the *k-ω* SST model with low Reynolds number corrections and compared to the data of Williams *et al.* [21]. As is common to RANS simulations, the adiabatic effectiveness results showed much less jet diffusion than the experimental measurements. This resulted in over-prediction of the performance for an attached jet and under-prediction of the performance of a separated jet. Because adiabatic effectiveness was not well matched, the overall effectiveness also showed a stronger influence from the jets than the experimental measurements. However, between the cooling jets and for separated jets there was agreement with the measurements within approximately 0.04. This indicated that at least the internal cooling was well predicted.

Analysis of the results lead to a realization that in the case of a separated jet there was still a measurable effect on the overall effectiveness due to the presence of the jet. This was an interesting result because conventional analysis using T_{aw} would predict that for $\eta = 0$ there would be no impact on the surface temperature. The CFD results were used to investigate the interaction of the separated jets. It was apparent that the thermal boundary layer was still interacting with the coolant jet, possibly due to the action of the counter-rotating vortex pair that accompanies stream-wise oriented coolant jets. It was found that there was no location between the jet and the wall that was as warm as T_{aw}, so the adiabatic wall assumption would produce widely inaccurate predictions of the heat flux into the wall. This was shown to be true even at more moderate coolant

flow rates. Though T_{aw} was found to be a good approximation for a more realistic momentum flux ratio of I = 0.35, for lower momentum flux ratios it was shown to be too cold.

10.5. Showerhead only simulations

This simulation compared a single momentum flux ratio, I^* = 0.77, to the experimental data of Nathan *et al.* [33]. “Adiabatic” effectiveness was simulated using a low conductivity conjugate model because the experimental data did not have a conduction correction. The changes caused by use of low conductivity model instead of a truly adiabatic surface were shown to be small except for very near the holes. This was also the first study to simulate overall effectiveness for a showerhead and compare to experimental data.

The agreement with the experimental data was very poor. The adiabatic effectiveness was greatly over-predicted. This was attributed to a failure to predict the correct level of jet separation in addition to the usual lack of jet diffusion. It was also possible that the experimental data were not span-wise periodic, which would cause additional error from the simulations because of the periodic condition imposed on the model. The result was η values 0.2 or more above the experiments. The overall effectiveness results were nearly as bad, typically 0.1 or more above the measurements. The overall effectiveness was not as far off because the external cooling was only one part of the overall effectiveness. Because this configuration used the same internal cooling configuration as the SS3 alone case, it is reasonable to assume that because the

SS3 alone case simulated the internal cooling well that the SH alone case did as well.

Off-the-wall temperature profiles showed that, like the SS3 alone case, the adiabatic wall temperature was not always the correct driving temperature where jet separation was evident. Additionally, considerably downstream of injection there were locations where the coolant was being warmed by the wall significantly. This situation meant that T_{aw} was inappropriate as the driving temperature for heat transfer.

Even though the effectiveness results were considerably off from the measurement, this configuration still provided some insight into a quantity that is very difficult to measure in the showerhead: the heat transfer coefficient augmentation due to film injection. The simulations showed that there were many locations where h_f/h_0 was greater than 2, indicating that the benefit of film cooling would be substantially degraded. However, overall effectiveness measurements still show substantial benefits from film cooling. These regions corresponded to the lee-ward side of the span-wise oriented film cooling jets. However, the simulations also showed regions with $h_f/h_0 < 1$ under the jets, which was not considered realistic. This may have been a result of using T_{aw} to compute h_f, because at these positions heat flux was reversed (*i.e.*, the wall temperature was greater than the jet temperature, something that never happens with T_{aw}).

10.6. Turbulence model evaluation

Six RANS turbulence models (standard k-ω and k-ε, k-ω SST, realizable k-ε, RNG k-ε, and Transition SST) were evaluated in terms of their ability to predict the thermal profiles off-the-wall of a turbine vane by comparing to the experimental data of Dees *et al*. [64]. This was undertaken to fill a gap in available data evaluating the thermal performance of RANS models. Because the development of the thermal boundary layer is linked to the hydrodynamic boundary layer, the results were contextualized by also comparing the performance for the mean velocity profile. Additionally, the RMS velocity measurements were converted into k and compared to the results of the simulations. All of these comparisons were made for low and high mainstream turbulence. Lastly, an attempt was made to improve the thermal boundary layer predictions by adjusting the turbulent Prandtl number.

10.6.1. Low mainstream turbulence

None of the models were able to predict the correct heart transfer coefficient on the pressure side. This was probably because the simulations greatly over-predicted the action of Taylor-Görtler vortices, which lead to Nu values ~ 40% greater than measured. Similar simulations performed as part of the Dees *et al*. series of studies did not have this problem, but they may not have been predicting the formation of Taylor-Görtler vortices. The use of low Reynolds number corrections allowed the k-ω SST model to correctly predict the heat transfer coefficient on the SS until very near transition. The location of transition was correctly predicted by Transition SST, which matched the heat transfer

coefficient very well up to that point on the SS. The *k-ε* models were “fully turbulent” so they did poorly at predicting *Nu* on the suction side prior to transition. However, after transition the fully turbulent models were close to the measurements while the Transition SST and *k-ω* SST models substantially under-predicted *Nu* (over 20%). This was not expected based on the skin friction results presented in the original formation of the model [106], but was observed by Dees *et al*.

On the pressure side, the turbulence models all generally did reasonably well predicting the mean velocity profile, though the *k-ε* models over-predicted the boundary layer thickness. Because the acceleration on the PS was strong enough to suppress transition to turbulence, it was not entirely unreasonable to expect that the turbulence models may predict the correct behavior, though the “fully turbulent” models did perform worse, as expected. Thermal performance was not as good, with all the models predicting much thicker boundary layers with differently shaped profiles than the measurements. The *k-ω* models did comparatively better, with 50% over-prediction compared to the 200-300% over-prediction by the *k-ε* models.

Like the PS, the SS1 position was laminar; however, there was less expectation that the turbulence models would be able to work here. Therefore, the fact that the turbulence models did well predicting the mean velocity profile was not expected. The thermal boundary layer was also well predicted. However, by the SS2 position transition was starting and the models were all way off from the measured mean velocity profile, which was somewhat odd for the Transition

SST model that had correctly predicted *Nu* at this position. The “fully turbulent” models showed an early transition, so they were much thicker than measured values (as expected). Even though the mean velocity profiles were completely wrong, the thermal profile was predicted almost exactly by the *k-ω* models. After transition no models were able to predict the mean velocity or thermal profile with any accuracy, even though the *k-ε* models matched experimental values for *Nu*.

The *k* profiles were not well predicted. As would be expected, the fully turbulent models greatly over-predicted the levels of *k* (by several orders of magnitude). For the laminar positions, the *k-ω* models at least predicted that there was very little turbulence, though Transition SST actually showed less turbulence than was measured experimentally. However, after transition they over-predicted the level of production, though they approximately matched the location where *k* fell off outside the boundary layer. The *k-ε* models predicted the correct *k* profile shape, but for a much thicker boundary layer with higher initial *k* values.

10.6.2. High mainstream turbulence

All of the models correctly captured the fact that increased mainstream tumescence increased *Nu* over the laminar portion of the vane and had no measureable effect downstream of transition. The *k-ω* models better predicted *Nu* on the PS, but *k-ω* SST predicted a continuous increase for $s/c < -0.25$. The *k-ε* models still under-predicted *Nu* on the PS, though they also showed an unrealistic increase for the downstream portion of the vane. Because the low Reynolds number corrections have not been calibrated for a wide range of flows,

it was not surprising that for high mainstream turbulence the *k-ω* models predicted the immediate onset of transition like the fully turbulent *k-ε* models. The Transition SST model once again correctly predicted the location of transition, an impressive accomplishment given the number of factors that can affect transition. However, it predicted *Nu* values that were ~ 10% low prior to transition. After transition, Transition SST was once again under-predicting *Nu* by 20% or more while the other models matched the results within uncertainty. The exception was the standard *k-ω* model, which over-predicted *Nu* slightly.

For this turbulence condition the turbulence models did a better job of predicting the mean velocity profiles, and were also generally close to matching the thermal profiles. However, they typically predicted a thermal boundary layer that was too thick compared to the experimental measurements. On the suction side, only the Transition SST model was very close to the mean velocity profiles (and in fact it matched within experimental uncertainty at several positions). The thermal profiles were once again typically far too thick, though once again Transition SST showed good agreement.

An interesting aspect of the boundary layers for this vane was that the thermal boundary layer was shown by Dees *et al*. [64] to be generally thicker than the hydrodynamic boundary layer. This was due to the effect of acceleration on the flow, creating a region between the edge of the hydrodynamic boundary layer and the edge of the thermal boundary layer, called the “superlayer”, where molecular diffusion is the dominant transport mechanism. While the turbulence models did not always match the thermal profiles very well, they did correctly

predict that the thermal boundary layer was much thicker than the hydrodynamic boundary layer. They also correctly predicted that the effect of mainstream turbulence was to greatly increase the thickness of this layer without affecting the hydrodynamic boundary layer nearly as much.

Though even the “fully turbulent” models correctly predicted that increased mainstream turbulence increased the overall *k* levels in the boundary layer and mainstream flow, their overall performance was typically poor. On the pressure side, the standard and SST *k-ω* models were reasonably close to the measurements near the wall on the PS, and near the measurements for the whole boundary layer at the PS3 position, but all the other models under-predicted the levels of turbulence. On the suction side after transition, the models were generally close to the measurements in the boundary layer, but tended to over-predict the level of freestream turbulence. Overall the *k-ω* SST and RNG *k-ε* performed the best, though Transition SST also did well.

10.6.3. Turbulent Prandtl number variation

It was shown that using an experimental correlation to match the correct behavior of Pr_t in the boundary layer rather than assuming a constant $Pr_t = 0.85$ (as is typically done) had no impact on the thermal boundary layer profile. This meant that the use of a constant Pr_t was well justified. The ratio of thermal to hydrodynamic boundary layer thicknesses showed that for most locations on the vane the turbulence models the default value of $Pr_t = 0.85$ was too small. The Transition SST model was tested with several higher values of Pr_t. As expected, the increased turbulent Prandtl numbers decreased the thermal boundary layer

thickness. However, because some locations on the vane were closer to the experimental value than others, there was not any one Pr_t that would work for all positions. A Pr_t of 0.95 was shown to be optimal for SS performance, but even doubling Pr_t to 1.7 did not match the thermal boundary layer measurements on the PS.

It was also shown that increasing the turbulent Prandtl number caused *Nu* to drop. This was counterintuitive because in most situations decreasing the thermal boundary layer thickness would increase the local heat transfer coefficient. The implication of this finding is that even if Pr_t were adjusted to optimize the thermal boundary layer, the values of *Nu* would be altered as well. For an overall effectiveness simulation, both parameters are important, so the modification of Pr_t must be considered carefully.

10.7. Recommendations for future work

One of the more interesting findings of this work was the apparent interaction of the thermal boundary layer with the film cooling jets. Though Dees *et al.* [103] attempted to make measurements that would verify this phenomenon, further study is warranted. Unfortunately, such measurements for the current configuration could not be completed in time, though they are forthcoming. Because the assumption that the adiabatic wall temperature is appropriate as the driving temperature for heat transfer is considered fundamental to film cooling, experimental verification that it is not the correct driving temperature for heat transfer is very important. Matched Biot number models provide the only known

means of evaluating this assumption. Additionally, in cases where T_{aw} is not appropriate, direct measurement of the wall heat flux under and around the jet would be a valuable step towards finding the correct driving temperature. This line of investigation would also be instrumental for determining a set of criteria that could be used to determine when the T_{aw} can be used and potentially a correction for cases where it is inaccurate.

Additional flow rates for the showerhead case would be instructive. However, because the experimental data are not span-wise periodic, this will require the simulation of the full vane. Additional advantages of this setup would be the evaluation of internal flow that is very difficult to measure experimentally. Any new simulations would also be able to take advantage of the RANS evaluation performed as a part of this work.

Completing the database for the C3X vane requires that h_f be measured for some or all of the conditions that have been tested over the last few years. Then all of the traditional measures of film cooling performance would be available (and NHFR could be computed). This may make it easier to determine the best use for overall effectiveness measurements in the design process, and will give another point of reference for computational simulations using these data as validation.

The performance of the RANS models for an uncooled vane was useful, but an extension of this analysis to a film cooled vane would be even more instructive. Some thermal data from Dees *et al.* [103] already exist, but it may be better to compare to the forthcoming thermal jet profile results. Such a simulation

may also provide a means of comparing more advanced methods for turbulent Prandtl number adjustment, such as the laterally varying model of Liu *et al.* [66]. However, the results of this study showed that matching the thermal boundary layer (which was too thick) and the film cooling jets (which are typically too thin) may be impossible using the turbulent Prandtl number. A better representation of thermal transport through the implementation of a Reynolds Averaged energy equation may be the preferred approach. Additionally, the use of more advanced RANS models with anisotropy calculations may produce improved predictions without modification of Pr_t. Finally, it would be instructive to compare an LES simulation using the same model to these results. This would allow a characterization of the benefit of the additional computational complexity.

Appendix A – Documentation for TC Locator Program

This program was written for Python 2 and requires Scipy and Numpy. The basic purpose of the code was to automate the process of locating a thermocouple in an IR image based on an initial guess. It operates on the assumption that the best parabolic curve fit through the data and the measurements will occur at the real location of the thermocouple.

A.1. Configuring the program

There are two configurations files for TC locator. The first (commonly tc-setup.txt) defines the search parameters and the location of the TC data. The program will search any text file given as the configuration file, ignoring lines that begin with #. The first uncommented line should be the relative path to the .csv file with the TC data and initial locations (described later). Absolute paths might work but the code has not been tested for anything but a file that resides in the same directory as the “tc-locator-v2.py” file. The second line should be the number of the first image file to use in the source data. Often the first few images are locating images that should not be used for calibration. The third line should be a comma delimited list of numbers that represent the distance that should be searched away from the initial guess. For example, “1, 2, 3” would tell the program to search three times, once looking only one pixel away (a 3x3 box), once two pixels away (a 5x5 box), and so on.

The next line is the “uniformity parameter”. This is the average over all images of the maximum temperature difference over the search area for each

image. It was intended as a means to determine if the thermocouple was in a region with too strong of a gradient to produce a good calibration, but the relation between uniformity parameter and calibration goodness has been hard to define. The limit given in the calibration file will determine when the code will “fail” a calibration, but won’t affect anything else.

The next line tells the program what scheme to use for the output file names. For example, “IRdata.csv” will produce a set of files named like “TC1-IRdata.csv” and “TC2-IRdata.csv”, where the first portion of each file name will be the name of the thermocouples defined in the TC data file.

The last configuration option reduces the output generated during operation. It is recommended that this always be set to TRUE.

The other configuration file is the TC data. This must be a CSV file. Each column must start with the name of the thermocouple. The name appears in the output as well. The second two rows of each column are the *x* and *y* pixel to use as the initial guess for the thermocouple location. All subsequent rows are the measured temperature values from the experiment. The first point must match the first image number given in the configuration file or the calibrations will not be any good.

A.2. Running the program

To operate the TC locator, place “tc-locator-v2.py”, a setup file, and the TC data CSV into the same folder with the .mat files for the test’s IR images. Start a command prompt and change directory to where .py is located. If Python

is installed properly, just type “python tc-locator-v2.py” to start the program. For fresh installs of python the python executable may need to be added to the system path. The program will ask for the location of the configuration file. Any text file can be used, but the default is “tc-setup.txt”. The code should run and create the desired output without issue.

The output file is a CSV file that has the IR temperature from the original guess position, and the best fit position for each search grid. The variance (r^2) for each fit is also given in addition to the uniformity parameter. These data should be used with caution. The code cannot distinguish between fits that are good because the data were very clean and fits that are good because a film cooling hole was in the search area and had the same temperature throughout the test. Always check the resulting location against the original image to make sure that they are reasonable.

Appendix B – Additional Notes on the FLUENT Data Reduction Process

One of the challenges facing the user of CFD tools is extracting the useful bits of data from the immense quantity of computed information found in the solution. This section outlines the process used to collect data for this study and describes the tools written to aid in data processing.

B.1. Extraction of surface data

Most of the time, the most interesting results are surface values of quantities such as temperature or heat flux. Unfortunately, FLUENT does not make it easy to "unwrap" a complex surface into an *s-z* plane. In fact, for the SS3 portion of the study no attempt was made to do so and the contours were obtained by aligning the viewing plane with the holes and taking a screen-shot. Because the vane was nearly flat at the position of the SS3 holes, the error introduced to the *s/d* axis by this was minimal (this was later confirmed using the technique outlined here). For the SH simulations it was necessary to create a program to unwrap the surface into something flat that could be compared to the experimental data.

The first step in extraction of surface data was to use FLUENT's built in plotting function to save an "*x-y* plot" of the desired values. Because these plots only include one coordinate with the value, it was also necessary to save files containing the *x* and *z* coordinates (the *y* coordinate was used as the plotting vector). The output of this process is three ".xy" files. This process was

automated using a FLUENT journal file, “get-surface-temps.jou”, which may be modified to collect other surface data.

The program “surfaceDataOrganizer.py” reads in these files and produces output .csv files for the PS and SS containing the *x*, *y*, and *z* coordinates along with the computed *z/d*, *s*, and *s/d* values for each point. The operation of this program is described more fully in the comments within the python file. Note that there is a known problem with the *s/d* computation. Cumulative addition error from *s/d* = 0 can significantly increase the apparent dimension of the vane. This error is most significant when large numbers of nodes are found within a very small *s/d* range (*i.e.*, a highly refined mesh). There are many constants used in the computation of the split between SS and PS that are unique to the C3X geometry.

The output from the surface data organizer was used to construct “sd.xls”, “zd.xls”, and “eta.xls” files for use with the “etaplot.m” Matlab file used for creating contours from experimental data. The operation of this program is described in the data processing documentation for experimental data processing. In addition to a contour plot of the data, Matlab also output “plotdata” files that contained the points used as backing data for the plot. This set of data are greatly reduced from the number of points used to generate the contour and occur at fixed positions based on the rules in “etaplot.m” , so they allowed easy comparisons of different surface quantities from different simulations (*e.g.*, the heat flux and T_{aw} could be used to compute h_f).

B.2. Extraction of thermal and velocity profiles

Though the full velocity, temperature, and turbulence fields were produced in the FLUENT solution, it was necessary to extract only the values along a line corresponding to the experimental measurements. Because the mesh quality varied somewhat across the span of the vane, it was necessary to average the values laterally to produce a smooth profile. The method chosen to accomplish this was to create rakes across the span at pre-defined *y* positions (where *y* was the wall-normal coordinate, not the *y* coordinate in the FLUENT mesh) for each measurement position, extract the data from these lines, and average them together.

The definition of the lines used to extract the data was done in the "location" tab of the "boundary layers" Excel file. At each measurement location, 100 points (in mesh *x*-*y* coordinates) were positioned off-the-wall. These points were selected somewhat arbitrarily, with more points concentrated near the walls. At each of the 100 *x*-*y* points, a rake containing 100 points across the *z* span was created for data collection. The creation of these 700 rakes was handled by a FLUENT journal file. Even writing the journal file would have taken too long, so a python program, "writeBLjou.py" was written to generate a journal file for each measurement position. These files were tested individually before being combined into "generate-Dees-profiles.jou", which would output .xy files for velocity, temperature, and u_{rms} data.

As with the surface data, these .xy files required further treatment before they were useful. Another python program, "convertFulentOutput2.py" was used

to convert each rake into a .csv file. These files were then opened and used to create the lateral average data at each position. This process could probably could have been automated, but there was enough variation in the output of the .xy files (“100 point” rakes contained anywhere from 5 to 103 points for some reason) that it was decided that it would take too long. The operation of the fluent conversion program is described in the code comments for that file. Parts of this code were used in the surface data organizer.

These average profiles are found in the data file associated with Chapter 9. Note that to normalize the thermal profiles it was necessary to get the surface temperature using the surface data process outlined in B.1.

References

[1] Siemens AG. (2011, December) Siemens Global Website. [Online]. http://www.siemens.com/entry/cc/en/turbine.html

[2] Office of Energy Statistics, "Annual Energy Review," U.S. Energy Information Administration, Washington D.C., DOE/EIA-0384(2010), 2010.

[3] Assistant Administrator for Energy Statistics, "Electric Power Annual," U.S. Energy Information Administration, Washington D.C., DOE/EIA-0348(2009), 2009. [Online]. http://www.eia.gov/cneaf/electricity/epa/epa_sum.html

[4] G. B. Brayton, "Improvement in Gas-Engines," 125166, April 2, 1872.

[5] Michael J. Moran and Howard N. Shapiro, *Fundamentals of Engineering Thermodynamics, 4th ed.* New York: John Wiley & Sons, Inc., 1999, pp. 441-477.

[6] Duk. (2006, March) Wikipedia.org. [Online]. http://en.wikipedia.org/wiki/File:Brayton_cycle.svg

[7] L. S. Langston, "Gas Turbine Industry Overview for 2010," IGTI, Storss, CT, 2010.

[8] Special Materials Corporation, "Inconel Alloy X-750," Product Spcifications SMC-067, 2004.

[9] R. S. Bunker, "Basics of Gas Turbine Heat Transfer," ASME Turbo Expo, Copenhagen, Denmark, Tutorial Session 2012.

[10] J.-C. Han, S. Dutta, and S. V. Ekkad, *Gas Turbine Heat Transfer and Cooling Technology*, 1st ed. New York, USA: Taylor & Francis, 2000.

[11] E. J. Terrell, "A Study of the Convective Heat Transfer through Film Cooling Holes of a Gas Turbine Leading Edge," The University of Texas, Austin, M. S. Thesis 2004.

[12] R. J. Goldstein, "Film Cooling," in *Advances in Heat Transfer*.: Academic Press, 1971, vol. 7, ch. 5, pp. 321-379.

[13] T. F. Fric and A. Roshko, "Vortical Structure in the Wake of a Transverse Jet," *J. Fluid Mech.*, vol. 279, pp. 1-47, Nov. 1994.

[14] W. J. Mick and R. E. Mayle, "Stagnation Film Cooling and Heat Transfer, Including Its Effect Within the Hole Pattern," *Journal of Turbomachinery*, vol. 110, pp. 66-72, 1988.

[15] B. Sen, D. L. Schmidt, and D. G. Bogard, "Film Cooling with Compound Angle Holes: Heat Transfer," *Journal of Turbomachinery*, vol. 118, no. 4, pp. 800-807, October 1996.

[16] A. K. Sinha, D. G. Bogard, and M. E. Crawford, "Film Cooling Effectiveness Downstream of a Single Row of Holes with Variable Density Ratio," in *ASME International Gas Turbine and Aeroengine Congress and Exposition*, Brussels, Belgium, 1990.

[17] J. P. Sellers, "Gaseous Film Cooling with Multiple Injection Stations," *AIAA J.*, vol. 1, pp. 2154-2156, 1963.

[18] D. E. Metzger, D. I. Takeuchi, and P. A. Kuenstler, "Effectiveness and Heat Transfer with Full-Coverage Film Cooling," *J. Eng. Power*, vol. 95, pp. 180-184, Jul. 1973.

[19] F. E. Ames, "Aspects of Vane Film Cooling with High Turbulence: Part II - Adiabatic Effectiveness," *J. Turbomach.*, vol. 120, pp. 777-784, Oct. 1998.

[20] J. E. Albert, D. G. Bogard, and F. Cunha, "Adiabatic and Overall Effectiveness for a Film Cooled Blade," in *ASME Turbo Expo*, Vienna, Austria, 2004, pp. GT2004-53998.

[21] R. P. Williams, T. E. Dyson, D. G. Bogard, and S. D. Bradshaw, "Sensitivity of the Overall Effectiveness to Film Cooling and Internal Cooling on a Turbine Vane Suction Side," in *ASME Turbo Expo*, Copenhagen, Denmark, 2012, pp. GT2012-69110.

[22] P. R. Spalart, "Strategies for Turbulence Modelling and Simulations," *Int. J. Heat Fluid Flow*, vol. 21, pp. 252-263, 2000.

[23] O. Reynolds, "The Mean and Relative Motions of a Medium," in *Papers on Mechanical and Physical Subjects Volume III: The Sub-Mechanics of the Universe*. London, UK: Cambridge University Press, 1903, ch. V, pp. 42-53.

[24] L. D. Hylton, M. S. Milhec, E. R. Turner, D. A. Nealy, and R. E. York, "Analytical and Experimental Evaluation of the Heat Transfer Distribution Over the Surface of Turbine Vanes," NASA, Contractor Report 168015, 1983.

[25] L. D. Hylton, V. Nirmalan, B. K. Sultanian, and R. M. Kaufman, "The Effects of Leading Edge and Downstream Film Cooling on Turbine Vane Heat Transfer," NASA, Contractor Report 182133, 1988.

[26] P. C. Sweeney and J. F. Rhodes, "An Infrared Technique for Evaluating Turbine Airfoil Cooling Designs," *J. Turbomach.*, vol. 122, pp. 170-177, Jan. 2000.

[27] B. D. Mouzon, E. J. Terrell, J. E. Albert, and D. G. Bogard, "Net Heat Flux Reduction and Overall Effectiveness for a Turbine Blade Leading Edge," in *ASME Turbo Expo*, Reno, NV, USA, 2005, pp. GT2005-69002.

[28] T. E. Dyson, D. G. Bogard, J. D. Piggush, and A. Kohli, "Overall Effectiveness for a Film Cooled Turbine Blade Leading Edge with Varying Hole Pitch," in *ASME Turbo Expo*, Glasgow, UK, 2010, pp. GT2010-23707.

[29] J. E. Dees, D. G. Bogard, G. A. Ledezma, G. M. Laskowski, and A. K. Tolpadi, "Experimental Measurements and Computational Predictions for an Internally Cooled Simulated Turbine Vane," *J. Turbomach.*, vol. 134, no. 6, Nov. 2012.

[30] J. E. Dees, D. G. Bogard, G. A. Ledezma, G. M. Laskowski, and A. K. Tolpadi, "Experimental Measurements and Computational Predictions for an Internally Cooled Simulated Trubine Vane with 90 Degree Rib Turbulators," *J. Turbomach.*, vol. 134, no. 6, Nov. 2012.

[31] J. E. Dees, D. G. Bogard, G. A. Ledezma, and G. M. Laskowski, "Overall and Adiabatic Effectiveness Values on a Scaled Up, Simulated Gas Turbine Vane: Part I - Experimental Measurements," in *ASME Turbo Expo*, Vancouver, BC, Canada, 2011, pp. GT2011-46612.

[32] J. E. Albert and D. G. Bogard, "Measurements of Adiabatic Film and Overall Cooling Effectiveness on a Turbine Vane Pressure Side with a Trench," in *ASME Turbo Expo*, Vancouver, BC, Canada, 2011, pp. GT2011-46703.

[33] M. L. Nathan, T. E. Dyson, D. G. Bogard, and S. D. Bradshaw, "Adiabatic and Overall Effecitveness for the Showerhead Film Cooling of a Turbine Vane," in *ASME Turbo Expo*, Copenhagen, Denmark, 2012, pp. GT2012-69109.

[34] R. J. Goldstein and J. R. Taylor, "Mass Transfer in the Neighborhood of Jets Entering a Crossflow," *J. Heat Trans.*, vol. 104, pp. 715-721, Nov. 1982.

[35] F. E. Ames, "Aspects of Vane Film Cooling with High Turbulence: Part I - Heat Transfer," *J. Turbomach.*, vol. 120, pp. 768-776, Oct. 1998.

[36] J. Dittmar, A. Schulz, and S. Wittig, "Adiabatic Effectiveness and Heat Transfer Coefficient of Shaped Film Cooling Holes on a Scaled Guide Vane Pressure Side Model," *Int. J. Rotating Mach.*, vol. 10, no. 5, pp. 345-354, 2004.

[37] J. M. Cutbirth and D. G. Bogard, "Evaluation of Pressure Side Film Cooling with Flow and Thermal Field Measurements - Part I: Showerhead Effects," *J. Turbomach.*, vol. 124, pp. 670-677, Oct. 2002.

[38] F. M. White, *Viscous Fluid Flow*, 1st ed. New York, NY: McGraw-Hill, 1974.

[39] P. Martini and A. Schulz, "Experimental and Numerical Investigation of Trailing Edge Film Cooling by Circular Coolant Wall Jets Ejected from a Slot with Internal Rib Arrays," *J. Turbomach.*, vol. 126, pp. 229-236, Apr. 2004.

[40] W. D. York and J. H. Leylek, "Leading-Edge Film-Cooling Physics: Part I - Adiabatic Effectiveness," in *ASME Turbo Expo*, Amsterdam, The Netherlands, 2002, pp. GT2002-30166.

[41] S. Mathew, S. Ravelli, and D. G. Bogard, "Evaluation of CFD Predictions Using Thermal Field Measurements on a Simulated Film Cooled Turbine Blade Leading Edge," in *ASME Turbo Expo*, Vancouver, BC, Canada, 2011, pp. GT2011-46619.

[42] E. M. Smirnov and P. E. Smirnov, "Application of an Unstructured Navier-Stokes Code to Prediction of Adiabatic Effectiveness of Endwall Flush-Slot-Cooling for a Stator Vane Passage," *J. Comput. Appl. Math.*, vol. 215, pp. 577-585, 2008.

[43] F. Nemdili, A. Azzi, G. Theodoridis, and B. A. Jubran, "Reynolds Stress Transport Modeling of Film Cooling at the Leading Edge of a Symmetrical Turbine Blade Model," *Heat Trans. Eng.*, vol. 29, no. 11, pp. 950-960, 2008.

[44] L. D. Dobrowolski, D. G. Bogard, J. Piggush, and A. Kohli, "Numerical Simulation of a Simulated Film Cooled Turbine Blade Leading Edge Including Conjugate Heat Transfer Effects," in *ASME International Mechanical Engineering Congress & Exposition*, Lake Buena Vista, FL, USA, 2009, pp. IMECE2009-11670.

[45] V. K. Garg and A. A. Ameri, "Comparison of Two-Equation Turbulence Models for Prediction of Heat Transfer on Film-Cooled Turbine Blades," *Numer. Heat Trans., Part A: Appl.*, vol. 32, no. 4, pp. 347-371, May 1997.

[46] K. L. Harrison and D. G. Bogard, "Comparison of RANS Turbulence Models for Prediction of Film Cooling Performance," in *ASME Turbo Expo*, Berlin, Germany, 2008, pp. GT2008-51423.

[47] S. Na, B. Williams, R. A. Dennis, K. M. Bryden, and T. I-P. Shih, "Internal and Film Cooling of a Flat Plate with Conjugate Heat Transfer," in *ASME Turbo Expo*, Montreal, QC, Canada, 2007, pp. GT2007-27599.

[48] R. H. Ni et al., "Conjugate Heat Transfer Analysis of a Film-Cooled Turbine Vane," in *ASME Turbo Expo*, Vancouver, BC, Canada, 2011, pp. GT2011-45920.

[49] J. D. Heidmann, A. J. Kassab, E. A. Divo, F. Rodriguez, and E. Steinthorsson, "Conjugate Heat Transfer Effects on a Realistic Film-Cooled Turbine Vane," in *ASME Turbo Expo*, Atlanta, GA, USA, 2003, pp. GT2003-38553.

[50] B. Facchini, A. Magi, and A. S. del Greco, "Conjugate Heat Transfer Simulation of a Radially Cooled Gas Turbine Vane," in *ASME Turbo Expo*, Vienna, Austria, 2004, pp. GT2004-54213.

[51] G. A. Ledezma, G. M. Laskowski, and A. K. Tolpadi, "Turbulence Model Assessment for Conjugate Heat Transfer in a High Pressure Turbine Vane Model," in *ASME Turbo Expo*, Berlin, Germany, 2008, pp. GT2008-50498.

[52] L. Mangani, M. Cerutti, M. Maritano, and M. Spel, "Conjugate Heat Transfer Analysis of NASA C3X Film Cooled Vane with an Object-Oriented Code," in *ASME Turbo Expo*, Glasgow, UK, 2010, pp. GT2010-23458.

[53] J. S. Maikell, D. G. Bogard, J. D. Piggush, and A. Kohli, "Experimental Simulation of a Film Cooled Turbine Blade Leading Edge Including Thermal Barrier Coating Effects," *J. Turbomach.*, vol. 133, no. 1, Jan. 2011.

[54] S. Ravelli, L. Dobrowolski, and D. G. Bogard, "Evaluating the Effects of Internal Impingement Cooling on a Film Cooled Turbine Blade Leading Edge," in *ASME Turbo Expo*, Glasgow, UK, 2010, pp. GT2010-23002.

[55] G. A. Ledezma, G. M. Laskowski, J. E. Dees, and D. G. Bogard, "Overall and Adiabatic Effectiveness Values on a Scaled Up Simulated Gas Turbine Vane: Part II - Numerical Simulations," in *ASME Turbo Expo*, Vancouver, BC, Canada, 2011, pp. GT2011-46616.

[56] C. L. V. Jayatilleke, "The Influence of Prandtl Number and Surface Roughness on the Resistance of the Laminar Sublayer to Momentum and Heat Transfer," in *Progress in Heat and Mass Transfer*, U. Grigull and E. Hahne, Eds. London, UK: Pergamon Press, 1969, p. 193.

[57] B. E. Launder, "On the Computation of Convective Heat Transfer in Complex Turbulent Flows," *J. Heat Trans.*, vol. 110, pp. 1112-1128, Nov. 1988.

[58] SAS IP, Inc., "Enhanced Wall Treatment for Momentum and Energy Equations," in *ANSYS FLUENT Theory Guide 13*. Canonsburg, PA, USA: ANSYS, Inc., 2010, ch. 4.13.4.2, pp. 126-129.

[59] B. A. Kader, "Temperature and Concentration Profikes in Fully Turbulent Boundary Layers," *Int. J. Heat Mass Trans.*, vol. 24, no. 9, pp. 1541-1544, 1981.

[60] F. M. White and G. H. Christoph, "A Simple New Analysis of Compressible Turbulent Two-Dimensional Skin Friction Under Arbitrary Conditions," Air Force Flight Dynamics Laboratory, Dayton, OH, Technical Report AFFDL-TR-70-133, 1971.

[61] P. G. Huang, P. Bradshaw, and T. J. Coakley, "Skin Friction and Velocity Profile Family for Compressible Turbulent Boundary Layers," *AIAA J.*, vol. 31, no. 9, pp. 1600-1604, Sept. 1993.

[62] W. M. Kays, "Turbulent Prandtl Number - Where Are We?," *J. Heat Trans.*, vol. 116, pp. 284-295, May 1994.

[63] V. Yakhot, S. Thangam, T. B. Gatski, S. A. Orszag, and C. G. Speziale, "Development of Turbulence Models for Shear Flows by a Double Expansion Technique," NASA, Hampton, VA, USA, Contractor Report 187611, 1991.

[64] J. E. Dees, D. G. Bogard, G. A. Ledezma, G. M. Laskowski, and A. K. Tolpadi, "Momentum and Thermal Boundary Layer Development on an Internally Cooled Turbine Vane," *J. Turbomach.*, vol. 134, no. 6, Nov. 2012.

[65] C. -L. Liu, H. -R. Zhu, and J. -T. Bai, "Effect of Turbulent Prandtl Number on the Computation of Film-Cooling Effectiveness," *Int. J. Heat Mass Trans.*, vol. 51, pp. 6208-6218, 2008.

[66] C. -L. Liu, H. -R. Zhu, and J. -T. Bai, "New Developlemt of the Turbulent Prandtl Number Models for the Computation of Film Cooling Effectiveness," *Int. J. Heat Mass Trans.*, vol. 54, pp. 874-886, 2011.

[67] D. Lakehal, "Near-Wall Modeling of Turbulent Convective Heat Transport in Film Cooling of Turbine Blades with the Aide of Direct Numerical Simulation Data," *J. Turbomach.*, vol. 124, pp. 485-498, Jul. 2002.

[68] A. Azzi and D. Lakehal, "Perspectives in Modeling Film Cooling of Turbine Blades by Transcending Conventional Two-Equation Turbulence Models," *J. Turbomach.*, vol. 124, pp. 472-484, Jul. 2002.

[69] S. D. Bradshaw, Personal Communication, 2011.

[70] Y. Pichon, "Turbulence Field Measurements for the Large Windtunnel," The University of Texas at Austin, Austin, TX USA, TTCRL Internal Report 2009.

[71] J. M. Cutbirth, "Turbulence and Three-Dimensional Effects on a Film Cooled Turbine Vane," The University of Texas, Austin, TX, USA, PhD Dissertation 2000.

[72] M. D. Polanka, V. C. Witteveld, and David G. Bogard, "Film Cooling Effectiveness in the Showerhead Region of a Gas Turbine Vane Part I: Stagnation Region and Near Pressure Side," in *ASME paper 99-GT-048*, Indianapolis, IN, USA, 1999.

[73] J. E. Dees, "Experimental Measurements of Conjugate Heat Transfer on a Scaled-up Gas Turbine Airfoil with Realistic Cooling Configuration," The University of Texas, Austin, TX, USA, PhD Dissertation 2010.

[74] General Plastics Manufacturing Co., "LAST-A-FOAM R-3315 Rigid Polyurethane Foam," Tacoma, WA, USA, Data Sheet 2010.

[75] E. I. DuPont de Nemours & Co., Inc., *Corian Fabrication Manual*., 2007.

[76] R. S. Bunker, "The Effects of Manufacturing Tolerances on Gas Turbine Cooling," *J. Turbomach.*, vol. 131, Oct. 2009.

[77] R. E. Chupp, H. E. Helms, P. W. McFadden, and T. R. Brown, "Evaluation of Internal Heat Transfer Coefficients for Impingement Cooled Turbine Airfoils," *J. Aircraft*, vol. 6, pp. 203-208, 1969.

[78] S. D. Bradshaw, Personal Communication, 2010.

[79] T. E. Dyson, *Design & Computation Book No. 3*., 2012.

[80] Thermon Manufacturing Co., "NH Nonhardening Heat Transfer Compound," San Marcos, TX, USA, Product Specification 2012.

[81] M. Gritsch, A. Schulz, and S. Wittig, "Effect of Crossflows on the Discharge Coefficient of Film Cooling Holes with Varying Angles of Inclination and Orientation," *J. Turbomach.*, vol. 123, pp. 781-787, Oct. 2001.

[82] J. E. Albert, "Experimental Simulation and Mitigation of Contaminant Deposition," The University of Texas, Austin, TX, USA, PhD Dissertation 2011.

[83] F. T. Davidson, "An Experimental Study of Film Cooling, Thermal Barrier Coatings and Contaminant Deposition on an Internally Cooled Turbine Airfoil Model," The Univeristy of Texas, Austin, TX, USA, PhD Dissertation 2012.

[84] S. K. Waye, "Film Cooling Effectiveness of Suction Side Axial Holes, Compound Angle Holes, and Axial Holes Embedded within an Overlying Transverse Trench," The University of Texas, Austin, TX, USA, Master's Thesis 2005.

[85] R. J. Moffat, "Using Uncertainty Analysis in the Planning of an Experiment," *J. Fluids Eng.*, no. 107, pp. 173-178, Jun. 1985.

[86] T. E. Dyson, "Effects of Hole Pitch Variation on Overall and Internal Effectiveness in the Leading Edge Region of a Simulated Turbine Blade with Heat Flux Measurements," The University of Texas, Austin, TX, USA, Master's Thesis 2010.

[87] J. P. Bons, R. B. Rivir, and C. D. Mac Arthur, "The Effect of High Freestream Turbulence on Film Cooling Effectiveness," Aero Propulsion & Power Directorate Wright Laboratory, Dayton, OH, USA, Technical Report WL-TR-96-2097, 1994.

[88] D. L. Schmidt and D. G. Bogard, "Effects of Free-Stream Turbulence and Surface Roughness on Film Cooling," in *ASME International Gas Turbine and Aeroengine Congress*, Birmingham, UK, 1996, pp. 96-GT-462.

[89] S. Ito, R. J. Goldstein, and E. R. G. Eckert, "Film Cooling of a Gas Turbine Blade," *J. Eng. Power*, vol. 100, pp. 476-481, Jul. 1978.

[90] V. C. Witteveld, M. D. Polanka, and David G. Bogard, "Film Cooling Effectiveness in the Showerhead Region of a Gas Turbine Vane Part II: Stagnation Region and Near Suction Side," in *ASME paper 99-GT-049*, Indianapolis, IN, USA, 1999.

[91] J. M. Cutbirth and D. G. Bogard, "Thermal Field and Flow Visualization Within the Stagnation Region of a Film-Cooled Turbine Vane," *J. Turbomach.*, vol. 124, pp. 200-206, Apr. 2002.

[92] E. J. Terrell, B. D. Mouzon, and D. G. Bogard, "Convective Heat Transfer through Film Cooling Holes of a Gas Turbine Leading Edge," in *ASME Turbo Expo*, Reno, NV, USA, 2005, pp. GT2005-69003.

[93] SAS IP, Inc., "Pressue Interpolation Schemes," in *ANSYS FLUENT Theory Guide*. Canonsburg, PA, USA: ANSYS , Inc., 2010, ch. 19.4.1.1, pp. 598-599.

[94] DuPont Corian Solid Surfaces, *The Corian Book: Design & Technical Information*.: www.corian.com, 2005.

[95] M. Silieti, A. J. Kassab, and E. Divo, "Film Cooling Effectiveness: Comparison of Adiabatic and Conjugate Heat Transfer CFD Models," *International Journal of Thermal Sciences*, vol. 48, pp. 2237-2248, April 2009.

[96] SAS IP, Inc., "Wall Functions vs. Near-Wall Model," in *ANSYS FLUENT 13 Theory Guide*. Canonsburg, PA, USA: ANSYS, Inc., 2010, ch. 4.13.1.1, pp. 115-116.

[97] R. Toé, A. Ajakh, and H. Peerhossaini, "Heat Transfer Enhancement by Görtler Instability," *Int. J. Heat Fluid Flow*, vol. 23, pp. 194-204, 2002.

[98] S. B. Pope, *Turbulent Flows*, 1st ed. New York, NY, USA: Cambridge University Press, 2006.

[99] M. D. Polanka, M. I. Ethridge, J. M. Cutbirth, and D. G. Bogard, "Effects of Showerhead Injection on Film Cooling Effectiveness for a Downstream Row of Holes," in *ASME Turbo Expo*, Munich, Germany, 2000, pp. 2000-GT-240.

[100] A. F. Mills, "Forced Flow in Tubes and Ducts," in *Heat Transfer 2nd Ed.* Upper Saddle River, NJ, USA: Prentice Hall, 1999, ch. 4.3.1, pp. 301-303.

[101] P. R. Spalart, "Direct Simulation of a Turbulent Boundary Layer Up to Rθ = 1410," *J. Fluid Mech.*, vol. 187, pp. 61-98, Feb. 1988.

[102] A. E. Alving, A. J. Smits, and J. H. Watmuff, "Turbulent Boundary Layer Relaxation From Convex Curvature," *J. Fluid Mech.*, vol. 211, pp. 529-556, Feb. 1990.

[103] J. E. Dees, D. G. Bogard, G. A. Ledezma, and G. M. Laskowski, "The Effects of Conjugate Heat Transfer on the Thermal Field Above a Film Cooled Wall," in *ASME Turbo Expo*, Vancouver, BC, Canada, 2011, pp. GT2011-46617.

[104] U. M. Yuki, David G. Bogard, and J. M. Cutbirth, "Effect of Coolant Injection on Heat Transfer for a Simulated Turbine Airfoil Leading Edge," in *ASME Turbo Expo*, Stockholm, Sweden, 1998.

[105] C. A. Johnston, D. G. Bogard, and M. A. McWaters, "Highly Turbulent Mainstream Effects on Film Cooling of a Simulated Turbine Airfoil Leading Edge," in *ASME Turbo Expo*, Indianapolis, IN, USA, 1999.

[106] F. R. Menter, R. B. Langtry, S. R. Likki, and Y. B. Suzen, "A Correlation-Based Transition Model Using Local Variables - Part I: Model Formulation," *J. Turbomach.*, vol. 128, no. 3, pp. 413-423, Jul. 2006.

[107] SAS IP, Inc., "Modeling Turbulence," in *ANSYS FLUENT 13 User's Guide*. Canonsburg, PA, USA: ANSYS, Inc., 2010, ch. 13, pp. 643-690.

[108] J. E. Dees, D. G. Bogard, G. A. Ledezma, G. M. Laskowski, and A. K. Tolpadi, "Experimental Measurements and Computational Predictions for an Internally Cooled Simulated Turbine Vane," in *ASME International Mechanical Engineering Congress & Exposition*, Lake Buena Vista, FL, USA, 2009, pp. IMECE2009-11622.

[109] S. Navarro-Martinez and O. R. Tutty, "Numerical Simulation of Gortler Vortices in Hypersonic Compression Ramps," *Comput. Fluids*, vol. 34, pp. 225-247, 2005.

[110] D. C. Wilcox, *Turbulence Modeling for CFD*, 1st ed. La Canada, CA, USA: DCW Industries, Inc., 1993.

[111] B. E. Launder and F. C. Lockwood, "An Aspect of Heat Transfer in Accelerating Turbulent Boundary Layer Flows," *J. Heat Trans.*, vol. 91, pp. 229-234, May 1969.

[112] W. M. Kays, R. J. Moffat, and W. H. Theilbahr, "Heat Transfer to the Highly Accelerated Turbulent Boundary Layer with and without Mass Addition," *J. Heat Trans.*, vol. 92, pp. 499-505, Aug. 1970.

[113] J. Sucec, "An Integral Solution for Heat Transfer in Accelerating Turbulent Boundary Layers," *J. Heat Trans.*, vol. 131, Nov. 2009.

[114] W. M. Kays and M. E. Crawford, "A Conduction Model for Turbulent Prandtl Number," in *Convective Heat and Mass Transfer*, J. J. Corrigan and J. M. Morriss, Eds. New York, NY, USA: McGraw-Hill, 1993, ch. 13, pp. 266-268.

Vita

Thomas Dyson was born in Webster, Texas. He lived there until he graduated from Clear Lake High School in 2001. Thomas then attended Texas A&M University's College Station campus. In December 2005, he received a B.S.M.E. from that institution.

While attending college, Thomas worked summers for Tietronix Software, Inc., a NASA contractor in Houston, Texas. Upon graduation, he accepted a position as a programmer/designer with Tietronix. He worked there until late 2007, when he moved to Austin to attend graduate school at the University of Texas at Austin starting in January of 2008.

Thomas worked in the Turbulence and Turbine Cooling Research Laboratory facility, and completed the requirements for a Master's of Science in Mechanical Engineering in May of 2010. During that time he was a UTSR Fellow, working with Pratt & Whitney as part of that program. Thomas accepted a position as part of the Turbine Heat Transfer Technology Lab at GE's Global Research Center in Schenectady, NY, where he began work in 2013.

Permanent Address: 15443 Runswick, Houston, TX 77062

This dissertation was typed by the author.